

---

# Primordial features and non-Gaussianities

---

by

**Dhiraj Kumar Hazra**

Enrolment Number : PHYS08200605006

Harish-Chandra Research Institute, Allahabad

A Thesis submitted to the  
Board of Studies in Physical Science Discipline  
in partial fulfillment of the requirements  
for the degree of

**DOCTOR OF PHILOSOPHY**  
of  
**Homi Bhabha National Institute**



October 2012



## Certificate

---

This is to certify that the Ph.D. thesis entitled **Primordial features and non-Gaussianities** submitted by **Dhiraj Kumar Hazra** for the award of the degree of Doctor of Philosophy is a record of bona fide research work done under my supervision. It is further certified that the thesis represents the independent work done by the candidate and collaboration was necessitated by the nature and scope of the problems dealt with.

**Dr. L. Sriramkumar**  
(Thesis Supervisor)

Date:



# Declaration

---

This thesis is a presentation of my original research work. Whenever contributions of others are involved, every effort is made to indicate this clearly, with due reference to the literature and acknowledgment of collaborative research and discussions.

The work is original and has not been submitted earlier as a whole or in part for a degree or diploma at this or any other institution or university.

This work was done under the guidance of Dr. L. Sriramkumar, at Harish Chandra Research Institute, Allahabad, India.

Date:

**Dhiraj Kumar Hazra**  
(Ph.D. Candidate)



**Dedicated to  
my uncle Abhijit Hazra**



## Acknowledgments

---

According to a popular adage in the scientific community, writing the acknowledgement is more challenging than writing the thesis itself. Because, there is always a risk of omission which can lead to friendly misunderstandings! So, accepting my inability to remember names and instances, I would like to thank all the people I have encountered in this significant journey of my life.

I owe a very special gratitude to my thesis supervisor Dr. L. Sriramkumar. Apart from providing me with interesting and relevant problems to work on, he helped me improve my way of thinking, showed me proper direction when I felt stuck and provided me with confidence in moments of frustration. I am really grateful for the way he guided me throughout my Ph.D., both academically and non-academically. Sriram has given me a lot of freedom and inspiration in exploring various aspects not only of cosmology but of physics as a whole. Like a family member, he has assisted me profoundly in life beyond physics during my entire Ph.D. career. I am simply indebted to Sriram in great many ways. I must also thank Sriram's wife Jaya for her appreciation and support.

I would like to thank my collaborators Prof. Tarun Souradeep and Prof. Jérôme Martin with whom a considerable part of this thesis work has been done. Discussions with Tarun and Jérôme have helped me a lot in understanding the physics behind the problems we were working on. I am also grateful to my other collaborator, Dr. Tapomoy Guha Sarkar, who introduced me to a completely new area of cosmology. I learnt a lot from Dr. Tirthankar Roy Choudhury, with whom I had done my project work that formed a part of the graduate program. I found the collaboration with Dr. Rajeev Kumar Jain and Dr. Moumita Aich a very pleasant experience. Prof. Soumitra Sengupta, being a mentor from my undergraduate days at Jadavpur University, Kolkata, constantly inspired me throughout my doctoral work.

My alma mater, Harish-Chandra Research Institute (HRI), where I spent more than six years during my Master's and Ph.D., offered a great learning atmosphere through the course-work, lectures and discussion sessions with friends and faculty members. Being an extensive numerical programmer, high performance computing facility is an absolute necessity. The cluster computing facility at HRI provided all the tools to pursue my research. I thank all the members who constituted the Astrophysics group at HRI.

Without the support of my family, especially my uncle Abhijit Hazra, to whom this

## ACKNOWLEDGMENTS

---

thesis is dedicated, I could not have completed the thesis. My wife Monalisa played a very vital role in my pursuing the Ph.D. degree. She understands perfectly how life is for a research scholar and makes things easier for me. Her constant support and inspiration elevated the level of my work.

When it comes to my friends, all the worries, frustrations and difficulties were smoothed over by their presence. My seniors Mama, Kaka, Subhada, JD had given me every possible advice to overcome many hurdles. Sanjoyda (a.k.a Harr), who is like my elder brother, taught me physics in the simplest way I could imagine. Being a friend from my undergraduate days at Jadavpur, Niyogi has always been a companion in my studies as well as in many aspects of life. I must mention Pandu, with whom I shared a passion to explore the new features of Linux. During my Master's and Ph.D. here at HRI, troubled times were always diluted by the indoor and outdoor games with Pandu, Sanjoyda and Niyogi. As a fellow post-B.Sc. student, Satya was an integral part of my journey in the field of research. Sharing jokes and fun with Bhuru was an inseparable part during my stay at HRI. I always enjoyed the sleepless nights at HRI with Sanjoyda, JD, Mama, Shamikda, Kaka, Niyogi, Pandu, Satya, Bhuru, Hochi, Ramva, Manoj, Jonthu, Rana and many more, discussing every possible topic on Earth. I salute the simple cup of tea at the HRI guest house which was the abstract source of energy for the research here. Sumitda from Jadavpur has been appreciative as well as critical of my efforts, and had also provided me with inspiration when I needed it. So, in a word, I have been privileged to have good friends, and I think my thesis has been enriched by their presence.

# Abstract

Currently, inflation is the most promising paradigm to describe the origin of the perturbations in the early universe. Most models of inflation permit a sufficiently long epoch of slow roll inflation, which, in turn, leads to a featureless, nearly scale invariant, power law, primordial scalar spectrum. Such a spectrum, along with the assumption of a spatially flat, concordant  $\Lambda$ CDM [*i.e.* involving the cosmological constant  $\Lambda$  and Cold Dark Matter CDM)] background cosmological model, provides a good fit to the recent observations of the anisotropies in the Cosmic Microwave Background (CMB) by missions such as the Wilkinson Microwave Anisotropy Probe (WMAP).

Even though, as a broad paradigm, inflation can be termed as a success, it would be fair to say that we are still some distance away from converging upon a specific model or even a class of models. There exist a wide variety of inflationary models that remain consistent with the data. While a nearly scale invariant, power law, scalar spectrum fits the observations of the anisotropies in the CMB quite well, there exist a few data points at the lower multipoles, which lie outside the cosmic variance associated with the conventional power law primordial spectrum. Statistically, a few outliers in a thousand or so data points are always expected. However, these outliers can be handy from the phenomenological perspective of attempting to constrain the models from the data, since only a more restricted class of inflationary models can be expected to provide an improved fit to these outliers. Therefore, it is a worthwhile exercise to explore models that lead to certain deviations from the standard power law, inflationary perturbation spectrum, and also provide a better fit to the data.

Over the last few years, it has been recognized that primordial non-Gaussianity can act as a powerful probe to help us discriminate further between the various inflationary models. For instance, it is known that slow roll inflation driven by the canonical scalar fields leads only to a small amount of non-Gaussianity. But, recent analyses of the WMAP data seem to suggest that primordial non-Gaussianity may possibly be large. Ongoing missions such as Planck are expected to determine the extent of non-Gaussianity in the

CMB more accurately. It is known that models which lead to features also generate a reasonably large amount of non-Gaussianity. One of the aims of this thesis work has been to systematically explore inflationary models that give rise to specific features in the perturbation spectrum which result in an improved fit to the data, and also lead to observed (or, observable) levels of non-Gaussianity.

Broadly, this thesis can be divided into two parts. While the first part can be said to be devoted to the signatures of features and non-Gaussianities on the CMB, the second focuses on their possible observational imprints in the matter dominated epoch. In the first part, we shall begin with a discussion on the generation of localized as well as non-local features (*i.e.* characteristic and repeated patterns that extend over a wide range of scales) in the inflationary scalar power spectrum that lead to a better fit to the CMB data than the more standard power law spectrum. We shall also investigate the bi-spectra that result in such scenarios, and study as to how they compare with the current observational limits on the non-Gaussianity parameter  $f_{\text{NL}}$ . In this context, we shall also discuss the effects of preheating in single field inflationary models on the evolution of the bi-spectrum. In the second part of the thesis, after considering the effects of primordial features on the formation of halos, we shall discuss the possibility of utilizing the observations of the Ly- $\alpha$  forest towards constraining primordial non-Gaussianity. In what follows, we shall provide a brief outline of these different issues. (The reference numbers that appear here correspond to the publications and preprints listed below.)

**Generation of localized features due to a step in the inflaton potential:** A short burst of oscillations over suitable scales in the primordial scalar power spectrum have been known to result in an improved fit to the outliers in the CMB data near the multipole moments of  $\ell = 22$  and 40. Typically, such features have been generated with the introduction of a step in the conventional, quadratic potential involving the canonical scalar field. Such a quadratic potential will cease to be consistent with the data, if the tensors remain undetected at a level corresponding to a tensor-to-scalar ratio of, say,  $r \simeq 0.1$ . Apart from the popular quadratic potential, we investigate the effects of the introduction of the step in a small field model as well as a tachyon model [1]. Further, motivated by possible applications to future datasets (such as, say, Planck), we evaluate the tensor power spectrum exactly, and include its contribution in our analysis. We compare the inflationary models with the WMAP (five as well as seven-year), the QUEST at DASI (QUaD) and the Arcminute Cosmology Bolometer Array Receiver (ACBAR) data. As expected, a step at a particular location and of a suitable magnitude and width is found to fit the outliers (near  $\ell = 22$  and 40) better, in all the models that we consider. We highlight the fact that, if the

tensors prove to be small (say,  $r \lesssim 0.01$ ), the quadratic potential and the tachyon model will not remain viable, and one would have to pay more attention to examples such as the small field models.

**Non-local features in the primordial spectrum:** Apart from localized features, such as those arising due to a step in the inflationary potentials, it is interesting to examine if non-local features—*i.e.* certain characteristic and repeated patterns that extend over a wide range of scales—in the scalar power spectrum can also provide a better fit to the CMB data than the conventional, nearly scale invariant, primordial spectrum. With such a motivation in mind, we consider the model described by a quadratic potential which is superposed by a sinusoidal modulation and the recently popular axion monodromy model. The oscillatory terms in these inflaton potentials lead to modulations in the corresponding scalar power spectra that extend over a wide range of scales [2]. Evaluating the scalar power spectra numerically, we compare the models with the WMAP data. Moreover, as the oscillations continue even onto smaller scales, we also include the small scale data from the Atacama Cosmology Telescope (ACT) in our analysis. Though, both the models, broadly, result in oscillations in the spectrum, interestingly, we find that, while the monodromy model leads to a considerably better fit to the data in comparison to the standard power law spectrum, the quadratic potential superposed with a sinusoidal modulation does not improve the fit to a similar extent.

**Bi-spectra associated with local and non-local features:** Presently, the primordial scalar bi-spectrum is often characterized by the parameter  $f_{\text{NL}}$ , which is a suitable dimensionless ratio of the scalar bi-spectrum to the corresponding power spectrum. We present the first complete calculation of the parameter  $f_{\text{NL}}$  for a variety of single field inflationary models that lead to features in the scalar power spectrum [3]. The calculation is based on the formalism due to Maldacena to evaluate the bi-spectrum in a given inflationary model. It is performed numerically by means of a new, efficient and accurate Fortran code that can evaluate all the contributions to the bi-spectrum for any configuration of the wavenumbers. We consider different sets of models that lead to similar features in the scalar power spectrum, and investigate if  $f_{\text{NL}}^{\text{eq}}$  (*viz.*  $f_{\text{NL}}$  evaluated in the equilateral configuration) can help us discriminate between the models. We find that certain differences in the background dynamics—reflected in the behavior of the slow roll parameters—can lead to a reasonably large difference in the  $f_{\text{NL}}^{\text{eq}}$  generated by the models.

**The scalar bi-spectrum during preheating:** In single field inflationary models, preheating refers to the phase that immediately follows inflation, but precedes the epoch of reheating. During this phase, the inflaton typically oscillates at the bottom of its potential

and gradually transfers its energy to radiation. At the same time, the amplitude of the fields coupled to the inflaton may undergo parametric resonance and, as a consequence, explosive particle production can take place. A priori, these phenomena could lead to an amplification of the super-Hubble scale curvature perturbations which, in turn, would modify the standard inflationary predictions. However, remarkably, it has been shown that, although the Mukhanov-Sasaki variable does undergo narrow parametric instability during preheating, the amplitude of the corresponding super-Hubble curvature perturbations remain constant. Therefore, in single field models, metric preheating does not affect the power spectrum of the large scale perturbations. We investigate the corresponding effect on the scalar bi-spectrum [4]. Using the above-mentioned Maldacena's formalism, we analytically show that, for modes of cosmological interest, the contributions to the scalar bi-spectrum as the curvature perturbations evolve on super-Hubble scales during preheating is completely negligible. Specifically, we illustrate that, certain terms in the third order action governing the curvature perturbations which may naively be expected to contribute significantly are exactly canceled by other contributions to the bi-spectrum. We corroborate selected analytical results by numerical investigations. We also discuss the possible wider implications of the results.

**Effects of primordial features on the formation of halos:** As we have repeatedly mentioned, features in the primordial scalar power spectrum provide a possible roadway to describe the outliers at the low multipoles in the WMAP data. Apart from the CMB angular power spectrum, these features can also alter the matter power spectrum and, thereby, the formation of the large scale structure. Carrying out a complete numerical analysis, we investigate the effects of primordial features on the formation rates of the halos. We consider a few different inflationary models that lead to features in the scalar power spectrum and an improved fit to the CMB data, and analyze the corresponding imprints on the formation of halos [5]. Performing a Markov Chain Monte Carlo analysis with the WMAP and the Sloan Digital Sky Survey (SDSS) data for the models of our interest, we arrive at the parameter space of the models allowed by the data. We illustrate that, inflationary potentials, such as the quadratic potential with sinusoidal modulations and the axion monodromy model, which generate certain repeated, oscillatory, features in the inflationary perturbation spectrum, do not induce substantial difference in the number density of halos at their best fit values, when compared with, say, a nearly scale invariant spectrum as is generated by the standard quadratic potential. However, we find that the number density and the formation rates of halos change by about 20% for halo masses ranging over  $10^4$ – $10^{14} M_{\odot}$ , corresponding to potential parameters that lie within  $2\text{-}\sigma$  from

the best fit values arrived at from the aforesaid joint constraints.

**Imprints of primordial non-Gaussianity in the Ly-alpha forest:** We investigate the possibility of constraining primordial non-Gaussianity using the three dimensional bispectrum of the Ly- $\alpha$  forest [6]. The strength of the quadratic non-Gaussian correction to an otherwise Gaussian primordial gravitational field is assumed to be dictated by the parameter  $f_{\text{NL}}$ . We present the first prediction for bounds on  $f_{\text{NL}}$  using Ly- $\alpha$  flux spectra along multiple lines of sight. The three dimensional Ly- $\alpha$  transmitted flux field is modeled as a biased tracer of the underlying matter distribution sampled along one dimensional skewers corresponding to quasars sight lines. The precision to which  $f_{\text{NL}}$  can be constrained depends on the survey volume, pixel noise and aliasing noise (arising from the discrete sampling of the density field). We consider various combinations of these factors to predict bounds on  $f_{\text{NL}}$ . We find that, in an idealized situation of full sky survey and negligible Poisson noise, one may constrain  $f_{\text{NL}} \sim 23$  in the equilateral limit. Assuming a Ly- $\alpha$  survey covering large parts of the sky ( $k_{\text{min}} = 8 \times 10^{-4} \text{ Mpc}^{-1}$ ) and with a quasar density of  $\bar{n} = 5 \times 10^{-3} \text{ Mpc}^{-2}$ , we show that it is possible to constrain  $f_{\text{NL}} \sim 23$  for the equilateral configurations. The possibility of measuring  $f_{\text{NL}}$  at a precision comparable to the large scale structure may be useful for joint constraining of inflationary scenarios using different data sets.

## List of publications and preprints

---

1. **D. K. Hazra**, M. Aich, R. K. Jain, L. Sriramkumar and T. Souradeep, *Primordial features due to a step in the inflaton potential*, *JCAP* **1010**, 008 (2010).
  2. M. Aich, **D. K. Hazra**, L. Sriramkumar and T. Souradeep, *Oscillations in the inflaton potential: Exact numerical analysis and comparison with the recent and forthcoming CMB datasets*, *arXiv:1106.2798v1 [astro-ph.CO]*.
  3. **D. K. Hazra**, L. Sriramkumar and J. Martin, *On the discriminating power of  $f_{\text{NL}}$* , *arXiv:1201.0926v1 [astro-ph.CO]*.
  4. **D. K. Hazra**, J. Martin and L. Sriramkumar, *The scalar bi-spectrum during preheating in single field inflationary models*, *Phys. Rev. D* **86**, 063523 (2012).
  5. **D. K. Hazra**, *Changes in the halo formation rates due to features in the primordial spectrum*, *In preparation*.
  6. **D. K. Hazra** and T. G. Sarkar, *Primordial non-Gaussianity in the forest: 3D bi-spectrum of Ly-alpha flux spectra along multiple lines of sight*, *Phys. Rev. Lett.* **109**, 121301, (2012).
-

# Contents

<b>1</b>	<b>Introduction</b>	<b>1</b>
1.1	The concordant, background cosmological model	5
1.2	The inflationary paradigm	7
1.2.1	The resolution of the horizon problem through inflation	7
1.2.2	Driving inflation with scalar fields	9
1.2.3	The generation of perturbations during inflation	11
1.3	The generation and imprints of non-Gaussianities	18
1.4	Post-inflationary dynamics	20
1.5	The formation of the large scale structure	20
1.6	Theme and outline of the thesis	22
1.7	Notations and conventions	23
<b>2</b>	<b>Generation of localized features</b>	<b>25</b>
2.1	The inflationary models of interest	27
2.1.1	The power law case	27
2.1.2	Canonical scalar field models	28
2.1.3	Tachyon model	28
2.1.4	Introduction of the step	29
2.2	Methodology, datasets, and priors	29
2.3	Bounds on the parameters	33
2.3.1	The best fit values and the effective least squares parameter $\chi_{\text{eff}}^2$	33
2.4	The scalar and the CMB angular power spectra	37
2.5	Discussion	40
<b>3</b>	<b>Non-local features in the primordial spectrum</b>	<b>43</b>
3.1	Models and methodology	44
3.1.1	The models	44

3.1.2	Priors . . . . .	45
3.1.3	Comparison with the recent CMB observations . . . . .	46
3.2	Results . . . . .	48
3.2.1	The best fit background and inflationary parameters . . . . .	48
3.2.2	The spectra and the improvement in the fit . . . . .	49
3.3	Discussion . . . . .	54
<b>4</b>	<b>Bi-spectra associated with local and non-local features</b>	<b>57</b>
4.1	Models of interest and power spectra . . . . .	59
4.1.1	Inflationary potentials with a step . . . . .	59
4.1.2	Oscillations in the inflaton potential . . . . .	60
4.1.3	Punctuated inflaton and the Starobinsky model . . . . .	60
4.1.4	The power spectra . . . . .	61
4.2	The scalar bi-spectrum in the Maldacena formalism . . . . .	63
4.3	The numerical computation of the scalar bi-spectrum . . . . .	65
4.3.1	The contributions to the bi-spectrum on super-Hubble scales . . . . .	65
4.3.2	An estimate of the super-Hubble contribution to the non-Gaussianity parameter . . . . .	70
4.3.3	Details of the numerical methods . . . . .	73
4.3.4	Comparison with the analytical results in the cases of power law inflation and the Starobinsky model . . . . .	76
4.4	Results in the equilateral limit . . . . .	81
4.5	Discussion . . . . .	84
<b>5</b>	<b>The scalar bi-spectrum during preheating</b>	<b>85</b>
5.1	Behavior of background and perturbations during preheating . . . . .	87
5.1.1	Background evolution about a quadratic minimum . . . . .	87
5.1.2	Evolution of the perturbations . . . . .	92
5.2	The contributions to the bi-spectrum during preheating . . . . .	98
5.2.1	The fourth and the seventh terms . . . . .	98
5.2.2	The second term . . . . .	99
5.2.3	The remaining terms . . . . .	100
5.2.4	The contribution to $f_{\text{NL}}$ during preheating . . . . .	103
5.3	Discussion . . . . .	104

---

<b>6</b>	<b>Effects of primordial features on the formation of halos</b>	<b>107</b>
6.1	Models and comparison with the data . . . . .	108
6.1.1	Comparison with the CMB and the LSS data . . . . .	110
6.2	From the primordial spectrum to the formation rate of halos . . . . .	111
6.2.1	The matter power spectrum . . . . .	111
6.2.2	Mass functions and the halo formation rates . . . . .	112
6.3	The numerical methods: Essentials . . . . .	113
6.4	Results . . . . .	114
6.4.1	Joint constraints from the WMAP and the SDSS data . . . . .	114
6.4.2	Effects of features in the number density and the formation rate of halos . . . . .	116
6.5	Discussion . . . . .	120
<b>7</b>	<b>Imprints of primordial non-Gaussianity in the Ly-alpha forest</b>	<b>123</b>
7.1	Formalism . . . . .	125
7.2	Results . . . . .	130
7.3	Conclusions . . . . .	133
<b>8</b>	<b>Summary and outlook</b>	<b>135</b>
8.1	Summary . . . . .	135
8.2	Outlook . . . . .	136



# List of Tables

2.1	The priors on the parameters in the inflationary models of interest . . . . .	32
2.2	The best fit values for the parameters of the power law primordial spectra, upon comparison with the various CMB datasets . . . . .	34
2.3	The best fit values for the inflationary models with a step, when compared with the different CMB datasets . . . . .	35
2.4	The $\chi_{\text{eff}}^2$ for the different inflationary models (with and without the step) and the datasets considered . . . . .	36
3.1	The priors on the parameters in the inflationary models considered . . . . .	46
3.2	The best fit values for the background and the inflationary parameters for potentials with oscillations . . . . .	49
3.3	The $\chi_{\text{eff}}^2$ for the different models and datasets considered . . . . .	50
6.1	Widened priors for the inflationary parameters in the case of potentials with oscillatory terms . . . . .	110
6.2	The best fit values for the background and the potential parameters arrived at upon comparison with the WMAP and the SDSS data . . . . .	115
7.1	The bounds on $(f_{\text{NL}}, b_1)$ obtained from a Fisher analysis for various combinations of $(k_{\text{min}}, \bar{n}, S/N)$ . . . . .	132



# List of Figures

1.1	A schematic timeline of the universe . . . . .	4
1.2	Evolution of the physical wavelength and the Hubble radius during the inflationary and the radiation dominated epochs . . . . .	9
1.3	The theoretical and the observed CMB (TT) angular power spectra . . . . .	17
2.1	The difference in $\chi_{\text{eff}}^2$ with and without the step, plotted as a function of the multipoles . . . . .	36
2.2	Typical evolution of the first slow roll parameter $\epsilon_1$ and the quantity $\eta$ around a step in an inflationary potential . . . . .	37
2.3	The scalar power spectra corresponding to the best fit values of the WMAP seven-year data for inflationary models with the step . . . . .	38
2.4	The CMB TT angular power spectra corresponding to the best fit values of the inflationary models for the WMAP seven-year data without and with the step . . . . .	39
3.1	The difference in $\chi_{\text{eff}}^2$ between the axion monodromy model and the reference model, plotted as a function of the multipoles . . . . .	51
3.2	The scalar power spectrum corresponding to the best fit values of inflationary potentials containing oscillatory terms . . . . .	52
3.3	The CMB TT angular power spectrum in inflationary models containing oscillatory terms in the potential . . . . .	53
4.1	The scalar power spectra in the different types of models that we consider . . . . .	62
4.2	The behavior of the different contributions to the bi-spectrum, plotted as a function of cut off parameter $\kappa$ , for the case of the quadratic potential . . . . .	75
4.3	The behavior of the different contributions to the bi-spectrum, plotted as a function of the upper limit of the integrals, for the case of the quadratic potential . . . . .	76

## LIST OF FIGURES

---

4.4	The spectral dependence of the non-vanishing contributions to the bi-spectrum and the corresponding non-Gaussianity parameter in power law inflation . . . . .	78
4.5	The different contributions to the bi-spectrum in the case of the Starobinsky model . . . . .	80
4.6	The various contributions to the bi-spectrum in the different inflationary models of our interest . . . . .	82
4.7	The non-Gaussianity parameter in the equilateral limit, <i>viz.</i> $f_{\text{NL}}^{\text{eq}}$ , in the different inflationary models considered . . . . .	83
5.1	The behavior of the scalar field and the first slow roll parameter during inflation and preheating . . . . .	88
5.2	The evolution of the second slow roll parameter during preheating . . . . .	90
5.3	The behavior of the curvature perturbation during preheating . . . . .	97
5.4	The behavior of the quantity $\mathcal{G}_2(k)$ during preheating . . . . .	101
6.1	The evolution of the first two slow roll parameters in inflationary potentials with a step and oscillatory terms . . . . .	109
6.2	One and two dimensional constraints on the inflationary parameters . . . . .	116
6.3	The scalar power spectrum for the models with local and non-local features . . . . .	117
6.4	The theoretical matter power spectrum for the models with features plotted against the SDSS data . . . . .	118
6.5	The change in the number density and the formation rate of halos for the models with features . . . . .	119
7.1	The likelihood contours of the non-Gaussianity and the bias parameters $f_{\text{NL}}$ and $b_1$ . . . . .	131

# Chapter 1

## Introduction

At a first glance, the universe around us appears to be highly clumpy, with matter seemingly distributed in a rather non-uniform fashion. However, observations of millions of galaxies by different galaxy surveys such as the Two-degree-Field (2dF) galaxy redshift survey [1, 2] and the Sloan Digital Sky Survey (SDSS) [3, 4] indicate the universe to be homogeneous and isotropic on suitably large scales. These surveys suggest that the transition to homogeneity of the galaxy distribution occurs at length scales of around 100 Mpc or so (in this context, see, for instance, Ref. [5]). On such large scales, it is General Relativity (GR) which is the theory that is expected to describe the universe. In GR, the fundamental quantity is the metric describing the spacetime, whose dynamics is determined by the matter through the Einstein field equations. The metric that describes the homogeneous and isotropic universe is referred to as the Friedmann-Lemaitre-Robertson-Walker (or, for convenience, simply Friedmann) line-element, which is essentially characterized by two quantities (see, for example, any of the following texts [6]). The first being the curvature of the spatial geometry of the universe, while the second is the scale factor  $a(t)$ , which allows one to account for the observed expansion of the universe. The quantity  $t$  denotes the cosmic time, *i.e.* the time as measured by clocks that are comoving with the expansion.

The behavior of the scale factor  $a(t)$  is governed by the constituents of the universe through the Friedmann equations, which are the Einstein equations applied to the case of the Friedmann metric. A variety of observations point to the density of the universe today being rather close to the so-called critical density (with the dimensionless ratio of the actual density to the critical density deviating from unity by about one part in  $10^2$ ), which corresponds to a geometry that is spatially rather flat. Till date, through different observations, we are aware of the fact that baryons (*i.e.* visible matter) and photons (*viz.* radiation)

together constitute less than 5% of the matter density of the universe today. The predictions of the theory of the formation of structures, when compared with the observations, point to the presence of another type of non-relativistic matter—commonly known as the cold or, nowadays, simply as the dark matter—in the universe, which interacts only with gravity. The dark matter, whose true nature remains to be understood, contributes to about 25% of the total matter density of the universe today. The rest of the universe is filled with dark energy, about which we only know that it possesses negative pressure and that it is responsible for the current accelerated expansion of the universe [6].

The evolution of the energy densities of the different components of the universe is determined by the corresponding equations of state. The energy densities of matter (both baryonic as well as dark matter) and radiation fall cubically and quartically, respectively, as the inverse power of scale factor  $a(t)$ . The energy density associated with the dark energy, though, remains largely constant in time. We mentioned above that it is the energy density of the dark energy that dominates the universe today. When one goes back in time, as the scale factor decreases, there arises an epoch when matter begins to dominate. Going further back in time leads to the era of radiation domination and, on proceeding beyond, one eventually encounters a singularity, which is popularly referred to as the big bang. Such a model of the universe wherein the universe emerges from a singularity, to evolve into epochs of radiation and matter domination is often called as the hot big bang model. It should be added here that the occurrence of the big bang singularity should not be a cause for concern, as it simply reflects a failure of GR. At these high energy scales, one expects quantum gravitational effects to play an important role leading to the possible avoidance of such singularities.

During the early phases of the radiation dominated era, the photons and the baryons, being strongly coupled to each other, remain in thermal equilibrium. We had pointed out above that, as the universe expands, the radiation density decreases faster than all the other components. As the radiation cools due to the expansion, there arises an epoch at which the interaction rate of the photons with the baryons falls below the expansion rate of the universe. At this stage, the radiation decouples from matter, starts streaming freely, and reaches us today, largely unhindered, except for possible interactions with the electrons that have been reionized at late times in the Inter Galactic Medium (IGM). The constant time hypersurface at the epoch of decoupling, when the radiation last scattered off the baryons, is known as the last scattering surface. It is the photons that travel freely off the last scattering surface that we observe today as the Cosmic Microwave Background (CMB). The CMB is almost perfectly thermal, corresponding to a temperature of

---

2.725 K. It is also found to be highly isotropic, to roughly one part in  $10^5$ , which reflects the fact that the inhomogeneities were rather small during the early stages of evolution of the universe. This observation further supports our description of the universe in terms of the homogeneous and isotropic Friedmann metric [6].

The anisotropies in the CMB are the imprints of the inhomogeneities in the early universe. Therefore, the pattern of the anisotropies in the CMB provide us with clues to the origin and evolution of the primordial perturbations. As we shall soon discuss, a major drawback of the hot big bang model is the fact that it is unable to provide a causal mechanism for the generation of the perturbations. Typically, it is the inflationary scenario, which corresponds to a brief period of accelerated expansion during the early stages of the radiation dominated epoch, that is invoked to explain the origin of the primordial inhomogeneities (see any of the following texts [6] or one of the following reviews [7]). Ever since the first observation of the CMB anisotropies by COBE [8, 9], various ground based observations such as QUEST at DASI (QUaD) [10, 11], the Arcminute Cosmology Bolometer Array Receiver (ACBAR) [12, 13] and the Atacama Cosmology Telescope (ACT) [14, 15] as well as satellite missions such as the Wilkinson Microwave Anisotropy Probe (WMAP) [16, 17, 18, 19] and Planck [20] have been mapping the anisotropies to greater and greater precision. The ever increasing quality of the CMB data allows us to constantly improve upon our understanding of the characteristics as well as the origin and the evolution of the primordial perturbations.

Post decoupling, the inhomogeneities present are amplified due to gravitational instability into the Large Scale Structure (LSS) that we see around us today. However, information regarding the epoch immediately after decoupling is hard to come by due to the lack of interaction of photons with the dominant dark matter and the absence of luminous objects, a period that is hence named as the dark ages. Once the structures begin to form, we again enter a regime offering a rich variety of sources for observations, such as quasars (*viz.* extremely luminous active galactic nuclei), galaxies and supernovae, just to name a few. Observations of events at these late times enable us to reconstruct the more recent history of the universe, involving the formation of structures, reionization and cosmic acceleration. This understanding, in turn, allows us to decode the nature of the primordial perturbations. Therefore, late time observables, such as the distribution of matter on the large scales today, supplement the CMB observations and aid us in constraining models of the early universe. In Figure 1.1, we have reproduced a popular and visually striking artist's impression of the timeline of the universe—beginning with the big bang through the origin of perturbations during inflation and their imprints on the CMB as anisotropies

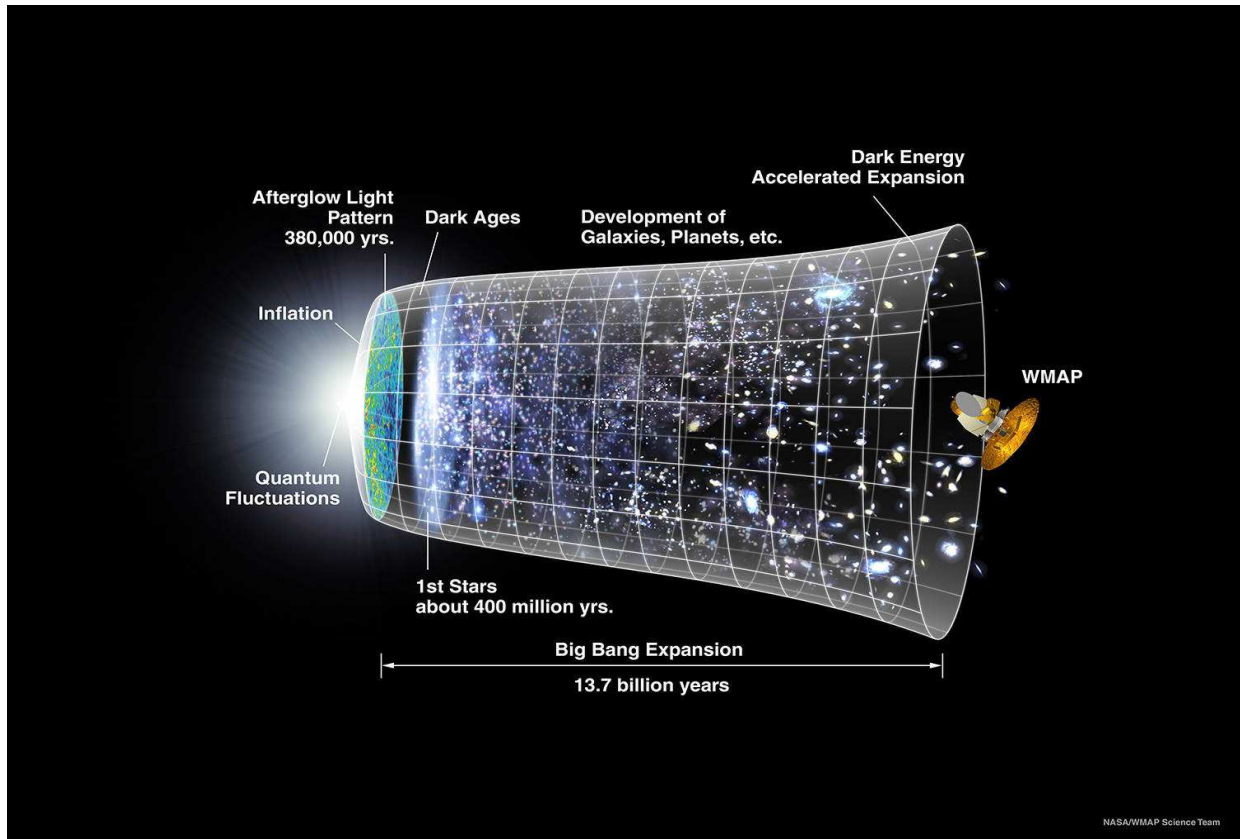


Figure 1.1: An artist’s rendering of the timeline of the universe, from the big bang through the epochs of inflation, decoupling, dark ages and the formation of structure, till the current accelerated expansion driven by dark energy. (Image courtesy: NASA/WMAP Science Team.)

to the formation of the LSS and the present epoch of accelerated expansion driven by dark energy—that we have outlined above.

The aims of this thesis, as we have outlined in the abstract, can be largely said to be twofold. Often in the literature, while considering models of inflation, attention is restricted to models which permit only slow roll. We shall instead focus on models that lead to deviations from slow roll, which result in specific features in the inflationary scalar perturbation spectrum. These features, not only lead to an improved fit to the observed CMB angular power spectrum, but, interestingly, as we shall illustrate, they also produce larger levels of non-Gaussianities, as is possibly suggested by the recent analysis of the WMAP data. As a related issue, we shall also discuss the extent of the contribution to the bi-spectrum due to the epoch of preheating that immediately succeeds the inflationary

era. In the latter part of the thesis, apart from considering the effects of the primordial features on the formation of halos, we shall outline a method that utilizes the observations of the Lyman (Ly)- $\alpha$  forest to arrive at constraints on the primordial non-Gaussianity.

The remainder of this introductory chapter is organized as follows. In the next section, we shall sketch the concordant, background cosmological model that has been arrived at from a variety of observations. After highlighting the drawbacks of the hot big bang model, in Section 1.2, we shall outline as to how the inflationary scenario, even as it helps in overcoming these difficulties, offers a mechanism for the creation of the perturbations. We shall also present a few essential details concerning linear perturbation theory, and discuss how the conventional power law perturbation spectra compare with the observations of the CMB anisotropies. In Section 1.3, we shall briefly discuss the generation of non-Gaussianities during inflation, which is one of the key issues studied in this thesis. We shall outline preheating, *viz.* the epoch that immediately follows inflation, in Section 1.4, while Section 1.5 contains some relevant details pertaining to the formation of structure during late times. In Section 1.6, we shall provide a chapter wise outline of the thesis. We shall conclude this chapter with a few remarks concerning the various conventions and notations that we shall adopt throughout this thesis.

## 1.1 The concordant, background cosmological model

We had mentioned that the homogeneous and isotropic universe is described by the Friedmann metric. We had also pointed out that various observations indicate the density of the universe to be close to the critical value, which corresponds to a spatially flat universe. It is worth noting here that the most direct constraint on the total density of the universe arises from the location of the first acoustic peak in the CMB (in this context, see, for instance, Refs. [6, 18, 19]). A spatially flat,  $(3 + 1)$ -dimensional Friedmann universe that is characterized by the scale factor  $a(t)$  is described by the line-element

$$ds^2 = dt^2 - a^2(t) d\mathbf{x}^2 = a^2(\eta) (d\eta^2 - d\mathbf{x}^2), \quad (1.1)$$

where, recall that,  $t$  represents the cosmic time, while  $\eta = \int dt/a$  denotes the conformal time coordinate.

The dynamics of the scale factor  $a(t)$  is governed by the Einstein equations, which, in

the spatially flat case of our interest, reduce to the following two Friedmann equations:

$$H^2 = \frac{8\pi G}{3} \rho, \quad (1.2a)$$

$$\frac{\ddot{a}}{a} = -\frac{4\pi G}{3} (\rho + 3p), \quad (1.2b)$$

where  $H = \dot{a}/a$  is the Hubble parameter and the overdots represent differentiation with respect to the cosmic time coordinate  $t$ . The quantities  $\rho$  and  $p$  denote the total energy density and the pressure of the constituents of the universe that are responsible for its expansion. We can write the first of the above two Friedmann equations as

$$\frac{H^2}{H_0^2} = \Omega_r \left(\frac{a_0}{a}\right)^4 + \Omega_m \left(\frac{a_0}{a}\right)^3 + \Omega_\Lambda, \quad (1.3)$$

where  $a_0$  denotes the scale factor today and  $H_0$  is the Hubble constant, *i.e.* the present value of the Hubble parameter which is usually expressed as  $h \text{ 100 km s}^{-1} \text{ Mpc}^{-1}$ . The quantities  $\Omega_r$  and  $\Omega_m$  represent the dimensionless density parameters (which we shall soon define) corresponding to radiation and matter (*i.e.* baryons plus the dark matter), respectively. The quantity  $\Omega_\Lambda$  is the density parameter associated with the cosmological constant, which is a specific type of dark energy, whose energy density is strictly a constant, while its pressure is exactly the negative of its energy density. The density parameter  $\Omega_s$  for the species  $S$  is defined in terms of its density today, say,  $\rho_s^0$ , as  $\Omega_s = \rho_s^0 / \rho_c$ , where  $\rho_c$  is the critical density that is given by  $\rho_c = 8\pi G / (3H_0^2)$ . The radiation energy density in the universe is dominated by the CMB, whose current temperature determines the value of  $\Omega_r$ . It is straightforward to show that  $\Omega_r h^2 \simeq 2.56 \times 10^{-5}$  [6]. Observations towards determining distances to a variety of galaxies by the Hubble Key Project point to  $h = 0.73 \pm 0.05$  [21, 22]. Note that  $\Omega_m = \Omega_b + \Omega_c$ , where  $\Omega_b$  and  $\Omega_c$  are the density parameters corresponding to the baryons and the Cold Dark Matter (CDM). The measurements of the primordial abundances of the light elements such as helium or deuterium and their comparison with detailed models of nucleosynthesis during the radiation dominated epoch lead to the constraint that  $\Omega_b h^2 \simeq 0.02$  (see, for example, Refs. [23, 24]). The determination of the luminosity distances to galaxies at high redshifts using type Ia supernovae as standard candles by the Supernova Cosmology Project [25, 26] and the Supernova Legacy Survey [27, 28, 29] suggest that  $\Omega_m \simeq 0.3$  and  $\Omega_\Lambda \simeq 0.7$ . It should be added that each of these constraints have been corroborated independently by other sets of observations. These allow us to arrive at the concordant, background,  $\Lambda$ CDM model of the universe, with about 70% of its energy density today being contributed by the cosmological constant, roughly 25% by cold dark matter, and the rest by the baryons.

## 1.2 The inflationary paradigm and the origin of the perturbations

Though, the conventional hot big bang model, with the inclusion of the cosmological constant, fits a variety of observations quite well, the model, within itself, proves to be incomplete. As we had pointed out earlier, the model lacks certain predictability because of its inability to provide a causal mechanism for the generation of perturbations in early universe, an issue that is commonly referred to as the horizon problem. The inflationary scenario, which corresponds to a brief period of accelerated expansion during the early stages of the radiation dominated epoch, helps in overcoming the horizon problem [30]. Inflation is often achieved with scalar fields as sources and, importantly, the quantum fluctuations associated with these scalar fields provide the seeds for the inhomogeneities in the early universe [31]. In this section, after an outline of the horizon problem and a description of how inflation aids in surmounting the issue, we shall sketch essential aspects of linear, cosmological perturbation theory, and discuss how power law primordial spectra, which are generated in certain models of inflation, compare with the recent CMB observations.

### 1.2.1 The resolution of the horizon problem through inflation

The horizon problem arises due to the large mismatch between the linear dimensions of the backward light cone from today to the epoch of decoupling and the forward light cone at the same epoch that had initially emerged from the big bang. If one assumes that the universe was radiation dominated until decoupling and matter dominated thereafter, then one finds that the ratio of the backward to the forward light cones at the epoch of last scattering turns out to be about 70. The ratio being greater than unity indicates the fact that the CMB photons originating from sufficiently widely separated directions on the last scattering surface could not have interacted before decoupling. Yet, one finds that the CMB photons arriving at us from even opposite directions in the sky possess the same temperature, suggesting that radiation over the entire last scattering surface was in thermal equilibrium. This is the essence of the horizon problem.

The horizon problem can also be stated in a different fashion, which is visually helpful in understanding the evolution of the Fourier modes associated with the inhomogeneities. Consider power law expansion of the form  $a(t) \propto t^q$  with  $q < 1$ , which can describe both the radiation and the matter dominated epochs. The physical length scale,

say,  $\lambda_p = \lambda a$ , associated with any mode of a given wavelength  $\lambda$ , always grows proportional to the scale factor. In contrast, the Hubble radius, say,  $d_H = H^{-1}$ , which reflects the size of the horizon in such cases, behaves as  $a^{1/q}$ . Therefore,  $\lambda_p/d_H \propto a^{(q-1)/q}$ , which, for  $q < 1$ , turns larger than unity at a sufficiently early time. In other words, the modes associated with the perturbations leave the Hubble radius as we go back in time. The fact that, at early times, the modes of cosmological interest (say, wavelengths larger than the scale of homogeneity today) are outside the Hubble radius in the hot big bang model implies that the model cannot provide a causal mechanism for seeding the perturbations.

Inflation, a period of rapid expansion during the stages of the radiation dominated epoch, solves the horizon problem (and, in fact, other issues too, such as, for example, the flatness problem) of the standard big bang cosmology in an elegant fashion [6, 7]. Evidently, the horizon problem can be resolved if we can have a phase during the early stages of radiation domination wherein the modes of cosmological interest are inside the Hubble radius. It is clear from the above discussion that this can be achieved, provided, during this period, the physical wavelengths of the modes decrease faster than the Hubble radius *as we go back in time*, i.e. if  $-d(\lambda_p/d_H)/dt < 0$ . This condition corresponds to  $\ddot{a} > 0$ , and it is such an era of accelerated expansion that is referred to as inflation. In most models of inflation, such as the slow roll scenarios that have drawn constant attention, the Hubble radius remains approximately constant. As illustrated in Figure 1.2, this property allows us to bring the modes of cosmological interest inside the Hubble radius at early times. It can be shown that, in order to ensure that the forward light cone at decoupling is at least as large as the backward light cone, one requires the universe to expand by a factor of about  $10^{28}$  during inflation<sup>1</sup>. For convenience, the extent of inflation is often measured in terms of the number of e-folds  $N$ , which is defined as the logarithmic ratio of the scale factor at any given instant to its value at another fixed time. It can, in fact, be expressed as

$$N = \int_{t_*}^t dt H = \int_{t_*}^t \frac{da}{a} = \ln \left[ \frac{a(t)}{a(t_*)} \right], \quad (1.4)$$

where  $t_*$  denotes some fixed time. Typically, one requires about 60–70 e-folds of inflation to overcome the horizon problem [6, 7]. As we shall soon discuss, the fact that the modes are inside the Hubble radius during the early phase of inflation allows us to impose well motivated initial conditions on the perturbations.

---

<sup>1</sup>It should be clarified that the factor of  $10^{28}$  that we have quoted is an approximate upper limit, and the actual number depends on the energy scale at which inflation takes place (in this context, see, for instance, Refs. [32]).

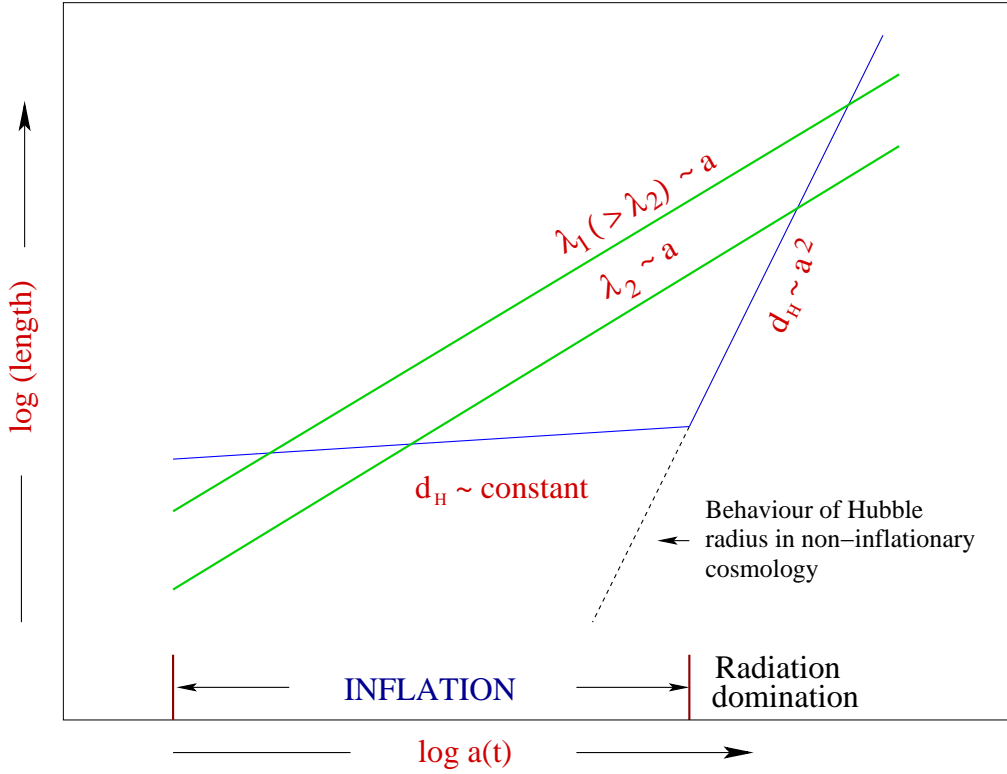


Figure 1.2: Evolution of the physical wavelength  $\lambda_p$  (in green) and the Hubble radius  $d_H$  (in blue) has been plotted as a function of the scale factor  $a$  on a logarithmic plot during the inflationary and the radiation dominated epochs. It is clear from the figure that a nearly constant Hubble radius (as is encountered in slow roll inflation) ensures that the modes emerge from inside the Hubble radius at a sufficiently early epoch, thereby resolving the horizon problem.

### 1.2.2 Driving inflation with scalar fields

It is evident from the second of the Friedmann equations, *viz.* Eq. (1.2b), that one requires  $(\rho + 3p) < 0$  for inflation, *i.e.* a period of accelerated expansion, to occur. Since neither matter corresponding to  $p_m = 0$  and radiation with  $p_r = \rho_r/3$  (and, needless to add, a positive energy density) do not satisfy the condition, they cannot drive inflation. As we have alluded to before, it is scalar fields that are often invoked to achieve inflation [30]. Consider a single, canonical scalar field, say,  $\phi$ , which is the dominant source for the expansion of the universe at a particular epoch. The energy density and pressure associated

with the scalar field are given by [6, 7]

$$\rho_\phi = \frac{\dot{\phi}^2}{2} + V(\phi), \quad (1.5a)$$

$$p_\phi = \frac{\dot{\phi}^2}{2} - V(\phi), \quad (1.5b)$$

where the overdots again represent differentiation with respect to the cosmic time, while  $V(\phi)$  denotes the potential that describes the inflaton<sup>2</sup>. For the above energy density and pressure, the condition that leads to an accelerated expansion reduces to  $\dot{\phi}^2 < V(\phi)$ , *i.e.* when the kinetic energy of the scalar field is less than the potential energy associated with the field.

The equation of motion satisfied by the scalar field in the homogeneous and isotropic Friedmann background is given by [6, 7]

$$\ddot{\phi} + 3H\dot{\phi} + V_\phi = 0, \quad (1.6)$$

where  $V_\phi = dV/d\phi$ . It is clear from this equation that, while the term  $V_\phi$  drives the field in the potential, the frictional term  $3H\dot{\phi}$ , which arises due to the expansion of the universe, slows the field down. We saw above that the condition for inflation to occur corresponds to  $\dot{\phi}^2 < V(\phi)$ . Though this condition ensures accelerated expansion, it is often demanded that the field rolls slowly in the potential so that one has  $\dot{\phi}^2 \ll V(\phi)$ , which guarantees that inflation does indeed take place. Moreover, the field also needs to be slowly rolling for a sufficient duration in order to achieve the necessary amount of inflation. A suitably long duration of inflation is accomplished provided the frictional term is strong enough to overcome the acceleration of the field, *i.e.* when  $\ddot{\phi} \ll 3H\dot{\phi}$ . The above two inequalities, in fact, constitute the conditions for the so-called slow roll inflationary scenario [33]. Actually, nowadays, it is more common to characterize the evolution of the scalar field in terms of a hierarchy of slow roll parameters. The first slow roll parameter is defined as

$$\epsilon_1 = -\frac{\dot{H}}{H^2}, \quad (1.7)$$

and it is useful to note here that the condition for inflation, *viz.*  $\ddot{a} > 0$ , corresponds to  $\epsilon_1 < 1$ . The second and the higher order slow roll parameters are defined in terms of the first as follows:

$$\epsilon_{i+1} = \frac{d \ln \epsilon_i}{dN}, \quad (1.8)$$

---

<sup>2</sup>It is common to refer to the scalar field that drives inflation as the inflaton.

where  $i \geq 1$  and  $N$  denotes the number of e-folds. Most models permit slow roll inflation for a range of values of the parameters describing the potential. During inflation, typically, the scalar field begins its journey far away from a minima of the potential. It rolls down the potential, joins the inflationary attractor (had it not been originally present on one such trajectory), and inflation is terminated (when  $\epsilon_1$  crosses unity) as it approaches the minimum.

### 1.2.3 The generation of perturbations during inflation

Inflation, besides resolving the horizon problem, also provides an attractive mechanism for the origin of perturbations in the early universe [31]. While the classical component of the scalar field drives inflation as we have described above, the quantum fluctuations associated with the field induce perturbations in the Friedmann metric. The accelerated expansion then converts the tiny quantum fluctuations into classical inhomogeneities that leave their signatures as anisotropies in the CMB. After decoupling, gravitational instability takes over, evolving the perturbations into the structures that we see today. In what follows, after a rapid outline of essential, linear, cosmological perturbation theory, we shall discuss the comparison of certain inflationary perturbation spectra with the recent observations of the CMB anisotropies.

#### Essential, linear, cosmological perturbation theory

The fluctuations in the scalar field can be related to the perturbations in the Friedmann metric through the Einstein field equations. These perturbations can be classified as scalars, vectors and tensors, depending on their transformation properties on the three dimensional spatial hypersurface [34]. While the vectors are divergence free, the tensors are traceless and transverse. In the  $(3 + 1)$ -dimensional Friedmann universe of our interest, it can be easily shown that these conditions lead to two independent degrees of freedom associated with each type of perturbation. At the linear order in the perturbation theory, the scalars, the vectors and the tensors evolve independently. The two degrees of freedom associated with the tensors correspond to the two polarizations of the gravitational waves, and it should be mentioned these perturbations can be generated even in the absence of tensor sources [35]. The vector perturbations, for example, can describe vorticity, and these are driven by vector sources. Due to the absence of such sources, no vector perturbations are generated during inflation [6, 7].

As we mentioned, the scalar perturbations associated with the Friedmann metric are

sourced by the perturbations in the inflaton. In the absence of any anisotropic stress, as it occurs in the context of scalar fields, the number of independent scalar degrees of freedom describing the perturbations in the Friedmann metric reduces to one. Therefore, upon taking into account the scalar and the tensor perturbations, the Friedmann line-element can be written as follows:

$$ds^2 = (1 + 2\Phi) dt^2 - a^2(t) [(1 - 2\Phi) \delta_{ij} + \mathbf{h}_{ij}] d\mathbf{x}^i d\mathbf{x}^j, \quad (1.9)$$

where the quantities  $\Phi$  and  $\mathbf{h}_{ij}$  depend on both time and space, while  $i$  and  $j$  are spatial indices that run from one through three. The quantity  $\Phi$  describes the scalar perturbation and is known as the Bardeen potential, while  $\mathbf{h}_{ij}$ , which is considered to be transverse and traceless, represents the tensor perturbations.

We had pointed out above that, at the linear order in perturbation theory, the scalars and the tensors evolve independently. If, say,  $\delta\rho$  and  $\delta p$  denote the perturbations in the energy density and pressure, one can show that, when no anisotropic stresses are present, the first order Einstein equations lead to the following equation of motion for the Bardeen potential  $\Phi$ :

$$\Phi'' + 3\mathcal{H} (1 + c_A^2) \Phi' - c_A^2 \nabla^2 \Phi + [2\mathcal{H}' + (1 + 3c_A^2) \mathcal{H}^2] \Phi = (4\pi G a^2) \delta p^{\text{NA}}, \quad (1.10)$$

where the overprimes refers to differentiation with respect to the conformal time  $\eta$ , and  $\mathcal{H}$  denotes the conformal Hubble parameter that is defined as  $\mathcal{H} = aH = a'/a$ . Moreover, the quantity  $\delta p^{\text{NA}}$  represents the non-adiabatic pressure perturbation which is defined by the relation (see, for example, Refs. [36, 37])

$$\delta p^{\text{NA}} = \delta p - c_A^2 \delta\rho, \quad (1.11)$$

where  $c_A^2 \equiv p'/\rho'$  is referred to as the adiabatic speed of the perturbations. It proves to be convenient to introduce a quantity  $\mathcal{R}$ , which is commonly known as the curvature perturbation (since it is proportional to the local three curvature on the spatial hypersurface), that is given in terms of the Bardeen potential  $\Phi$  by the expression

$$\mathcal{R} = \Phi + \frac{2\rho}{3\mathcal{H}} \left( \frac{\Phi' + \mathcal{H}\Phi}{\rho + p} \right). \quad (1.12)$$

In Fourier space, the equation of motion (1.10) for the Bardeen potential then leads to the following differential equation governing the curvature perturbation:

$$\mathcal{R}'_{\mathbf{k}} = \frac{\mathcal{H}}{\mathcal{H}^2 - \mathcal{H}'} [(4\pi G a^2) \delta p_{\mathbf{k}}^{\text{NA}} - c_A^2 k^2 \Phi_{\mathbf{k}}], \quad (1.13)$$

where the sub-script  $\mathbf{k}$  refers to the wavevector of the Fourier modes of the perturbations. The above equation has an important implication for modes which are well outside the Hubble radius either during the late phase of the inflationary epoch or the early stages of the radiation dominated epoch (in this context, see Figure 1.2). Such modes satisfy the condition  $\lambda_p = \lambda a \gg d_H = H^{-1}$  or, equivalently,  $k/(aH) \ll 1$ , where  $k$  is the wavenumber associated with the wavelength  $\lambda$ . Consider a situation when the non-adiabatic pressure perturbation is absent, *i.e.*  $\delta p^{\text{NA}} = 0$  [38]. In such a case, on super-Hubble scales, *viz.* when  $k/(aH) \ll 1$ , the first term within the square brackets on the right hand side of Eq. (1.13) above vanishes, while the second term can be neglected, so that one has  $\mathcal{R}'_{\mathbf{k}} \simeq 0$ . This implies that, for adiabatic perturbations, the curvature perturbation is conserved on super-Hubble scales [39]. As we shall see later, this property comes in very handy while evaluating the inflationary perturbation spectra.

The above discussion and conclusions for the scalar perturbations actually apply to any scalar source that does not possess anisotropic stress. Let us now our attention to the original case of our interest, *viz.* perturbations induced by the inflaton. From the stress energy tensor for the scalar field, one can arrive at the expressions for the perturbations in the energy density and the pressure, which can then be utilized to show that the corresponding non-adiabatic pressure perturbation  $\delta p^{\text{NA}}$  can be written as

$$\delta p^{\text{NA}} = \frac{1 - c_{\Lambda}^2}{4\pi G a^2} \nabla^2 \Phi. \quad (1.14)$$

Upon substituting this expression in Eq. (1.10) and making use of Eq. (1.13), one arrives at the following differential equation that governs the Fourier modes of the curvature perturbation during inflation:

$$\mathcal{R}_{\mathbf{k}}'' + 2 \frac{z'}{z} \mathcal{R}'_{\mathbf{k}} + k^2 \mathcal{R}_{\mathbf{k}} = 0, \quad (1.15)$$

where  $z = \sqrt{2\epsilon_1} M_{\text{pl}} a$ . At this stage, one often introduces the so-called Mukhanov-Sasaki variable  $v_{\mathbf{k}} = z \mathcal{R}_{\mathbf{k}}$  which satisfies the equation [40]

$$v_{\mathbf{k}}'' + \left( k^2 - \frac{z''}{z} \right) v_{\mathbf{k}} = 0. \quad (1.16)$$

The first order Einstein equations lead to a similar equation of motion for the tensor perturbations as well. In fact, one finds that the Fourier modes of all the components of the tensor  $h_{ij}$  are governed by the same differential equation, which is given by

$$h_{\mathbf{k}}'' + 2 \frac{a'}{a} h'_{\mathbf{k}} + k^2 h_{\mathbf{k}} = 0, \quad (1.17)$$

where the quantity  $h_k$  represents the amplitude of the tensor modes. Following the case of scalars, if we set  $u_k = a h_k$ , then one obtains the equation satisfied by  $u_k$  to be

$$u_k'' + \left( k^2 - \frac{a''}{a} \right) u_k = 0. \quad (1.18)$$

### The inflationary scalar and tensor perturbation spectra

It is essentially the spectrum of the Bardeen potential when the modes enter the Hubble radius during the radiation and the matter dominated epochs that determines the pattern of the anisotropies in the CMB and the formation of the LSS [6]. The correlations in the Bardeen potential or, equivalently, in the curvature perturbation, originate due to the quantum fluctuations associated the scalar field. As it directly involves the perturbation in the scalar field, it is the curvature perturbation  $\mathcal{R}$  that is elevated to a quantum operator. On quantization, the operator corresponding to the curvature perturbation  $\mathcal{R}$  can be expressed as

$$\begin{aligned} \hat{\mathcal{R}}(\eta, \mathbf{x}) &= \int \frac{d^3 \mathbf{k}}{(2\pi)^{3/2}} \hat{\mathcal{R}}_{\mathbf{k}}(\eta) e^{i \mathbf{k} \cdot \mathbf{x}} \\ &= \int \frac{d^3 \mathbf{k}}{(2\pi)^{3/2}} \left[ \hat{a}_{\mathbf{k}} f_{\mathbf{k}}(\eta) e^{i \mathbf{k} \cdot \mathbf{x}} + \hat{a}_{\mathbf{k}}^\dagger f_{\mathbf{k}}^*(\eta) e^{-i \mathbf{k} \cdot \mathbf{x}} \right], \end{aligned} \quad (1.19)$$

where  $\hat{a}_{\mathbf{k}}$  and  $\hat{a}_{\mathbf{k}}^\dagger$  are the usual creation and annihilation operators that satisfy the standard commutation relations, while the modes  $f_{\mathbf{k}}$  are governed by the differential equation (1.15). The dimensionless scalar power spectrum  $\mathcal{P}_s(k)$  is given in terms of the correlation function of the Fourier modes of the curvature perturbation  $\hat{\mathcal{R}}_{\mathbf{k}}$  by the following relation:

$$\langle 0 | \hat{\mathcal{R}}_{\mathbf{k}} \hat{\mathcal{R}}_{\mathbf{p}} | 0 \rangle = \frac{(2\pi)^2}{2 k^3} \mathcal{P}_s(k) \delta^{(3)}(\mathbf{k} + \mathbf{p}), \quad (1.20)$$

where  $|0\rangle$  denotes the vacuum state that is defined as  $\hat{a}_{\mathbf{k}}|0\rangle = 0 \forall \mathbf{k}$ . In terms of the modes  $f_{\mathbf{k}}$  and the Mukhanov-Sasaki variable  $v_{\mathbf{k}}$ , the scalar power spectrum is given by

$$\mathcal{P}_s(k) = \frac{k^3}{2\pi^2} |f_{\mathbf{k}}|^2 = \frac{k^3}{2\pi^2} \left( \frac{|v_{\mathbf{k}}|}{z} \right)^2, \quad (1.21)$$

with the expression on the right hand side to be evaluated on super-Hubble scales [*i.e.* when  $k/(aH) \ll 1$ ], as the curvature perturbation approaches a constant value<sup>3</sup>.

---

<sup>3</sup>Earlier, we had illustrated that, if the non-adiabatic pressure perturbation  $\delta p^{NA}$  can be neglected, then the curvature perturbation is conserved on super-Hubble scales. It can be shown that the non-adiabatic pressure perturbation associated with the inflaton [*cf.* Eq. (1.14)] decays exponentially on super-Hubble scales and, hence, can be ignored. In fact, it is because of this reason that the scalar perturbations produced by single scalar fields are termed as adiabatic.

The tensor perturbations can be quantized in a similar fashion, and the tensor spectrum can then be expressed in terms of the modes  $h_{\mathbf{k}}$  and  $u_{\mathbf{k}}$  as follows:

$$\mathcal{P}_{\text{T}}(k) = \frac{8}{M_{\text{Pl}}^2} \frac{k^3}{2\pi^2} |h_{\mathbf{k}}|^2 = \frac{8}{M_{\text{Pl}}^2} \frac{k^3}{2\pi^2} \left( \frac{|u_{\mathbf{k}}|}{a} \right)^2, \quad (1.22)$$

where  $M_{\text{Pl}} = (8\pi G)^{-1/2}$  denotes the Planck mass. The Planck mass appears since it is part of the gravitational action, while the additional factor of 8 arises when all the components of the tensor perturbation  $h_{ij}$  are taken into account. As in case of the curvature perturbation, the tensor amplitude  $h$  is also known to quickly attain a constant value once the modes leave the Hubble radius during inflation. Therefore, the quantities on the right hand side of the above expression are to be evaluated on super-Hubble scales, as in the case of the scalar spectrum.

During inflation, the initial conditions on the perturbations are imposed when the modes are well inside the Hubble radius, *i.e.* when  $k/(aH) \gg 1$ . It is clear from Eqs. (1.16) and (1.18) that, on sub-Hubble scales, it is the  $k^2$  term that will dominate, as result of which neither  $v_{\mathbf{k}}$  nor  $u_{\mathbf{k}}$  feel the effects due to the curvature of the spacetime, reflected in the terms  $z''/z$  and the  $a''/a$ . Therefore, in the sub-Hubble limit, they have the following, Minkowskian form:  $e^{\pm ik\eta}$ . Demanding that the perturbations are in the vacuum state upon quantization corresponds to choosing the solutions to be the positive frequency modes, *i.e.*

$$\lim_{k/(aH) \rightarrow \infty} [v_{\mathbf{k}}(\eta), u_{\mathbf{k}}(\eta)] = \frac{1}{\sqrt{2}k} e^{-ik\eta}. \quad (1.23)$$

The vacuum state that is associated with such an initial condition is popularly known as the Bunch-Davies vacuum [41]. Beginning with this initial condition, the scalar and tensor modes are evolved to super-Hubble scales, and the corresponding perturbation spectra are evaluated as their amplitudes approach a constant value.

### Comparison with the CMB observations

Let us now turn to discussing as to how inflationary models compare with the recent observations of the anisotropies in the CMB. As we have alluded to before, many models permit the so-called slow roll inflationary scenario. It can be shown in a model independent manner that slow rolling canonical scalar fields lead to nearly scale invariant inflationary perturbation spectra [42]. The scalar and the tensor perturbation spectra that

arise in such cases are often written in the following power law form:

$$\mathcal{P}_S(k) = A_S \left( \frac{k}{k_*} \right)^{n_S-1}, \quad (1.24a)$$

$$\mathcal{P}_T(k) = A_T \left( \frac{k}{k_*} \right)^{n_T}. \quad (1.24b)$$

The quantities  $A_S$  and  $A_T$  denote the amplitude of the scalar and tensor spectra, while  $n_S$  and  $n_T$  denote the corresponding spectral indices. The quantity  $k_*$  is the pivot scale at which the amplitudes of the power spectra are quoted. Given the scalar and the tensor spectra, *i.e.*  $\mathcal{P}_S(k)$  and  $\mathcal{P}_T(k)$ , the tensor-to-scalar ratio is defined as

$$r(k) = \frac{\mathcal{P}_T(k)}{\mathcal{P}_S(k)}. \quad (1.25)$$

It is the scalar amplitude  $A_S$ , the tensor-to-scalar ratio  $r$ , and the scalar and the tensor indices  $n_S$  and  $n_T$  that are typically treated as the observables associated with slow roll inflationary models. Upon comparing with the observations, one arrives at constraints on these four quantities which, in turn, indicate how these models perform against the data.

The physics involved in the propagation of the perturbations from their primordial origins (say, during inflation) to their corresponding signatures as anisotropies in the CMB is well understood, at least at the linear order in the perturbation theory [6]. In fact, there exist highly developed and accurate numerical codes such as the Cosmological Boltzmann Code CAMB [43, 44] to arrive at the CMB angular power spectra from the primordial scalar and tensor spectra. These codes, when coupled to Cosmological Monte Carlo codes like COSMOMC [45, 46], greatly facilitate the comparison of inflationary models with the observations of the CMB anisotropies as well as other cosmological data sets such as those involving the LSS. The observed anisotropies in the CMB are usually expressed in terms of the CMB angular power spectra and cross-correlations involving the temperature and the  $E$  and the  $B$  types of polarizations, *viz.*  $\mathcal{C}_\ell^{TT}$ ,  $\mathcal{C}_\ell^{TE}$ ,  $\mathcal{C}_\ell^{EE}$  and  $\mathcal{C}_\ell^{BB}$ . It is often found that perturbation spectra generated by slow roll inflationary models fit the CMB data from the various missions such as WMAP [17, 18, 19], QUaD [10, 11], ACBAR [13] and ACT [15] rather well (for a more detailed discussion on this topic, see, for example, Ref. [47] and references therein). For instance, one finds that the best fit power law scalar spectra corresponds to the scalar amplitude  $A_S \simeq 2.193 \times 10^{-9}$  at the pivot scale of  $0.05 \text{ Mpc}^{-1}$  (a constraint that is often referred to as COBE normalization [48]), and a spectral index of  $n_S \simeq 0.97$  (in this context, see Chapter 2). However, it should be emphasized that we are

yet to detect any tensor perturbations. The tensor spectral index in the theoretical models often proves to be small enough that it is usually set to be zero when comparing with the observations, while the seven-year WMAP data [19] and the ACT data [15] suggest the upper bound on the tensor-to-scalar ratio  $r$  to be 0.24 at 95% Confidence Level (CL). Figure 1.3 below contains a plot of the observed TT angular power spectrum arrived at from seven years of WMAP data and the best fit theoretical angular power spectrum corresponding to power law primordial spectra [19]. It is evident from the figure that the theoretical predictions seem to agree well with the observations.

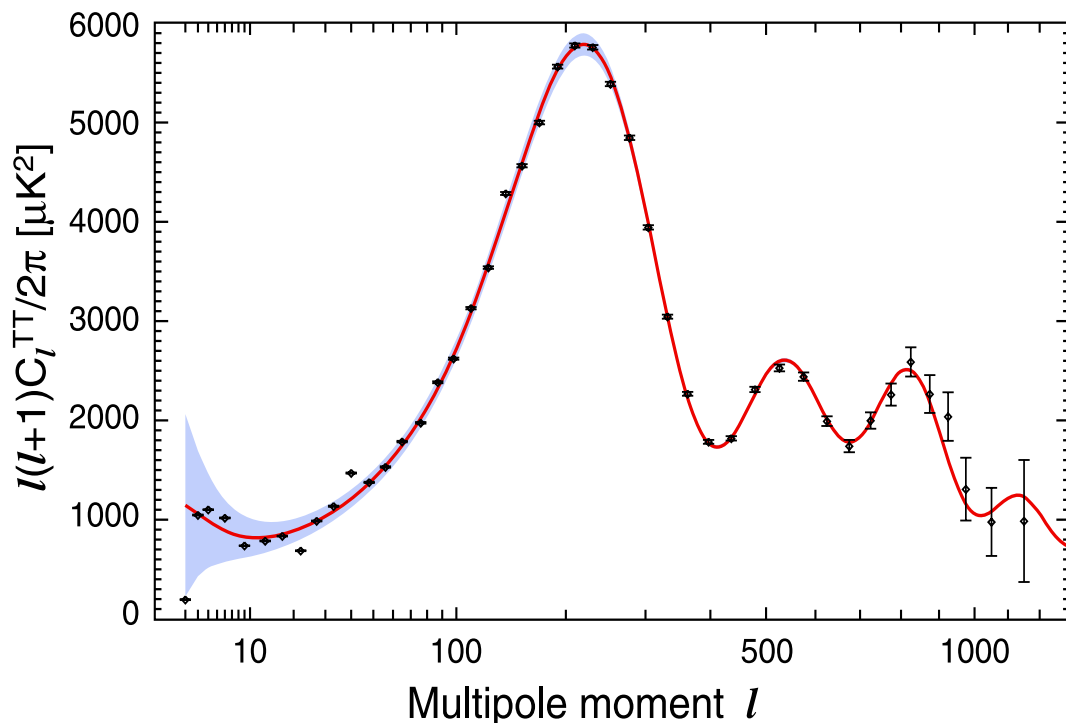


Figure 1.3: The theoretical and the observed CMB (TT) angular power spectra have been plotted as a function of the multipoles  $l$ . The black dots with the error bars are the binned data points from seven years of WMAP data [19]. The solid red curve is the analytical best fit angular power spectrum corresponding to power law primordial spectra [cf. Eqs. (1.24)] with values of parameters as quoted in the discussion above. The blue band represents cosmic variance [6]. Clearly, the theoretically predicted curve seem to agree with the observations rather well. (Image courtesy: NASA/LAMBDA data products.)

### 1.3 The generation and imprints of non-Gaussianities

So far, we have discussed the generation of correlations during inflation and the comparison of the theoretical predictions with the observational evidence at the level of the two point function, *viz.* the primordial and the CMB angular power spectra. Over the last decade, there has been frenetic activity towards gaining a theoretical understanding of the amplitude and the form of the three and the four point functions that are produced during inflation. In particular, a large fraction of these investigations have been dedicated to analyzing inflationary and post-inflationary dynamics that lead to deviations from Gaussianity (see Refs. [49, 50, 51, 52, 53, 54, 55]; for earlier efforts in this direction, see Refs. [56]). At the same time, there has also been a constant effort to arrive at increasingly tighter constraints on the actual extent of primordial non-Gaussianities observed in the CMB and the LSS data [57, 58]. It is now commonly recognized that non-Gaussianities, if detected, can play a significant role in helping us discriminate between the various inflationary as well as the post-inflationary scenarios.

In a linear theory described by a quadratic action, when one works with vacuum initial states, the correlations prove to be Gaussian in nature. It is the non-linearities in the action governing the variable of interest that leads to deviations from Gaussianities in the correlation functions. The simplest signature of non-Gaussianity is a non-zero three point function, which, in a given theory, will be determined by the cubic terms in the action. Then, evidently, the first step towards evaluating the three point correlation functions generated in an inflationary model would be to arrive at the action describing the scalar and tensor perturbations at the next higher, *i.e.* the cubic, order [49, 51]. Having obtained such an action, one can make use of the standard procedures of quantum field theory to arrive at the corresponding scalar and tensor bi-spectra, *viz.* the three point functions in Fourier space, as well as cross-correlations between the scalars and the tensors, corresponding to the cubic order action. Based on these arguments, there now exists a standard formalism, originally due to Maldacena [49], to evaluate the bi-spectrum generated during inflation (for more details, see Chapter 4).

The scalar bi-spectrum, say,  $\mathcal{B}_s(\mathbf{k}_1, \mathbf{k}_2, \mathbf{k}_3)$ , associated with the modes  $\hat{\mathcal{R}}_{\mathbf{k}}$  of the curvature perturbation is defined as

$$\langle \hat{\mathcal{R}}_{\mathbf{k}_1} \hat{\mathcal{R}}_{\mathbf{k}_2} \hat{\mathcal{R}}_{\mathbf{k}_3} \rangle = (2\pi)^3 \mathcal{B}_s(\mathbf{k}_1, \mathbf{k}_2, \mathbf{k}_3) \delta^{(3)}(\mathbf{k}_1 + \mathbf{k}_2 + \mathbf{k}_3). \quad (1.26)$$

Ideally, one would have liked to compute the CMB angular bi-spectrum corresponding to the primordial bi-spectrum generated during inflation and compare with the observa-

tions, as is done in the case of the power spectra. However, some of the issues towards carrying out such comparison still remain to be resolved (in this context, see, for instance, Ref. [59]). Further, efficient computational tools that will be required for such an analysis are yet to be thoroughly developed. As a result, for convenience in characterizing the observations on the one hand and the theoretical models on the other, a dimensionless parameter  $f_{\text{NL}}$  is often introduced to reflect the amplitude of the deviations from Gaussianity in the curvature perturbation through the relation [57]

$$\mathcal{R} = \mathcal{R}_{\text{G}} - \frac{3f_{\text{NL}}}{5} (\mathcal{R}_{\text{G}}^2 - \langle \mathcal{R}_{\text{G}}^2 \rangle), \quad (1.27)$$

where  $\mathcal{R}_{\text{G}}$  denotes the Gaussian quantity, and the factor of  $3/5$  arises due to the relation between the Bardeen potential and the curvature perturbation during the matter dominated epoch. Upon making use of the corresponding relation between  $\mathcal{R}$  and  $\mathcal{R}_{\text{G}}$  in Fourier space and the Wick's theorem, which applies to Gaussian distributions, one obtains that [49, 51, 52]

$$\begin{aligned} \langle \hat{\mathcal{R}}_{\mathbf{k}_1} \hat{\mathcal{R}}_{\mathbf{k}_2} \hat{\mathcal{R}}_{\mathbf{k}_3} \rangle &= -\frac{3f_{\text{NL}}}{10} (2\pi)^4 (2\pi)^{-3/2} \frac{1}{k_1^3 k_2^3 k_3^3} \delta^{(3)}(\mathbf{k}_1 + \mathbf{k}_2 + \mathbf{k}_3) \\ &\times [k_1^3 \mathcal{P}_{\text{s}}(k_2) \mathcal{P}_{\text{s}}(k_3) + \text{two permutations}]. \end{aligned} \quad (1.28)$$

This expression can then be utilized to arrive at the following relation between the non-Gaussianity parameter  $f_{\text{NL}}(\mathbf{k}_1, \mathbf{k}_2, \mathbf{k}_3)$  and the scalar bi-spectrum  $\mathcal{B}_{\text{s}}(\mathbf{k}_1, \mathbf{k}_2, \mathbf{k}_3)$  [53, 54]:

$$\begin{aligned} f_{\text{NL}}(\mathbf{k}_1, \mathbf{k}_2, \mathbf{k}_3) &= -\frac{10}{3} (2\pi)^{-4} (2\pi)^{9/2} k_1^3 k_2^3 k_3^3 \mathcal{B}_{\text{s}}(\mathbf{k}_1, \mathbf{k}_2, \mathbf{k}_3) \\ &\times [k_1^3 \mathcal{P}_{\text{s}}(k_2) \mathcal{P}_{\text{s}}(k_3) + \text{two permutations}]^{-1}, \end{aligned} \quad (1.29)$$

which suggests that the non-Gaussianity parameter is, in fact, a suitable ratio of the scalar bi-spectrum to the corresponding power spectrum.

Note that the presence of the delta-function in the definition (1.26) of the bi-spectrum  $\mathcal{B}_{\text{s}}(\mathbf{k}_1, \mathbf{k}_2, \mathbf{k}_3)$  implies that the wavevectors  $\mathbf{k}_1$ ,  $\mathbf{k}_2$  and  $\mathbf{k}_3$  have to constitute a triangle. The present observational constraints on the non-Gaussianity parameter  $f_{\text{NL}}(\mathbf{k}_1, \mathbf{k}_2, \mathbf{k}_3)$  are often quoted in the equilateral (*i.e.* when  $k_1 = k_2 = k_3$ ) and the squeezed (or the local) limits (*i.e.* when, say,  $k_1 = k_2 \gg k_3$ ). In the equilateral limit, analysis of the WMAP seven-year data indicates that  $f_{\text{NL}} = 26 \pm 140$ , whereas in the squeezed limit one has  $f_{\text{NL}} = 32 \pm 21$ , with the errors denoting the  $1\text{-}\sigma$  deviations from the mean values [19, 57, 58]. It is worth mentioning that, while a Gaussian distribution lies within  $2\text{-}\sigma$ , the mean values seem to suggest relatively large levels of non-Gaussianity. For instance, slow

roll inflationary models involving the canonical scalar fields, which produce nearly scale invariant perturbation spectra that are remarkably consistent with the observations at the level of the power spectra generate rather insignificant amount of non-Gaussianities. The  $f_{\text{NL}}$  typically created in such models turn out to be far less than unity [49].

## 1.4 Post-inflationary dynamics

We had discussed earlier that, during inflation, the scalar field rolls down the potential towards a minima, and inflation ends as the field approaches the minimum [6, 7]. Typically, in models involving the canonical scalar field, immediately after inflation, the field oscillates about the minimum of the potential [60]. Thereafter, due to its coupling to other fields, the inflaton is expected to decay into various particles. The resultant products then thermalize and reheat the universe, thereby commencing the radiation dominated epoch associated with the conventional hot big bang model [61].

In single field inflationary models, preheating refers to the phase that is sandwiched between the epochs of inflation and reheating [60]. As the field oscillates at the bottom of its potential during this phase, the amplitude of the fields coupled to the inflaton may undergo parametric resonance resulting in an extremely rapid production of particles. Such a resonant phenomenon can, in principle, lead to an amplification of the super-Hubble scale curvature perturbations which, in turn, would affect the spectrum generated during inflation. Interestingly, in single fields models, it has been shown that, despite the parametric instability, the amplitude of the curvature perturbations remain unaltered [62, 63, 64]. Needless to add, the effects of such post-inflationary dynamics needs to be understood satisfactorily if we are to arrive at constraints on the inflationary models from the observations of the CMB and the LSS.

## 1.5 The formation of the large scale structure

Till now, we have focussed on the comparison of models of the early universe with the observations of the anisotropies in the CMB. We have discussed the imprints of power spectra and non-Gaussianities on the CMB. Apart from influencing the CMB anisotropies, the primordial perturbations also affect the formation of the LSS. For instance, given a primordial scalar power spectrum, say,  $\mathcal{P}_s(k)$ , the matter power spectrum  $P_{\text{M}}(k, z)$  at the

redshift  $z$  is usually written as (see Refs. [6], in this context, also see, for example, Ref. [65])

$$P_M(k, z) = \left(\frac{2}{5\Omega_m}\right)^2 \left(\frac{k}{a_0 H_0}\right)^4 \left(\frac{2\pi^2}{k^3}\right) \mathcal{P}_s(k) T^2(k) D_+^2(z), \quad (1.30)$$

a quantity that is usually expressed in units of  $\text{Mpc}^3$ . In the above expression,  $T(k)$  denotes the CDM transfer function, while  $D_+(z)$  represent the linear growth factor associated with the total matter perturbation. The quantities  $\Omega_m$ ,  $a_0$ , and  $H_0$  are ones that we have encountered earlier. They represent the non-relativistic dimensionless density parameter, the scale factor and the Hubble parameter today, respectively. The matter power spectrum, which reflects the level of the deviations in the matter density from the smooth, background value, in turn, determines the extent of dark matter halos, *viz.* stable virialized structures, that have formed at late times. The strongest constraints on the matter power spectrum is arrived at from the SDSS data, upon making use of galaxies as observable objects [4]. The observed matter power spectrum complements the CMB observations and provides additional constraints on the character and form of the primordial perturbations.

Quasi-stellar radio sources, commonly known as quasars, are extremely luminous active galactic nuclei that are located at large distances. As the light from the far away quasars travels towards us, they are absorbed by the neutral hydrogen present in the IGM, which leads to a forest of Ly- $\alpha$  spectral lines [6]. The Ly- $\alpha$  forest proves to be a powerful probe to aid us understand the history of formation of structures and, in particular, determine the epoch of reionization. The forest spectra provide an estimate of the neutral hydrogen density and its distribution along the line of sight. The pixel flux distribution function in a given Ly- $\alpha$  forest is assumed to be produced by the probability distribution associated with the overdensity, say,  $\delta$ , on large scales. This assumption helps one to map the distribution function of the flux onto the distribution of  $\delta$ , which, in turn, allows the reconstruction of the primordial power spectrum (see, for instance, the review [66]). Mostly, Ly- $\alpha$  studies have concentrated on correlations of the one dimensional transmitted flux field related to single quasar line of sight. As ongoing surveys such as the Baryon Oscillation Spectroscopic Survey (BOSS) [67] and BigBOSS [68] begin to gather increasing amount of quasar data covering a large fraction of the sky, it should be possible to measure the three-dimensional (3D) power spectrum of the Ly- $\alpha$  forest along multiple lines of sight. It then becomes interesting to investigate the extent to which such data can help in constraining the primordial bi-spectrum or the non-Gaussianity parameter  $f_{\text{NL}}$ .

## 1.6 Theme and outline of the thesis

Earlier, we had discussed as to how nearly scale independent perturbation spectra produced by slow roll inflationary scenarios are in good agreement with the observations of the anisotropies in the CMB. But, a closer look at Figure 1.3 reveals the fact that there exist a few data points at the lower multipoles that lie beyond the cosmic variance associated with the best fit theoretical CMB angular power spectrum. Though some outliers are always to be expected, it is interesting to examine if these outliers point to non-trivial inflationary dynamics. As we shall see, certain features in the primordial spectrum, generated due to deviations from slow roll, lead a better fit to the data. Further, in the context of non-Gaussianities, we had also mentioned as to how, while slow roll scenarios lead to relatively small values for the non-Gaussianity parameter  $f_{\text{NL}}$ , the observed mean values seem to be large. Importantly, it is found that the deviations from slow roll that help in fitting the above-mentioned outliers in the CMB angular power spectrum also result in increased levels of non-Gaussianities as is possibly suggested by the data. These points provide the essential motivations for the issues studied in this thesis. The two themes that have been investigated are the possibility of features in the primordial scalar spectrum and non-Gaussianities. The initial part of the thesis focuses on analyzing localized as well non-local features in the inflationary scalar power spectrum that result in an improved fit to the observed CMB angular power spectrum. We shall also consider in detail the scalar bi-spectrum generated in models that lead to such features in the power spectrum. Moreover, we shall analyze the contributions to the bi-spectrum during preheating in single field models. The latter part of the thesis is dedicated to the imprint of features and non-Gaussianities on the LSS. In this context, we shall study the effects of primordial features on the halo formation rates. We shall also discuss a proposal to arrive at stronger bounds on the non-Gaussianity parameter  $f_{\text{NL}}$  from the observations of the Ly- $\alpha$  forest. In what follows, we shall provide a brief, chapter wise outline of the thesis.

In Chapter 2, we shall discuss the effects of introducing a step in otherwise smooth inflaton potentials. As we shall see, the presence of the step leads to a small period of departure from slow roll. The deviation from slow roll, in turn, leads a localized burst of oscillations which provides an improved fit to some of the outliers at the low multipoles in the CMB data.

Chapter 3 considers inflationary potentials that contain oscillatory terms. The oscillations in the potentials lead to persistent modulations in the slow parameters and the scalar power spectrum. Interestingly, as we shall discuss, such non-local features too

result in a better fit to the data than the conventional power law primordial spectrum.

In Chapter 4, we shall discuss the scalar bi-spectrum that arise in inflationary models that lead to local and non-local features in the power spectrum and an improved fit to the data. After a rapid outline of the Maldacena formalism, we utilize the formalism to construct an efficient numerical code to evaluate the bi-spectrum in a given inflationary model. Apart from considering the models discussed in Chapters 2 and 3, we shall also consider another model that results in sharp features in the power spectrum (and, not to mention, an improved fit to the data), and evaluate the scalar bi-spectrum in the equilateral limit in these models.

Chapter 5 considers the effects of preheating on the inflationary bi-spectrum in single field models. Since they prove to be analytically tractable, we shall focus on inflationary models wherein the potentials behave quadratically near the minimum. We shall show that, as in the case of the power spectrum, the bi-spectrum too remains largely unaffected by the epoch of preheating in any single field inflationary model. We shall also estimate the actual extent of the contribution due to preheating to the non-Gaussianity parameter  $f_{\text{NL}}$ .

In Chapter 6, we shall discuss the effects of primordial features on the matter power spectrum and the formation of halos. We shall show that certain features in the inflationary perturbation spectrum, which are consistent with the CMB data, can affect the number of halos formed to a good extent.

Chapter 7 considers the possibility of utilizing the three dimensional Ly- $\alpha$  flux spectra along multiple lines of sight to constrain the primordial bi-spectrum.

Finally, we shall close with a summary and outlook in Chapter 8.

## 1.7 Notations and conventions

Before we proceed, for convenience, let us summarize certain notations and conventions that we shall follow throughout this thesis. As we have done until now, we shall adopt units such that  $c = \hbar = 1$ , and we shall set  $M_{\text{pl}}^2 = (8\pi G)^{-1}$ . However, we should mention that, in Chapter 7, we shall retain  $c$  for convenience in making certain estimates. We shall always work with the  $(3 + 1)$ -dimensional, spatially flat, Friedmann universe. Moreover, as we have mentioned, an overdot and an overprime shall denote differentiation with respect to the cosmic time  $t$  and the conformal time  $\eta$ , respectively. Further,  $N$  shall represent the number of e-folds. Lastly, in Chapter 5, double angular brackets shall denote averaging over the oscillations during preheating.



## Chapter 2

# Generation of localized features due to a step in the inflaton potential

As we have discussed in the previous chapter, the inflationary paradigm has been performing remarkably well against the observational data. There exist many inflationary models that permit a suitably long epoch of slow roll, thereby leading to a nearly scale independent primordial scalar power spectrum. Such a spectrum, along with the assumption of the spatially flat, concordant  $\Lambda$ CDM background cosmological model, provides a good fit to the recent observations of the anisotropies in the CMB [11, 13, 15, 18, 19]. The challenge before the other competing scenarios is to match the simplicity and efficiency of inflation.

However, the efficacy of the inflationary scenario also seems to be responsible for an important drawback. Though, as a paradigm, inflation can be considered to be a success, it would be fair to say that we are rather far from converging on a specific model or even a class of models of inflation. A multitude of inflationary models still remain consistent with the data. We mentioned above that a nearly scale invariant, power law, scalar spectrum fits the observations of the anisotropies in the CMB quite well. But, as we had pointed out, there exist a few data points at the lower multipoles—notably, at the quadrupole ( $\ell = 2$ ) and near the multipole moments of  $\ell = 22$  and 40—which lie outside the cosmic variance associated with the power law primordial spectrum. Needless to add, statistically, a few outliers in a thousand or so data points can always be expected. These outliers were noticed in the WMAP first-year data [17], and they continue to be present even in the most recent, seven-year data [19], making them unlikely to be artifacts of data analysis. It seems possible that they actually point to non-trivial inflationary dynamics. In that case, these outliers are important from the phenomenological perspec-

tive of attempting to constrain the models from the data, because only a more restricted class of inflationary models can be expected to provide an improved fit to these outliers. Therefore, it is a worthwhile exercise to systematically explore models that lead to specific deviations from the standard power law, inflationary perturbation spectrum, and also provide an improved fit to the data.

Various efforts towards a model independent reconstruction of the primordial spectrum from the observed pattern of the CMB anisotropies seem to indicate the presence of certain features in the spectrum [69]. (However, we should add that there also exist other views on the possibility of features in the primordial spectrum; in this context, see, for example, Refs. [70].) In particular, a burst of oscillations in the primordial spectrum seems to provide a better fit to the CMB angular power spectrum near the multipole moments of  $\ell = 22$  and 40. Generating these oscillations requires a short period of deviation from slow roll inflation [71, 72], and such a departure has often been achieved by introducing a small step in the popular, quadratic potential describing the canonical scalar field (see Refs. [73, 74, 75]; for a discussion on other models, see, for instance, Refs. [76, 77]). At the cost of three additional parameters which characterize the location, the height and the width of the step, it has been found that this model provides a considerably better fit to the CMB data with the least squares parameter  $\chi_{\text{eff}}^2$  typically improving by about 7, when compared to the nearly scale invariant spectrum that would have resulted in the absence of the step [74, 75]. But, such a chaotic inflation model leads to a reasonable amount of tensors, and these models will be ruled out if tensors are not detected corresponding to a tensor-to-scalar ratio of, say,  $r \simeq 0.1$ .

Our aims in this chapter are twofold. Firstly, we wish to examine whether, with the introduction of a step, other inflationary models too perform equally well against the CMB data, as the quadratic potential does. Secondly, we would also like to consider a model that leads to a tensor-to-scalar ratio of  $r < 0.1$ , so that suitable alternative models exist if the tensor contribution turns out to be smaller. Motivated by these considerations, apart from revisiting the popular quadratic potential, we shall investigate the effects of the step in a small field model (in this context, see, for example, Ref. [78]) and a tachyon model [79]. Also, with possible applications to future datasets in mind (such as the ongoing Planck mission [20]), we shall evaluate the tensor power spectrum exactly, and include its contribution in our analysis. We shall compare the models with the CMB data from the WMAP, QUaD and ACBAR missions. We shall consider the five as well as the seven-year WMAP data [18, 19], the QUaD June 2009 data [11] and the ACBAR 2008 data [13] to arrive at the observational constraints on the inflationary parameters. We find

that, as one may expect, a step at a suitable location and of a certain magnitude and width improves the fit to the outliers (near  $\ell = 22$  and 40) in all the cases. We point out that, if the amplitude of the tensors prove to be small, the quadratic potential and the tachyon model will become inviable, and we will have to turn our attention to examples such as the small field models.

This chapter is organized as follows. In the following section, we shall outline the different inflationary models that we shall be focusing on. In Section 2.2, we shall discuss the methodology that we adopt for comparing the inflationary models with the data, the datasets that we use for our analysis, and the priors on the various parameters that we work with. In Section 2.3, we shall present the results of our comparison of the theoretical CMB angular power spectra that arise from the various models with the WMAP five-year as well as seven-year data, the QUaD and the ACBAR data. We shall tabulate the best fit values that we obtain on the background cosmological parameters and the parameters describing the inflationary models. We shall also illustrate the constraints that we arrive at on the parameters describing the step in the case of the small field model. Further, we shall explicitly show that the models with the step perform better against the data because of the fact that they lead to an improvement in the fit to the outliers around  $\ell = 22$  and 40. In Section 2.4, we shall illustrate the scalar power spectra and the CMB angular power spectra corresponding to the best fit values of the parameters of some of the models that we consider. Finally, in Section 2.5, we shall close with a brief summary, and a few comments on certain implications of our results.

## 2.1 The inflationary models of interest

In this section, we shall list the different inflationary models that we shall consider, and briefly outline the parameters involved in each of these cases.

### 2.1.1 The power law case

Recall that, the conventional power law, scalar and tensor spectra are given by Eqs. (1.24). We shall treat this power law case as our reference model with respect to which we shall compare the performance of the other models against the data. Often, when comparing the power law case with the observations, the following slow roll consistency condition is further assumed:  $r = -8n_T$  [11, 13, 18, 19]. But, we shall *not* impose this condition so that, while comparing the power law case with the data, we shall work with all the four

parameters, *viz.* the scalar amplitude  $A_s$ , the scalar spectral index  $n_s$ , the tensor-to-scalar ratio  $r$  and the tensor spectral index  $n_T$ .

### 2.1.2 Canonical scalar field models

We shall work with two types of canonical scalar field models. We shall firstly revisit the large field, quadratic model described by the potential

$$V(\phi) = \frac{1}{2} m^2 \phi^2, \quad (2.1)$$

where  $m$  represents the mass of the inflaton. The parameter  $m$  is essentially determined by the amplitude of the scalar power spectrum. To achieve the required number, say, 60 e-folds of inflation, in such a model, the field has to start at a suitably large value (in units of the Planck mass). The field rolls down the potential, and inflation ends as the field nears the minimum of the potential [6, 7].

The small field inflationary models offer an important alternative to the large field models. In fact, in certain cases, the small field models are possibly better motivated from the high energy physics perspective than the simple large field models (see, for example, Refs. [80]). Therefore, in addition to the quadratic potential mentioned above, we shall consider the small field model governed by the potential

$$V(\phi) = V_0 \left[ 1 - \left( \frac{\phi}{\mu} \right)^{p_0} \right]. \quad (2.2)$$

The field starts at small values in such models, and inflation is terminated naturally as the field approaches the value  $\mu$ . As is well known (and, as we shall also discuss), the quadratic potential (2.1) leads to a tensor-to-scalar ratio of  $r \simeq 0.1$  [75]. The small field model (2.2) can lead to a smaller tensor-to-scalar ratio for suitable values of  $p_0$  and  $\mu$  (in this context, see Ref. [78]). Also, when  $p_0 < 4$ , the model is known to result in a substantial red tilt. We find that, if we choose  $p_0 = 4$  and  $\mu = 15 M_{\text{Pl}}$ , the model leads to a tilt that is consistent with observations, and a tensor-to-scalar ratio of  $r \simeq 0.01$ . So while comparing with the data, we shall work with these specific values of  $p_0$  and  $\mu$ , but vary  $V_0$ .

### 2.1.3 Tachyon model

Tachyonic inflationary potentials are usually written in terms of two parameters, say,  $\lambda$  and  $\phi_*$ , in the following form [79]:

$$V(\phi) = \lambda \mathcal{V}(\phi/\phi_*), \quad (2.3)$$

where  $\mathcal{V}(\phi/\phi_*)$  is a function which has a maximum at the origin and vanishes as  $\phi \rightarrow \infty$ . The tachyon model that we shall consider is described by the potential

$$V(\phi) = \frac{\lambda}{\cosh(\phi/\phi_*)}. \quad (2.4)$$

In such a potential, inflation typically occurs around  $\phi \simeq \phi_*$ . The field rolls down the potential, and inflation ends at suitably large values of the field. It is found that the quantity  $\lambda \phi_*^2$  has to be much larger than unity to ensure that inflation lasts for a sufficiently long time [79]. We find that the amplitude of the scalar perturbations is more sensitive to  $\phi_*$  than  $\lambda$ . Hence, while comparing with the data, we shall fix the value of  $\lambda$ , and vary  $\phi_*$ . We shall set  $\lambda = 8.9 \times 10^{-4} M_{\text{Pl}}^4$ . We shall then choose the priors on  $\phi_*$  such that  $\lambda \phi_*^2$  is relatively large in order to achieve the required duration of slow roll inflation.

### 2.1.4 Introduction of the step

Given a potential, say,  $V(\phi)$ , we shall introduce the step by *multiplying* the potential by the following function:

$$g_{\text{step}}(\phi) = \left[ 1 + d \tanh\left(\frac{\phi - \phi_0}{\Delta\phi}\right) \right], \quad (2.5)$$

as is often done in the literature [17, 73, 74, 75]. It should be pointed out that the quantity  $d$  is positive in the case of the quadratic potential Eq. (2.1), whereas it is negative in the cases of the small field model (2.2) and the tachyon model (2.4). Evidently,  $d$  denotes the height of the step,  $\phi_0$  its location, and  $\Delta\phi$  its width. When comparing with the data, in addition to the potential parameters, we shall vary these three parameters, along with the background cosmological parameters, to arrive at the observational constraints.

## 2.2 Methodology, datasets, and priors

We shall evaluate the inflationary power spectra numerically. In addition to the scalar power spectrum, we shall evaluate the tensor spectrum exactly, and include it in our analysis. We shall describe the details regarding the numerical evaluation of the inflationary perturbation spectra in Chapter 4 (see Subsection 4.3.3), wherein we shall discuss the computation of the scalar bi-spectrum in the equilateral limit, *viz.*  $\mathcal{B}_s(k)$  [*cf.* Eq. (1.26)], and the corresponding non-Gaussianity parameter  $f_{\text{NL}}(k)$  [*cf.* Eq. (1.29)] that arise in inflationary models leading to features (such as the ones that we consider here). At this stage, it should suffice to say that we evolve the equations governing the background

and the perturbations using a fast and accurate Fortran 90 code that treats the e-folds  $N$  as the independent variable. The perturbations are evolved using the governing equations (1.16) and (1.18) from the Bunch-Davies initial conditions (1.23) imposed when the modes are well inside the Hubble radius. The power spectra [cf. Eqs. (1.21) and (1.22)] are evaluated when the modes are sufficiently outside the Hubble radius, when the amplitude of the perturbations have reached their asymptotic values [81, 82]. We should add here that, while the speed of propagation of the curvature perturbations induced by the canonical scalar field is a constant (and, equal to unity), it changes with time in the case of the tachyon models [79, 83]. This point needs to be carefully taken into account, while imposing the initial conditions on the modes as well as when evolving them from the sub-Hubble to the super-Hubble scales.

In order to arrive at the constraints on the various background cosmological parameters and the parameters describing the inflaton potential, we perform a Markov Chain Monte Carlo (MCMC) sampling of the parameter space. To do so, we make use of the publicly available COSMOMC package [45, 46], which in turn uses the CMB anisotropy code CAMB [44, 43] to generate the CMB angular power spectra from the primordial scalar and tensor spectra. We evaluate the scalar and the tensor spectra for all the modes that are required by CAMB to arrive at the CMB angular power spectra. For our analysis, we consider the following CMB datasets: the WMAP five-year [18] and seven-year data [19], the QUaD June 2009 data [11], and the the ACBAR 2008 data [13]. We have separately compared the models with the WMAP five-year and seven-year data. We have also compared the models with the WMAP five-year data along with the QUaD data, and with the QUaD as well as the ACBAR data. We have used the October 2009 version of COSMOMC (and CAMB) while comparing with the WMAP five-year and the QUaD and the ACBAR datasets. When comparing with the WMAP seven-year data, we have made use of a more recent version (*i.e.* the January 2010 version) of COSMOMC and CAMB.

In our analysis, we take gravitational lensing into account. Note that, to generate highly accurate lensed CMB spectra, CAMB requires  $\ell_{\max \text{ scalar}} \simeq (\ell_{\max} + 500)$ , where  $\ell_{\max}$  is, say, the largest multipole moment for which the data is available. The WMAP data is available up to  $\ell \simeq 1200$ , the QUaD data goes up to  $\ell \simeq 2000$ , while the ACBAR data is available up to  $\ell \simeq 2700$ . So, we set  $\ell_{\max \text{ scalar}} = 2500$  when dealing with the WMAP and the QUaD datasets and, when we include the ACBAR data, we set  $\ell_{\max \text{ scalar}} = 3300$ . Since the datasets involve rather large multipole moments (say,  $\ell \gtrsim 1000$ ), we also take into account the Sunyaev-Zeldovich effect, and marginalize over the  $A_{\text{SZ}}$  parameter. For the power law case, we set the pivot scale to be  $k_* = 0.05 \text{ Mpc}^{-1}$  [cf. Eq. (1.24)]. We

have made use of the publicly available WMAP likelihood code from the LAMBDA website [84] to determine the performance of the models against the data. We have set the Gelman and Rubin parameter  $|R - 1|$  to be 0.03 for convergence. Lastly, we should add that we have used the Gibbs option (for the CMB TT spectrum at the low multipoles) in the WMAP likelihood code to evaluate the least square parameter  $\chi_{\text{eff}}^2$ .

As we had mentioned earlier, we incorporate the tensor perturbations in our analysis. Recall that, in the power law case, when the consistency condition between the tensor-to-scalar ratio  $r$  and the tensor spectral index  $n_T$  is not imposed, both these quantities are required to describe the tensor power spectrum. They need to be specified along with the scalar amplitude  $A_s$  and the corresponding spectral index  $n_s$ , in order to completely determine the primordial spectra. We should emphasize that, in the other inflationary models, once the parameters that govern the potential have been specified, no further parameters are required to describe the tensor power spectrum. The potential parameters determine the amplitude and shape of *both* the scalar and the tensor spectra.

We shall assume the background to be a spatially flat,  $\Lambda$ CDM model described by the four standard parameters, *viz.*  $\Omega_b h^2$  and  $\Omega_c h^2$ , which represent the baryon and CDM densities (with  $h$  being related to the Hubble parameter), respectively, the ratio of the sound horizon to the angular diameter distance at decoupling  $\theta$ , and  $\tau$  which denotes the optical depth to reionization. We shall work with the following priors on these parameters:  $0.005 \leq \Omega_b h^2 \leq 0.1$ ,  $0.01 \leq \Omega_c h^2 \leq 0.99$ ,  $0.5 \leq \theta \leq 10.0$  and  $0.01 \leq \tau \leq 0.8$ . We should add that we keep the same priors on the background parameters for all the models and datasets that we shall consider in our analysis. In Table 2.1, we have listed the priors that we choose on the different parameters which describe the various inflationary models that we consider.

Models	Parameter	Lower limit	Upper limit
Power law case	$\ln (10^{10} A_S)$	2.7	4.0
	$n_s$	0.5	1.5
	$r$	0.0	1.0
	$n_T$	-0.5	0.5
Quadratic model with a step	$\ln (10^{10} m^2/M_{Pl}^2)$	-0.77	-0.58
	$d$	$1.3 \times 10^{-3}$	$1.7 \times 10^{-3}$
	$\phi_0/M_{Pl}$	13.0	15.0
	$\Delta\phi/M_{Pl}$	0.015	0.03
Small field model with a step	$\ln (10^{10} V_0/M_{Pl}^4)$	1.50	1.86
	$-d$	$1.0 \times 10^{-4}$	$2.0 \times 10^{-4}$
	$\phi_0/M_{Pl}$	7.8	8.1
	$\Delta\phi/M_{Pl}$	$5.0 \times 10^{-3}$	$1.0 \times 10^{-2}$
Tachyon model with a step	$\ln (10^{10} \phi_*/M_{Pl})$	34.506	34.518
	$-d$	$1.3 \times 10^{-3}$	$1.9 \times 10^{-3}$
	$\phi_0/M_{Pl}$	$7.81 \times 10^5$	$7.83 \times 10^5$
	$\Delta\phi/M_{Pl}$	340	410

Table 2.1: The priors on the various parameters that describe the primordial spectrum in the power law case, and the inflationary potential in all the other cases. We work with these priors when comparing the models with all the datasets.

## 2.3 Bounds on the background and the inflationary parameters

In this section, we shall present the results of our analysis. As we mentioned above, we have separately compared the models with the WMAP five-year and seven-year data. We have also compared the models with the WMAP five-year data along with the QUaD data, and with the QUaD as well as the ACBAR data. We shall tabulate below the best fit values that we arrive at on the various background and inflationary parameters for the power law case and for the inflationary models with the step. We shall also provide the least squares parameter  $\chi_{\text{eff}}^2$  in all the cases, *viz.* the power law case and the three inflationary models, with and without the step.

### 2.3.1 The best fit values and the effective least squares parameter $\chi_{\text{eff}}^2$

In Tables 2.2 and 2.3, we have listed the best fit values for the various parameters in the power law case and in the three inflationary models with the step. These tables contain the results that we arrive at upon comparing the models with the WMAP five-year (denoted as WMAP-5) and seven-year (denoted as WMAP-7) data, the QUaD as well as the ACBAR data sets. Note that we have only presented the results for the power law case, and when the step (2.5) has been introduced in the quadratic potential (2.1), the small field model (2.2) and the tachyon model (2.4). We find that the values we have obtained upon comparing the power law case with the WMAP five and seven-year data and the QUaD and the ACBAR data match well with the results quoted by the WMAP [18, 19] and the QUaD teams [11]. Also, the results for the quadratic potential with the step agree well with the results quoted in the recent work [75].

In Table 2.4, we have listed the least squares parameter  $\chi_{\text{eff}}^2$  for all the different models and datasets of our interest. It is clear from the table that the presence of the step leads to a reduction in  $\chi_{\text{eff}}^2$  by about 7-9 in all the three inflationary models that we have considered. Also, note that such an improvement is achieved in all the datasets that we have compared the models with. When we compare the contribution to the  $\chi_{\text{eff}}^2$  at the low multipoles (*i.e.* up to  $\ell = 32$ , see Refs. [18, 19]) from the output of the WMAP likelihood code for, say, the WMAP seven-year data, we find that the introduction of the step in the inflaton potential reduces the  $\chi_{\text{eff}}^2$  for the TT data over this range by about 5-6 in all the cases. In Figure 2.1, we have plotted the difference in  $\chi_{\text{eff}}^2$  with and without the step, as a function of the multipoles when  $\ell > 32$ , for the WMAP seven-year data. We have plotted

Datasets Parameters	WMAP-5	WMAP-5 + QUaD	WMAP-5 + QUaD + ACBAR	WMAP-7
$\Omega_b h^2$	0.0232	0.0235	0.0229	0.0226
$\Omega_c h^2$	0.1051	0.1011	0.1071	0.1108
$\theta$	1.041	1.043	1.042	1.040
$\tau$	0.0833	0.0957	0.0884	0.0895
$\ln(10^{10} A_s)$	3.040	3.047	3.053	3.088
$n_s$	0.9764	0.9835	0.9677	0.9726
$r$	0.3841	0.4150	0.0667	0.1128
$n_T$	0.4112	0.4088	0.4109	0.3581

Table 2.2: The best fit values that we arrive at for the input parameters upon comparing the power law primordial spectra (1.24) with the WMAP five and seven-year, the QUaD and the ACBAR data sets. We should point out that the best fit values that we have arrived at on using the WMAP five and seven-year data match well with the values quoted by the WMAP teams [18, 19]. Similarly, we find that the values we have obtained upon comparing with the WMAP five-year and the QUaD and the ACBAR data are in good agreement with the results arrived at by, say, the QUaD team [11]. Note that, while the WMAP teams [18, 19] had worked with the pivot point of  $k_* = 0.002 \text{ Mpc}^{-1}$ , the QUaD team had set the pivot scale to be  $k_* = 0.05 \text{ Mpc}^{-1}$ , as we do. However, we should clarify that, whereas the WMAP and the QUaD teams had imposed the consistency condition between the tensor-to-scalar ratio  $r$  and the tensor spectral index  $n_T$ , we have not done so in our analysis.

the difference in  $\chi_{\text{eff}}^2$  for the cases of the quadratic potential and the small field model. It is clear from the figure that the additional improvement by about 2 arises due to a better fit near  $\ell = 40$ . (There also seems to be a ‘loss’ of about unity in  $\chi_{\text{eff}}^2$  at  $\ell \lesssim 40$ .) In other words, the step essentially improves the fit to the data at the lower multipoles. This point will be further evident in the following section, wherein we discuss the resulting CMB angular power spectrum.

We should add here that the one-dimensional likelihood curves for the various potential parameters indicates that the data constrain the location of the step quite well in all the models. However, we find that the bounds on the height and the width of the step do not prove to be equally tight. Interestingly, we find that the data constrain the ratio of the height to the width of the step fairly tightly (see Ref. [85]; in this context, also see Ref. [86]).

Models	Datasets Parameters	WMAP-5	WMAP-5 + QUaD	WMAP-5 + QUaD + ACBAR	WMAP-7
Quadratic potential with step	$\Omega_b h^2$	0.0228	0.0227	0.0228	0.0224
	$\Omega_c h^2$	0.1109	0.1091	0.1094	0.1108
	$\theta$	1.041	1.041	1.042	1.0397
	$\tau$	0.0814	0.0869	0.0902	0.0848
	$\ln(10^{10} m^2/M_{\text{Pl}}^2)$	-0.6893	-0.6849	-0.6774	-0.6717
	$d \times 10^4$	13.96	15.02	13.95	16.06
	$\phi_0/M_{\text{Pl}}$	14.67	14.67	14.67	14.67
	$\Delta\phi/M_{\text{Pl}}$	0.0257	0.0259	0.0290	0.0311
Small field model with step	$\Omega_b h^2$	0.0228	0.0228	0.0229	0.0222
	$\Omega_c h^2$	0.1082	0.1084	0.1096	0.1114
	$\theta$	1.041	1.041	1.042	1.038
	$\tau$	0.0857	0.0868	0.0847	0.0813
	$\ln(10^{10} V_0/M_{\text{Pl}}^4)$	1.684	1.690	1.689	1.705
	$-d \times 10^3$	0.1153	0.1371	0.1701	0.1569
	$\phi_0/M_{\text{Pl}}$	7.888	7.887	7.887	7.888
	$\Delta\phi/M_{\text{Pl}}$	0.0070	0.0076	0.0089	0.0090
Tachyon model with step	$\Omega_b h^2$	0.0226	0.0228	0.0227	0.0222
	$\Omega_c h^2$	0.1113	0.1103	0.1104	0.1129
	$\theta$	1.040	1.041	1.042	1.039
	$\tau$	0.0908	0.0937	0.0926	0.0829
	$\ln(10^{10} \phi_*/M_{\text{Pl}})$	34.51	34.51	34.51	34.51
	$-d$	0.0014	0.0016	0.0014	0.0015
	$\phi_0 \times 10^{-6}/M_{\text{Pl}}$	0.7818	0.7828	0.7826	0.7813
	$\Delta\phi/M_{\text{Pl}}$	378.8	371.9	341.1	352.4

Table 2.3: The best fit values for the various input parameters corresponding to the three inflationary models with the step. We should point out that the best fit values for the parameters that we have arrived at for the quadratic potential with the step and the WMAP five-year data are in good agreement with the results quoted in the recent work [75].

Datasets	WMAP-5	WMAP-5 + QUaD	WMAP-5 + QUaD + ACBAR	WMAP-7
Models				
Power law case (4, 4)	2658.40	2757.34	2779.12	7474.48
Quadratic potential (1, 1)	2658.22 (-0.18)	2757.54 (+0.20)	2779.02 (-0.10)	7474.78 (+0.30)
Quadratic potential + step (4, 4)	2651.00 (-7.40)	2750.38 (-6.96)	2771.72 (-7.40)	7466.28 (-8.20)
Small field model (3, 1)	2658.26 (-0.14)	2757.46 (+0.12)	2779.06 (-0.06)	7474.78 (+0.30)
Small field model + step (6, 4)	2650.96 (-7.44)	2750.26 (-7.08)	2771.92 (-7.20)	7466.00 (-8.48)
Tachyonic model (2, 1)	2658.26 (-0.14)	2757.60 (+0.26)	2779.10 (-0.02)	7474.56 (+0.08)
Tachyonic model + step (5, 4)	2651.14 (-7.26)	2750.50 (-6.84)	2772.06 (-7.06)	7465.92 (-8.56)

Table 2.4: The  $\chi_{\text{eff}}^2$  for the different models and datasets that we have considered. The two quantities that appear within the brackets in the leftmost column indicate the number of inflationary parameters available in the different models and the number of parameters that we have varied when comparing the models against the data, in that order. The quantities within the brackets in the remaining columns indicate the difference in the  $\chi_{\text{eff}}^2$  between the model and the power law case for that dataset, with a negative value indicating an improvement in the fit. Note that, as we had mentioned earlier, the Gibbs approach in the WMAP likelihood code has been used to calculate the  $\chi_{\text{eff}}^2$  for the CMB TT spectrum at the low multipoles (*i.e.* for  $\ell < 32$ ) [18, 19]. Without the step, all the inflationary models perform just as well as the power law case. And, evidently, the introduction of the step reduces the  $\chi_{\text{eff}}^2$  by about 7-9 in *all* the cases.

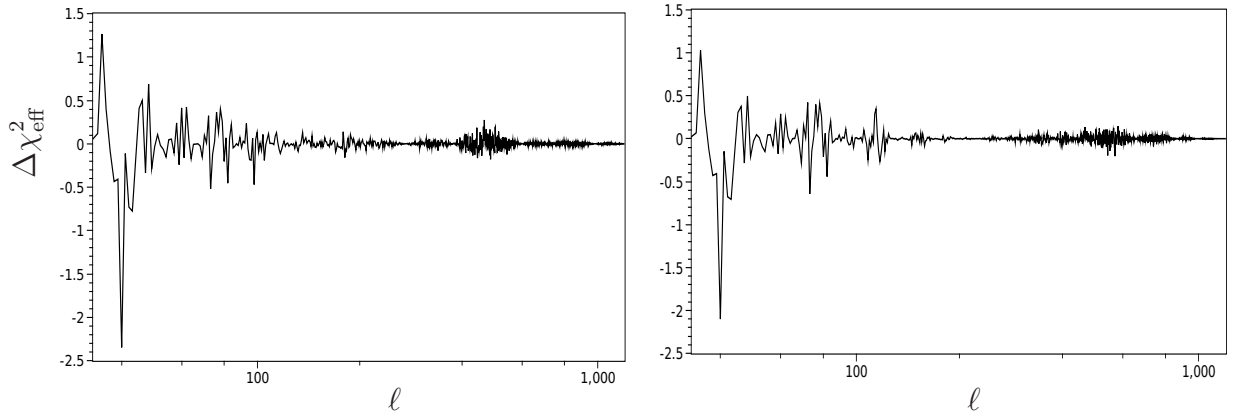


Figure 2.1: The difference in  $\chi_{\text{eff}}^2$  for the WMAP seven-year data with and without the step has been plotted as a function of the multipole moment for  $\ell > 32$ . The plot on the left corresponds to the quadratic potential, while the one on the right is for the small field model. The two figures are strikingly similar, and it is clear that the improvement in  $\chi_{\text{eff}}^2$  occurs near  $\ell \simeq 40$  in both the cases. We find that the corresponding result for the tachyon model behaves in essentially the same fashion.

## 2.4 The scalar and the CMB angular power spectra

As we had mentioned in the opening section, the introduction of the step leads to a small deviation from slow roll inflation [74, 75]. We have illustrated this behavior in Figure 2.2, wherein we have plotted the evolution of the first slow roll parameter  $\epsilon_1$  and the quantity  $\eta = \epsilon_1 - \epsilon_2/2$  around the time when the field crosses the step in the small field model. We find that essentially the same behavior arises in all the three inflationary models that we have considered. The small deviation from slow roll inflation leads to a burst of oscil-

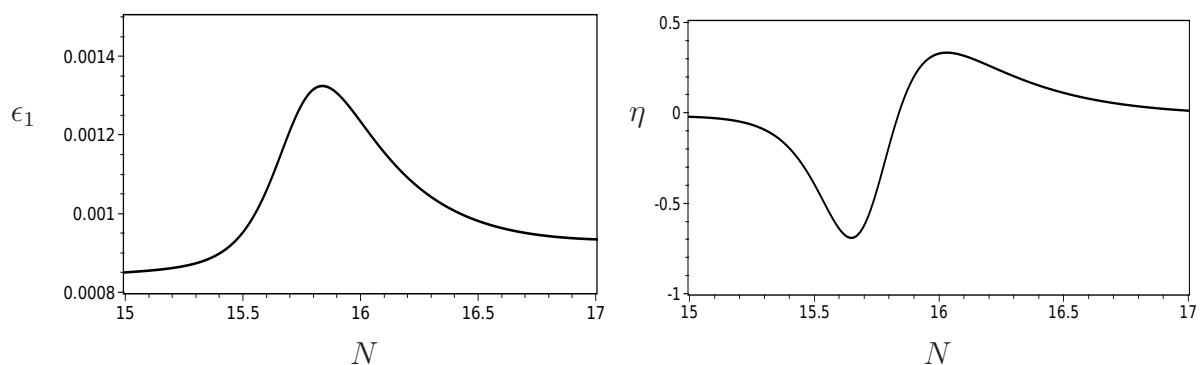


Figure 2.2: Typical evolution of the first slow roll parameter  $\epsilon_1$  and the quantity  $\eta = \epsilon_1 - \epsilon_2/2$ , with the introduction of the step for the three inflationary models that we have considered. We have plotted the quantities as a function of the e-folds  $N$  for the small field model around the time when the field crosses the step in the potential.

lations superimposed on the otherwise nearly scale invariant scalar power spectrum, as we have illustrated in Figure 2.3. We should add that, since the deviation from slow roll is relatively small, the introduction of the step hardly affects the tensor spectrum. It remains nearly scale invariant in all the cases. At the pivot point  $k_* = 0.05 \text{ Mpc}^{-1}$ , we find the tensor-to-scalar ratio  $r$  to be about 0.16, 0.016 and 0.16 in the cases of the quadratic potential, the small field and the tachyon models, respectively.

The burst of oscillations in the scalar power spectrum in turn results in a feature in the CMB TT angular power spectrum, which leads to the improvement in the fit to the data at the lower multipoles. This behavior is evident in Figure 2.4 wherein we have plotted the CMB TT angular power spectra for the quadratic potential without and with the step, and for the small field model with the step.

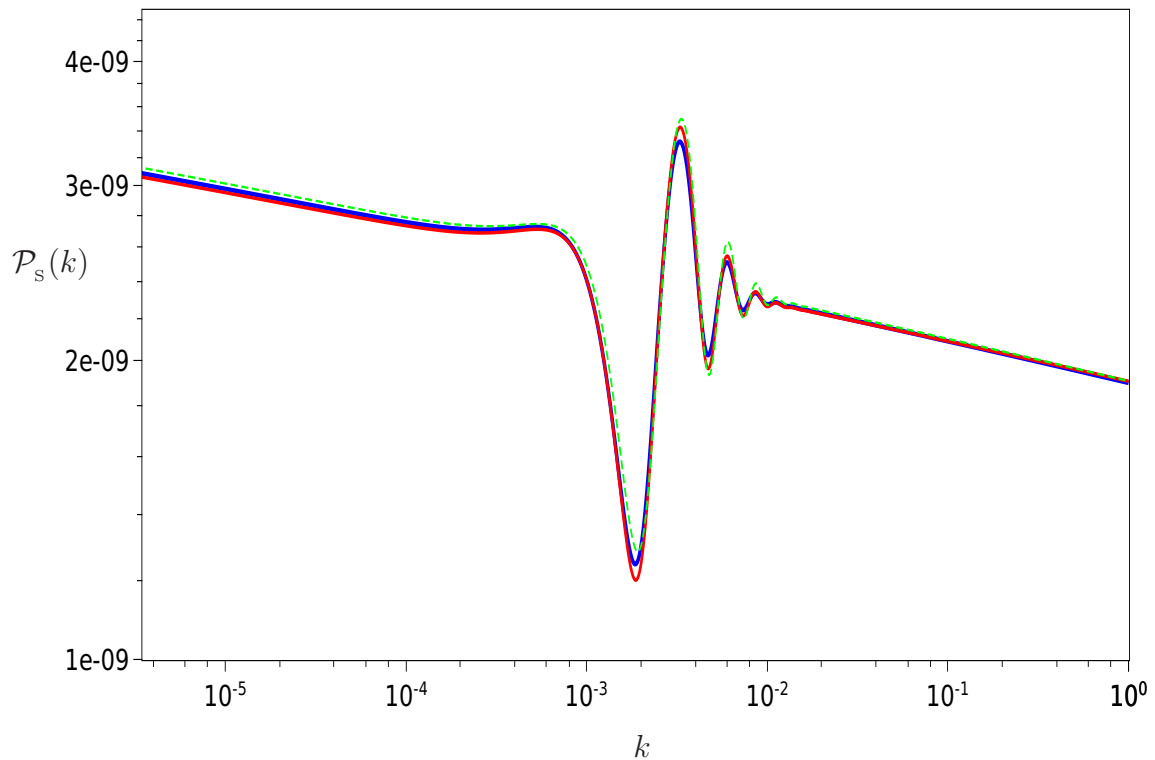


Figure 2.3: The scalar power spectra corresponding to the best fit values of the WMAP seven-year data for the inflationary models with the step. The solid blue, the solid red, and the dashed green curves describe the scalar power spectra in the cases of the quadratic potential, the small field model, and the tachyon model, respectively. Evidently, the three spectra are hardly distinguishable. And, obviously, the oscillations will not arise in the absence of the step.

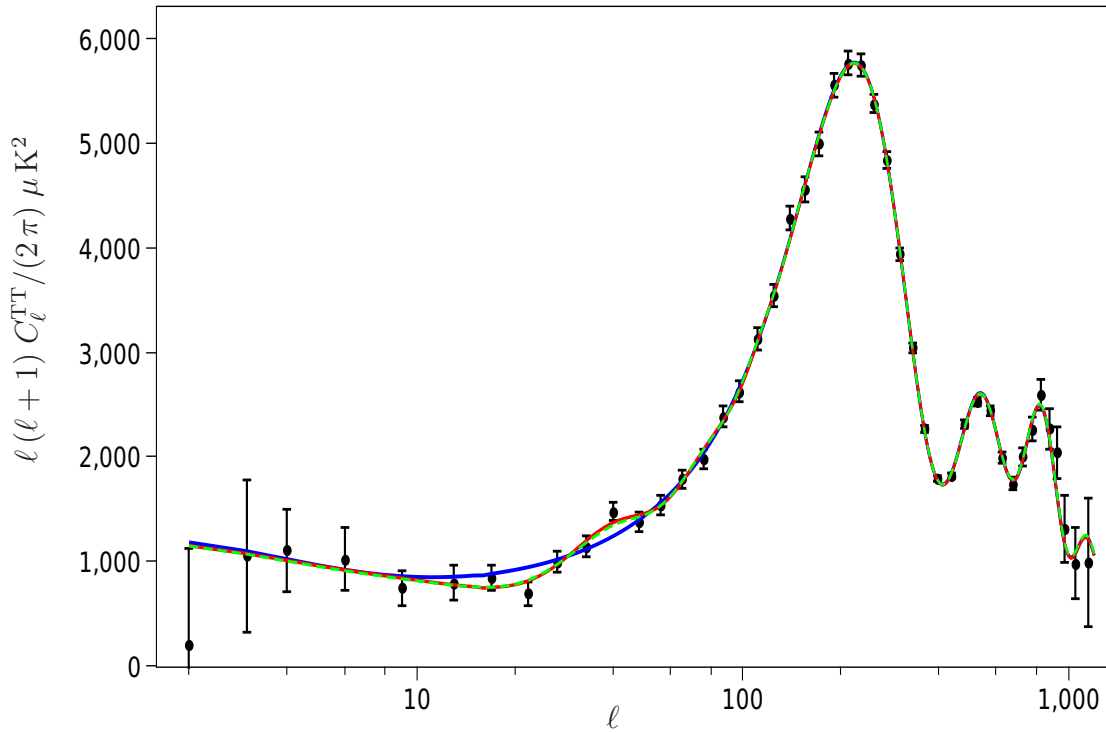


Figure 2.4: The CMB TT angular power spectra corresponding to the best fit values of the inflationary models for the WMAP seven-year data without and with the step. The solid blue and the solid red curves correspond to the quadratic potential without and with the step, respectively. The dashed green curve corresponds to the best fit small field model with the step. We find that the results for the tachyon model behave in exactly the same fashion. The black dots with error bars denote the WMAP seven-year data. It is visually evident that, with the introduction of the step, the models lead to a better fit to the data near the multipole moments of  $\ell = 22$  and  $40$ .

## 2.5 Discussion

In this chapter, we have investigated the effects of introducing a step in certain inflationary models. In addition to revisiting the case of the quadratic potential that has been considered earlier, we have studied the effects of the step in a small field model and a tachyon model. The introduction of the step leads to a small deviation from slow roll inflation, which results in a burst of oscillations in the scalar power spectrum. These oscillations, in turn, leave their imprints as specific features in the CMB angular power spectrum. Actually, we have also evaluated the tensor power spectrum exactly, and have included it in our analysis. We believe that this is a timely effort considering the fact that results from, say, the ongoing Planck mission might necessitate such an analysis [87]. Upon comparing the inflationary models with the WMAP, the QUaD and the ACBAR data, we find that, with the step, all the models lead to an improvement in  $\chi_{\text{eff}}^2$  by about 7-9 over the smooth, nearly scale invariant, slow roll spectrum, at the expense of three additional parameters describing the location, the height and the width of the step in the inflaton potential. The output of the WMAP likelihood code and a plot of the difference in  $\chi_{\text{eff}}^2$  with and without the step clearly illustrate that the improvement occurs because of a better fit to the data at the lower multipoles due to the presence of the step [85]. Evidently, if future observations indicate that the amplitude of the tensors are rather small, then the quadratic potential and the tachyon model will be ruled out, while a suitable small field model with a step can be expected to perform well against the data.

The introduction of the step in an inflationary model can possibly be viewed as an abrupt change in a potential parameter [73]. But, it has to be admitted that it is rather ad-hoc, and one needs to explore the generation of features and a resulting improvement in the fit in better motivated inflationary models. Two field models offer such a possibility. For instance, with suitably chosen parameters, the two field models can easily lead to a brief departure from slow roll inflation (in this context, see, for example, Refs. [76, 88, 89]). However, iso-curvature perturbations arise whenever more than one field is involved [36, 90], and they need to be carefully taken into account when comparing these models with the data. It will be a worthwhile effort to systematically explore the two field models, including the effects due to the iso-curvature perturbations, in an attempt to fit the outliers near the multipole moments of  $\ell = 22$  and 40.

Over the last few years, it has been recognized that primordial non-Gaussianity can act as a powerful observational tool that can help us discriminate further between the various inflationary models. For example, it has been shown that slow roll inflation driven

by the canonical scalar fields leads only to a small amount of non-Gaussianity [49, 52]. However, recent analysis of the CMB data seem to suggest that the extent of primordial non-Gaussianity may possibly be large [19, 57, 58]. It is known that models which lead to features, such as the ones we have considered here, also generate a reasonably large non-Gaussianity [53]. While the different models that we have considered in this chapter lead to virtually the same scalar power spectrum and almost the same extent of improvement in the fit (*i.e.* with the introduction of the step) to the CMB data, it is important to examine whether they lead to the same extent of non-Gaussianity as well. We shall touch upon this issue in Chapter 4.



## Chapter 3

# Non-local features in the primordial spectrum

In the previous chapter, we had discussed as to how certain features in the scalar power spectrum, generated due to a step introduced in otherwise smooth inflationary potentials, results in a better fit to the CMB data than the more conventional power law primordial spectrum. In fact, there exist a wide variety of inflationary models that lead to localized features in the primordial spectrum and an improved fit to the data (for an inherently incomplete list of such models, see, for instance, Refs. [76, 77, 88, 91, 92] and references therein). It should be noted here that generating such localized features require either one or more periods of deviation from slow roll inflation [71, 72] or modifications to the initial conditions on the perturbations [93].

Apart from localized features, it is interesting to examine whether the CMB data also point to non-local features—*i.e.* certain characteristic and repeated behavior that extend over a wide range of scales—in the primordial spectrum. A quick glance at the unbinned CMB data seems to suggest that, after all, such an eventuality need not altogether be surprising. In fact, earlier investigations on possible Planck scale modifications to the primordial spectrum have indicated that continuing oscillations in the power spectrum can lead to a substantial improvement in the fit at the cost of two or three additional parameters (see Refs. [94, 95]; in this context, also see Ref. [96]). In this chapter, we shall investigate two inflationary models involving the canonical scalar field that lead to similar oscillations over all scales in the curvature perturbation spectrum. We shall consider a model described by the conventional quadratic potential, but superposed by a sinusoidal modulation [53, 97] and the presently popular axion monodromy model (see, for example, Refs. [53, 98]). It should be mentioned here that these models have been com-

pared with the WMAP data recently [97, 98, 99, 100]. However, all the earlier analyses had resorted to evaluating the scalar power spectrum in the slow roll approximation. In contrast, we shall compute the scalar power spectrum *exactly* using a highly accurate numerical code. And, we shall evaluate the tensor spectrum too accurately and include it in our analysis. Moreover, as the oscillations in the inflationary scalar power spectrum continue even over smaller scales, in addition to the WMAP seven-year data [19], we shall compare the models with the small scale data from ACT [15]. While both the models that we consider lead to oscillations in the spectrum, we find that the monodromy model results in a superior fit to the data.

This chapter is organized as follows. In the following section, we shall briefly describe the models that we shall consider and the methodology that we shall adopt to compare the models with the data. In the subsequent section, we shall present the results of our analysis. We shall conclude with a brief summary and discussion in the final section.

## 3.1 Models and methodology

In this section, we shall briefly describe the models that we shall work with and the methodology we shall adopt to compare the models with the data.

### 3.1.1 The models

As we mentioned, we shall consider two models, both of which involve the canonical scalar field, say,  $\phi$ . The first of the two is the chaotic inflationary model that is modulated by sinusoidal oscillations and described by the potential [97]

$$V(\phi) = \frac{1}{2} m^2 \phi^2 \left[ 1 + \alpha \sin \left( \frac{\phi}{\beta} + \delta \right) \right], \quad (3.1)$$

where  $m$  is the parameter that characterizes the original quadratic potential, while the parameters  $\alpha$  and  $\beta$  describe the amplitude and the frequency of the superimposed oscillations. We have also included the parameter  $\delta$ , which shifts the oscillations within one period, in our analysis. The second model that we shall consider is the axion monodromy model which is motivated by string theory [53, 98, 99]. The inflaton potential in such a case is given by

$$V(\phi) = \lambda \left[ \phi + \alpha \cos \left( \frac{\phi}{\beta} + \delta \right) \right]. \quad (3.2)$$

Note that, while the amplitude of the oscillation is fixed in the axion monodromy model, in the chaotic model described by the potential (3.1), the amplitude depends quadratically

on the field. The inflaton oscillates as it rolls down these potentials, and these oscillations continue all the way until the end of inflation (in this context, see Figure 6.1). This behavior leads to small oscillations in the slow roll parameters, which in turn results in continuing oscillations in the primordial scalar power spectrum. Our goal is to examine the extent to which such oscillations are admitted by the CMB data.

As we had done in the last chapter, we shall compare the performance of the above two inflationary models with the conventional, power law, primordial spectra [cf. Eqs. (1.24)]. However, in the power law case, unlike the previous chapter, for the sake of simplicity, we shall now impose the slow roll consistency condition, *viz.* that  $r = -8 n_T$ . Therefore, the power law spectra are completely described by the scalar amplitude  $A_s$ , the scalar spectral index  $n_s$  and the tensor-to-scalar ratio  $r$ .

### 3.1.2 Priors

We shall assume the background cosmological model to be the standard, spatially flat,  $\Lambda$ CDM model. Also, we shall work with the same set of priors on the four background parameters, *viz.*  $\Omega_b h^2$ ,  $\Omega_c h^2$ ,  $\theta$  and  $\tau$ , that we had worked with in the previous chapter. Further, we shall also include the tensor perturbations in our analysis. As we had pointed out earlier, in inflationary models, the potentials completely determine the scalar *as well as* the tensor spectra.

It is clear that, in the absence of oscillations in the potential, the two inflationary models of our interest will lead to nearly scale invariant spectra. Therefore, the main parameter that describes the two models, *viz.*  $m$  in the chaotic inflationary model and  $\lambda$  in the case of the axion monodromy model, are essentially determined by COBE normalization [48]. In the absence of oscillations in the potential, we find that the best fit chaotic model leads to a power law spectrum with a scalar spectral index of about 0.96, while the monodromy model corresponds to  $n_s \simeq 0.97$ . Also, as one would have anticipated, both of them perform almost equally well against the data. However, when the oscillations in the potential are taken into account, they induce modulations in the slow roll parameters, which in turn lead to oscillations in the scalar power spectrum. (These small oscillations hardly modify the tensor spectrum, and hence it remains nearly scale invariant.) As we shall see, when the oscillations are included, the monodromy model performs better against the data than the chaotic inflation model.

We have chosen the priors on the two inflationary models such that the amplitude of the resulting scalar spectra remain close to the COBE value, lead to the desired spectral

Model	Parameter	Lower limit	Upper limit
Power law case	$\ln (10^{10} A_s)$	2.7	4.0
	$n_s$	0.5	1.5
	$r$	0.0	1.0
Chaotic model with sinusoidal modulation	$\ln (10^{10} m^2/M_{\text{Pl}}^2)$	-0.77	-0.58
	$\alpha$	0	$2 \times 10^{-3}$
	$\beta/M_{\text{Pl}}$	$2 \times 10^{-2}$	1
	$\delta$	$-\pi$	$\pi$
Axion monodromy model	$\ln (10^{10} \lambda/M_{\text{Pl}}^3)$	0.7	1.25
	$\alpha$	0	$2 \times 10^{-4}$
	$\beta/M_{\text{Pl}}$	$3 \times 10^{-4}$	$1 \times 10^{-3}$
	$\delta$	$-\pi$	$\pi$

Table 3.1: The priors on the three parameters that describe the primordial spectra in the power law case, and the parameters that describe the two inflationary potentials of our interest. We work with the same priors when comparing the models with the WMAP as well as the ACT data.

index, and result in a certain minimum duration of inflation. We have listed the priors that we have worked with on the inflationary models in Table 2.1.

### 3.1.3 Comparison with the recent CMB observations

To compare our models with the recent CMB observations, we perform the MCMC sampling of the parameter space using the publicly available COSMOMC package [45, 46], as we had discussed while considering localized features in the previous chapter. As we had mentioned, the COSMOMC code in turn utilizes the Boltzmann code CAMB [43, 44] to arrive at the CMB angular power spectrum from given primordial scalar and tensor spectra. We evaluate the inflationary scalar as well as tensor spectra using an accurate and efficient numerical code, feed these spectra into CAMB to obtain the corresponding CMB angular power spectra. We shall discuss the essential details pertaining to the numerical computation of the inflationary spectra in Chapter 4 (see Subsection 4.3.3). However, two points concerning the evaluation of the inflationary power spectra in potentials with oscillatory terms needs to be stressed at this stage of our discussion. Firstly, in contrast to smooth inflationary potentials, oscillatory potentials such as those of our interest here can exhibit certain resonant behavior. In order to capture this behavior, depending on the

values of the potential parameters, it can become necessary to integrate from deeper inside the Hubble radius than is usually done (in this context, see, for instance, Refs. [98]). We impose the initial conditions on the modes when  $k/(aH) \simeq 250$  [rather than when  $k/(aH) \simeq 100$ , as is usually done] which we find to be suitable for the range of parameters of the potentials that we work with. Secondly, we should emphasize that we actually evolve *all the modes* that are required by CAMB from the sub to the super-Hubble scales to obtain the perturbation spectra, rather than evolve for a smaller set of modes and interpolate to arrive at the complete spectrum. This becomes imperative in the models of our interest which (as one would expect, and as we shall illustrate below) contain fine features in the scalar power spectrum. It should be pointed out here that, while the chaotic model leads to a tensor-to-scalar ratio of 0.16, the monodromy model results in  $r \simeq 0.06$ . Though these tensor amplitudes are rather small to make any significant changes to the results, we have developed the code to evaluate the inflationary power spectra with future datasets (such as, say, Planck) in mind, and hence we nevertheless take the tensors into account exactly.

For our analysis, we consider the WMAP seven-year data and the small scale data from ACT [15]. We have worked with the May 2010 versions of the COSMOMC and CAMB codes [45, 46, 43, 44], and we have made use of the WMAP (version v4p1) and the ACT likelihoods while comparing with the corresponding data [84]. While ACT has observed CMB at the frequencies of 148 GHz as well as 218 GHz, we shall only consider the 148 GHz data. Moreover, though the ACT data spans over a wide range of multipoles ( $500 \lesssim \ell \lesssim 10000$ ), for the sake of numerical efficiency (as has been implemented in Ref. [15]), we have set the CMB spectrum to zero for  $\ell > 4000$ , since the contribution at larger multipoles is negligible. When considering the ACT data, following the earlier work [15], in the power law case, we have marginalized over the three secondary parameters  $A_{\text{SZ}}$ ,  $A_{\text{p}}$  and  $A_{\text{c}}$ , where  $A_{\text{SZ}}$  denotes the Sunyaev-Zeldovich amplitude,  $A_{\text{p}}$  the amplitude for the Poisson power from radio and infrared point sources, while  $A_{\text{c}}$  is the amplitude corresponding to the cluster power. However, when comparing the oscillatory inflationary potentials with the ACT data, we have only marginalized over  $A_{\text{SZ}}$  and have fixed the values of the other two parameters  $A_{\text{p}}$  and  $A_{\text{c}}$ .

We take gravitational lensing into account. As we had pointed out in the last chapter, to generate highly accurate lensed CMB spectra, CAMB requires  $\ell_{\text{max scalar}} \simeq (\ell_{\text{max}} + 500)$ , where  $\ell_{\text{max}}$  is the largest multipole moment for which the data is available. The WMAP seven-year data is available up to  $\ell \simeq 1200$ , while the ACT data is available up to  $\ell \simeq 10000$ . For the WMAP seven-year data, we set  $\ell_{\text{max scalar}} \simeq 1800$ , and for ACT we choose

$\ell_{\max \text{ scalar}} \simeq 4500$  since we are ignoring the data for  $\ell > 4000$ . We set  $\ell_{\max \text{ tensor}} \simeq 400$  for all the datasets, as they decay down quickly thereafter. ACT has measured only  $C_\ell^{\text{TT}}$ , so the constraints from polarization, if any, will arise only from the WMAP data.

Lastly, since the scalar perturbation spectra that we expect to arise in the inflationary models of our interest contain repeated patterns extending over a wide range of scales, one can anticipate that equivalent patterns would be present in the CMB angular power spectrum running over all angular scales. It is well known that the Boltzmann code CAMB uses an effective sampling and a highly accurate spline interpolation to determine the CMB angular power spectrum over the multipoles of interest [44, 43]. However, when the underlying potential power spectra contain oscillations, this default technique might not be accurate [94, 98, 100]. Following a method adopted earlier in a similar context [94], we incorporate certain changes in the standard CAMB and COSMOMC packages to avoid limited sampling, and evaluate the angular power spectrum at all the multipoles.

## 3.2 Results

In this section, we shall discuss the results of our analysis. We shall present the best fit values of the various parameters and also discuss the resulting primordial and CMB angular power spectra.

### 3.2.1 The best fit background and inflationary parameters

We shall tabulate the best fit parameters in this subsection. We find that our results for the power law case are in good agreement with the WMAP seven-year [19] and the ACT results [15]. In fact, we have cross checked our results with and without the tensor contribution. As stated earlier, we have made use of the three secondary parameters  $A_{\text{SZ}}$ ,  $A_{\text{p}}$  and  $A_{\text{c}}$  when comparing the power law case with the combined WMAP seven-year and ACT data. In this case, we obtain the mean value of  $A_{\text{p}}$  to be 16.0, whereas  $A_{\text{c}}$  is described by a single tailed distribution which suggests that  $A_{\text{c}} < 8.4$  at 95% CL (when the tensors are not taken into account). We find that, for the power law spectra, if we fix  $A_{\text{p}}$  at the above-mentioned mean value and set  $A_{\text{c}}$  to be zero, the least squared parameter  $\chi_{\text{eff}}^2$  changes by a negligible amount (in fact,  $\Delta\chi_{\text{eff}}^2 \simeq 0.2\text{--}0.3$ ), and the best fit, the mean values and the deviations too do not change appreciably. So, in the case of the two inflationary models of our interest, we have set  $A_{\text{p}} = 16.0$ ,  $A_{\text{c}} = 0$ , and have marginalized over  $A_{\text{SZ}}$ . In Table 3.2 below, we have listed the best fit values that we arrive at for the background

	Datasets	WMAP-7	WMAP-7 + ACT
Model	Parameter	Best fit	Best fit
Chaotic model with sinusoidal modulation	$\Omega_b h^2$	0.0220	0.0218
	$\Omega_c h^2$	0.1164	0.1215
	$\theta$	1.038	1.040
	$\tau$	0.0850	0.0876
	$\ln(10^{10} m^2/M_{\text{Pl}}^2)$	-0.667	-0.687
	$\alpha$	$0.256 \times 10^{-3}$	$0.998 \times 10^{-3}$
	$\beta/M_{\text{Pl}}$	0.1624	0.2106
	$\delta$	2.256	-2.2
Axion monodromy model	$\Omega_b h^2$	0.0227	0.0223
	$\Omega_c h^2$	0.1079	0.1119
	$\theta$	1.040	1.041
	$\tau$	0.0921	0.0884
	$\ln(10^{10} \lambda/M_{\text{Pl}}^3)$	0.9213	0.9332
	$\alpha$	$1.84 \times 10^{-4}$	$1.75 \times 10^{-4}$
	$\beta/M_{\text{Pl}}$	$4.50 \times 10^{-4}$	$5.42 \times 10^{-4}$
	$\delta$	0.336	-0.6342

Table 3.2: The best fit values for the two inflationary models on comparing with the WMAP seven-year data (denoted as WMAP-7 here, and in the following table) alone, and along with the ACT data.

cosmological parameters and the parameters that describe the chaotic inflationary model with superposed oscillations and the axion monodromy model.

### 3.2.2 The spectra and the improvement in the fit

In Table 3.3, we have listed the least squares parameter  $\chi_{\text{eff}}^2$  for the different models and datasets that we have considered. From the table it is clear that the monodromy model leads to a much better fit with  $\chi_{\text{eff}}^2$  improving by about 13 in the case of the WMAP seven-year data and by about 5 when the ACT data has also been included. (We will discuss the reason for this difference in the concluding section.) The table also seems to indicate two further points. Firstly, even though the chaotic model with the sinusoidal modulation does not perform as well as the monodromy model, the fact that the model performs

Datasets	WMAP-7	WMAP-7 + ACT
Model		
Power law case	7468.4	7500.4
Chaotic model with sinusoidal modulation	7468.0	7498.2
Axion monodromy model	7455.3	7495.2

Table 3.3: The  $\chi_{\text{eff}}^2$  for the different models and datasets that we have considered. Note that we have used the Gibbs approach in the WMAP likelihood code to calculate the  $\chi_{\text{eff}}^2$  for the CMB TT spectrum at the low multipoles (*i.e.* for  $\ell < 32$ ) [18, 19].

better when the small scale data from ACT is included suggests that oscillations can be favored by the data. Secondly, oscillations of fixed amplitude in the potential as in the monodromy model seem to be more favored by the data than the oscillations of varying amplitude as in the case of the chaotic model with sinusoidal modulations. In fact, this strengthens similar conclusions that has been arrived at earlier [94, 95], wherein Planck scale oscillations of a certain amplitude in the primordial spectrum was found to lead to a considerably better fit to the data.

It is now interesting to enquire as to whether there exist localized windows of multipoles over which the improvement in the fit occurs. We find that, in the case of the chaotic model with sinusoidal modulations, as far as the WMAP seven-year data is concerned, there is an improvement of at most unity in all the multipoles combined. In Figure 3.1, after binning suitably, we have plotted the difference  $\Delta\chi_{\text{eff}}^2 = \chi_{\text{eff}}^2(\text{model}) - \chi_{\text{eff}}^2(\text{power law})$  as a function of the multipoles for the WMAP seven-year TT and TE data in the case of the axion monodromy model. It is clear from the figure that the source of the improvement in the fit is not confined to any specific set of multipoles, and it arises due to small increments that accrue over the entire range of available data. In Figures 3.2 and 3.3, we have plotted the scalar power spectra and the corresponding CMB TT angular power spectra for the best fit values of the WMAP seven-year data in the two inflationary models that we have considered.

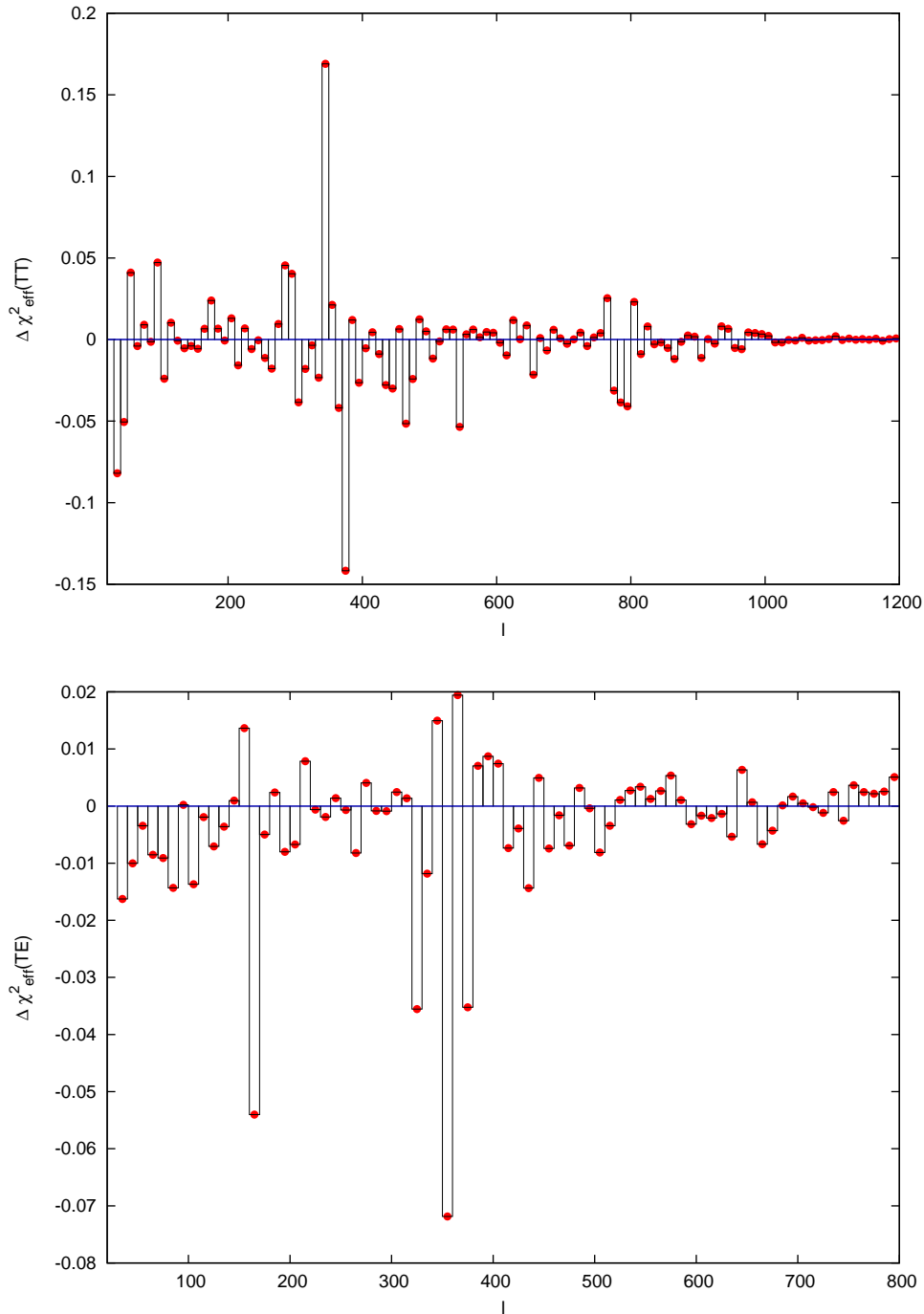


Figure 3.1: The difference in  $\chi_{\text{eff}}^2$  with respect to the reference model, *i.e.*  $\Delta\chi_{\text{eff}}^2 = \chi_{\text{eff}}^2(\text{model}) - \chi_{\text{eff}}^2(\text{power law})$ , in the case of the axion monodromy model has been plotted as a function of the multipole moment for the WMAP seven-year data, after binning in the multipole space with  $\ell_{\text{bin}} = 10$ . While the figure on top corresponds to the WMAP seven-year TT data (for  $\ell > 32$ ), the lower one is for the TE data (for  $\ell > 24$ ).

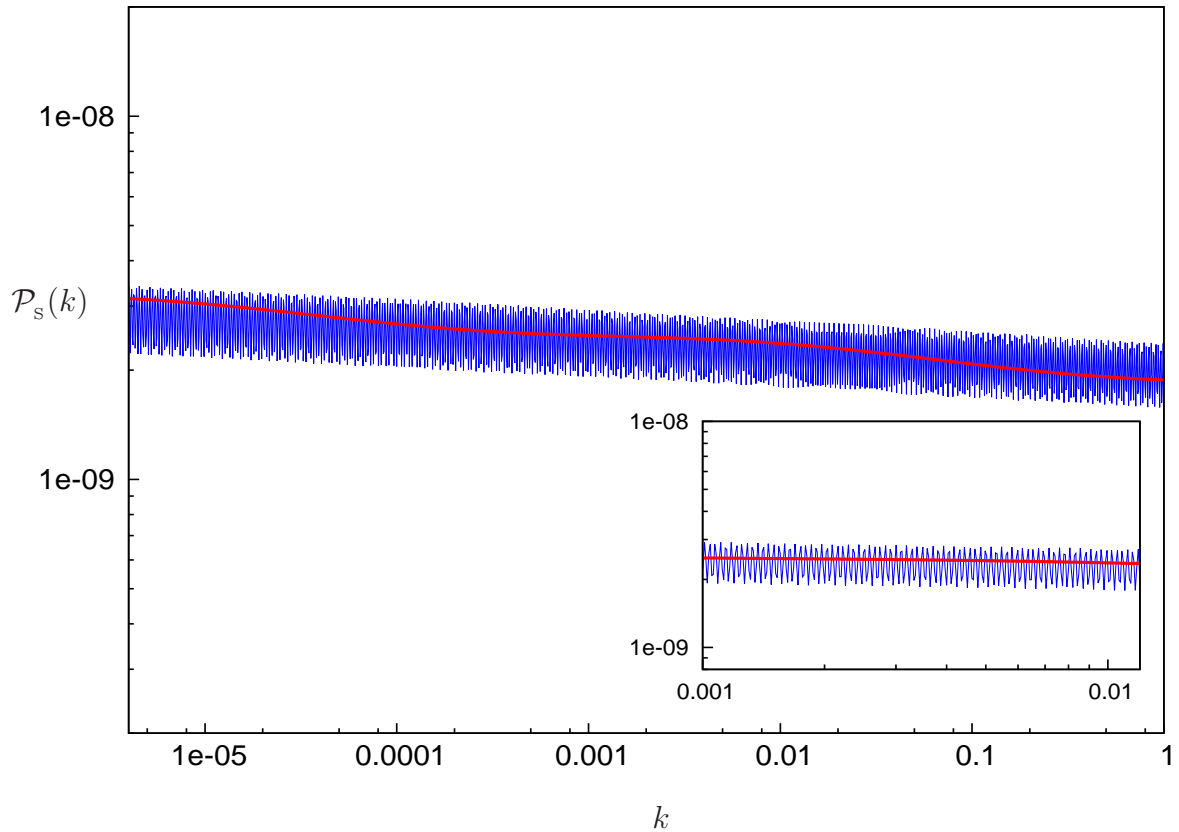


Figure 3.2: The scalar power spectra corresponding to the best fit values of the WMAP seven-year data for the two inflationary models that we have considered. The solid red and blue lines describe the scalar power spectra in the cases of the chaotic model with a sinusoidal modulation and the axion monodromy model, respectively. The spectrum corresponding to the best fit power law model would essentially be the same as in the chaotic model with sinusoidal modulations, but without any oscillations. The extraordinary extent of persistent oscillations in the case of the monodromy model is highlighted in the inset.

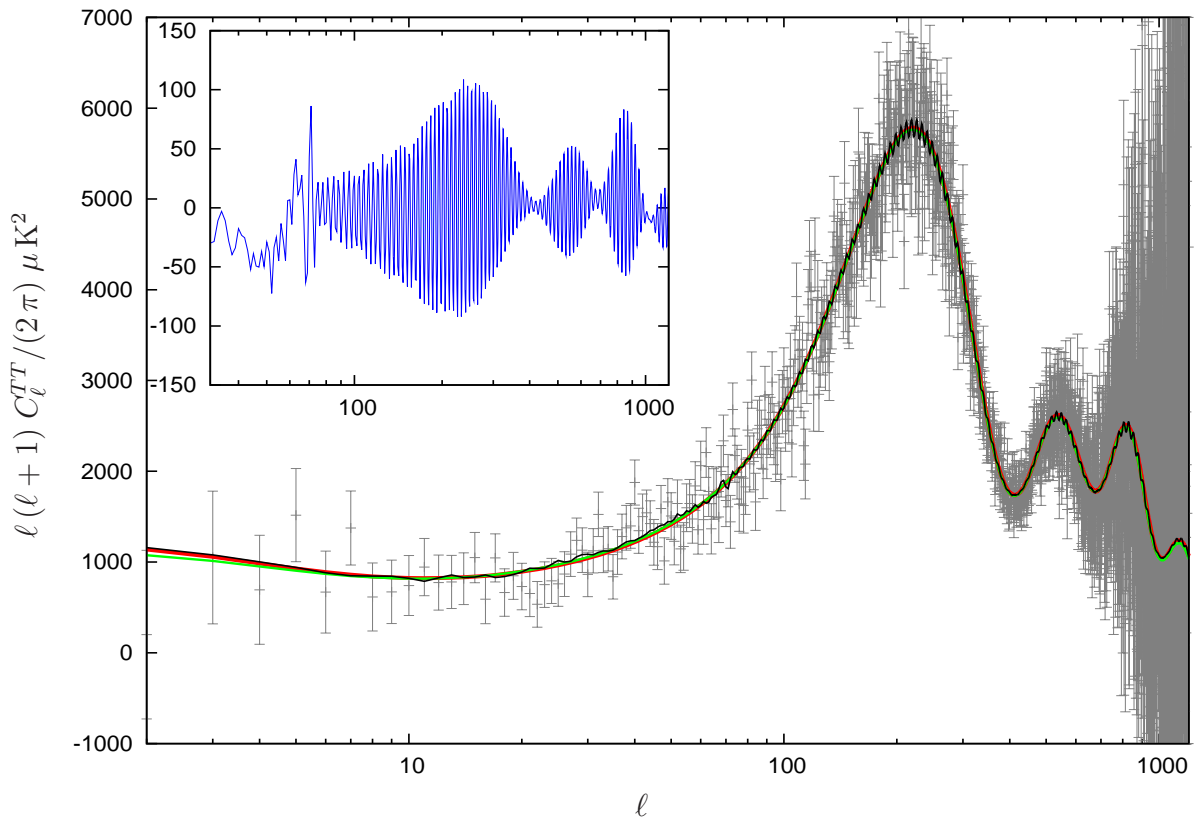


Figure 3.3: The CMB TT angular power spectra corresponding to the best fit values of the different models of our interest for the WMAP seven-year data. The solid red, green and black curves correspond to the power law model, the chaotic model with sinusoidal modulation and the axion monodromy model, respectively. The gray circles with error bars denote the WMAP seven-year *unbinned* data. The inset highlights the difference in the angular power spectrum between the monodromy model and the power law case. In the case of the axion monodromy model, the tiny and continued oscillations in the scalar power spectrum results in persistent modulations in CMB TT angular power spectrum. It is these oscillations that lead to small improvements in the fit to the data over a wide range of multipoles, which eventually add up to a good extent.

### 3.3 Discussion

In this chapter, our main aim has been to investigate if the CMB data support certain non-local features—*i.e.* a certain repeated and characteristic pattern that extends over a wide range of scales—in the primordial scalar power spectrum. With this goal in mind, we have studied two models of inflation, both of which contain oscillatory terms in the inflaton potential. The oscillations in the potential produces oscillations in the slow roll parameters, which in turn generate oscillations in the primordial as well as the CMB power spectra. Earlier work in this context had utilized the analytical expressions for the primordial power spectra, obtained in the slow roll approximation, to compare such models with the data [97, 98, 99]. Instead, we have used an accurate and efficient numerical code to arrive at the inflationary scalar and tensor power spectra. In fact, in order to ensure a good level of accuracy, rather than evolve a finite set of modes and interpolate, we have evolved and computed the inflationary perturbation spectra for all the modes that is required by CAMB to arrive at the corresponding CMB angular power spectra. While this reflects the extent of the numerical accuracy of our computations, the efficiency of the code can be gauged by the fact that we have been able to complete the required runs within a reasonable amount of time despite such additional demands.

Prior experience, gained in a different context, had already suggested the possibility that small and continued oscillations in the scalar power spectra can lead to a better fit to the data [94]. This experience has been corroborated by the earlier [97, 98, 99] and our current analysis (in this context, see, however, Ref. [100]; we shall comment further on this point below). We find that, oscillations, such as those occur in the axion monodromy model lead to a superior fit to the data. In fact, as far as the WMAP seven-year data is concerned, on evaluating the CMB angular power spectrum at all the required multipoles without any interpolation, we obtain an improvement of about 13 in the least squares parameter  $\chi_{\text{eff}}^2$  for the axion monodromy model, just as the earlier analytical efforts had [98]. The time taken to compute the uninterpolated inflationary power spectra depends not only on the number of points required, but also on the frequency of the oscillations in the inflaton potentials that we have considered. In the case of the axion monodromy model, over the range of parameters that we have worked with, our code takes about 3–12 seconds to calculate the inflationary power spectra (both scalar and tensor) for the nearly 2000  $k$ -points which are required by CAMB. While such a level efficiency seems adequate for comparing the models of our interest with the WMAP seven-year data, we found that evaluating the uninterpolated CMB angular power spectra for comparing with the

WMAP as well as the ACT data sets did not prove to be feasible in reasonable amount of time. As a result, we were forced to use the default, interpolated CMB angular power spectra obtained by CAMB in this situation. It is for this reason that we have not been able to achieve an equivalent improvement in the  $\chi_{\text{eff}}^2$  for the monodromy model when the ACT data has been included [101].

Nevertheless, we believe that the limited level of comparison with the ACT data has its own role to play. The ACT data we have used in our analysis is the binned data provided in the ACT likelihood software. For a small sky coverage experiment such as ACT, a lot of systematics are involved in reconstructing the unbinned data. The difference in  $\chi_{\text{eff}}^2$  values using only WMAP dataset and both the WMAP and ACT datasets approximately corresponds to the number of binned data points in the ACT dataset. The reason we have incorporated the ACT dataset is to cover the large multipole regime in the angular power spectrum. For the monodromy model, we see that the tiny oscillations do continue till small scales which does not overlap with the WMAP seven-year dataset, but can be probed using the ACT dataset. Combining the two datasets, one can form an informed estimate of the model parameters over a wide range of angular scales.

It is worth adding here that, upon carrying out forecasting of the parameters using simulated Planck data for both the models suggests that the Planck mock data performs considerably better in constraining the model parameters as compared to the presently available CMB datasets [86, 101].

Finally, before closing, it is important that we comment on a recent work wherein it has been argued that fine features in the primordial spectrum as generated in models such as the axion monodromy model have been not conclusively detected by the data [100]. It should be emphasized that, in this work, we have evaluated an uninterpolated CMB angular power spectrum while comparing the models with the data. Moreover, the resulting best fit CMB angular power spectrum does indeed contain the tiny and persistent features encountered in the recent [100] as well as the earlier work [94, 95, 98]. Also, as we have highlighted before, the results from our numerical evaluation of the inflationary power spectra largely match the earlier results arrived at from the corresponding analytical spectra. While it may be true that the evidence for the oscillations may still not be conclusive, repeated analyses have unambiguously pointed to the fact that they are more favored by the data than a simpler and smooth primordial spectrum. As we have mentioned, we believe that Planck may be able to provide a definitive proof in this regard.



## Chapter 4

# Bi-spectra associated with local and non-local features in the primordial scalar power spectrum

In the last two chapters, we have discussed as to how, though nearly scale invariant primordial spectra as is generated in slow roll inflationary scenarios are rather consistent with the CMB observations, certain features in the inflationary scalar power spectra lead to an improved fit to the data. Though the statistical significance of such features remain to be understood completely satisfactorily [69, 70], they gain importance from the phenomenological perspective of comparing the models with the data, because only a smaller class of single field inflationary models, which allow for departures from slow roll, can generate them.

Over the last half-a-dozen years, it has been increasingly realized that the detection of non-Gaussianities in the primordial perturbations can considerably help in constraining the inflationary models (see Refs. [49, 51, 52]; for early efforts in this direction, see Refs. [56]). In particular, the detection of a high value for the  $f_{\text{NL}}$  parameter that is used to describe the extent of non-Gaussianity [*cf.* Eq. (1.29)] can rule out a wide class of models. If, indeed, the extent of non-Gaussianity proves to be as large as the mean values of  $f_{\text{NL}}$  arrived at from the recent WMAP data [19, 57, 58], then canonical scalar field models that lead to slow roll inflation and nearly scale invariant primordial spectra will cease to be consistent with the data. But, interestingly, demanding the presence of features in the scalar power spectrum seems to generically lead to larger non-Gaussianities (see, for example, Refs. [53]). Therefore, features may offer the only route (unless one works with non-vacuum initial states [102]) for the canonical scalar fields to remain viable if  $f_{\text{NL}}$  turns out to be significant.

The above discussion raises two important issues. Firstly, if indeed the presence of features turns out to be the correct reason behind possibly large non-Gaussianities, can we observationally identify the correct underlying inflationary scenario, in particular, given the fact that different models can lead to similar features in the scalar power spectrum? In other words, to what extent can the non-Gaussianity parameter  $f_{\text{NL}}$  help us discriminate between the inflationary models that permit features? To address this question, we shall consider a few typical inflationary models leading to features (including those considered in the previous two chapters), assuming that they can be viewed as representatives of such a class of scenarios. Concretely, we shall consider the Starobinsky model [71] and the punctuated inflationary scenario [77], both of which result in a sharp drop in power at large scales that is followed by oscillations. We shall also study large and small field models with an additional step introduced in the inflaton potential that we had considered in Chapter 2 [53, 74, 75, 85]. As we had seen, the step leads to a burst of oscillations in the scalar power spectrum which improve the fit to the outliers near the multipole moments of  $\ell = 22$  and 40 in the CMB angular power spectrum. We shall also consider oscillating inflaton potentials such as the one that arises in the axion monodromy model discussed in the last chapter. As we had illustrated, such oscillatory potentials lead to modulations in the power spectrum over a wide range of scales and result in a considerable betterment in the fit to the data [53, 97, 98, 99, 101].

The second issue pertains to the calculation of non-Gaussianities in models where the slow roll approximation is not satisfied. Usually, the slow roll approximation is utilized to arrive at analytical expressions for the non-Gaussianity parameter  $f_{\text{NL}}$ . Clearly, this is no longer possible when departures from slow roll occur. We shall use a new Fortran numerical code to evaluate the non-Gaussianities in such situations. Although, some partial numerical results have already been published in the literature, we believe that it is for the first time that a general (we shall restrict ourselves to the equilateral case here, but the code can compute for any configuration), and efficient (that can arrive at results within a few minutes) code has been put together. Moreover, as we shall demonstrate, the code can also compute all the different contributions to the bi-spectrum.

The plan of this chapter is as follows. In the following section, we shall briefly describe the inflationary models of interest and discuss the scalar power spectra that arise in these models. In the succeeding section, we shall quickly describe the essential details pertaining to the evaluation of the bi-spectrum and the non-Gaussianity parameter  $f_{\text{NL}}$  in inflationary models involving a single, canonical, scalar field. In Section 4.3, after demonstrating that the super-Hubble contributions to the complete bi-spectrum during inflation

prove to be negligible, we shall describe the method that we adopt to numerically compute the bi-spectrum and the non-Gaussianity parameter  $f_{\text{NL}}$  in the equilateral limit. We shall also illustrate the extent of accuracy of the computations by comparing our numerical results in the equilateral limit with the bi-spectra expected in power law inflation and the analytical results that have recently been obtained in the case of the Starobinsky model (see Ref. [54]; however, in this context, also see Refs. [55]). In Section 4.4, we shall present the main results, and compare the  $f_{\text{NL}}$  that arise in the various models of our interest. We shall finally conclude this chapter with a brief discussion on the implications of our results.

## 4.1 The inflationary models of interest and the resulting power spectra

Broadly, the models that we shall consider can be categorized into three classes. The first class shall involve potentials which admit a relatively mild and brief departure from slow roll. The second class shall contain small but repeated deviations from slow roll, while the third and the last class shall involve a short but rather sharp departure from slow roll. In this section, we shall briefly outline the different inflationary models that we shall consider under these classes and discuss the scalar power spectra that are generated in these models.

### 4.1.1 Inflationary potentials with a step

Under the first class, we shall consider models with a step that we had discussed in Chapter 2. We shall consider the effects of the introduction of the step (2.5) in the archetypical quadratic large field model (2.1) and the small field model governed by the potential (2.2). In the case of the small field model, we shall specifically focus on the situation wherein  $p_0 = 4$  and  $\mu = 15 M_{\text{Pl}}$ , as we had done earlier. Moreover, in both these cases, we shall work with values of the parameters that correspond to the best fit values arrived at upon comparing the models with the WMAP seven-year data, as quoted in Table 2.3. Further, we shall assume that the field starts on the inflationary attractor at an initial value, say,  $\phi_i$ , such that at least 60 e-folds of inflation takes place. We choose  $\phi_i$  to be  $16.5 M_{\text{Pl}}$  and  $7.3 M_{\text{Pl}}$  in the cases of the quadratic and the small field models with the step, respectively.

### 4.1.2 Oscillations in the inflaton potential

The second class of models that we shall consider are those which lead to small but repeated deviations from slow roll as in the case of potentials containing oscillatory terms that we had discussed in the previous chapter. In this context, we shall consider both the potentials, *viz.* the quadratic potential modulated by sinusoidal oscillations (3.1) as well as the axion monodromy model (3.2), that we had discussed. Again, we shall work with the best fit values corresponding to the WMAP seven-year data, as listed in Table 3.2. Moreover, we shall assume that the field starts on the inflationary attractor at the initial value  $\phi_i$  of  $16 M_{\text{Pl}}$  and  $12 M_{\text{Pl}}$  in the cases of the quadratic potential with sinusoidal oscillations and the axion monodromy model, respectively.

### 4.1.3 Punctuated inflaton and the Starobinsky model

We shall consider two models under the last class, both of which are known to lead to brief but sharp departures from slow roll. The first of the inflationary models that we shall consider in this class is described by the following potential containing two parameters  $m$  and  $\lambda$ :

$$V(\phi) = \frac{m^2}{2} \phi^2 - \frac{\sqrt{2\lambda(n-1)}m}{n} \phi^n + \frac{\lambda}{4} \phi^{2(n-1)}. \quad (4.1)$$

The third quantity  $n$  that appears in the potential is an integer which takes values greater than two. Such potentials are known to arise in certain minimal supersymmetric extensions of the standard model [103]. It is worthwhile noting here that the case of  $n = 3$  has been considered much earlier for reasons similar to what we shall consider here, *viz.* towards producing certain features in the scalar power spectrum [104]. In the above potential, the coefficient of the  $\phi^n$  term is chosen such that the potential contains a point of inflection at, say,  $\phi = \phi_0$  (*i.e.* the location where both  $dV/d\phi$  and  $d^2V/d\phi^2$  vanish), so that  $\phi_0$  given by

$$\phi_0 = \left[ \frac{2m^2}{(n-1)\lambda} \right]^{\frac{1}{2(n-2)}}. \quad (4.2)$$

If one starts at a suitable value of the field beyond the point the inflection in the above potential, it is found that one can achieve two epochs of slow roll inflation sandwiching a brief period of departure from inflation (lasting for a little less than a  $e$ -fold), a scenario which has been dubbed as punctuated inflation [77]. In fact, it is the point of inflection, around which the potential exhibits a plateau with an extremely small curvature, which permits such an evolution to be possible. It is found that the following values for the potential parameters results in a power spectrum that leads to an improved fit to the

CMB data in the  $n = 3$  case:  $m = 1.5012 \times 10^{-7} M_{\text{Pl}}$  and  $\phi_0 = 1.95964 M_{\text{Pl}}$ . It should be added that the field is assumed to start from rest at an initial value of  $\phi_i = 11.5 M_{\text{Pl}}$  to arrive at the required behavior.

The second model that we shall consider is the Starobinsky model [71], which, as we shall see, leads to a scalar power spectrum that has a certain resemblance to the spectrum generated by punctuated inflation. The model consists of a linear potential with a sharp change in its slope at a given point, and can be described as follows:

$$V(\phi) = \begin{cases} V_0 + A_+ (\phi - \phi_0) & \text{for } \phi > \phi_0, \\ V_0 + A_- (\phi - \phi_0) & \text{for } \phi < \phi_0. \end{cases} \quad (4.3)$$

Evidently, while the value of the scalar field where the slope changes abruptly is  $\phi_0$ , the slope of the potential above and below  $\phi_0$  are given by  $A_+$  and  $A_-$ , respectively. Moreover, the quantity  $V_0$  denotes the value of the potential at  $\phi = \phi_0$ . A crucial assumption of the Starobinsky model is that the value of  $V_0$  is sufficiently large so that the behavior of the scale factor always remains close to that of de Sitter. The change in the slope causes a short period of deviation from slow roll as the field crosses  $\phi_0$ . However, in contrast to the case of the punctuated inflationary scenario, where one encounters a brief departure from inflation, inflation continues uninterrupted in the Starobinsky model. We have not compared the Starobinsky model with the data, and we shall work with two different sets of values for the parameters of the model. We shall choose one set to allow for comparison of the analytical results that have been obtained in this case (see Refs. [54, 55]) with the corresponding numerical ones. The other set shall be chosen to lead to a spectrum that closely mimics the power spectrum encountered in punctuated inflation. In the case of the former, we shall choose the following values of the parameters:  $V_0 = 2.36 \times 10^{-12} M_{\text{Pl}}^4$ ,  $A_+ = 3.35 \times 10^{-14} M_{\text{Pl}}^3$ ,  $A_- = 7.26 \times 10^{-15} M_{\text{Pl}}^3$  and  $\phi_0 = 0.707 M_{\text{Pl}}$ , while in the case of the latter, we shall work with the same values of  $A_+$  and  $\phi_0$ , but shall set  $V_0 = 2.94 \times 10^{-13} M_{\text{Pl}}^4$ , and  $A_- = 3.35 \times 10^{-16} M_{\text{Pl}}^3$ . Also, we shall work with an initial value of  $\phi_i = 0.849 M_{\text{Pl}}$  in the first instance and with  $\phi_i = 1.8 M_{\text{Pl}}$  in the second. Further, we shall start with field velocities that are determined by the slow roll conditions in both the cases.

#### 4.1.4 The power spectra

We shall now discuss the scalar power spectra that arise in the inflationary models that we have listed above. As we have mentioned, we shall provide the details concerning the numerical evolution of the governing equations and the evaluation of the scalar power spectrum a little later in Section 4.3. In Figure 4.1, we have illustrated the scalar power

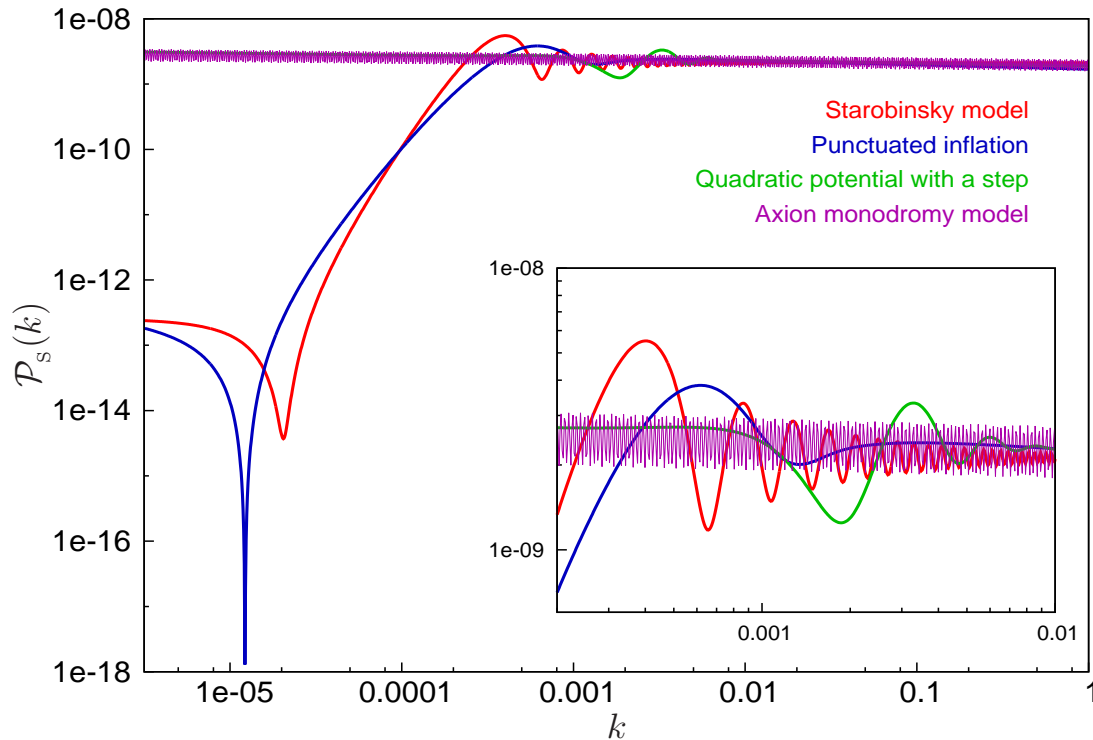


Figure 4.1: The scalar power spectrum in the different types of inflationary models that we consider. The parameters of the Starobinsky model [71] has been chosen such that the resulting power spectrum closely resembles the spectrum that arises in the punctuated inflationary scenario which is known to lead to an improved fit to the CMB data [77]. As we have seen in the previous two chapters, while the models with a step [74, 75, 85] lead to a burst of oscillations over a specific range of scales, inflaton potentials with oscillating terms produce modulations over a wide range of scales in the power spectrum [101]. The inset highlights the differences in the various power spectra over a smaller range of scales. We have emphasized certain aspects of these different power spectra in some detail in the text.

spectra that arise in the different classes of models of our interest. At this stage, we shall emphasize a few points concerning the various power spectra that we have assembled in the figure.

Since we have already discussed the scalar power spectra that are produced by potentials that contain a step and oscillatory terms, let us focus on the spectra that arise in the examples of our interest that lead to sharp departures from slow roll, *viz.* the Starobinsky model [71] and the punctuated inflationary scenario [77]. Note that, both these models lead to a step like feature as well as a spike in the power spectrum. The spikes arise due to the sharp departure from slow roll that occurs in these models. While the first slow roll

parameter  $\epsilon_1$  remains small in the Starobinsky model as the field crosses the transition, the second slow parameter  $\epsilon_2$  turns very large briefly [54, 55]. In the case of punctuated inflation,  $\epsilon_1$  itself grows to a large value thereby actually interrupting inflation for about a  $e$ -fold. It is this property that results in a sharper spike in the case of punctuated inflation than the Starobinsky model. The overall step in these models is easier to understand, and it simply arises due to the difference in the Hubble scales associated with the slow roll epoch before and after the period of fast roll. Both these models also lead to oscillations before the spectra turn nearly scale invariant on small scales. The spectra that arises in punctuated inflation, in addition to leading to a better fit to the outliers at very small multipoles (because of the drop in power on these scales), also provides an improvement in the fit to the outlier at  $\ell \simeq 22$  [77]. It is interesting to notice that the spectra of punctuated inflation and the model with a step in the potential match briefly as they oscillate near scales corresponding to  $\ell \simeq 22$ .

## 4.2 The scalar bi-spectrum in the Maldacena formalism

As we had mentioned in the introductory chapter, there now exists a standard formalism, initially proposed by Maldacena, that allows one to evaluate the bi-spectrum in a given inflationary model. In the Maldacena formalism [49], the bi-spectrum is evaluated using the standard rules of perturbative quantum field theory, based on the interaction Hamiltonian that depends cubically on the curvature perturbation. For the case of the canonical scalar field of our interest, the action at the cubic order in the curvature perturbation is found to be [49, 51, 52]

$$\begin{aligned} \mathcal{S}_3[\mathcal{R}] = & M_{\text{Pl}}^2 \int d\eta \int d^3\mathbf{x} \left[ a^2 \epsilon_1^2 \mathcal{R} \mathcal{R}'^2 + a^2 \epsilon_1^2 \mathcal{R} (\partial\mathcal{R})^2 - 2 a \epsilon_1 \mathcal{R}' (\partial^i \mathcal{R}) (\partial_i \chi) \right. \\ & \left. + \frac{a^2}{2} \epsilon_1 \epsilon_2' \mathcal{R}^2 \mathcal{R}' + \frac{\epsilon_1}{2} (\partial^i \mathcal{R}) (\partial_i \chi) (\partial^2 \chi) + \frac{\epsilon_1}{4} (\partial^2 \mathcal{R}) (\partial \chi)^2 + a \mathcal{F} \left( \frac{\delta \mathcal{L}_2}{\delta \mathcal{R}} \right) \right], \end{aligned} \quad (4.4)$$

where the Latin indices denote the spatial coordinates, while the function  $\chi$  is defined through the relation

$$\partial^2 \chi \equiv a \epsilon_1 \mathcal{R}'. \quad (4.5)$$

The quantity  $\delta \mathcal{L}_2 / \delta \mathcal{R}$  denotes the variation of the Lagrangian density corresponding to the following quadratic action:

$$\mathcal{S}_2[\mathcal{R}] = \frac{1}{2} \int d\eta \int d^3\mathbf{x} \ z^2 \left[ \mathcal{R}'^2 - (\partial\mathcal{R})^2 \right], \quad (4.6)$$

which, for instance, leads to the equation of motion (1.15) for the curvature perturbation  $\mathcal{R}$ , and can be written as

$$\frac{\delta\mathcal{L}_2}{\delta\mathcal{R}} = \dot{\Lambda} + H \Lambda - \epsilon_1 (\partial^2\mathcal{R}). \quad (4.7)$$

The term  $\mathcal{F}(\delta\mathcal{L}_2/\delta\mathcal{R})$  that has been introduced in the above cubic order action refers to the following expression [51, 54]:

$$\begin{aligned} \mathcal{F}\left(\frac{\delta\mathcal{L}_2}{\delta\mathcal{R}}\right) &= \frac{1}{2aH} \left\{ \left[ a^2 H \epsilon_2 \mathcal{R}^2 + 4a \mathcal{R} \mathcal{R}' + (\partial^i \mathcal{R})(\partial_i \chi) - \frac{1}{H} (\partial\mathcal{R})^2 \right] \frac{\delta\mathcal{L}_2}{\delta\mathcal{R}} \right. \\ &\quad + \left[ \Lambda (\partial_i \mathcal{R}) + (\partial^2 \mathcal{R}) (\partial_i \chi) \right] \delta^{ij} \partial_j \left[ \partial^{-2} \left( \frac{\delta\mathcal{L}_2}{\delta\mathcal{R}} \right) \right] \\ &\quad \left. + \frac{1}{H} \delta^{im} \delta^{jn} (\partial_i \mathcal{R}) (\partial_j \mathcal{R}) \partial_m \partial_n \left[ \partial^{-2} \left( \frac{\delta\mathcal{L}_2}{\delta\mathcal{R}} \right) \right] \right\}. \end{aligned} \quad (4.8)$$

where, again, the Latin indices represent the spatial coordinates.

For convenience, we shall introduce a new quantity  $G(\mathbf{k}_1, \mathbf{k}_2, \mathbf{k}_3)$  that is related to the bi-spectrum  $\mathcal{B}_s(\mathbf{k}_1, \mathbf{k}_2, \mathbf{k}_3)$  by a constant factor as follows:

$$G(\mathbf{k}_1, \mathbf{k}_2, \mathbf{k}_3) = (2\pi)^{9/2} \mathcal{B}_s(\mathbf{k}_1, \mathbf{k}_2, \mathbf{k}_3). \quad (4.9)$$

It can be shown that the quantity  $G(\mathbf{k}_1, \mathbf{k}_2, \mathbf{k}_3)$ , which results from the interaction Hamiltonian corresponding to the cubic action (4.4), evaluated towards the end of inflation, say, at the conformal time  $\eta_e$ , can be expressed as [49, 51, 52, 53, 54]

$$\begin{aligned} G(\mathbf{k}_1, \mathbf{k}_2, \mathbf{k}_3) &\equiv \sum_{C=1}^7 G_C(\mathbf{k}_1, \mathbf{k}_2, \mathbf{k}_3) \\ &\equiv M_{\text{Pl}}^2 \sum_{C=1}^6 \left\{ [f_{\mathbf{k}_1}(\eta_e) f_{\mathbf{k}_2}(\eta_e) f_{\mathbf{k}_3}(\eta_e)] \mathcal{G}_C(\mathbf{k}_1, \mathbf{k}_2, \mathbf{k}_3) \right. \\ &\quad \left. + [f_{\mathbf{k}_1}^*(\eta_e) f_{\mathbf{k}_2}^*(\eta_e) f_{\mathbf{k}_3}^*(\eta_e)] \mathcal{G}_C^*(\mathbf{k}_1, \mathbf{k}_2, \mathbf{k}_3) \right\} + G_7(\mathbf{k}_1, \mathbf{k}_2, \mathbf{k}_3), \end{aligned} \quad (4.10)$$

where  $f_{\mathbf{k}}$  are the Fourier modes associated with the curvature perturbation [cf. Eq. (1.19)] that satisfy the differential equation (1.15). The quantities  $\mathcal{G}_C(\mathbf{k}_1, \mathbf{k}_2, \mathbf{k}_3)$  with  $C = (1, 6)$  correspond to the six terms in the interaction Hamiltonian, and are described by the inte-

grals

$$\mathcal{G}_1(\mathbf{k}_1, \mathbf{k}_2, \mathbf{k}_3) = 2i \int_{\eta_i}^{\eta_e} d\eta a^2 \epsilon_1^2 (f_{\mathbf{k}_1}^* f_{\mathbf{k}_2}^{\prime*} f_{\mathbf{k}_3}^{\prime*} + \text{two permutations}), \quad (4.11a)$$

$$\mathcal{G}_2(\mathbf{k}_1, \mathbf{k}_2, \mathbf{k}_3) = -2i (\mathbf{k}_1 \cdot \mathbf{k}_2 + \text{two permutations}) \int_{\eta_i}^{\eta_e} d\eta a^2 \epsilon_1^2 f_{\mathbf{k}_1}^* f_{\mathbf{k}_2}^* f_{\mathbf{k}_3}^*, \quad (4.11b)$$

$$\mathcal{G}_3(\mathbf{k}_1, \mathbf{k}_2, \mathbf{k}_3) = -2i \int_{\eta_i}^{\eta_e} d\eta a^2 \epsilon_1^2 \left[ \left( \frac{\mathbf{k}_1 \cdot \mathbf{k}_2}{k_2^2} \right) f_{\mathbf{k}_1}^* f_{\mathbf{k}_2}^{\prime*} f_{\mathbf{k}_3}^{\prime*} + \text{five permutations} \right], \quad (4.11c)$$

$$\mathcal{G}_4(\mathbf{k}_1, \mathbf{k}_2, \mathbf{k}_3) = i \int_{\eta_i}^{\eta_e} d\eta a^2 \epsilon_1 \epsilon_2' (f_{\mathbf{k}_1}^* f_{\mathbf{k}_2}^* f_{\mathbf{k}_3}^{\prime*} + \text{two permutations}), \quad (4.11d)$$

$$\mathcal{G}_5(\mathbf{k}_1, \mathbf{k}_2, \mathbf{k}_3) = \frac{i}{2} \int_{\eta_i}^{\eta_e} d\eta a^2 \epsilon_1^3 \left[ \left( \frac{\mathbf{k}_1 \cdot \mathbf{k}_2}{k_2^2} \right) f_{\mathbf{k}_1}^* f_{\mathbf{k}_2}^{\prime*} f_{\mathbf{k}_3}^{\prime*} + \text{five permutations} \right], \quad (4.11e)$$

$$\mathcal{G}_6(\mathbf{k}_1, \mathbf{k}_2, \mathbf{k}_3) = \frac{i}{2} \int_{\eta_i}^{\eta_e} d\eta a^2 \epsilon_1^3 \left\{ \left[ \frac{k_1^2 (\mathbf{k}_2 \cdot \mathbf{k}_3)}{k_2^2 k_3^2} \right] f_{\mathbf{k}_1}^* f_{\mathbf{k}_2}^{\prime*} f_{\mathbf{k}_3}^{\prime*} + \text{two permutations} \right\}, \quad (4.11f)$$

where  $\epsilon_2$  is the second slow roll parameter that is defined with respect to the first through the expression (1.8). The lower limit of the above integrals, *viz.*  $\eta_i$ , denotes a sufficiently early time when the initial conditions [say, the Bunch-Davies conditions (1.23)] are imposed on the modes  $f_{\mathbf{k}}$ . The additional, seventh term  $G_7(\mathbf{k}_1, \mathbf{k}_2, \mathbf{k}_3)$  arises due to a field redefinition (in this context, see, Refs. [49, 51, 53]), and its contribution to  $G(\mathbf{k}_1, \mathbf{k}_2, \mathbf{k}_3)$  is given by

$$G_7(\mathbf{k}_1, \mathbf{k}_2, \mathbf{k}_3) = \frac{\epsilon_2(\eta_e)}{2} (|f_{\mathbf{k}_2}(\eta_e)|^2 |f_{\mathbf{k}_3}(\eta_e)|^2 + \text{two permutations}). \quad (4.12)$$

### 4.3 The numerical computation of the scalar bi-spectrum

In this section, after illustrating that the super-Hubble contributions to the complete bi-spectrum during inflation proves to be negligible, we shall outline the methods that we adopt to numerically evolve the equations governing the background and the perturbations, and eventually evaluate the inflationary scalar power and bi-spectra. Also, we shall illustrate the extent of accuracy of the numerical methods by comparing them with the expected form of the bi-spectrum in the equilateral limit in power law inflation and the analytical results that are available in the case of the Starobinsky model [54, 55].

#### 4.3.1 The contributions to the bi-spectrum on super-Hubble scales

It is clear from the above expressions that the evaluation of the bi-spectrum involves integrals over the mode  $f_{\mathbf{k}}$  and its derivative  $f_{\mathbf{k}}'$  as well as the slow roll parameters  $\epsilon_1$ ,

$\epsilon_2$  and the derivative  $\epsilon_2'$ . While evaluating the power spectra, it is well known that it suffices to evolve the curvature perturbation from an initial time when the modes are sufficiently inside the Hubble radius to a suitably late time when the amplitude of the curvature perturbation settles down to a constant value [81, 82]. We shall illustrate that many of the contributions to the bi-spectrum prove to be negligible when the modes evolve on super-Hubble scales. Interestingly, we shall also show that, those contributions to the bi-spectrum which turn out to be significant at late times when the modes are well outside the Hubble radius are canceled by certain other contributions that arise. As a consequence, we shall argue that, numerically, it suffices to evaluate the integrals over the period of time during which the curvature perturbations have been conventionally evolved to arrive at the power spectra, *viz.* from the sub-Hubble to the super-Hubble scales.

### Evolution of $f_k$ on super-Hubble scales

During inflation, when the modes are on super-Hubble scales, it is well known that the solution to  $f_k$  can be written as [6, 7]

$$f_k(\eta) \simeq A_k + B_k \int^{\eta} \frac{d\tilde{\eta}}{z^2(\tilde{\eta})}, \quad (4.13)$$

where  $A_k$  and  $B_k$  are  $k$ -dependent constants which are determined by the initial conditions imposed on the modes in the sub Hubble-limit. The first term involving  $A_k$  is the growing mode, which is actually a constant, while the term containing  $B_k$  represents the decaying mode. Therefore, on super-Hubble scales, the mode  $f_k$  simplifies to

$$f_k(\eta) \simeq A_k. \quad (4.14)$$

Moreover, the leading non-zero contribution to its derivative is determined by the decaying mode, and is given by

$$f_k'(\eta) \simeq \frac{B_k}{z^2} = \frac{\bar{B}_k}{a^2 \epsilon_1}, \quad (4.15)$$

where we have set  $\bar{B}_k = B_k/(2 M_{\text{pl}}^2)$ .

It is now a matter of making use of the above solutions for  $f_k$  and  $f_k'$  to determine the super-Hubble contributions to the bi-spectrum during inflation.

### The various contributions

To begin with, note that, each of the integrals  $\mathcal{G}_C(\mathbf{k}_1, \mathbf{k}_2, \mathbf{k}_3)$ , where  $C = (1, 6)$ , can be divided into two parts as follows:

$$\mathcal{G}_C(\mathbf{k}_1, \mathbf{k}_2, \mathbf{k}_3) = \mathcal{G}_C^{\text{is}}(\mathbf{k}_1, \mathbf{k}_2, \mathbf{k}_3) + \mathcal{G}_C^{\text{se}}(\mathbf{k}_1, \mathbf{k}_2, \mathbf{k}_3). \quad (4.16)$$

The integrals in the first term  $\mathcal{G}_C^{\text{is}}(\mathbf{k}_1, \mathbf{k}_2, \mathbf{k}_3)$  run from the earliest time (*i.e.*  $\eta_i$ ) when the smallest of the three wavenumbers  $k_1$ ,  $k_2$  and  $k_3$  is sufficiently inside the Hubble radius [typically corresponding to  $k/(aH) \simeq 100$ ] to the time (say,  $\eta_s$ ) when the largest of the three wavenumbers is well outside the Hubble radius [say, when  $k/(aH) \simeq 10^{-5}$ ]. Then, evidently, the second term  $\mathcal{G}_C^{\text{se}}(\mathbf{k}_1, \mathbf{k}_2, \mathbf{k}_3)$  will involve integrals which run from the latter time  $\eta_s$  to the end of inflation at  $\eta_e$ . In what follows, we shall discuss the various contributions to the bi-spectrum due to the terms  $\mathcal{G}_C^{\text{se}}(\mathbf{k}_1, \mathbf{k}_2, \mathbf{k}_3)$ . We shall show that the corresponding contribution either remains small or, when it proves to be large, it is exactly canceled by another contribution to the bi-spectrum.

**The contributions due to the fourth and the seventh terms** Let us first focus on the fourth term  $G_4(\mathbf{k}_1, \mathbf{k}_2, \mathbf{k}_3)$  since it has often been found to lead to the largest contribution to the bi-spectrum when deviations from slow roll occur [53, 54, 55]. As the slow roll parameters turn large towards the end of inflation, we can expect this term to contribute significantly at late times. However, as we shall quickly illustrate, such a late time contribution is exactly canceled by the contribution from  $G_7(\mathbf{k}_1, \mathbf{k}_2, \mathbf{k}_3)$  which arises due to the field redefinition.

Upon using the form (4.14) of the mode  $f_{\mathbf{k}}$  and its derivative (4.15) on super-Hubble scales in the expression (4.11d), one obtains that

$$\mathcal{G}_4^{\text{se}}(\mathbf{k}_1, \mathbf{k}_2, \mathbf{k}_3) \simeq i (A_{\mathbf{k}_1}^* A_{\mathbf{k}_2}^* \bar{B}_{\mathbf{k}_3}^* + \text{two permutations}) \int_{\eta_s}^{\eta_e} d\eta \epsilon'_2. \quad (4.17)$$

This expression can be trivially integrated to yield

$$\mathcal{G}_4^{\text{se}}(\mathbf{k}_1, \mathbf{k}_2, \mathbf{k}_3) \simeq i (A_{\mathbf{k}_1}^* A_{\mathbf{k}_2}^* \bar{B}_{\mathbf{k}_3}^* + \text{two permutations}) [\epsilon_2(\eta_e) - \epsilon_2(\eta_s)], \quad (4.18)$$

so that the corresponding contribution to the bi-spectrum can be expressed as

$$G_4^{\text{se}}(\mathbf{k}_1, \mathbf{k}_2, \mathbf{k}_3) \simeq i M_{\text{Pl}}^2 [\epsilon_2(\eta_e) - \epsilon_2(\eta_s)] \left[ |A_{\mathbf{k}_1}|^2 |A_{\mathbf{k}_2}|^2 (A_{\mathbf{k}_3} \bar{B}_{\mathbf{k}_3}^* - A_{\mathbf{k}_3}^* \bar{B}_{\mathbf{k}_3}) + \text{two permutations} \right]. \quad (4.19)$$

Since this expression depends on the value of  $\epsilon_2$  at the end of inflation, it suggests that the contributions to the bi-spectrum at late times during inflation could be considerable. But, as we shall soon show, this large contribution is canceled by a similar contribution from the seventh term that arises due to the field redefinition [cf. Eq. (4.12)].

Now, consider the Wronskian

$$\mathcal{W} = f_{\mathbf{k}} f_{\mathbf{k}}'^* - f_{\mathbf{k}}^* f_{\mathbf{k}}' \quad (4.20)$$

Upon using the equation of motion (1.15) for  $f_{\mathbf{k}}$ , one can show that,  $\mathcal{W} = W/z^2$ , where  $W$  is a constant. It is important to note that this result is valid on all scales, even in the sub-Hubble limit during inflation. In this limit, as we had mentioned, the modes  $v_{\mathbf{k}}$  satisfy the Bunch-Davies initial condition (1.23). On making use of this sub-Hubble behavior in the above definition of the Wronskian  $\mathcal{W}$ , one obtains that  $W = i$ . In the super-Hubble limit, we have, on using the corresponding solution (4.14) and its derivative (4.15),

$$\mathcal{W} = \frac{2 M_{\text{Pl}}^2}{z^2} (A_{\mathbf{k}} \bar{B}_{\mathbf{k}}^* - A_{\mathbf{k}}^* \bar{B}_{\mathbf{k}}) = \frac{i}{z^2}. \quad (4.21)$$

Therefore, we obtain that

$$A_{\mathbf{k}} \bar{B}_{\mathbf{k}}^* - A_{\mathbf{k}}^* \bar{B}_{\mathbf{k}} = \frac{i}{2 M_{\text{Pl}}^2}, \quad (4.22)$$

and, hence, the expression (4.19) for  $G_4^{\text{se}}(\mathbf{k}_1, \mathbf{k}_2, \mathbf{k}_3)$  simplifies to

$$G_4^{\text{se}}(\mathbf{k}_1, \mathbf{k}_2, \mathbf{k}_3) \simeq -\frac{1}{2} [\epsilon_2(\eta_e) - \epsilon_2(\eta_s)] (|A_{\mathbf{k}_1}|^2 |A_{\mathbf{k}_2}|^2 + \text{two permutations}). \quad (4.23)$$

The first of these terms involving the value of  $\epsilon_2$  at the end of inflation *exactly* cancels the contribution  $G_7(\mathbf{k}_1, \mathbf{k}_2, \mathbf{k}_3)$  [with  $f_{\mathbf{k}}$  set to  $A_{\mathbf{k}}$  in Eq. (4.12)] that arises due to the field redefinition. But, the remaining contribution cannot be ignored and needs to be taken into account. It is useful to note that this term is essentially the same as the one due to the field redefinition, but which is now evaluated on super-Hubble scales (*i.e.* at  $\eta_s$ ) rather than at the end of inflation. In other words, if we consider the fourth and the seventh terms together, it is equivalent to evaluating the contribution to the bi-spectrum corresponding to  $\mathcal{G}_4^{\text{is}}(\mathbf{k}_1, \mathbf{k}_2, \mathbf{k}_3)$ , and adding to it the contribution due to the seventh term  $G_7(\mathbf{k}_1, \mathbf{k}_2, \mathbf{k}_3)$  evaluated at  $\eta_s$ , instead of at the end of inflation.

**The contribution due to the second term** Let us now turn to the contribution due to the second term, which can occasionally prove to be comparable to the contribution due to

the fourth term [54]. Upon making use of the behavior of the mode  $f_{\mathbf{k}}$  on super-Hubble scales in the integral (4.11b), we have

$$\mathcal{G}_2^{\text{se}}(\mathbf{k}_1, \mathbf{k}_2, \mathbf{k}_3) = -2i (\mathbf{k}_1 \cdot \mathbf{k}_2 + \text{two permutations}) A_{\mathbf{k}_1}^* A_{\mathbf{k}_2}^* A_{\mathbf{k}_3}^* I_2(\eta_e, \eta_s), \quad (4.24)$$

where  $I_2(\eta_e, \eta_s)$  denotes the integral

$$I_2(\eta_e, \eta_s) = \int_{\eta_s}^{\eta_e} d\eta a^2 \epsilon_1^2, \quad (4.25)$$

so that the corresponding contribution to the bi-spectrum is given by

$$\begin{aligned} G_2^{\text{se}}(\mathbf{k}_1, \mathbf{k}_2, \mathbf{k}_3) &= -2i M_{\text{Pl}}^2 (\mathbf{k}_1 \cdot \mathbf{k}_2 + \text{two permutations}) \\ &\times |A_{\mathbf{k}_1}|^2 |A_{\mathbf{k}_2}|^2 |A_{\mathbf{k}_3}|^2 [I_2(\eta_e, \eta_s) - I_2^*(\eta_e, \eta_s)]. \end{aligned} \quad (4.26)$$

Note that, due to quadratic dependence on the scale factor, actually,  $I_2(\eta_e, \eta_s)$  is a rapidly growing quantity at late times. However, the complete super-Hubble contribution to the bi-spectrum vanishes identically since the integral  $I_2(\eta_e, \eta_s)$  is a purely real quantity. Hence, in the case of the second term, it is sufficient to evaluate the contribution to the bi-spectrum due to  $\mathcal{G}_2^{\text{is}}(\mathbf{k}_1, \mathbf{k}_2, \mathbf{k}_3)$ .

**The remaining terms** Let us now compute the contributions due to the remaining terms, *viz.* the first, the third, the fifth and the sixth. Notice that, the first term  $G_1(\mathbf{k}_1, \mathbf{k}_2, \mathbf{k}_3)$  and the third term  $G_3(\mathbf{k}_1, \mathbf{k}_2, \mathbf{k}_3)$  involve the same integrals. Therefore, these two contributions to the bi-spectrum can be clubbed together. Similarly, the fifth and the sixth terms, *viz.*  $G_5(\mathbf{k}_1, \mathbf{k}_2, \mathbf{k}_3)$  and  $G_6(\mathbf{k}_1, \mathbf{k}_2, \mathbf{k}_3)$ , also contain integrals of the same type, and hence their contributions too can be combined. On making use of the super-Hubble behavior (4.14) and (4.15) of the mode  $f_{\mathbf{k}}$  and its derivative, we obtain that

$$\mathcal{G}_1^{\text{se}}(\mathbf{k}_1, \mathbf{k}_2, \mathbf{k}_3) \simeq 2i (A_{\mathbf{k}_1}^* \bar{B}_{\mathbf{k}_2}^* \bar{B}_{\mathbf{k}_3}^* + \text{two permutations}) I_{13}(\eta_e, \eta_s) \quad (4.27)$$

and

$$\mathcal{G}_3^{\text{se}}(\mathbf{k}_1, \mathbf{k}_2, \mathbf{k}_3) \simeq -2i \left[ \left( \frac{\mathbf{k}_1 \cdot \mathbf{k}_2}{k_2^2} \right) A_{\mathbf{k}_1}^* \bar{B}_{\mathbf{k}_2}^* \bar{B}_{\mathbf{k}_3}^* + \text{five permutations} \right] I_{13}(\eta_e, \eta_s), \quad (4.28)$$

where the quantity  $I_{13}(\eta_e, \eta_s)$  represents the integral

$$I_{13}(\eta_e, \eta_s) = \int_{\eta_s}^{\eta_e} \frac{d\eta}{a^2}. \quad (4.29)$$

From these results, one can easily show that the super-Hubble contributions due to the first and the third terms to the bi-spectrum can be written as

$$\begin{aligned}
 G_1^{\text{se}}(\mathbf{k}_1, \mathbf{k}_2, \mathbf{k}_3) + G_3^{\text{se}}(\mathbf{k}_1, \mathbf{k}_2, \mathbf{k}_3) &= 2i M_{\text{Pl}}^2 \left[ \left( 1 - \frac{\mathbf{k}_1 \cdot \mathbf{k}_2}{k_2^2} - \frac{\mathbf{k}_1 \cdot \mathbf{k}_3}{k_3^2} \right) |A_{\mathbf{k}_1}|^2 \right. \\
 &\quad \times \left( A_{\mathbf{k}_2} \bar{B}_{\mathbf{k}_2}^* A_{\mathbf{k}_3} \bar{B}_{\mathbf{k}_3}^* - A_{\mathbf{k}_2}^* \bar{B}_{\mathbf{k}_2} A_{\mathbf{k}_3}^* \bar{B}_{\mathbf{k}_3} \right) \\
 &\quad \left. + \text{two permutations} \right] I_{13}(\eta_e, \eta_s). \quad (4.30)
 \end{aligned}$$

The corresponding contributions due to the fifth and the sixth terms can be arrived at in a similar fashion. We find that

$$\begin{aligned}
 G_5^{\text{se}}(\mathbf{k}_1, \mathbf{k}_2, \mathbf{k}_3) + G_6^{\text{se}}(\mathbf{k}_1, \mathbf{k}_2, \mathbf{k}_3) &= \frac{i M_{\text{Pl}}^2}{2} \left\{ \left[ \frac{\mathbf{k}_1 \cdot \mathbf{k}_2}{k_2^2} + \frac{\mathbf{k}_1 \cdot \mathbf{k}_3}{k_3^2} + \frac{k_1^2 (\mathbf{k}_2 \cdot \mathbf{k}_3)}{k_2^2 k_3^2} \right] \right. \\
 &\quad \times |A_{\mathbf{k}_1}|^2 \left( A_{\mathbf{k}_2} \bar{B}_{\mathbf{k}_2}^* A_{\mathbf{k}_3} \bar{B}_{\mathbf{k}_3}^* - A_{\mathbf{k}_2}^* \bar{B}_{\mathbf{k}_2} A_{\mathbf{k}_3}^* \bar{B}_{\mathbf{k}_3} \right) \\
 &\quad \left. + \text{two permutations} \right\} I_{56}(\eta_e, \eta_s), \quad (4.31)
 \end{aligned}$$

where the quantity  $I_{56}(\eta_e, \eta_s)$  is described by the integral

$$I_{56}(\eta_e, \eta_s) = \int_{\eta_s}^{\eta_e} \frac{d\eta}{a^2} \epsilon_1. \quad (4.32)$$

Hence, the non-zero, super-Hubble contribution to the bi-spectrum is determined by the sum of the contribution due to the first, the third, the fifth and the sixth terms arrived at above. In order to illustrate that this contribution is insignificant, we shall now turn to estimating the amplitude of the corresponding contribution to the non-Gaussianity parameter  $f_{\text{NL}}$ .

### 4.3.2 An estimate of the super-Hubble contribution to the non-Gaussianity parameter

Let us restrict ourselves to the equilateral limit, *i.e.* when  $k_1 = k_2 = k_3 = k$ , for simplicity. In such a case, the super-Hubble contributions to the bi-spectrum, say,  $G_{\text{eq}}^{\text{es}}(k)$ , due to the first, the third, the fifth and the sixth terms, as given by the expressions (4.30) and (4.31), add up to be

$$G_{\text{eq}}^{\text{es}}(k) = i M_{\text{Pl}}^2 |A_{\mathbf{k}}|^2 \left( A_{\mathbf{k}}^2 \bar{B}_{\mathbf{k}}^{*2} - A_{\mathbf{k}}^{*2} \bar{B}_{\mathbf{k}}^2 \right) \left[ 12 I_{13}(\eta_e, \eta_s) - \frac{9}{4} I_{56}(\eta_e, \eta_s) \right]. \quad (4.33)$$

In the equilateral limit, the expression (1.29) for the non-Gaussianity parameter  $f_{\text{NL}}(\mathbf{k}_1, \mathbf{k}_2, \mathbf{k}_3)$  simplifies to

$$f_{\text{NL}}^{\text{eq}}(k) = -\frac{10}{9} \frac{1}{(2\pi)^4} \frac{k^6 G_{\text{eq}}(k)}{\mathcal{P}_s^2(k)}, \quad (4.34)$$

where  $\mathcal{P}_s(k)$  is the scalar power spectrum defined in Eq. (1.21). It is straightforward to show that the  $f_{\text{NL}}$  corresponding to the super-Hubble contribution to the bi-spectrum  $G_{\text{eq}}^{\text{es}}(k)$  above is given by

$$f_{\text{NL}}^{\text{eq(se)}}(k) \simeq -\frac{5i M_{\text{Pl}}^2}{18} \left( \frac{A_{\mathbf{k}}^2 \bar{B}_{\mathbf{k}}^{*2} - A_{\mathbf{k}}^{*2} \bar{B}_{\mathbf{k}}^2}{|A_{\mathbf{k}}|^2} \right) \left[ 12 I_{13}(\eta_e, \eta_s) - \frac{9}{4} I_{56}(\eta_e, \eta_s) \right], \quad (4.35)$$

where we have made use of the fact that  $f_{\mathbf{k}} \simeq A_{\mathbf{k}}$  at late times in order to arrive at the power spectrum.

To estimate the above super-Hubble contribution to the non-Gaussianity parameter  $f_{\text{NL}}^{\text{eq(se)}}$ , let us choose to work with power law inflation because it permits exact calculations, and it can also mimic slow roll inflation. During power law expansion, the scale factor can be written as

$$a(\eta) = a_1 \left( \frac{\eta}{\eta_1} \right)^{\gamma+1}, \quad (4.36)$$

where  $a_1$  and  $\eta_1$  are constants, while  $\gamma$  is a free index. It is useful to note that, in such a case, the first slow roll parameter is a constant and is given by  $\epsilon_1 = (\gamma + 2)/(\gamma + 1)$ . The current observational constraints on the scalar spectral index suggest that  $\gamma \lesssim -2$ , which implies that the corresponding scale factor is close to that of de Sitter.

In power law inflation, the exact solution to Eq. (1.16) can be expressed in terms of the Bessel function  $J_\nu(x)$  as follows (see, for instance, Refs. [105]):

$$v_{\mathbf{k}}(\eta) = \sqrt{-k\eta} [C_{\mathbf{k}} J_\nu(-k\eta) + D_{\mathbf{k}} J_{-\nu}(-k\eta)], \quad (4.37)$$

where  $\nu = (\gamma + 1/2)$ , and the quantities  $C_{\mathbf{k}}$  and  $D_{\mathbf{k}}$  are constants that are determined by the initial conditions. Upon demanding that the above solution satisfies the Bunch-Davies initial condition (1.23), one obtains that

$$C_{\mathbf{k}} = -D_{\mathbf{k}} e^{-i\pi(\gamma+1/2)}, \quad (4.38a)$$

$$D_{\mathbf{k}} = \sqrt{\frac{\pi}{k}} \frac{e^{i\pi\gamma/2}}{2 \cos(\pi\gamma)}. \quad (4.38b)$$

Since  $f_{\mathbf{k}} = v_{\mathbf{k}}/z$ , with  $z = \sqrt{2\epsilon_1} M_{\text{Pl}} a$ , and as  $\epsilon_1$  is a constant in power law inflation, we can arrive at the constants  $A_{\mathbf{k}}$  and  $B_{\mathbf{k}}$  [cf. Eqs. (4.14) and Eqs. (4.15)] from the super-Hubble

limit of the solution (4.37), which are found to be

$$A_{\mathbf{k}} = \frac{2^{-(\gamma+1/2)}}{\Gamma(\gamma+3/2)} \frac{(-k\eta_1)^{\gamma+1}}{\sqrt{2}\epsilon_1 a_1 M_{\text{Pl}}} C_{\mathbf{k}}, \quad (4.39a)$$

$$B_{\mathbf{k}} = -\frac{(2\gamma+1)2^{\gamma+1/2}}{\Gamma(-\gamma+1/2)} \frac{\sqrt{2}\epsilon_1 a_1 M_{\text{Pl}}}{\eta_1}, (-k\eta_1)^{-\gamma} D_{\mathbf{k}}. \quad (4.39b)$$

Then, upon inserting the above expressions for the quantities  $A_{\mathbf{k}}$  and  $B_{\mathbf{k}}$  in Eq. (4.35), we obtain that

$$\begin{aligned} f_{\text{NL}}^{\text{eq(se)}}(k) &= \frac{5}{72\pi} \left[ 12 - \frac{9(\gamma+2)}{4(\gamma+1)} \right] \Gamma^2 \left( \gamma + \frac{1}{2} \right) 2^{2\gamma+1} (2\gamma+1) (\gamma+2) \\ &\times (\gamma+1)^{-2(\gamma+1)} \sin(2\pi\gamma) \left[ 1 - \frac{H_s}{H_e} e^{-3(N_e-N_s)} \right] \left( \frac{k}{a_s H_s} \right)^{-(2\gamma+1)}. \end{aligned} \quad (4.40)$$

It should be mentioned that, in arriving at this expression, for convenience, we have set  $\eta_1$  to be  $\eta_s$ , which corresponds to  $a_1$  being  $a_s$ , *viz.* the scale factor at  $\eta_s$ . Moreover, while  $N_s$  and  $N_e$  denote the e-folds corresponding to  $\eta_s$  and  $\eta_e$ ,  $H_s$  and  $H_e$  represent the Hubble scales at these times, respectively. Recall that,  $\eta_s$  denotes the conformal time when the largest wavenumber of interest, say,  $k_s$ , is well outside the Hubble radius, *i.e.* when  $k_s/(aH) \simeq 10^{-5}$ . Since  $(N_e - N_s)$  is expected to be at least 40 for the smallest cosmological scale, it is clear that the factor involving  $\exp[-3(N_e - N_s)]$  can be completely neglected. As we mentioned above, observations point to the fact that  $\gamma \lesssim -2$ . Therefore, if we further assume that  $\gamma = -(2 + \varepsilon)$ , where  $\varepsilon \simeq 10^{-2}$ , we find that the above estimate for the non-Gaussianity parameter reduces to

$$f_{\text{NL}}^{\text{eq(se)}}(k) \lesssim -\frac{5\varepsilon^2}{9} \left( \frac{k_s}{a_s H_s} \right)^3 \simeq -10^{-19}, \quad (4.41)$$

where, in obtaining the final value, we have set  $k_s/(a_s H_s) = 10^{-5}$ . The inequality above arises due to the fact that, for larger scales, *i.e.* when  $k < k_s$ ,  $k/(aH) < 10^{-5}$  at  $\eta_s$ . In models involving the canonical scalar field, the smallest values of  $f_{\text{NL}}$  are typically generated in slow roll inflationary scenarios, wherein the non-Gaussianity parameter has been calculated to be of the order of the first slow roll parameter [49, 52]. The above estimate clearly points to fact that the super-Hubble contributions to the complete bi-spectrum and the non-Gaussianity parameter  $f_{\text{NL}}$  can be entirely ignored.

In summary, to determine the scalar bi-spectrum, it suffices to evaluate the contributions to the bi-spectrum due to the quantities  $\mathcal{G}_C^{\text{is}}(\mathbf{k}_1, \mathbf{k}_2, \mathbf{k}_3)$ , with  $C = (1, 6)$ , which involve integrals running from the initial time  $\eta_i$  to the time  $\eta_s$  when the smallest of the

three modes reaches super-Hubble scales. Further, the addition of the contribution due to the field redefinition evaluated at  $\eta_s$  ensures that no non-trivial super-Hubble contributions are ignored. In the following sub-section, with the help of a specific example, we shall also corroborate these conclusions numerically.

### 4.3.3 Details of the numerical methods

The scalar bi-spectrum and the parameter  $f_{\text{NL}}$  can be easily evaluated analytically in the slow roll inflationary scenario [49]. However, barring some exceptional cases [54, 55, 72], it often proves to be difficult to evaluate the bi-spectrum analytically when departures from slow roll occur. Hence, one has to resort to numerical computations in such cases.

We solve the background as well as the perturbation equations using a Bulirsch-Stoer algorithm with an adaptive step size control routine [106]. As we had mentioned earlier in Section 2.2, we shall treat the number of e-folds as the independent variable, which allows for efficient and accurate computation. To obtain the power spectrum, we impose the standard Bunch-Davies initial conditions [cf. Eq. (1.23)] on the perturbations when the modes are well inside the Hubble radius, and evolve them until suitably late times. Typically, in the case of smooth inflaton potentials, it suffices to evolve the modes  $f_k$  from an initial time when  $k/(aH) = 100$ . However, as we had pointed out in Subsection 3.1.3, in the case of the axion monodromy model, for the best fit values of the parameters of our interest, the modes have to be evolved from an earlier initial time, when  $k/(aH) \simeq 250$ , so that the resonance that occurs in these models due to the oscillations in the potential is captured [53, 101]. The scalar power spectra displayed in Figure 4.1 have been evaluated at super-Hubble scales, say, when  $k/(aH) \simeq 10^{-5}$ , which is typically when the amplitude of the curvature perturbations freeze in<sup>1</sup>.

Having obtained the behavior of the background and the modes, we carry out the integrals involved in arriving at the bi-spectrum using the method of adaptive quadrature [107]. Since we shall be focusing on the equilateral limit of the bi-spectrum, we can evolve each of the modes of interest independently and calculate the integrals for each of

---

<sup>1</sup>Recall that, in the last two chapters, wherein we had compared certain inflationary models with the CMB data, apart from the scalar power spectrum, we had also evaluated the tensor power spectrum and had incorporated it in our analysis. We should add here that the tensor modes are evolved and the corresponding power spectrum is evaluated in the same fashion as the scalar spectrum. Moreover, since it is only the scalar modes that exhibit resonance in oscillatory inflationary potentials, no special considerations need to be paid to the tensors even in cases such as the axion monodromy model. Actually, barring cases wherein extreme departures from slow roll occur (such as, for example, in the punctuated inflationary scenario, see Refs. [77]), the tensor spectra largely prove to be nearly scale independent.

the modes separately. The integrals  $\mathcal{G}_n$  actually contain a cut-off in the sub-Hubble limit, which is essential for singling out the perturbative vacuum [49, 51, 52]. Numerically, the presence of the cut-off is fortunate since it controls the contributions due to the continuing oscillations that would otherwise occur. Generalizing the cut off that is often introduced analytically in the slow roll case, we impose a cut off of the form  $\exp[-\kappa k/(aH)]$ , where  $\kappa$  is a small parameter. In the previous subsection, we had discussed as to how the integrals need to be carried out from the early time  $\eta_i$  when the largest scale is well inside the Hubble radius to the late time  $\eta_s$  when the smallest scale is sufficiently outside. In the equilateral configuration of our interest, rather than integrate from  $\eta_i$  to  $\eta_s$ , it suffices to compute the integrals for the modes from the time when each of them satisfy the sub-Hubble condition, say,  $k/(aH) = 100$ , to the time when they are well outside the Hubble radius, say, when  $k/(aH) = 10^{-5}$ . In other words, one carries out the integrals exactly over the period the modes are evolved to obtain the power spectrum. The presence of the cut-off ensures that the contributions at early times, *i.e.* near  $\eta_i$ , are negligible. Furthermore, it should be noted that, in such a case, the corresponding super-Hubble contribution to  $f_{\text{NL}}^{\text{eq}}$  will saturate the bound (4.41) in power law inflation for all modes.

With the help of specific example, let us now illustrate that, for a judicious choice of  $\kappa$ , the results that we obtain are largely independent of the upper and the lower limits of the integrals. In fact, we shall demonstrate these points in two steps for the case of the standard quadratic potential (2.1). Firstly, focusing on a specific mode (recall that we are working in the equilateral limit), we shall fix the upper limit of the integral to be the time when  $k/(aH) = 10^{-5}$ . Evolving the mode from different initial times, we shall evaluate the integrals involved from these initial times to the fixed final time for different values of  $\kappa$ . This exercise helps us to identify at an optimal value for  $\kappa$  when we shall eventually carry out the integrals from  $k/(aH) = 100$ . Secondly, upon choosing the optimal value for  $\kappa$  and integrating from  $k/(aH) = 100$ , we shall calculate the integrals for different upper limits. For reasons outlined in the previous subsection, it proves to be necessary to consider the contributions to the bi-spectrum due to the fourth and the seventh terms together. Moreover, since the first and the third, and the fifth and the sixth, have similar structure, it turns out to be convenient to club these terms as have discussed before. In Figure 4.2, we have plotted the value of  $k^6$  times the different contributions to the bi-spectrum, *viz.*  $G_1 + G_3$ ,  $G_2$ ,  $G_4 + G_7$  and  $G_5 + G_6$ , as a function of  $\kappa$  when the integrals have been carried out from  $k/(aH)$  of  $10^2$ ,  $10^3$  and  $10^4$  for a mode which leaves the Hubble radius around 53 e-folds before the end of inflation. The figure clearly indicates  $\kappa = 0.1$  to be a highly suitable value. A larger  $\kappa$  leads to a sharper cut-off reducing the value of

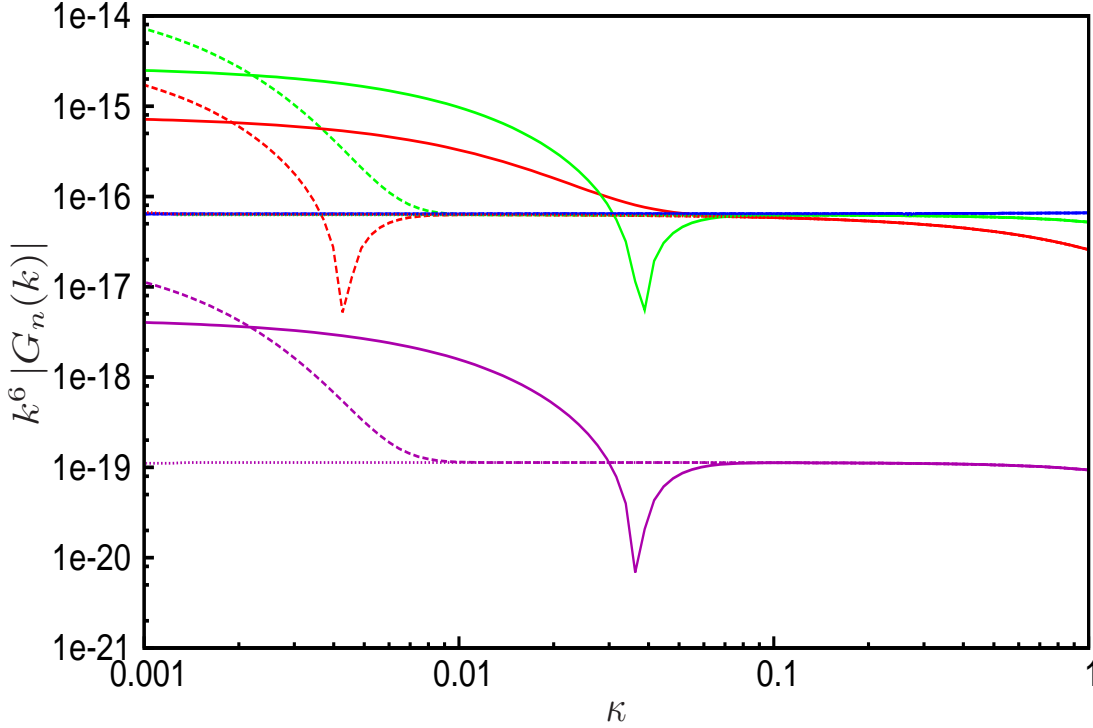


Figure 4.2: The quantities  $k^6$  times the absolute values of  $G_1 + G_3$  (in green),  $G_2$  (in red),  $G_4 + G_7$  (in blue) and  $G_5 + G_6$  (in purple) have been plotted as a function of the cut off parameter  $\kappa$  for a given mode in the case of the conventional, quadratic inflationary potential. Note that these values have been arrived at with a fixed upper limit [*viz.* corresponding to  $k/(aH) = 10^{-5}$ ] for the integrals involved. The solid, dashed and the dotted lines correspond to integrating from  $k/(aH)$  of  $10^2$ ,  $10^3$  and  $10^4$ , respectively. It is clear that the results converge for  $\kappa = 0.1$ , which suggests it to be an optimal value. While evaluating the bi-spectrum for the other models, we shall choose to work a  $\kappa$  of 0.1 and impose the initial conditions as well as carry out the integrals from  $k/(aH)$  of  $10^2$  (barring the case of the axion monodromy model, as we have discussed in the text). An additional point that is worth noticing is the fact the term  $G_4 + G_7$  seems to be hardly dependent of the cut-off parameter  $\kappa$ . This can possibly be attributed to the dependence of  $G_4$  on  $\epsilon'_2$  which can be rather small during slow roll, thereby effectively acting as a cut off.

the integrals. One could work with a smaller  $\kappa$ , in which case, the figure suggests that, one would also need to necessarily integrate from deeper inside the Hubble radius. In Figure 4.3, after fixing  $\kappa$  to be 0.1 and, with the initial conditions imposed at  $k/(aH) = 10^2$ , we have plotted the four contributions to the bi-spectrum for a mode that leaves the Hubble radius at 50 e-folds before the end of inflation as a function of the upper limit of the integrals. It is evident from the figure that the values of the integrals converge quickly once the mode leave the Hubble radius. For efficient numerical integration, as

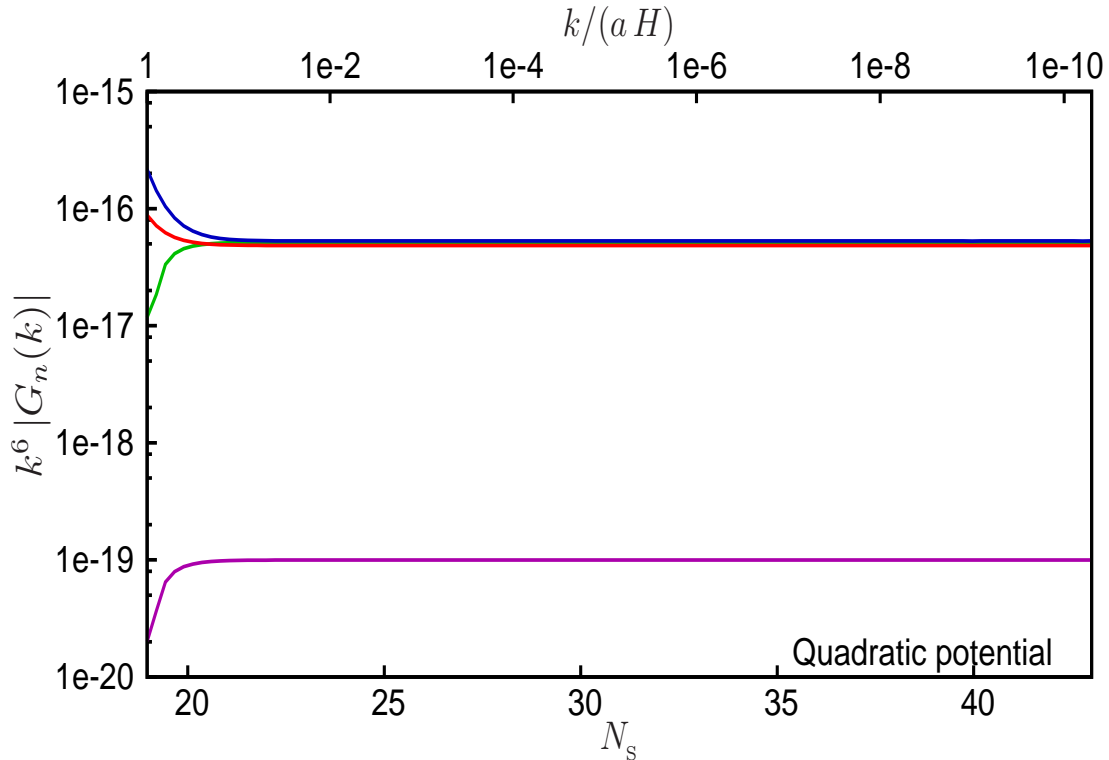


Figure 4.3: The quantities  $k^6$  times the absolute values of  $G_1 + G_3$ ,  $G_2$ ,  $G_4 + G_7$  and  $G_5 + G_6$  have been plotted (with the same choice of colors as in the previous figure) as a function of the upper limit of the integrals involved for a given mode in the case of the quadratic potential. Evidently, the integrals converge fairly rapidly to their final values once the mode leaves the Hubble radius. The independence of the results on the upper limit support the conclusions that we had earlier arrived at analytically in the last subsection, *viz.* that the super-Hubble contributions to the bi-spectrum are entirely negligible.

in the case of the power spectrum, we have chosen the super-Hubble limit to correspond to  $k/(aH) = 10^{-5}$ . We have repeated similar tests for the other models of our interest too. These tests confirm the conclusions that we have arrived at above, indicating the robustness of the numerical methods and procedures that we have adopted.

#### 4.3.4 Comparison with the analytical results in the cases of power law inflation and the Starobinsky model

Before we go on to consider the bi-spectra generated in the inflationary models of our interest, we shall compare the numerical results we obtain with the analytical results that can be arrived at in two cases in the equilateral limit. The first case that we shall consider is power law inflation wherein, as we shall soon outline, the spectral shape of the non-

zero contributions to the bi-spectrum can be easily calculated. The second example that we shall discuss is the Starobinsky model described by the potential (4.3) wherein, under certain conditions, the complete scalar bi-spectrum can be evaluated in the equilateral limit (see Ref. [54]; in this context, also see Refs. [55]).

Let us first consider the case of power law inflation described by the scale factor (4.36) with  $\gamma \leq -2$ . In such a case, as we have seen,  $\epsilon_1$  is a constant and, hence,  $\epsilon_2$  and  $\epsilon'_2$ , which involve derivatives of  $\epsilon_1$ , reduce to zero. Since the contributions due to the fourth and the seventh terms, *viz.*  $G_4(k)$  and  $G_7(k)$ , depend on  $\epsilon'_2$  and  $\epsilon_2$ , respectively [cf. Eqs. (4.11d) and (4.12)], these terms vanish identically in power law inflation. Note that the modes  $v_k$  given by Eq. (4.37) depend only on the combination  $k\eta$ . Moreover, as  $\epsilon_1$  is a constant in power law inflation, we have  $f_k \propto v_k/a$ . Under these conditions, with a simple rescaling of the variable of integration in the expressions (4.11a), (4.11b), (4.11c), (4.11e) and (4.11f), it is straightforward to show that, in the equilateral limit we are focusing on, the quantities  $\mathcal{G}_1, \mathcal{G}_2, \mathcal{G}_3, \mathcal{G}_5$  and  $\mathcal{G}_6$ , all depend on the wavenumber as  $k^{\gamma+1/2}$ . Then, upon making use of the asymptotic form of the modes  $f_k$ , it is easy to illustrate that the corresponding contributions to the bi-spectrum, *viz.*  $G_1 + G_3, G_2$  and  $G_5 + G_6$ , all behave as  $k^{2(2\gamma+1)}$ . Since the power spectrum in power law inflation is known to have the form  $k^{2(\gamma+2)}$  (see, for example, Refs. [105]), the expression (4.34) for  $f_{\text{NL}}^{\text{eq}}$  then immediately suggests that the quantity will be strictly scale invariant for all  $\gamma$ . In fact, apart from these results, it is also simple to establish the following relation between the different contributions:  $G_5 + G_6 = -(3\epsilon_1/16)(G_1 + G_3)$ , a result, which, in fact, also holds in slow roll inflation [54]. In other words, in power law inflation, it is possible to arrive at the spectral dependence of the non-zero contributions to the bi-spectrum without having to explicitly calculate the integrals involved. Further, one can establish that the non-Gaussianity parameter  $f_{\text{NL}}^{\text{eq}}$  is exactly scale independent for any value of  $\gamma$ . While these arguments does not help us in determining the amplitude of the various contributions to the bi-spectrum or the non-Gaussianity parameter, their spectral shape and the relative magnitude of the above-mentioned terms provide crucial analytical results to crosscheck our numerical code. In Figure 4.4, we have plotted the different non-zero contributions to the bi-spectrum computed using our numerical code and the spectral dependence we have arrived at above analytically for two different values of  $\gamma$  in the case of power law inflation. We have also indicated the relative magnitude of the first and the third and the fifth and the sixth terms arrived at numerically. Lastly, we have also illustrated the scale independent behaviour of the non-Gaussianity parameter  $f_{\text{NL}}^{\text{eq}}$  for both the values of  $\gamma$ . It is clear from the figure that the numerical results agree well with the results and conclusions that we arrived at

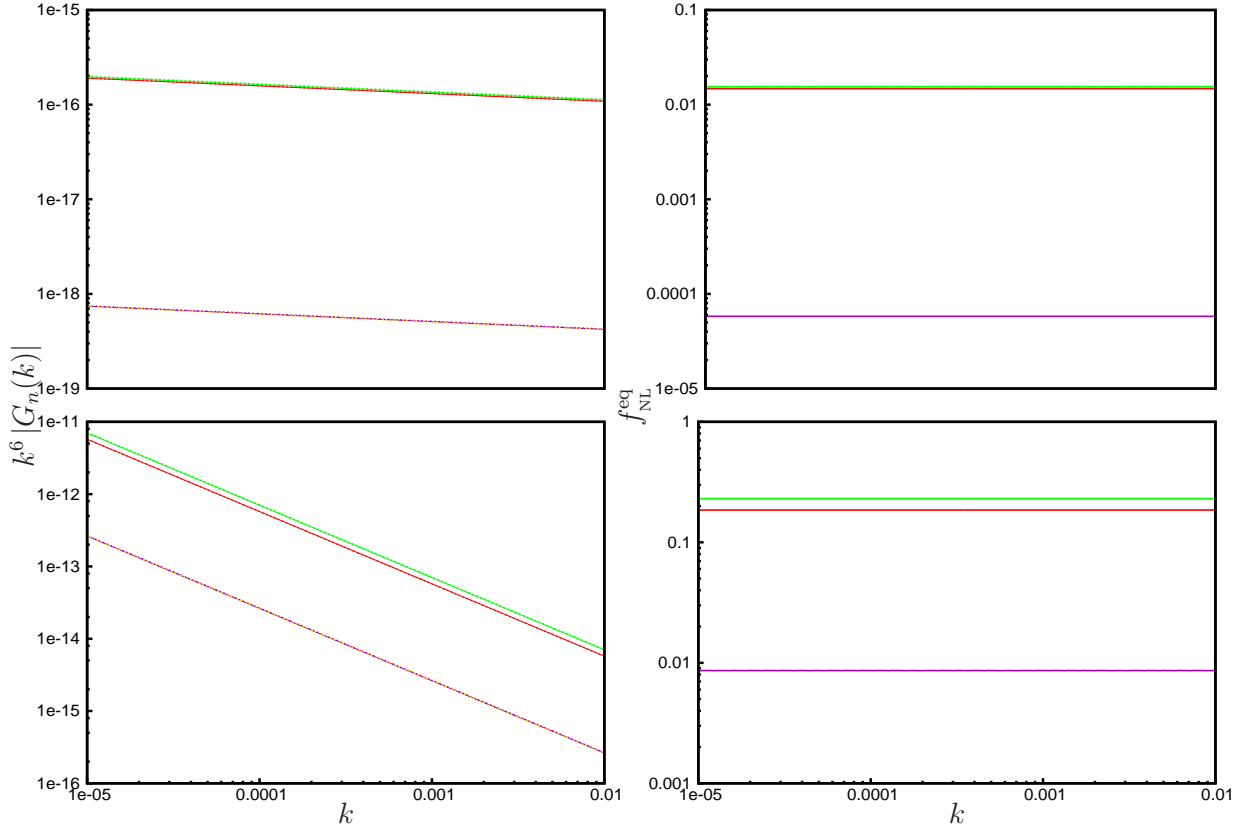


Figure 4.4: The quantities  $k^6$  times the absolute values of the non-zero contributions in the power law case, *viz.*  $G_1 + G_3$ ,  $G_2$  and  $G_5 + G_6$ , obtained numerically, have been plotted on the left for two different values of  $\gamma$  ( $\gamma = -2.02$  on top and  $\gamma = -2.25$  below), as solid curves with the same choice of colors to represent the different quantities as in the previous two figures. Note that we have followed the same color scheme to represent the differential quantities as in the previous two figures. The dots on these curves are the spectral shape arrived at from the analytical arguments, with amplitudes chosen to match the numerical results at a specific wavenumber. The dots of a different color on the solid purple curves represents  $G_5 + G_6$  obtained from its relation to  $G_1 + G_3$  discussed in the text. The plots on the right are the non-Gaussianity parameter  $f_{\text{NL}}^{\text{eq}}$  associated with the different contributions, arrived at using the numerical code. Note that, as indicated by the analytical arguments, the quantity  $f_{\text{NL}}^{\text{eq}}$  corresponding to all the contributions turns out to be strictly scale invariant for both values of  $\gamma$ .

above analytically.

Let us now turn to the Starobinsky model. As we have discussed earlier, in this case, the change in the slope causes a brief period of fast roll which leads to sharp features in the scalar power spectrum (as we had illustrated in Figure 4.1). It was known that, for certain range of parameters, one could evaluate the scalar power spectrum analytically

in the Starobinsky model, which matches the actual, numerically computed spectrum exceptionally well [71, 54]. Interestingly, it has been recently shown that, in the equilateral limit, the model allows the analytic evaluation of the scalar bi-spectrum too (see Ref. [54]; in this context, also see Refs. [55]) In Figure 4.5, we have plotted the numerical as well as the analytical results for the functions  $G_1+G_3$ ,  $G_2$ ,  $G_4+G_7$ , and  $G_5+G_6$  for the Starobinsky model. We have plotted for parameters of the model for which the analytical results are considered to be a good approximation [54]. It is evident from the figure that the numerical results match the analytical ones very well. Importantly, the agreement proves to be excellent in the case of the dominant contribution  $G_4+G_7$ . A couple of points concerning the numerical results in the case of the Starobinsky model (both in Figure 4.1 wherein we have plotted the power spectrum as well as in Figure 4.5 above containing the bi-spectrum) require some clarification. The derivatives of the potential (4.3) evidently contain discontinuity. These discontinuities need to be smoothed in order for the problem to be numerically tractable. The spectra and the bi-spectra in the Starobinsky model we have illustrated have been computed with a suitable smoothing of the discontinuity, while at the same time retaining a sufficient level of sharpness so that they closely correspond to the analytical results that have been arrived at [54, 55].

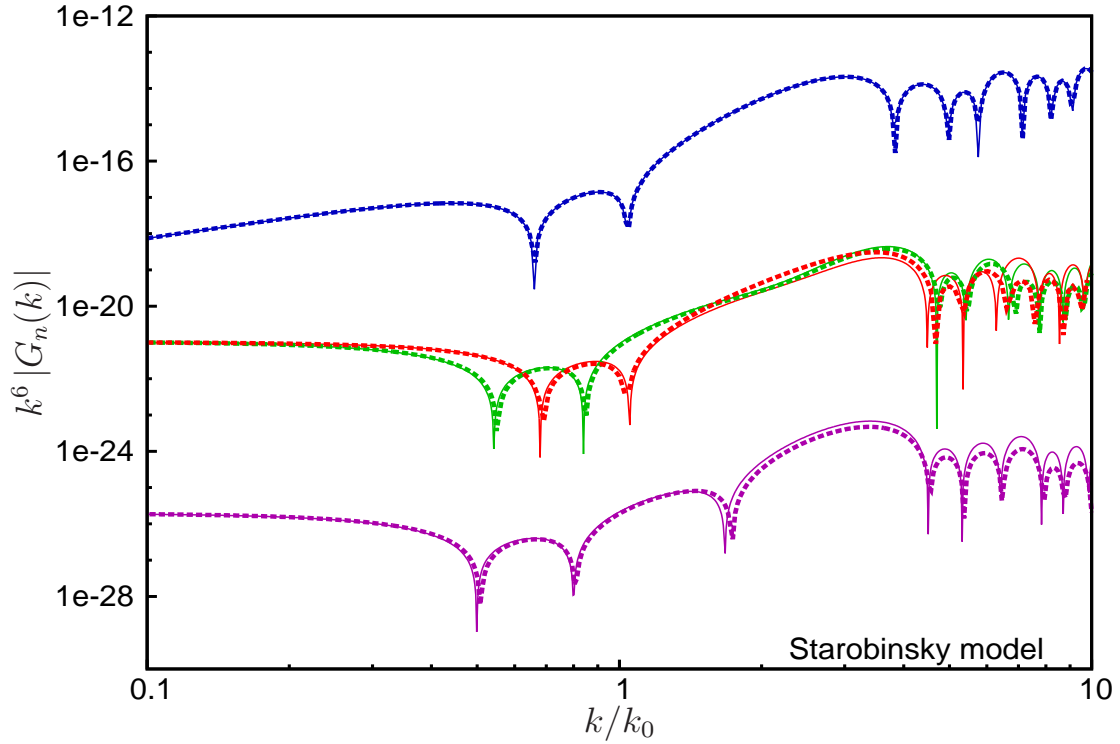


Figure 4.5: The quantities  $k^6$  times the absolute values of  $G_1 + G_3$  (in green),  $G_2$  (in red),  $G_4 + G_7$  (in blue) and  $G_5 + G_6$  (in purple) have been plotted as a function of  $k/k_0$  for the Starobinsky model. These plots correspond to the following values of the model parameters:  $V_0 = 2.36 \times 10^{-12} M_{\text{Pl}}^4$ ,  $A_+ = 3.35 \times 10^{-14} M_{\text{Pl}}^3$ ,  $A_- = 7.26 \times 10^{-15} M_{\text{Pl}}^3$  and  $\phi_0 = 0.707 M_{\text{Pl}}$ . Note that  $k_0$  is the wavenumber which leaves the Hubble radius when the scalar field crosses the break in the potential at  $\phi_0$ . The solid curves represent the analytical expressions that have been obtained recently [54, 55], while the dashed curves denote the numerical results computed using our Fortran code. We should mention that we have also arrived at these results independently using a Mathematica [108] code. We find that the numerical results match the analytical results exceptionally well in the case of the crucial, dominant contribution to the  $f_{\text{NL}}$ , *viz.* due to  $G_4 + G_7$ .

## 4.4 Results in the equilateral limit

We shall now discuss the bi-spectra arrived at numerically in the various models of our interest. In Figure 4.6, we have plotted the various contributions, *viz.*  $G_1 + G_3$ ,  $G_2$ ,  $G_4 + G_7$  and  $G_5 + G_6$  (in the equilateral limit) for the punctuated inflationary scenario driven by the potential (4.1), the quadratic potential (2.1) with the step (2.5), and the axion monodromy model (3.2) which contains oscillations in the inflaton potential. These plots and the one in previous figure clearly point to the fact that it is the combination  $G_4 + G_7$  that contributes the most to the scalar bi-spectrum in these cases [53].

In Figure 4.7, we have plotted the quantity  $f_{\text{NL}}^{\text{eq}}$  due to the dominant contribution that arises in the various models that we have considered. It is clear from this figure that, while in certain cases  $f_{\text{NL}}^{\text{eq}}$  can prove to be a good discriminator, it cannot help in others, and its ability to discriminate depends strongly on the differences in the background dynamics. For instance, the evolution of the first two slow roll parameters are very similar when a step is introduced in either the quadratic potential or a small field model [85]. Hence, it is not surprising that the  $f_{\text{NL}}^{\text{eq}}$  behaves in a similar fashion in both these models. Whereas,  $f_{\text{NL}}^{\text{eq}}$  proves to be substantially different in punctuated inflation and the Starobinsky model. Recall that, in the Starobinsky model, the first slow roll parameter remains small throughout the evolution. In contrast, it grows above unity for a very short period (leading to a brief interruption of the accelerated expansion) in the punctuated inflationary scenario. It is this departure from inflation that leads to a sharp drop in the power spectrum and a correspondingly sharp rise in the parameter  $f_{\text{NL}}^{\text{eq}}$  in punctuated inflation. In fact, this occurs for modes that leave the Hubble radius just before inflation is interrupted [83]. However, note that,  $f_{\text{NL}}^{\text{eq}}$  grows with  $k$  at large wavenumbers in the Starobinsky model. This can be attributed to the fact that  $\epsilon'_2$ , which determines the contribution due to the fourth term, diverges due to the discontinuity in the second derivative of the potential [55]. Similarly, we find that  $f_{\text{NL}}^{\text{eq}}$  is rather large in the axion monodromy model in contrast to the case wherein the conventional quadratic potential is modulated by an oscillatory term. The large value of  $f_{\text{NL}}^{\text{eq}}$  that arises in the monodromy model can be attributed to the resonant behavior encountered in the model [98, 53, 101]. In fact, we have also evaluated the  $f_{\text{NL}}^{\text{eq}}$  for the case of quadratic potential modulated by sinusoidal oscillations, which too leads to continuing, periodic features in the scalar power spectrum as we had seen in the last chapter. However, we find that the  $f_{\text{NL}}^{\text{eq}}$  in such a case proves to be rather small (of the order  $10^{-2}$  or so).

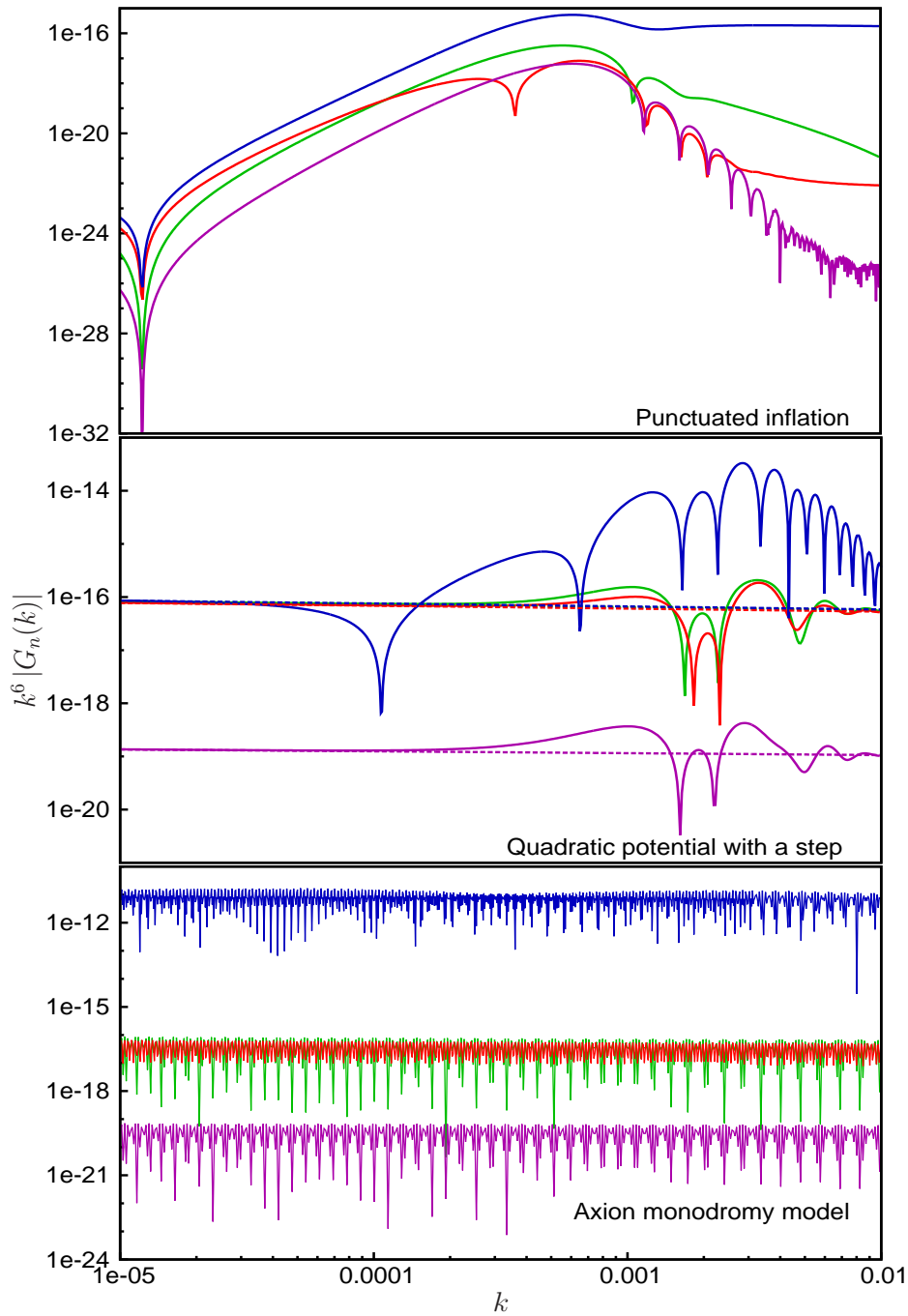


Figure 4.6: The set of quantities  $k^6 |G_n(k)|$  plotted as in the previous figure with the same choice of colors to represent the different  $G_n(k)$ . The figures on top, in the middle and at the bottom correspond to punctuated inflation, the quadratic potential with a step and the axion monodromy model, respectively, and they have been plotted for values of the parameters that lead to the best fit to the WMAP data [77, 85, 101]. In the middle figure, the dashed lines correspond to the quadratic potential when the step is not present.

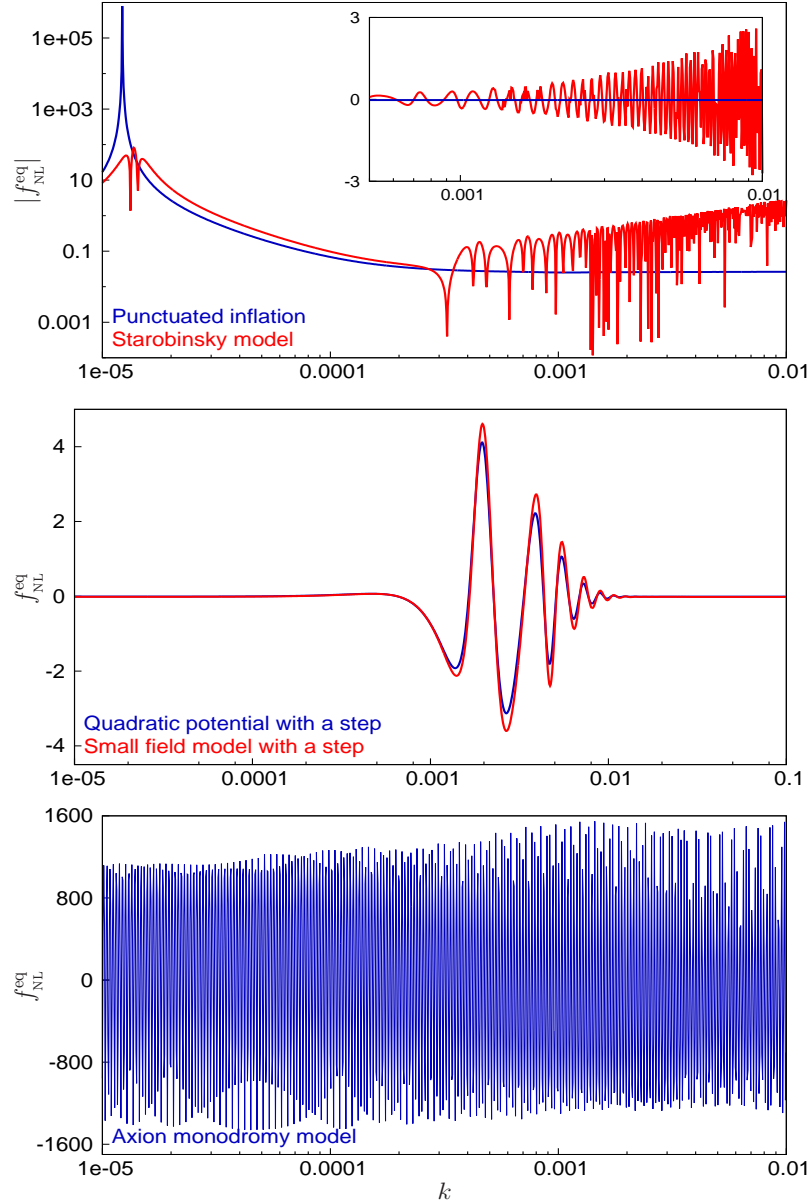


Figure 4.7: A plot of  $f_{NL}^{eq}$  corresponding to the various models that we have considered. The figure at the top contains the absolute value of  $f_{NL}^{eq}$ , plotted on a logarithmic scale (for convenience in illustrating the extremely large values that arise), in the Starobinsky model and the punctuated inflationary scenario. The inset highlights the growth in  $f_{NL}^{eq}$  at large wavenumbers in the case of the Starobinsky model, in conformity with the conclusions that have also been arrived at analytically [55]. The figure in the middle contains  $f_{NL}^{eq}$  for the cases wherein a step has been introduced in a quadratic potential and a small field model. The figure at the bottom corresponds to that of the axion monodromy model. As we had mentioned before, these sets of models lead to scalar power spectra with certain common characteristics. Needless to say, while  $f_{NL}^{eq}$  is considerably different in the first and the last sets of models, it is almost the same in the case of models with a step. These similarities and differences can be attributed completely to the background dynamics.

## 4.5 Discussion

In this chapter, we have been interested in examining the power of the non-Gaussianity parameter  $f_{\text{NL}}$  to discriminate between various single field inflationary models involving the canonical scalar field. With this goal in mind, using a new numerical code which can efficiently calculate the bi-spectrum for any triangular configuration, we have evaluated the quantity  $f_{\text{NL}}^{\text{eq}}$  in a slew of models that generate features in the scalar perturbation spectrum [109]. We find that the amplitude of  $f_{\text{NL}}^{\text{eq}}$  proves to be rather different when the dynamics of the background turns out reasonably different, which, in retrospect, need not be surprising at all. For instance, models such as the punctuated inflationary scenario and the Starobinsky model which lead to very sharp features in the power spectrum also lead to substantially large  $f_{\text{NL}}$ . Such possibilities can aid us discriminate between the models to some extent. We had focused on evaluating the quantity  $f_{\text{NL}}$  in the equilateral limit. It will be worthwhile to compute the corresponding values in the other limits, such as the squeezed and the orthogonal limits as well. In particular, it will be interesting to examine if the so-called consistency relation between the non-Gaussianity parameter  $f_{\text{NL}}$  between the equilateral and the squeezed limits is valid even in situations wherein extreme deviations from slow roll occur (in this context, see Refs. [53, 110, 111]).

We would like to conclude by highlighting one important point. Having computed the primordial bi-spectrum, the next logical step would be to compute the corresponding CMB bi-spectrum, an issue which we have not touched upon as it is beyond the scope of the current work. While tools seem to be available to evaluate the CMB bi-spectrum based on the first order brightness function, the contribution due to the brightness function at the second order remains to be understood satisfactorily (in this context, see Ref. [59] and the last reference in Ref. [58]). This seems to be an important aspect that is worth investigating closer.

## Chapter 5

# The scalar bi-spectrum during preheating in single field inflationary models

In the standard picture, at the end of the inflationary epoch, the inflaton, which is coupled to the other fields of the standard model, decays into relativistic particles thereby transferring its energy to radiation (see, for instance, Refs. [7] and also Refs. [60, 61, 112]). These decay products are then expected to thermalize [113] in order for the radiation dominated epoch corresponding to the conventional hot big bang model to start.

In many models, inflation is terminated when the scalar field has rolled down close to a minimum of the potential. Thereafter, the scalar field usually oscillates at the bottom of the potential with an ever decreasing amplitude. There exists a period during this regime, immediately after inflation but prior to the epoch of reheating, a phase that is often referred to as preheating [60]. During this brief phase, as in the inflationary era, the scalar field continues to remain the dominant source that drives the expansion of the universe. Though the modes of cosmological interest (corresponding to comoving wavenumbers  $k$  such that, say,  $10^{-4} < k < 1 \text{ Mpc}^{-1}$ ) are well outside the Hubble radius during this phase, the conventional super-Hubble solutions to the curvature perturbations that are applicable during inflation do not a priori hold at this stage. In fact, careful analysis is required to evolve these modes during the phase of preheating. However, despite the subtle effects that need to be accounted for, it can be shown that, in single field inflationary models, the amplitude of the curvature perturbations and, hence, the amplitude as well as the shape of the scalar power spectrum associated with the scales of cosmological interest remain unaffected by the process of preheating (for the original effort, see Ref. [62]; for more recent discussions, see Refs. [63, 64]).

Over the last decade, there has been a tremendous theoretical interest in understand-

ing the extent of the non-Gaussianities that are generated during inflation [49, 51, 52, 53, 54, 55, 56, 102, 109]. Simultaneously, there has been a constant effort to arrive at increasingly tighter constraints on the dimensionless non-Gaussianity parameter  $f_{\text{NL}}$  that is often used to characterize the amplitude of the reduced scalar bi-spectrum from the available CMB data [57, 58]. For instance, as we have already mentioned, it has been theoretically established that slow roll inflation driven by the canonical scalar field typically leads to rather small values of  $f_{\text{NL}}$  (of the order of the first slow roll parameter) [56, 49]. In contrast, though a Gaussian primordial perturbation lies well within  $2\text{-}\sigma$ , the mean values of  $f_{\text{NL}}$  from the CMB observations seem to indicate a significant amount of non-Gaussianity [57, 58]. Such large levels for the parameter  $f_{\text{NL}}$  can be generated when one considers non-canonical scalar fields [51] or when there exist deviations from slow roll inflation as we had discussed in the last chapter [53, 109].

We mentioned above that, in single field models, the epoch of preheating does not affect the curvature perturbations and the scalar power spectrum generated during inflation on cosmologically relevant scales. Note that, the scalar power spectrum is essentially determined by the amplitude of the curvature perturbation. Whereas, as we had seen in the last chapter, the scalar bi-spectrum generated during inflation involves integrals over the curvature perturbations as well as the slow roll parameters [49, 51, 52, 53, 109]. If indeed deviations from slow roll inflation can result in high levels of non-Gaussianity, then, naively, one may imagine that the termination of inflation and the regime of preheating—both of which involve large values for the slow roll parameters—can also lead to large non-Gaussianities. In other words, it may seem that the epoch of preheating can contribute significantly to the scalar bi-spectrum. In this chapter, we shall investigate the contributions to the scalar bi-spectrum during preheating in single field inflationary models. Remarkably, though the epoch of preheating actually amplifies specific contributions to the bi-spectrum, as we shall illustrate, certain cancellations arise (as in the case of the super-Hubble contributions during inflation) that leave the total bi-spectrum generated during inflation virtually unaltered.

This chapter is organized as follows. In the following section, we shall highlight the essential aspects of preheating in single field inflationary models. In particular, we shall discuss the behavior of the scalar field as well as the scale factor, when a canonical scalar field is oscillating at the bottom of an inflationary potential which behaves quadratically near its minimum. We shall also discuss a few important points concerning the evolution of the curvature perturbation on super-Hubble scales during preheating. In Section 5.2, using the Maldacena formalism that we had described in last chapter, we shall evaluate

the contributions to the bi-spectrum for super-Hubble modes as the scalar field oscillates in the quadratic potential, and show that the total contribution during this epoch proves to be insignificant for these modes. We shall also support certain analytical results with the corresponding numerical computations. Finally, in Section 5.3, we shall conclude with a brief summary and outlook.

## 5.1 Behavior of the background and the large scale perturbations during preheating

In this section, we shall discuss the behavior of the background and the evolution of the curvature perturbation on super-Hubble scales during preheating. We shall consider a model involving the canonical scalar field and assume that the inflationary potential behaves quadratically around its minimum.

### 5.1.1 Background evolution about a quadratic minimum

Consider a canonical scalar field  $\phi$  that is governed by the quadratic potential  $V(\phi) = m^2 \phi^2/2$  near its minimum. It is well known that, in such cases, slow roll inflation can be realized if the field starts sufficiently far away from the minimum, with suitably small values for its velocity [6, 7]. Provided the initial conditions fall in the basin of the inflationary attractor, the number of e-folds of inflation achieved largely depends only on the initial value of the field, and inflation ends as the field nears the bottom of the potential. In fact, according to the slow roll approximation, in an inflationary potential that consists of no terms other than the above-mentioned quadratic one, inflation gets terminated as the field crosses  $\phi_e \simeq \sqrt{2} M_{\text{Pl}}$ . Thereafter, the scalar field oscillates about the minimum with a constantly decreasing amplitude because of the friction caused due to the expansion. These behavior are clearly evident from Figure 5.1, where we have plotted the evolution of the scalar field and the first slow roll parameter  $\epsilon_1$ , arrived at numerically, both during and immediately after inflation for the quadratic potential. We should emphasize here that focusing on single field models can be considered to be essentially equivalent to assuming that the coupling of the inflaton to other fields is suitably weak during preheating. The weak coupling will allow the condensate to live sufficiently long for a few oscillations to take place about the minimum of the inflaton potential.

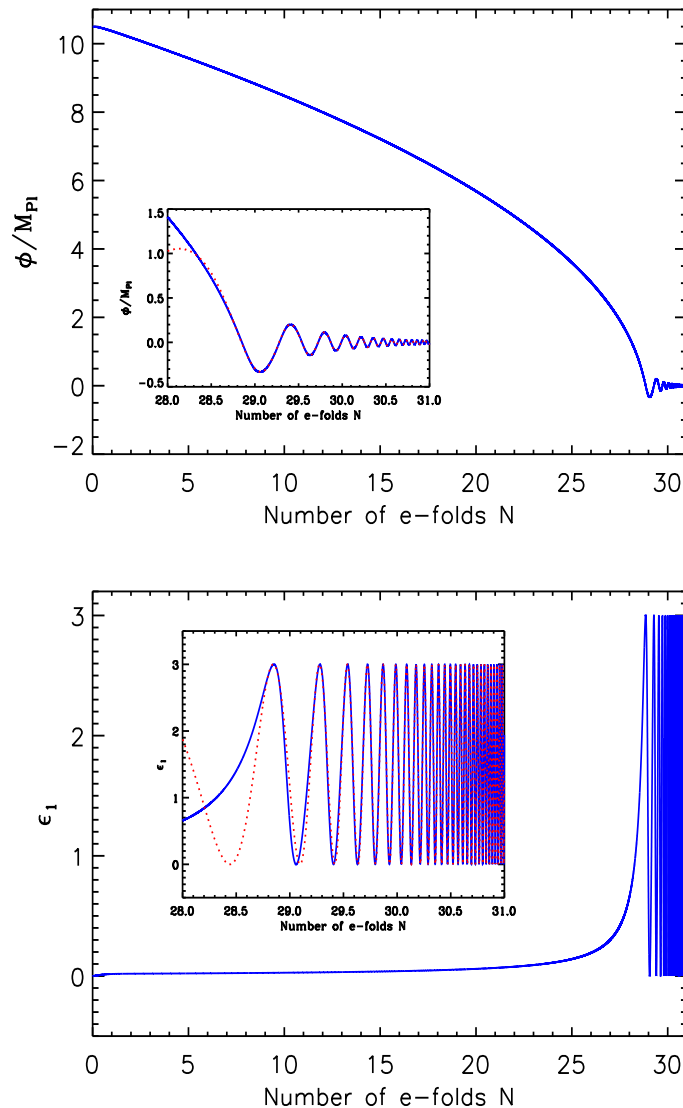


Figure 5.1: The behavior of the scalar field (top panel) and the evolution of the first slow roll parameter  $\epsilon_1$  (bottom panel) during the epochs of inflation and preheating have been plotted as a function of the number of e-folds for the case of the archetypical chaotic inflationary model described by the quadratic potential. The blue curves denote the numerical results, while the dotted red curves in the insets represent the analytical results given by Eqs. (5.4) and (5.6) that are applicable during preheating. The analytical results evidently match the numerical ones quite well. Note that, for the choice parameters and initial conditions that we have worked with,  $\epsilon_1$  turns unity at the e-fold of  $N_e \simeq 28.3$ , indicating the termination of inflation at the point. The fact that the field oscillates with a smaller and smaller amplitude once inflation has ended is clear from the inset (in the top panel). We should mention that we have worked with a smaller range of e-folds just for convenience.

Recall that, the first slow roll parameter  $\epsilon_1$  is given by [cf. Eq. (1.7)]

$$\epsilon_1 = -\frac{\dot{H}}{H^2} = \frac{\dot{\phi}^2}{2H^2 M_{\text{Pl}}^2}, \quad (5.1)$$

while the second slow roll parameter  $\epsilon_2$  can be expressed in terms of the first as follows [cf. Eq. (1.8)]:

$$\epsilon_2 \equiv \frac{1}{\epsilon_1} \frac{d\epsilon_1}{dN} = \frac{\dot{\epsilon}_1}{H\epsilon_1}. \quad (5.2)$$

Since the field is oscillating at the bottom of the potential post inflation,  $\dot{\phi} = 0$  at the ‘turning points’ and, hence,  $\epsilon_1 = 0$  at such instances. Also, when the field is at the bottom of the potential,  $V(\phi = 0) = 0$  so that  $6H^2 M_{\text{Pl}}^2 = \dot{\phi}^2$ , corresponding to  $\epsilon_1 = 3$ . Hence, we can expect  $\epsilon_1$  to oscillate between these two extreme values. Moreover, the above expression for the second slow roll parameter in terms of the first suggests that  $\epsilon_2$  will vanish whenever  $\epsilon_1$  reaches the maximum value (*i.e.* at the bottom of the potential wherein  $\dot{\epsilon}_1 = 0$ ), and that it will diverge at the ‘turning points’ wherein  $\epsilon_1$  vanishes. These behavior too are indeed reflected in the plot of  $\epsilon_1$  in Figure 5.1 and, in Figure 5.2, where we have plotted  $\epsilon_2$ .

Let us now try to arrive at the complete behavior of the background scalar field analytically. During the phase of preheating, one finds that the period of the oscillations (characterized by the inverse mass in the case of the quadratic potential of our interest) is much smaller than the time scales associated with the expansion, *i.e.* the inverse of the Hubble parameter  $H^{-1}$ . In such a situation, to understand the effects of the scalar field on the scale factor, one can average over the oscillations and make use of the averaged energy density of the scalar field to solve the first Friedmann equation. One finds that, in the quadratic potential of our interest, the expansion behaves as in a matter dominated epoch, with the scale factor growing as  $a(t) \propto t^{2/3}$ , so that the Hubble parameter behaves as  $H = 2/(3t)$  [6, 7, 60].

Therefore, at the time of preheating, the oscillating scalar field satisfies the differential equation [cf. Eq. (1.6)]

$$\ddot{\phi} + \frac{2}{t} \dot{\phi} + m^2 \phi = 0. \quad (5.3)$$

The solution to this differential equation can be immediately written down to be

$$\frac{\phi(t)}{M_{\text{Pl}}} = \frac{\alpha}{mt} \sin(mt + \Delta), \quad (5.4)$$

where  $\alpha$  is a dimensionless constant that we shall soon determine, while  $\Delta$  is an arbitrary phase chosen suitably to match the transition from inflation to the matter dominated era.

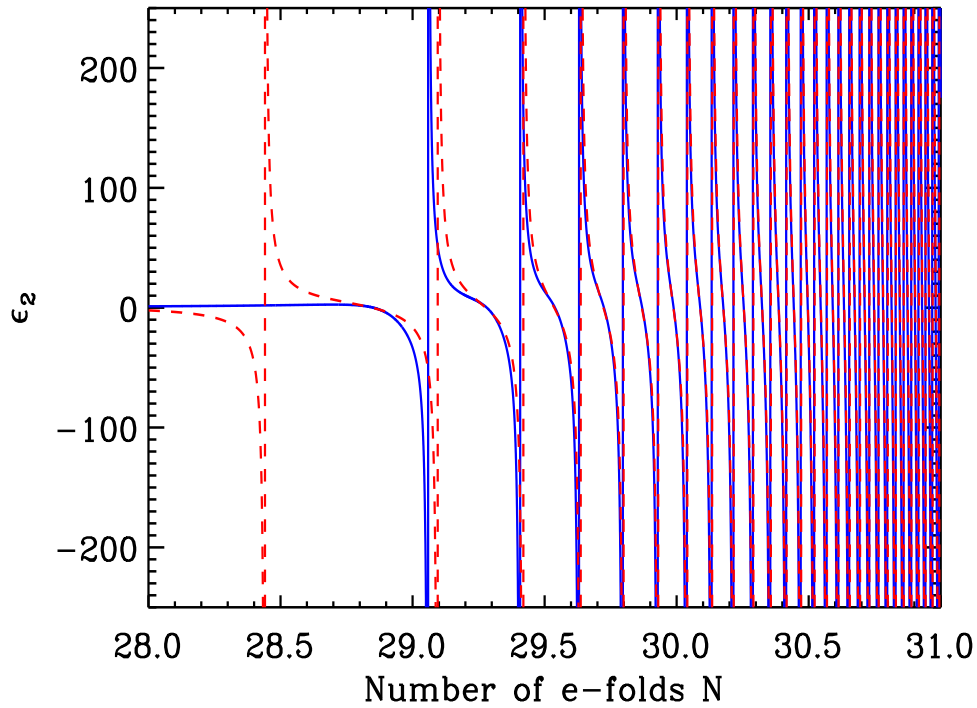


Figure 5.2: The behavior of the second slow roll parameter  $\epsilon_2$  immediately after the termination of inflation has been plotted as a function of e-folds. As in the previous figure, the blue curve represents the numerical result, while the dashed red curve denotes the analytical result during preheating [*viz.* Eq. (5.7)]. Upon comparing this plot with the earlier plot of  $\epsilon_1$ , it is clear that  $\epsilon_2$  diverges exactly at the turning points where  $\epsilon_1$  vanishes, while  $\epsilon_2$  itself vanishes whenever the field is at the bottom of the potential at which point  $\epsilon_1$  attains its maximum value.

The ‘velocity’ of the field is then given by

$$\begin{aligned}\frac{\dot{\phi}(t)}{M_{\text{Pl}}} &= \frac{\alpha}{t} \left[ \cos(mt + \Delta) - \frac{1}{mt} \sin(mt + \Delta) \right] \\ &\simeq \frac{\alpha}{t} \cos(mt + \Delta),\end{aligned}\tag{5.5}$$

where, in arriving at the second expression, for the sake of consistency (*i.e.* in having made use of the averaged energy density in the first Friedmann equation to arrive at the scale factor), we have ignored the second term involving  $t^{-2}$ . Upon using the above expressions for  $\phi$  and  $\dot{\phi}$  and the fact that  $H = 2/(3t)$  in the first Friedmann equation, we obtain that  $\alpha = \sqrt{8/3}$ . Under these conditions, we find that the first slow roll parameter simplifies to

$$\epsilon_1 \simeq 3 \cos^2(mt + \Delta)\tag{5.6}$$

which, upon averaging, reduces to  $3/2$ , as is expected in a matter dominated epoch. It is represented in Figure 5.1 (bottom panel). On using the above result for  $\epsilon_1$  in the definition (5.2), the second slow roll parameter can be obtained to be

$$\epsilon_2(t) \simeq -3mt \tan(mt + \Delta),\tag{5.7}$$

which is illustrated in Figure 5.2.

During preheating, we can write  $a(t) = a_e (t/t_e)^{2/3}$ , where  $t_e$  and  $a_e$  denote the cosmic time and the scale factor at the end of inflation. We should mention here that, in addition to the phase  $\Delta$ , one requires the value of  $t_e$  in order to match the above analytical results for the scalar field and the slow roll parameters with the numerical results. After setting  $t_e = \gamma [2/(3H_e)]$ , where  $H_e$  is the value of the Hubble parameter at the end of inflation, we have chosen the quantity  $\gamma$  and the phase  $\Delta$  suitably so as to match the analytical expressions with the numerical results. It is clear from Figures 5.1 and 5.2 that the agreement between the numerical and the analytical results is indeed very good. We should mention here that, for the results to match, we seem to require a  $\gamma$  that is slightly larger than unity. Actually, for the values of the parameters that we have worked with, we find that we need to choose  $\gamma$  to be about 1.18 for the analytical results to match the numerical ones. The fact that  $\gamma$  is not strictly unity need not come as a surprise. After all, some time is bound to elapse as the universe makes the transition from an inflationary epoch to the behavior as in a matter dominated era.

### 5.1.2 Evolution of the perturbations

As we had described in the last chapter, the scalar bi-spectrum generated during inflation involves integrals over the modes  $f_{\mathbf{k}}$  and its derivative  $f'_{\mathbf{k}}$  as well as the slow roll parameters  $\epsilon_1, \epsilon_2$  and the derivative  $\epsilon'_2$ . Since the scalar field continues to dominate the background evolution during preheating, the Maldacena formalism that we had outlined in Section 4.2 applies to the epoch of preheating as well. So, in order to analyze the effects on the bi-spectrum due to preheating, it becomes imperative that, in addition to the behavior of the slow roll parameters, we also understand the evolution of the mode  $f_{\mathbf{k}}$  and its derivative during this epoch. We have already studied the behavior of the first two slow roll parameters in the previous subsection. Therefore, our immediate aim will be to understand the evolution of the curvature perturbations for scales of cosmological interest during the preheating phase.

Since the modes of cosmological interest are well outside the Hubble radius [*i.e.*  $k/(aH) \ll 1$ ] at late times, we need to arrive at the super-Hubble solution for the mode  $f_{\mathbf{k}}$  or, equivalently, the Mukhanov-Sasaki variable  $v_{\mathbf{k}}$ . In a slow roll inflationary regime, *i.e.* when  $(\epsilon_1, \epsilon_2, \epsilon_3) \ll 1$ , the effective potential  $z''/z$  that governs the evolution of  $v_{\mathbf{k}}$  [*cf.* Eq. (1.16)] can be written as

$$\frac{z''}{z} = a^2 H^2 [2 + \mathcal{O}(\epsilon_1, \epsilon_2, \epsilon_3)] \simeq 2 a^2 H^2. \quad (5.8)$$

Due to this reason, during slow roll inflation, the super-Hubble condition  $k/(aH) \ll 1$  amounts to neglecting the  $k^2$  term with respect to the effective potential  $z''/z$  in the differential equation (1.16). In such a case, it is straightforward to show that the super-Hubble solution to  $v_{\mathbf{k}}$  up to the order  $k^2$  can be expressed as follows [6, 7]:

$$\begin{aligned} v_{\mathbf{k}}(\eta) \simeq & A_{\mathbf{k}} z(\eta) \left[ 1 - k^2 \int^{\eta} \frac{d\bar{\eta}}{z^2(\bar{\eta})} \int^{\bar{\eta}} d\tilde{\eta} z^2(\tilde{\eta}) \right] \\ & + B_{\mathbf{k}} z(\eta) \int^{\eta} \frac{d\bar{\eta}}{z^2(\bar{\eta})} \left[ 1 - k^2 \int^{\bar{\eta}} d\tilde{\eta} z^2(\tilde{\eta}) \int^{\tilde{\eta}} \frac{d\check{\eta}}{z^2(\check{\eta})} \right], \end{aligned} \quad (5.9)$$

where  $A_{\mathbf{k}}$  and  $B_{\mathbf{k}}$  are  $k$ -dependent constants that are determined by the Bunch-Davies initial condition (1.23) imposed in the sub-Hubble limit. As is well known, the first term involving  $A_{\mathbf{k}}$  represents the growing mode, while the second containing  $B_{\mathbf{k}}$  corresponds to the decaying mode. In fact, it is the  $f_{\mathbf{k}}$  and  $f'_{\mathbf{k}}$  corresponding to the dominant terms in the above expression for  $v_{\mathbf{k}}$  that we had made use of in the last chapter when calculating the super-Hubble contributions to the bi-spectrum during inflation [*cf.* Eqs. (4.14) and (4.15)]. However, it is important to realize that, at the time of preheating, the effective

potential  $z''/z$  is no longer given by the slow roll expression (5.8). It is clear that the effective potential will contain oscillatory functions and, hence, it can even possibly vanish. So, it is not a priori obvious that one can use the same approach as in the inflationary epoch and simply ignore the  $k^2$  term in the differential equation (1.16) for arriving at the behavior of the super-Hubble modes. Moreover, it is known that, during the preheating phase, one has to deal with the resonant behavior exhibited by the equation of motion under certain conditions [62, 63]. As a consequence, at this stage, it becomes necessary that we remain cautious and analyze equation (1.16) more carefully.

In order to study the perturbations during the preheating phase, it proves to be more convenient to work in terms of cosmic time and use a new rescaled variable  $\mathcal{V}_k$  that is related to the Mukhanov-Sasaki variable as follows:  $\mathcal{V}_k \equiv a^{1/2} v_k$ . Then, one finds that Eq. (1.16) takes the form [62, 63]

$$\ddot{\mathcal{V}}_k + \left[ \frac{k^2}{a^2} + \frac{d^2V}{d\phi^2} + \frac{3\dot{\phi}^2}{M_{\text{Pl}}^2} - \frac{\dot{\phi}^4}{2H^2M_{\text{Pl}}^4} + \frac{3}{4M_{\text{Pl}}^2} \left( \frac{\dot{\phi}^2}{2} - V \right) + \frac{2\dot{\phi}}{HM_{\text{Pl}}^2} \frac{dV}{d\phi} \right] \mathcal{V}_k = 0. \quad (5.10)$$

Recall that, in the quadratic potential of our interest, soon after inflation, the evolution of the scalar field  $\phi(t)$  is given by Eq. (5.4). Using this solution and its derivative (5.5), it is then easy to show that, while the third, fourth and the fifth terms within the square brackets in the above differential equation decay as  $a^{-3}$ , the last term decays more slowly as it scales as  $a^{-3/2}$ . Upon retaining only the first, second and the last terms and neglecting the others, one arrives at an equation of the form

$$\frac{d^2\mathcal{V}_k}{d\sigma^2} + \left[ 1 + \frac{k^2}{m^2 a^2} - \frac{4}{m t_e} \left( \frac{a_e}{a} \right)^{3/2} \cos(2\sigma + 2\Delta) \right] \mathcal{V}_k = 0, \quad (5.11)$$

where the new independent variable  $\sigma$  is a dimensionless quantity which we have defined to be  $\sigma \equiv m t + \pi/4$ . We can rewrite the above equation as

$$\frac{d^2\mathcal{V}_k}{d\sigma^2} + [\mathcal{A}_k - 2q \cos(2\sigma + 2\Delta)] \mathcal{V}_k = 0, \quad (5.12)$$

with  $\mathcal{A}_k$  and  $q$  being given by

$$\mathcal{A}_k = 1 + \frac{k^2}{m^2 a^2}, \quad (5.13)$$

$$q = \frac{2}{m t_e} \left( \frac{a_e}{a} \right)^{3/2}, \quad (5.14)$$

where, as we mentioned,  $t_e$  and  $a_e$  denote the cosmic time and the scale factor when inflation ends. The above equation is similar in form to the Mathieu equation (see, for

instance, Ref. [114]). The Mathieu equation possesses unstable solutions that are known to grow rapidly when the values of the parameters fall in certain domains known as the resonant bands. As discussed in detail in Refs. [60, 63], since  $q \ll 1$  in the situation of our interest, one falls in the narrow resonance regime. In such a case, the first instability band is delineated by the condition  $1 - q < \mathcal{A}_k < 1 + q$ , which turns out to be equivalent to the condition

$$0 < \frac{k}{a} < \sqrt{3 H m}. \quad (5.15)$$

It should be emphasized here that the time evolution of the quantities  $\mathcal{A}_k$  and  $q$  are such that, once a mode has entered the resonance band, it remains inside it during the entire oscillatory phase.

Note that, in Eq. (5.11), we can neglect the term involving  $k^2$  provided  $k^2/(m^2 a^2) \ll 1$ . This condition can be rewritten as

$$\left( \frac{k}{a H} \right)^2 \frac{H^2}{m^2} \ll 1. \quad (5.16)$$

On the other hand, the condition to fall in the first instability band, *viz.* Eq. (5.15), can be expressed as [63]

$$\left( \frac{k}{a H} \right)^2 \frac{H}{3 m} \ll 1. \quad (5.17)$$

Given that,  $H < m$  immediately after inflation, it is evident that the first of the above two conditions will be satisfied if the second is. In other words, being in the first instability band implies that one can indeed neglect the  $k^2$  term in Eq. (5.11). But, clearly, this is completely equivalent to ignoring the  $k^2$  term in the original equation (1.16). Therefore, we can conclude that, provided we fall in the first instability band (which is the case for the range of modes and parameters of our interest), it is perfectly valid to work with the super-Hubble solution (5.9) even during the preheating phase.

The above conclusion can also supported by the following arguments. As discussed in Ref. [63], in the first instability band, the Floquet index is given by  $\mu = q/2$ . In such a case, the mode  $\mathcal{V}_k$  behaves as  $\mathcal{V}_k \propto e^{\mu \sigma}$ . However, in the situation of our interest, since we have a time dependent Floquet index, the corresponding solution can be written as

$$\mathcal{V}_k(\eta) \propto \exp \left( \int \mu d\sigma \right) \propto a^{3/2} \quad (5.18)$$

which, in turn, implies that  $v_k = \mathcal{V}_k/a^{1/2} \propto a$ . Further, since,  $f_k = v_k/z$  and  $z \propto a$  during preheating (*i.e.* if one makes use of the fact that  $\epsilon_1 = 3/2$  on the average), we arrive at

the result that  $f_k$  remains a constant during this phase. This property is indeed the well known behavior one obtains if one simply retains the very first term of the growing mode in the super-Hubble solution (5.9). But, it should be realized that the above arguments also demonstrate another important point. Note that  $f_k$  is a constant not only for modes on super-Hubble scales but, for all the modes (even those that remain in the sub-Hubble domain), provided they fall in the resonance band. This behavior can possibly be attributed to the background. After all, it is common knowledge that the amplitude of the curvature perturbations remain constant on all scales in a matter dominated era [6, 7].

We have proven that, in the first instability band and on super-Hubble scales, the solution (5.9) is valid during preheating. Let us now analyze this solution in further detail. In particular, in order to check the extent of its validity, let us compare the analytical estimate for the curvature perturbation with the numerical solution. It is clear that the solution (5.9) leads to the following expression for the growing mode:

$$f_k(\eta) \simeq A_k \left[ 1 - k^2 \int^{\eta} \frac{d\bar{\eta}}{z^2(\bar{\eta})} \int^{\bar{\eta}} d\tilde{\eta} z^2(\tilde{\eta}) \right], \quad (5.19)$$

where we have retained the scale dependent correction for comparison with the numerical result. Since it is the contribution due to the growing mode that will prove to be dominant, we shall compare the behavior of the above solution during preheating with the corresponding numerical result. We shall carry out the comparison for a suitably small scale mode so that the second term in the above expression is not completely insignificant.

We now need to evaluate the double integral in the above expression for  $f_k$  during preheating. Let us write

$$K(t) = \int^{\eta} \frac{d\bar{\eta}}{z^2(\bar{\eta})} J(\bar{\eta}) = \int^t \frac{d\bar{t}}{a(\bar{t}) z^2(\bar{t})} J(\bar{t}), \quad (5.20)$$

where

$$J(\bar{t}) = \int^{\bar{\eta}} d\tilde{\eta} z^2(\tilde{\eta}) = \int^{\bar{t}} \frac{d\tilde{t}}{a(\tilde{t})} z^2(\tilde{t}). \quad (5.21)$$

Upon making use of the matter dominated behavior of the scale factor and the expression (5.6) for  $\epsilon_1$ , we find that the integral  $J(\bar{t})$  can be performed exactly. We obtain that

$$\begin{aligned} J(\bar{t}) = & \frac{3}{2} M_{\text{Pl}}^2 a_e t_e \left[ \frac{6}{5} \left( \frac{\bar{t}}{t_e} \right)^{5/3} + e^{2i\Delta} (-2im t_e)^{-5/3} \gamma \left( \frac{5}{3}, -2im \bar{t} \right) \right. \\ & \left. + e^{-2i\Delta} (2im t_e)^{-5/3} \gamma \left( \frac{5}{3}, 2im \bar{t} \right) + \mathcal{C} \right], \end{aligned} \quad (5.22)$$

where  $\gamma(b, x)$  is the incomplete Gamma function (see, for example, Refs. [115, 116]), while the quantity  $\mathcal{C}$  is a dimensionless constant of integration. Then, the relation between the incomplete Gamma and the Gamma functions allows us to express the function  $K(t)$  as follows:

$$\begin{aligned}
 K(t) &\simeq \frac{t_e}{4 a_e^2} \int^t \frac{d\bar{t}}{\cos^2(m\bar{t} + \Delta)} \left[ \frac{6}{5} \left(\frac{t_e}{\bar{t}}\right)^{1/3} + e^{2i\Delta} (-2im t_e)^{-5/3} \Gamma\left(\frac{5}{3}\right) \left(\frac{t_e}{\bar{t}}\right)^2 \right. \\
 &\quad - e^{2i(m\bar{t} + \Delta)} (-2im t_e)^{-1} \left(\frac{t_e}{\bar{t}}\right)^{4/3} + e^{-2i\Delta} (2im t_e)^{-5/3} \Gamma\left(\frac{5}{3}\right) \left(\frac{t_e}{\bar{t}}\right)^2 \\
 &\quad \left. - e^{-2i(m\bar{t} + \Delta)} (2im t_e)^{-1} \left(\frac{t_e}{\bar{t}}\right)^{4/3} + \mathcal{C} \left(\frac{t_e}{\bar{t}}\right)^2 \right] \\
 &\simeq \frac{3 t_e^{4/3}}{10 a_e^2} \int^t \frac{d\bar{t} \bar{t}^{-1/3}}{\cos^2(m\bar{t} + \Delta)} + \dots \quad (5.23)
 \end{aligned}$$

In arriving at the final equality, we have used the asymptotic property of the incomplete Gamma function [115, 116] and have retained only the dominant term in inverse power of  $mt$ . The final expression above can be integrated by parts to arrive at

$$K(t) \simeq \frac{3 t_e^{4/3}}{10 m a_e^2} t^{-1/3} \tan(mt + \Delta) + \frac{t_e^{4/3}}{10 m a_e^2} \int^t d\bar{t} \bar{t}^{-4/3} \tan(m\bar{t} + \Delta). \quad (5.24)$$

The second term containing the integral in this expression is of the order of the other terms that we have already neglected and, hence, it too can be ignored. As a result, the growing mode of the curvature perturbation can be written as

$$\begin{aligned}
 f_{\mathbf{k}} &\simeq A_{\mathbf{k}} \left[ 1 - \frac{3}{10} \frac{k^2 t_e^{4/3}}{a_e^2 m t^{1/3}} \tan(mt + \Delta) \right] \\
 &= A_{\mathbf{k}} \left[ 1 - \frac{1}{5} \left(\frac{k}{aH}\right)^2 \frac{H}{m} \tan(mt + \Delta) \right], \quad (5.25)
 \end{aligned}$$

in perfect agreement with the result that has been obtained recently in the literature [64]. It is evident from the above expression that the evolution of the curvature perturbation will contain sharp spikes during preheating, a feature that is clearly visible in Figure 5.3 wherein we have plotted the above analytical expression as well as the corresponding numerical result (in this context, also see Figure 4 in the first reference in Refs. [63], where the spikes are also clearly visible).

It is important that we make a couple of remarks concerning the appearance of the spikes in the evolution of the curvature perturbation. Firstly, as the spikes are encountered both analytically and numerically, evidently, they are not artifacts of the adopted

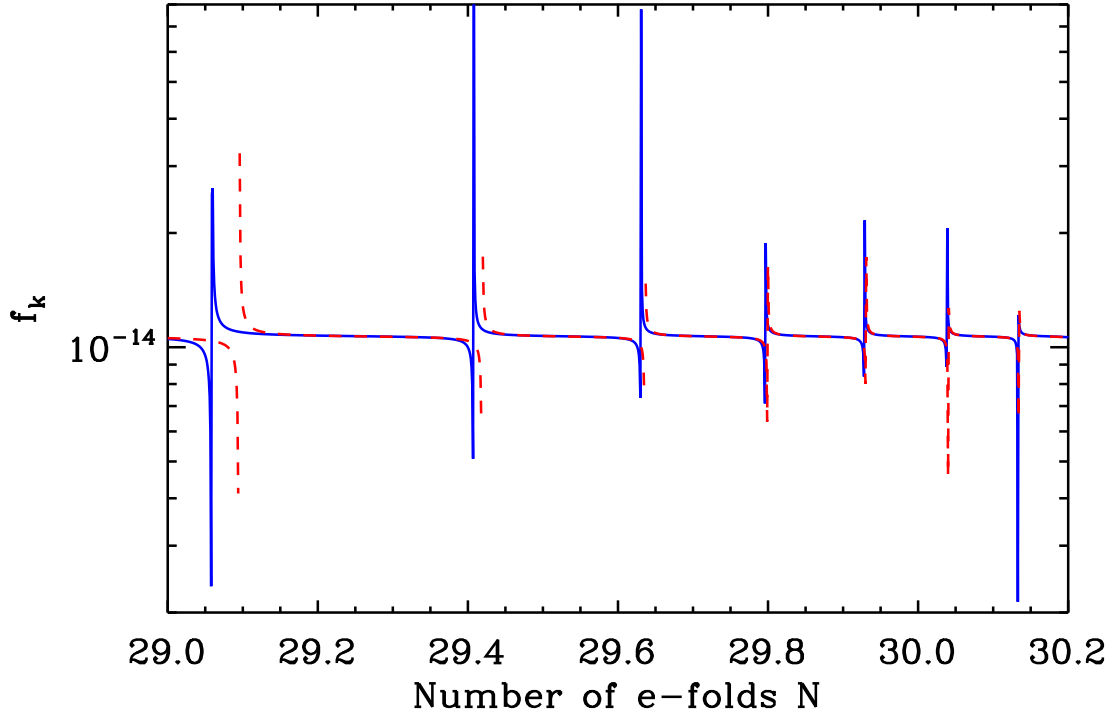


Figure 5.3: The behavior of the curvature perturbation during preheating. The blue curve denotes the numerical result, while the dashed red curve represents the analytical solution (5.25). We have chosen to work with a very small scale mode  $k$  that leaves the Hubble radius at about two e-folds before the end of inflation. We have made use of the same value of  $\Delta$  as in the previous two figures and we have fixed  $A_k$  [cf. Eq. (5.25)] by choosing it to be the numerical value of the curvature perturbation at a suitable time close to the end of inflation. It is clear that the agreement between the analytical and the numerical results is quite good.

approach. Secondly, one may fear that the perturbation theory would break down as soon as one encounters a spike, which indicates a rather large value for the perturbation variable of interest. We believe that such issues could possibly be avoided when one couples the inflaton to radiation, as is needed to reheat the universe.

## 5.2 The contributions to the scalar bi-spectrum during preheating

As we mentioned, because of the fact that the scalar field continues to be the dominant source driving the expansion during preheating, the Maldacena formalism that we had outlined in the last chapter can be utilized to evaluate the contributions to the scalar bi-spectrum due to the epoch. Our goal now is to use the formalism and determine the different contributions to the bi-spectrum due to preheating for modes of cosmological interest.

Let  $\eta_e$  denote the conformal time at the end of inflation (as in the previous chapter), while  $\eta_f$  represent a suitably late time during preheating at which we are interested in computing the scalar bi-spectrum. Then, evidently, during preheating, the various integrals describing the quantities  $\mathcal{G}_1$ – $\mathcal{G}_6$  [cf. Eqs. (4.11a)–(4.11f)] that determine the scalar bi-spectrum [cf. Eq. (4.10)] will run from  $\eta_e$  to  $\eta_f$ . Further, the contribution due to the field redefinition, *viz.*  $G_7$ , needs to be evaluated at  $\eta_f$ . It is clear from the discussion in the last section that, despite the non-trivial background evolution, during preheating, the leading behaviour of the mode  $f_k$  and its derivative  $f'_k$  continue to be described by the conventional, inflationary, super-Hubble solutions [cf. Eqs. (4.14) and (4.15)]. Therefore, barring the differences that arise due to the behavior of the background and the slow roll parameters, we can expect that the arguments we had presented in the last chapter, while calculating the super-Hubble contributions to the bi-spectrum, to apply for the case of preheating as well. In what follows, we shall rapidly extend these arguments to the epoch of preheating and estimate the corresponding contribution to the non-Gaussianity parameter in the equilateral limit, *viz.*  $f_{\text{NL}}^{\text{eq}}$ .

### 5.2.1 The fourth and the seventh terms

Recall that, the conclusions we had arrived at in the last chapter regarding the super-Hubble contributions due to the fourth and the seventh terms, *viz.*  $G_4$  and  $G_7$ , was only based on the behavior of the large scale modes (cf. Section 4.3.1). Since these behavior

continue even after inflation, provided the background continues to be dominated by the scalar field, these arguments will hold even during preheating. Therefore, it is evident that the corresponding contribution due to the fourth term can be obtained to be

$$G_4(\mathbf{k}_1, \mathbf{k}_2, \mathbf{k}_3) \simeq -\frac{1}{2} [\epsilon_2(\eta_f) - \epsilon_2(\eta_e)] \left[ |A_{\mathbf{k}_1}|^2 |A_{\mathbf{k}_2}|^2 + \text{two permutations} \right]. \quad (5.26)$$

Though the second slow roll parameter  $\epsilon_2$  grows extremely large during preheating [see Eq. (5.7) as well as Figure 5.2], as in the case of super-Hubble modes during inflation, the first of these terms [involving  $\epsilon_2(\eta_f)$ ] *exactly* cancels the contribution  $G_7(\mathbf{k}_1, \mathbf{k}_2, \mathbf{k}_3)$  [cf. Eq. (4.12)] that arises due to the field redefinition (with  $f_k$  set to  $A_k$ ). In other words, though individual contributions turn out to be large, the sum of the contributions due to the fourth and the seventh terms prove to be insignificant during preheating.

Before we go on to discuss the behavior of the other contributions, we should emphasize here that the above result for the fourth and the seventh terms applies to all single field models. It is important to appreciate the fact that we have made no assumptions whatsoever about the inflationary potential in arriving at the above conclusion. However, one should keep in mind that, regarding its behavior near the minima, we have made use of the fact that the potential can be approximated by a parabola. Indeed, it is with this explicit form that we have been able to identify a solution to the Mukhanov-Sasaki equation that leads to a constant curvature perturbation.

### 5.2.2 The second term

Upon using the behavior (4.14) of the large scale modes, it is straightforward to show that, during preheating, the contribution to the bi-spectrum due to the second term is given by

$$G_2(\mathbf{k}_1, \mathbf{k}_2, \mathbf{k}_3) = -2i M_{\text{pl}}^2 (\mathbf{k}_1 \cdot \mathbf{k}_2 + \text{two permutations}) |A_{\mathbf{k}_1}|^2 |A_{\mathbf{k}_2}|^2 |A_{\mathbf{k}_3}|^2 \times [I_2(\eta_f, \eta_e) - I_2^*(\eta_f, \eta_e)], \quad (5.27)$$

where the quantity  $I_2(\eta_f, \eta_e)$  is described by the integral

$$I_2(\eta_f, \eta_e) = \int_{\eta_e}^{\eta_f} d\eta a^2 \epsilon_1^2. \quad (5.28)$$

Clearly, as in the case of the super-Hubble contributions during inflation,  $G_2(\mathbf{k}_1, \mathbf{k}_2, \mathbf{k}_3)$  identically vanishes since  $I_2(\eta_f, \eta_e)$  is real. Needless to add, this implies that the second term does not contribute to the bi-spectrum during preheating. Again we should emphasize the fact that, as in the case of the fourth and the seventh terms, this result holds good

for any inflationary model provided it can be approximated by a parabola in the vicinity of its minimum.

In order to check that our assumptions and approximations are indeed valid, let us now estimate the quantity  $\mathcal{G}_2(\mathbf{k}_1, \mathbf{k}_2, \mathbf{k}_3)$  analytically during preheating for the case of the quadratic potential and compare with the corresponding numerical result. In such a case, the integral  $I_2(\eta_f, \eta_e)$  can be carried out along similar lines to the integral  $J(\bar{t})$  that we had evaluated earlier [cf. Eq. (5.22)]. We find that it can be expressed in terms of the incomplete Gamma function  $\gamma(b, x)$  as follows:

$$\begin{aligned}
 I_2(\eta_f, \eta_e) = & \frac{9 a_e t_e}{16} (m t_e)^{-5/3} \left( \frac{18}{5} (m t_e)^{5/3} [e^{5(N_f - N_e)/2} - 1] \right. \\
 & + 4 (-2i)^{-5/3} e^{2i\Delta} \left\{ \gamma \left[ \frac{5}{3}, -2i m t_e e^{3(N_f - N_e)/2} \right] - \gamma \left( \frac{5}{3}, -2i m t_e \right) \right\} \\
 & + 4 (2i)^{-5/3} e^{-2i\Delta} \left\{ \gamma \left[ \frac{5}{3}, 2i m t_e e^{3(N_f - N_e)/2} \right] - \gamma \left( \frac{5}{3}, 2i m t_e \right) \right\} \\
 & + (-4i)^{-5/3} e^{4i\Delta} \left\{ \gamma \left[ \frac{5}{3}, -4i m t_e e^{3(N_f - N_e)/2} \right] - \gamma \left( \frac{5}{3}, -4i m t_e \right) \right\} \\
 & \left. + (4i)^{-5/3} e^{-4i\Delta} \left\{ \gamma \left[ \frac{5}{3}, 4i m t_e e^{3(N_f - N_e)/2} \right] - \gamma \left( \frac{5}{3}, 4i m t_e \right) \right\} \right), \quad (5.29)
 \end{aligned}$$

where  $N_e$  and  $N_f$  denote the e-folds corresponding to the conformal times  $\eta_e$  and  $\eta_f$ , respectively. On the other hand, had we ignored the oscillations during preheating, and assumed that the background behavior is exactly the same as in a matter dominated era, then, since,  $\langle\langle \epsilon_1 \rangle\rangle = 3/2$ , the quantity  $\langle\langle I_2(\eta_f, \eta_e) \rangle\rangle$  can be trivially evaluated to yield

$$\langle\langle I_2(\eta_f, \eta_e) \rangle\rangle = \frac{27 a_e t_e}{20} [e^{5(N_f - N_e)/2} - 1]. \quad (5.30)$$

We have plotted the quantity  $\mathcal{G}_2(\mathbf{k}_1, \mathbf{k}_2, \mathbf{k}_3)$  in the equilateral limit, *i.e.* when  $k_1 = k_2 = k_3 = k$ , corresponding to the analytical expressions (5.29) and (5.30) as well as the numerical result as a function of upper limit  $N_f$  during preheating in Figure 5.4. The agreement between the analytical and the numerical results is indeed striking.

### 5.2.3 The remaining terms

The contributions due to the remaining terms, *viz.* the first, the third, the fifth and the sixth, can be easily evaluated as in the case of the super-Hubble contributions during inflation. We find that the contribution to the bi-spectrum due to the first and the third

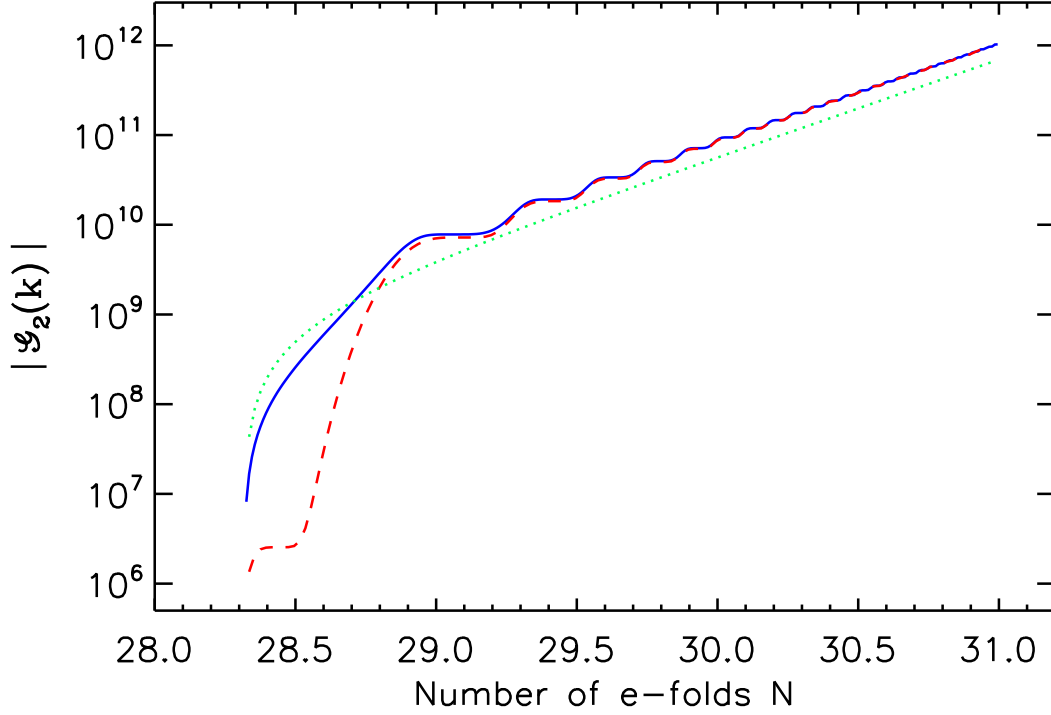


Figure 5.4: The behavior of the quantity  $\mathcal{G}_2(\mathbf{k}_1, \mathbf{k}_2, \mathbf{k}_3)$  in the equilateral limit, *i.e.* when  $k_1 = k_2 = k_3 = k$ , for a mode that leaves the Hubble radius at about 20 e-folds before the end of inflation. The blue curve represents the numerical result. The dashed red curve denotes the analytical result arrived at using the integral (5.29) and with the same choice of  $\Delta$  as in the last three figures. The dotted green curve corresponds to the integral (5.30) obtained when the oscillations have been ignored. As in the previous figure, the value of  $A_k$  has been fixed by choosing it to be the numerical value of the curvature perturbation on super-Hubble scales. Needless to add, the match between the analytical and the numerical results is excellent.

terms during preheating can be written as

$$\begin{aligned}
 G_1(\mathbf{k}_1, \mathbf{k}_2, \mathbf{k}_3) + G_3(\mathbf{k}_1, \mathbf{k}_2, \mathbf{k}_3) &= 2 i M_{\text{Pl}}^2 \left[ \left( 1 - \frac{\mathbf{k}_1 \cdot \mathbf{k}_2}{k_2^2} - \frac{\mathbf{k}_1 \cdot \mathbf{k}_3}{k_3^2} \right) |A_{\mathbf{k}_1}|^2 \right. \\
 &\quad \times \left( A_{\mathbf{k}_2} \bar{B}_{\mathbf{k}_2}^* A_{\mathbf{k}_3} \bar{B}_{\mathbf{k}_3}^* - A_{\mathbf{k}_2}^* \bar{B}_{\mathbf{k}_2} A_{\mathbf{k}_3}^* \bar{B}_{\mathbf{k}_3} \right) \\
 &\quad \left. + \text{two permutations} \right] I_{13}(\eta_f, \eta_e), \tag{5.31}
 \end{aligned}$$

where the quantity  $I_{13}(\eta_f, \eta_e)$  represents the integral

$$I_{13}(\eta_f, \eta_e) = \int_{\eta_e}^{\eta_f} \frac{d\eta}{a^2}. \tag{5.32}$$

This integral can be trivially carried out during preheating to yield

$$I_{13}(\eta_f, \eta_e) = \frac{t_e}{a_e^3} [1 - e^{-3(N_f - N_e)/2}]. \tag{5.33}$$

Since the second term in this expression for  $I_{13}(\eta_f, \eta_e)$  dies quickly with growing  $N_f$ , the corresponding contribution to the bi-spectrum proves to be negligible.

The contributions due to the fifth and the sixth terms during preheating can be arrived at in a similar fashion. We obtain that

$$\begin{aligned}
 G_5(\mathbf{k}_1, \mathbf{k}_2, \mathbf{k}_3) + G_6(\mathbf{k}_1, \mathbf{k}_2, \mathbf{k}_3) &= \frac{i M_{\text{Pl}}^2}{2} \left\{ \left[ \frac{\mathbf{k}_1 \cdot \mathbf{k}_2}{k_2^2} + \frac{\mathbf{k}_1 \cdot \mathbf{k}_3}{k_3^2} + \frac{k_1^2 (\mathbf{k}_2 \cdot \mathbf{k}_3)}{k_2^2 k_3^2} \right] |A_{\mathbf{k}_1}|^2 \right. \\
 &\quad \left. \left( A_{\mathbf{k}_2} \bar{B}_{\mathbf{k}_2}^* A_{\mathbf{k}_3} \bar{B}_{\mathbf{k}_3}^* - A_{\mathbf{k}_2}^* \bar{B}_{\mathbf{k}_2} A_{\mathbf{k}_3}^* \bar{B}_{\mathbf{k}_3} \right) \right. \\
 &\quad \left. + \text{two permutations} \right\} I_{56}(\eta_f, \eta_e), \tag{5.34}
 \end{aligned}$$

with  $I_{56}(\eta_f, \eta_e)$  denoting the integral

$$I_{56}(\eta_f, \eta_e) = \int_{\eta_e}^{\eta_f} \frac{d\eta}{a^2} \epsilon_1. \tag{5.35}$$

This integral too can be evaluated rather easily to arrive at the following expression:

$$\begin{aligned}
 I_{56}(\eta_f, \eta_e) &= \frac{3 t_e}{a_e^3} \left( \cos^2(m t_e + \Delta) - e^{-3(N_f - N_e)/2} \cos^2 [m t_e e^{3(N_f - N_e)/2} + \Delta] \right. \\
 &\quad + m t_e \cos(2 \Delta) \{ \text{Si}(2 m t_e) - \text{Si} [2 m t_e e^{3(N_f - N_e)/2}] \} \\
 &\quad \left. + m t_e \sin(2 \Delta) \{ \text{Ci}(2 m t_e) - \text{Ci} [2 m t_e e^{3(N_f - N_e)/2}] \} \right), \tag{5.36}
 \end{aligned}$$

where  $\text{Si}(x)$  and  $\text{Ci}(x)$  are the sine and the cosine integral functions [115, 116]. And, had we ignored the oscillations, we would have arrived at

$$\langle\langle I_{56}(\eta_f, \eta_e) \rangle\rangle = \frac{3 t_e}{2 a_e^3} [1 - e^{-3(N_f - N_e)/2}], \quad (5.37)$$

which is of the same order as  $I_{13}(\eta_f, \eta_e)$ , and hence completely negligible as we had discussed.

#### 5.2.4 The contribution to $f_{\text{NL}}$ during preheating

Let us now actually estimate the extent of the contribution to the non-Gaussianity parameter  $f_{\text{NL}}$  during preheating. Since the contributions due to the combination of the fourth plus the seventh and the second term completely vanish at late times, the non-zero contribution to the bi-spectrum during preheating is determined by the first, the third, the fifth and the sixth terms. Note that, if one ignores the oscillations post inflation, then one has  $I_{56}(\eta_f, \eta_e) = 3 I_{13}(\eta_f, \eta_e)/2$ . In such a situation, we find that the non-trivial contributions lead to the following bi-spectrum in the simpler case of the equilateral limit:

$$G_{\text{eq}}(k) = \frac{69 i M_{\text{Pl}}^2}{8} |A_{\mathbf{k}}|^2 (A_{\mathbf{k}}^2 \bar{B}_{\mathbf{k}}^{*2} - A_{\mathbf{k}}^{*2} \bar{B}_{\mathbf{k}}^2) I_{13}(\eta_f, \eta_e). \quad (5.38)$$

Upon making use of the fact that  $f_{\mathbf{k}} \simeq A_{\mathbf{k}}$  at late times, we then obtain the contribution to the non-Gaussianity parameter in the equilateral limit, *viz.*  $f_{\text{NL}}^{\text{eq}}$  [*cf.* Eq. (4.34)], during preheating to be

$$f_{\text{NL}}^{\text{eq}}(k) \simeq -\frac{115 i M_{\text{Pl}}^2}{48} \left( \frac{A_{\mathbf{k}}^2 \bar{B}_{\mathbf{k}}^{*2} - A_{\mathbf{k}}^{*2} \bar{B}_{\mathbf{k}}^2}{|A_{\mathbf{k}}|^2} \right) I_{13}(\eta_f, \eta_e). \quad (5.39)$$

In order to explicitly calculate the parameter  $f_{\text{NL}}$ , we need to first specify the inflationary scenario. We shall choose to work with power law inflation, as we had done in the last chapter while estimating the super-Hubble contributions to the non-Gaussianity parameter  $f_{\text{NL}}$  during inflation. In such a case, upon inserting the corresponding expressions for the quantities  $A_{\mathbf{k}}$  and  $B_{\mathbf{k}}$  [*cf.* Eqs. (4.39)] in Eq. (5.39) above, we arrive at

$$\begin{aligned} f_{\text{NL}}^{\text{eq}}(k) &= \frac{115 \epsilon_1}{288 \pi} \Gamma^2 \left( \gamma + \frac{1}{2} \right) 2^{2\gamma+1} (2\gamma+1)^2 \sin(2\pi\gamma) |\gamma+1|^{-2(\gamma+1)} \\ &\times [1 - e^{-3(N_f - N_e)/2}] \left( \frac{k}{a_e H_e} \right)^{-(2\gamma+1)}. \end{aligned} \quad (5.40)$$

This expression can also be rewritten in terms of the parameters describing the post-inflationary evolution. We obtain that [117]

$$\begin{aligned}
 f_{\text{NL}}^{\text{eq}}(k) &= \frac{115 \epsilon_1}{288 \pi} \Gamma^2 \left( \gamma + \frac{1}{2} \right) 2^{2\gamma+1} (2\gamma+1)^2 \sin(2\pi\gamma) |\gamma+1|^{-2(\gamma+1)} [1 - e^{-3(N_f - N_e)/2}] \\
 &\times \left[ \left( \frac{\pi^2 g_*}{30} \right)^{-1/4} (1 + z_{\text{eq}})^{1/4} \frac{\rho_c^{1/4}}{T_{\text{rh}}} \right]^{-(2\gamma+1)} \left( \frac{k}{a_0 H_0} \right)^{-(2\beta+1)}, \quad (5.41)
 \end{aligned}$$

where  $g_*$  denotes the effective number of relativistic degrees of freedom at reheating,  $T_{\text{rh}}$  the reheating temperature and  $z_{\text{eq}}$  the redshift at the epoch of equality. Also, recall that,  $\rho_c$ ,  $a_0$  and  $H_0$  represent the critical energy density, the scale factor and the Hubble parameter today, respectively. The above expression is mainly determined by the ratio  $\rho_c^{1/4}/T_{\text{rh}}$ . For a model with  $\gamma \simeq -2$  and a reheating temperature of  $T_{\text{rh}} \simeq 10^{10}$  GeV, one obtains that  $f_{\text{NL}} \sim 10^{-60}$  for the modes of cosmological interest (*i.e.* for  $k$  such that  $k/a_0 \simeq H_0$ ), a value which is completely unobservable. This confirms and quantifies our result that, in the case of single field inflation, the epoch of preheating does not alter the amplitude of the scalar bi-spectrum generated during inflation [118]. However, it is worthwhile to add that, while the amplitude of the above non-Gaussianity parameter  $f_{\text{NL}}$  is small, it seems to be strongly scale dependent.

We believe that a couple of points require further emphasis at this stage of our discussion. Recall that, to fall within the first instability band during preheating, the modes need to satisfy the condition (5.15). But, in order to neglect the term involving  $k^2$  in the differential equation (5.11), the modes of interest are actually required to satisfy the condition (5.16). As we have emphasized earlier, evidently, the condition (5.16) will be easily satisfied by the large scale modes that already lie within the instability band and thereby satisfying the condition (5.17). Therefore, it is important to appreciate the fact that the conclusions we have arrived at above apply to all cosmologically relevant scales.

### 5.3 Discussion

In this chapter, we have analyzed the effects of preheating on the primordial bi-spectrum in inflationary models involving a single canonical scalar field. We have illustrated that, certain contributions to the bi-spectrum, such as those due to the combination of the fourth and the seventh terms and that due to the second term, vanish identically at late times. Further, assuming the inflationary potential to be quadratic around its minimum, we have shown that the remaining contributions to the bi-spectrum are completely in-

significant during the epoch of preheating when the scalar field is oscillating at the bottom of the potential immediately after inflation. It is important to appreciate the fact that the results we have arrived at apply to any single field inflationary potential that has a parabolic shape near the minimum.

A couple of other points also need to be stressed regarding the conclusions we have arrived at. The results we have obtained supplement the earlier results wherein it has been shown that the power spectrum generated during inflation remains unaffected during the epoch of preheating (see, Ref. [62]; in this context, also see Ref. [119]). Moreover, our results are in support of earlier discussions which had pointed to the fact that the contributions to the correlation functions at late times will be insignificant if the interaction terms in the actions at the cubic and the higher orders depend on either a time or a spatial derivative of the curvature perturbation [120].

Broadly, our effort needs to be extended in two different directions. Firstly, it is important to confirm that the conclusions we have arrived at hold true for potentials which behave differently, say, quartically, near the minima. Further, the exercise needs to be repeated for models involving non-canonical scalar fields [121, 122]. In this context, it is worth mentioning that the generalization of the conserved quantity  $\mathcal{R}_k$  in the Dirac-Born-Infeld case has been shown to stay constant in amplitude on scales larger than the sonic horizon, a property which allows us to propagate the spectrum from horizon exit till the beginning of the radiation dominated era [121]. Secondly, as we had mentioned, preheating is followed by an epoch of reheating when the energy from the inflaton is expected to be transferred to radiation. It will be interesting to examine the evolution of the bi-spectrum during reheating. However, in order to achieve reheating, the scalar field needs to be coupled to radiation. It is clear that the formalism for evaluating the bi-spectrum involving just the inflaton is required to be extended to a situation wherein radiation too is present and is also coupled to the scalar field.

However, possibly, the most interesting direction opened up by our work concerns multi-field inflation and associated non-Gaussianities [123]. Unlike single field models wherein the curvature perturbation associated with the large scale modes is conserved at late times, such a behavior is not necessarily true in multi-field inflation. When many fields are present, the entropy (*i.e.* the iso-curvature) fluctuations can cause the evolution of curvature perturbations even on super-Hubble scales. Further, in the case of multi-field inflation, it is known that the two-point correlation function can be affected by metric preheating [124]. In other words, the power spectrum calculated at the end of multi-field inflation is not necessarily the power spectrum observed in, say, the CMB data because

the post-inflationary dynamics (that is to say preheating instabilities) can modify it. In the same manner, it is tempting to conjecture that the scalar bi-spectrum calculated at the end of multi-field inflation will not necessarily be the same as the one observed in the data [125]. In particular, the so-called consistency relations [52], which relate the three-point and the four-point correlation functions (or, equivalently, the corresponding dimensionless non-Gaussianity parameters  $f_{\text{NL}}$  and  $\tau_{\text{NL}}$ ) might receive corrections in a multi-field context due to metric preheating.

## Chapter 6

# Effects of primordial features on the formation of halos

As we had described in the introductory chapter, apart from the CMB, the LSS data too are expected to provide constraints on the pattern as well as the characteristics of the primordial perturbations. Any significant change in the primordial scalar power spectrum will correspondingly modify the matter power spectrum [*cf.* Eq. (1.30)] evaluated today. Hence, the features in the inflationary scalar perturbation spectrum that we had discussed extensively in Chapters 2 and 3, in addition to their imprints on the CMB, will affect the matter power spectrum which, in turn, will leave its signatures on the formation rates of the dark matter halos. In fact, the effects of steps or oscillations in the inflaton potential on the predicted number of halos was investigated recently [126]. The analysis was carried out with the inflationary perturbation spectrum evaluated using the slow roll approximation. But, the slow roll parameters can turn large in the presence of steps or oscillatory terms in the inflationary potentials and, as a result, the power spectrum evaluated in the slow roll approximation can differ considerably from the actual power spectrum. Moreover, with the ever increasing quality of the LSS observations, in particular, the halo power spectrum constructed using the Luminous Red Galaxies (LRG) from the seventh data release (DR7) of SDSS [3, 4], it may be a worthwhile exercise to actually compare the models with the available data to arrive at additional constraints on the primordial features that we had considered in the preceding chapters.

With the above points in mind, in this chapter, we shall utilize the code that we have developed to compute the inflationary perturbation spectrum (*cf.* Section 4.3.3) and, thereby, evaluate the corresponding matter power spectrum and the number of halos formed. We shall compute the number densities and the formation rates of halos in the

inflationary models with the step and oscillations that we had considered in Chapters 2 and 3. Our goal will be to estimate the maximum possible change in the number density and the formation rate of halos in these models, when compared with, say, inflation driven by the simplest quadratic potential. In order to arrive at the parameter space of interest, we shall compare the models with the CMB as well as the LSS data. Towards this end, we shall make use of the WMAP seven-year (WMAP-7) data [19] and the LRG halo power spectrum data from SDSS DR7 [4]. We find that the power spectra with features that correspond to the best fit values of the inflationary parameters do not typically lead to substantial deviations in the formation rates of halos. However, we find that, in certain models that we consider, the potential parameters that lie within  $2\text{-}\sigma$  of the best fit values obtained from the joint constraints of WMAP and SDSS can lead to a 20% change in the number of halos formed for halo masses ranging over  $10^4\text{--}10^{14} M_\odot$ .

This chapter is organized as follows. In the following section, we shall quickly list the inflationary models of our interest, which lead to specific features in the primordial scalar power spectrum. We shall also outline the method that we adopt to compare the models with the data. In Section 6.2, we shall describe the formalism to arrive at the halo formation rate from the inflationary power spectra. In Section 6.3, we shall provide a few essential details concerning the numerical procedures that we follow. We shall discuss the results in Section 6.4, and we shall close with a few concluding remarks regarding the implications of our results in Section 6.5.

## 6.1 Models and comparison with the data

In this section, we shall quickly discuss the inflationary models of our interest and the scalar power spectra produced by them.

We shall work with the simplest case of inflation driven by the canonical scalar field. We shall treat the conventional quadratic potential (2.1) to be our reference model. We shall consider features generated due to the step (2.5) introduced in the quadratic potential, and the potentials (3.1) and (3.2) which contain oscillatory terms. As we have discussed earlier, these models result in features that lead to an improved fit to the CMB data. In Figure 6.1, we have plotted the behavior of the first two slow roll parameters in these models. As we have emphasized before, it is the deviations from slow roll seen in the figure that lead to features in the scalar power spectra.

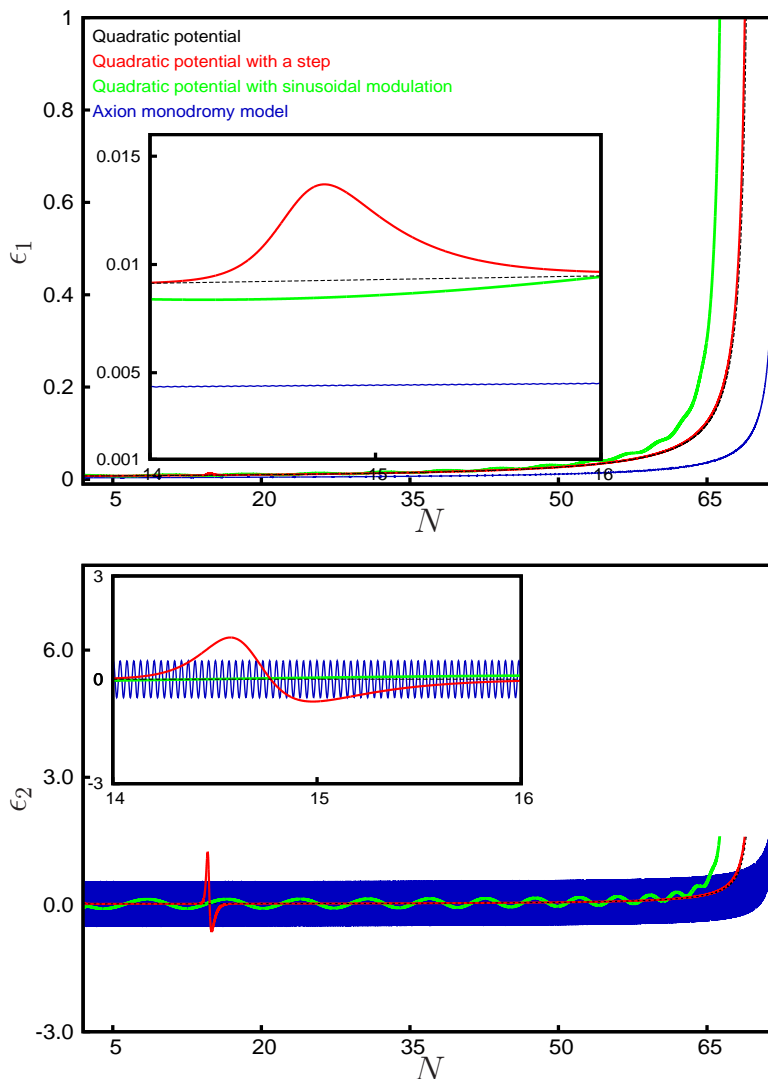


Figure 6.1: Evolution of first two slow roll parameters  $\epsilon_1$  and  $\epsilon_2$  have been plotted as a function of the number of e-folds  $N$  for the quadratic potential without and with the step (the black and the red curves, respectively), the quadratic potential superimposed by sinusoidal modulations (the green curve) and the axion monodromy model (the blue curve). The curves have been plotted for potential parameters that lead to the best fit to the recent CMB and LSS data. In the quadratic potential without the step, as is well known, the field continues to roll slowly until the end of inflation, whereas, when the step is introduced, it briefly deviates from slow roll around the time the field crosses the step. In the case of the potentials with oscillations, for the best fit values, the axion monodromy model leads to strong departures from slow roll, with  $\epsilon_2$  turning ‘large’ repeatedly, right till the termination of inflation. The insets provide a closer view of the behavior of the slow roll parameters over a smaller range of e-folds.

### 6.1.1 Comparison with the CMB and the LSS data

We compare the models with the CMB as well as the LSS data. We have worked with the WMAP-7 data [18] and the halo power spectrum data arrived at from the LRG in SDSS DR7 [4]. We have made use of the LSS data to ensure that the parameter values we eventually work with to obtain the formation rate of the halos are consistent with the observed matter power spectrum. As discussed in Chapters 2 and 3, we couple the code we have developed for computing the inflationary perturbation spectrum to CAMB [44, 43] and COSMOMC [45, 46] to arrive at, not only the CMB angular power spectrum, but also the corresponding matter power spectrum, in order to compare them with the data.

We have assumed the background to be the spatially flat  $\Lambda$ CDM model and have worked with the same priors as we have done in our earlier analysis [*cf.* Chapters 2 and 3]. As far as the priors on the inflationary parameters are concerned, for the case of the quadratic potential with the step, we have worked with the same priors that we had mentioned in Chapter 2. In the case of the two potentials with oscillatory terms, *viz.* the quadratic potential superimposed with sinusoidal oscillations (3.1) and the axion monodromy model (3.2), we have worked with the same priors on the primary parameters  $m$  and  $\lambda$  as we had done in Chapter 3. However, as should be evident from Table 6.1, we have widened the priors of the parameters  $\alpha$  and  $\beta$  for these potentials, when compared to the values listed in Table 3.1. We should add that we have allowed the phase parameter  $\delta$  to vary from  $-\pi$  to  $\pi$  as before. The motivations for choosing these priors are two fold. Firstly, the parameters  $m$  and  $\lambda$  determine the amplitude of the scalar power spectrum. We find that choosing them to be close to their COBE normalized values allows

Model	Potential parameter	Lower limit	Upper limit
Quadratic potential with sine modulation	$\alpha$	0	$2 \times 10^{-3}$
	$\ln(\beta/M_{\text{Pl}})$	-3.9	0
Axion monodromy model	$\alpha$	0	$2 \times 10^{-4}$
	$\ln(\beta/M_{\text{Pl}})$	-8	0

Table 6.1: The priors that we work with on the parameters  $\alpha$  and  $\beta$  which characterize the potentials that contain oscillatory terms [*cf.* Eqs. (3.1) and (3.2)]. Note that the priors are wider than the priors we had chosen in Chapter 3 (*cf.* Table 3.1). Also, to help us cover a larger range, we have worked with the logarithmic value of  $\beta$ .

for a faster convergence of the Markov Chains. Secondly, we have chosen the priors on  $\alpha$  and  $\beta$  such that the scalar field does not get trapped by the oscillations in the potential.

We should also note that unlike in Chapters 2 and 3, we have *not* included the tensor perturbations, as the corresponding effects are negligible. Moreover, as we have discussed in Chapter 3, in the case of potentials with oscillations, which lead to fine features in the scalar power spectrum, we will have to modify CAMB in order to ensure that the CMB angular power spectrum is evaluated for every multipole, and compare them with the data [98, 101]. But, we have not implemented this point here since we are only interested in the marginalized probabilities of the potential parameters. These probabilities shall indicate the extent to which deviations from a nearly scale invariant spectrum is allowed by the data, which we shall then make use of to study the corresponding effects on the formation of dark matter halos. We should also mention that we not taken the non-linear [127] effects on the matter power spectrum, but have included the SZ effect and the effects due to gravitational lensing in our analysis. Finally, as in our earlier analysis, we shall set the Gelman and Rubin parameter  $|R - 1|$  to be 0.03 for convergence in all the cases.

## 6.2 From the primordial spectrum to the formation rate of halos

In this section, we shall quickly outline the standard formalism to arrive at the formation rate of halos from the primordial power spectrum.

### 6.2.1 The matter power spectrum

Recall that the matter power spectrum at a given redshift  $P_M(k, z)$  is related to the primordial power spectrum  $\mathcal{P}_s(k)$  through the expression (1.30). Evidently, given the primordial spectrum, we require the CDM transfer function  $T(k)$  and the growth factor  $D_+(z)$  to arrive at the matter power spectrum.

If we define  $D_+(a) = g(a)/a$ , then, one finds that, in the spatially flat  $\Lambda$ CDM model, the quantity  $g$  satisfies the differential equation [18, 128]

$$\frac{d^2g}{d \ln a^2} + \frac{1}{2} [5 + 3 \Omega_\Lambda(a)] \frac{dg}{d \ln a} + 3 \Omega_{\text{eff}}(a) g = 0, \quad (6.1)$$

where  $\Omega_{\text{eff}}(a) = \Omega_\Lambda H_0^2/H^2$ , with  $\Omega_\Lambda$  denoting the dimensionless density parameter associated with the cosmological constant today. We shall solve this differential equa-

tion with suitable initial conditions to obtain the growth factor  $D_+(a)$ . We shall utilize CAMB [44, 43] to determine the transfer function  $T(k)$ . Using these quantities, we shall eventually arrive at the matter power spectrum from the primordial spectrum obtained in the inflationary model of interest (see the next section on numerical methods for further details).

## 6.2.2 Mass functions and the halo formation rates

To arrive at the formation rate of dark matter halos, we shall first require the number density of collapsed halos with mass in the range of  $M$  and  $M + \delta M$  in a comoving volume element. This number density, say,  $n(M)$ , is defined in terms of the root mean square fluctuation in mass  $\sigma$  through the so-called mass function  $f(\sigma)$  as follows [129]:

$$\frac{dn}{d \ln M} = -\frac{2 \rho_m}{M} \left( \frac{d \ln \sigma(R)}{d \ln M} \right) f(\sigma), \quad (6.2)$$

where  $\rho_m$  is the mean density of non-relativistic matter in the universe. Following the convention (see, for example, Refs. [6]), we shall define the root mean square fluctuation in mass at the scale  $R$  to be

$$\sigma^2(R) = \int_0^\infty d \ln k \mathcal{P}_M(k) \widetilde{W}^2(k, R), \quad (6.3)$$

where

$$\mathcal{P}_M(k) \equiv \frac{k^3}{2\pi^2} P_M(k) \quad (6.4)$$

denotes the *dimensionless* matter power spectrum, while  $\widetilde{W}(k, R)$  is the Fourier transform of the window function  $W(x, R)$  that is introduced to smooth out the density perturbation. We shall work with the commonly used spherical top hat window function, whose Fourier transform is given by

$$\widetilde{W}(k, R) = \widetilde{W}(k R) = 3 \frac{\sin(k R) - k R \cos(k R)}{(k R)^3}, \quad (6.5)$$

corresponding to the volume  $V(R) = 4\pi R^3/3$ . Note that the halo mass  $M$  within the window of radius  $R$  is given by  $M(R) = \rho_m V(R)$ .

We shall make use of the Sheth-Tormen mass function to evaluate the number density of the halos [130]. In contrast to the more conventional Press-Schechter mass function [131], it has been found that the Sheth-Tormen mass function fits the data from the  $N$ -body simulations better. Actually, the Sheth-Tormen mass function is a generalization

of the original Press-Schechter formalism for spherical collapse to the case of ellipsoidal collapse. The Sheth-Tormen mass function is defined in terms of two additional parameters  $b$  and  $p$  (when compared to the Press-Schechter case) as follows:

$$f(\sigma) = \mathcal{A} \sqrt{\frac{b\nu}{2\pi}} [1 + (b\nu)^{-p}] \exp - (b\nu/2), \quad (6.6)$$

where  $\nu = (\delta_c/\sigma)^2$ , with  $\delta_c = 1.686$  being the threshold linear overdensity for collapse. The Press-Schechter mass function corresponds to  $\mathcal{A} = 1/2$ ,  $b = 1$  and  $p = 0$ . However, upon comparing with the  $N$ -body simulation data, the best fit values for  $b$  and  $p$  are found out to be 0.707 and 0.3, respectively. The value of  $\mathcal{A}$  can then be arrived at from the normalization condition on  $f(\nu)$ , *viz.* that the integral of  $f(\nu)/\nu$  over all  $\nu$  is unity, which leads to  $\mathcal{A} = 0.3222$ .

The number density of halos associated with the above Sheth-Tormen mass function is then given by

$$\frac{dn}{d \ln M} = -\frac{\mathcal{A} \rho_m}{M} \sqrt{\frac{2b\nu}{\pi}} [1 + (b\nu)^{-p}] \left( \frac{d \ln \sigma}{d \ln M} \right) \exp - (b\nu/2). \quad (6.7)$$

The corresponding formation rates of the halos can be easily obtained to be [132]

$$R(M, z) = -\frac{dD_+(z)}{dz} \frac{dz}{dt} \frac{1}{D_+(z)} \left[ \frac{2p}{1 + (b\nu)^{-p}} - b\nu \right] \frac{dn}{dM}. \quad (6.8)$$

Note that the quantity  $dD_+/dz$  proves to be negative, since the growth factor decreases as the redshift increases. As a result, it is known that the above formation rate of halos can become negative for some mass scales (when  $2p/[1 + (b\nu)^{-p}] > b\nu$ ), which in practice can not occur. Therefore, to avoid this issue and simultaneously illustrate the effects of features, we shall only plot the ratio of the formation rates in the inflationary models leading to features and the conventional, smooth, quadratic potential.

### 6.3 The numerical methods: Essentials

Having computed the inflationary scalar perturbation spectrum (in the fashion described in Subsection 4.3.3), we arrive at the matter power spectrum using the transfer function and the growth factor. As we had remarked earlier, while we obtain the transfer function from CAMB, we evaluate the growth factor by solving the differential equation (6.1). It should be mentioned here that the initial conditions are chosen such that  $g$  is a constant

and equal to unity in the early matter dominated epoch, *i.e.* at a sufficiently high redshift of, say,  $z \simeq 30$  [18, 133].

After having obtained the matter power spectrum, we calculate the variance  $\sigma(R)$  using Eq. (6.3). The integral can be evaluated numerically with the simplest of algorithms, provided the power spectrum proves to be smooth and devoid of any features. In contrast, when these exist features such as repeated oscillations, certain care is required, and we have made use of an adaptive integration routine to compute the integral involved [107]. We have carried out the integral from a suitably small mode (such as  $k = 10^{-5} \text{Mpc}^{-1}$ ) up to a mode where the window function cuts off the integrand. Finally, we obtain at the quantity  $d \ln \sigma / d \ln M$  by numerical differentiation. We should stress here that, keeping in mind the presence of oscillations in the power spectra, we have computed  $\sigma$  and  $d \ln \sigma / d \ln M$  with care and high accuracy. We should also add that we have cross checked our result by fitting the numerical values of  $\sigma(R)$  to the Chebyshev polynomials and calculating the corresponding derivative from the polynomial (in this context, see Ref. [133]).

## 6.4 Results

In this section, we shall present the results of our comparison of the models of our interest with the CMB and the LSS data. We shall also discuss the effects of primordial spectra with features on the formation of halos.

### 6.4.1 Joint constraints from the WMAP and the SDSS data

In Table 6.2 below, we have tabulated the best fit values of the background and the potential parameters obtained from the MCMC analysis using the WMAP-7 and the SDSS LRG DR7 data. We have also listed the effective least squared parameter  $\chi_{\text{eff}}^2$  in each of the cases. For the case of the quadratic potential with and without the step, we have arrived at results similar to what we have obtained earlier in Chapter 2. Also, as one would expect, we find that the background parameters are better constrained with the inclusion of the additional SDSS data [134]. Moreover, it is obvious from Table 6.2 that the axion monodromy model does not lead to the same extent of improvement in the fit as we had obtained in Chapter 3. This occurs due to the fact that, unlike in the earlier analysis, we have not evaluated the CMB angular power at each multipole, but have worked with the inbuilt effective sampling and interpolation routine in CAMB. However, we should

Model	Quadratic	Quadratic + step	Quadratic + sine	Axion monodromy
$\Omega_b h^2$	0.0222	0.0221	0.0216	0.0225
$\Omega_c h^2$	0.1162	0.1159	0.1168	0.1154
$\theta$	1.038	1.039	1.036	1.039
$\tau$	0.0824	0.0875	0.0836	0.0856
$\ln(10^{10} A)$	-0.6545	-0.6406	-0.6448	0.9649
$\alpha$	-	$1.61 \times 10^{-3}$	$6.35 \times 10^{-5}$	$4.4 \times 10^{-5}$
$\phi_0/M_{\text{Pl}}$	-	14.664	-	-
$\Delta\phi/M_{\text{Pl}}$	-	$3.22 \times 10^{-3}$	-	-
$\ln(\beta/M_{\text{Pl}})$	-	-	-2.576	-7.61
$\delta$	-	-	2.208	-1.178
$\chi_{\text{eff}}^2$	7515.57	7507.3	7515.12	7509.56

Table 6.2: The best fit values for the background and the potential parameters for the different models of interest obtained from the MCMC analysis using the WMAP-7 and the SDSS LRG DR7 data. We should mention here that the parameter  $A$  denotes  $\lambda/M_{\text{Pl}}^3$  in the case of axion monodromy model and  $m^2/M_{\text{Pl}}^2$  in the rest of the cases. As we have discussed before, the quadratic potential with the step improves the fit to the outliers in the CMB data around the multipoles of  $\ell = 22$  and 40. Moreover, as we have seen, while the superimposed sinusoidal modulation to the quadratic potential does not provide a better fit to the data when compared to the quadratic potential, the axion monodromy model improves the fit to a good extent. However, note that, the monodromy model does not improve the fit to the data to the same extent that we had discussed in Chapter 3. As we have pointed out in the text, this arises due to the limited sampling and interpolation by CAMB over the multipoles of interest which we have chosen to work with.

stress that this does not affect our conclusions since our focus here lies on the maximum change in the formation of halos. Therefore, we are more interested in the allowed regions of the parameter space rather in arriving at the precise best fit point. Also, importantly, as we shall discuss in the following subsection, for violent oscillations in the primordial power spectrum (when one requires computing the CMB angular power spectrum at each multipole explicitly), the percentage change in the number density of halos proves to be negligible in the observable mass bins.

In Figure 6.2, we have illustrated the one dimensional likelihood on the parameter  $\phi_0$  in the case of the quadratic potential with a step, and it is clear that the location of the step is highly constrained by data. The step affects the number density of halos only over

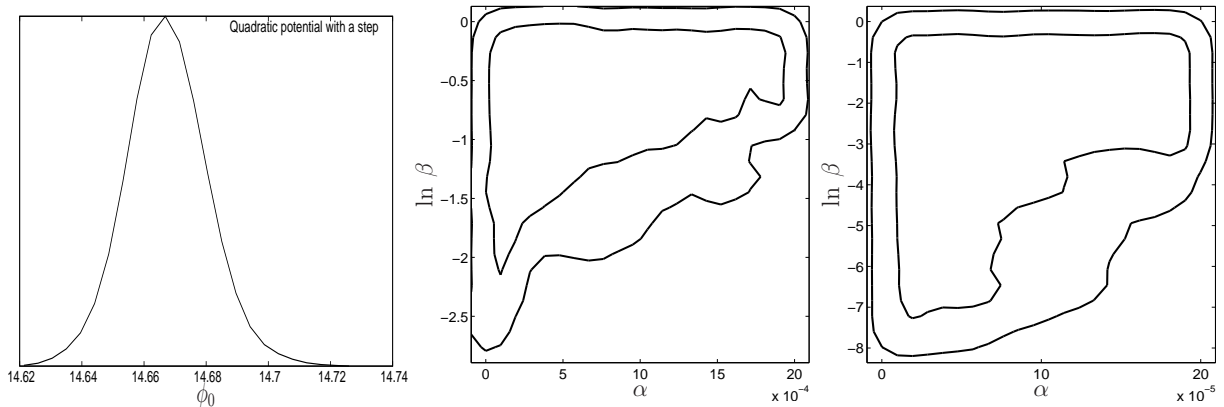


Figure 6.2: The one dimensional likelihood on the parameter  $\phi_0$  in the case of the quadratic potential with a step (on the left) and the two dimensional constraints on the parameters  $\alpha$  and  $\beta$  in the cases of the quadratic potential with sinusoidal modulations (in the middle) and the axion monodromy model (on the right). Note that the location of the step  $\phi_0$  is well constrained. The inner and the outer curves (in the figure in the middle and the one on the right) correspond to the 1- $\sigma$  and the 2- $\sigma$  confidence contours.

highly localized mass scales. We have also plotted the marginalized two dimensional constraints on the parameters  $\alpha$  and  $\beta$  for the cases of the two oscillatory potentials. It is noteworthy that the constraints are strikingly similar. In fact, the roughly triangular shape of the contours can also be understood. As the parameter  $\beta$  decreases, the resulting oscillations in the potential and, therefore, in the inflationary perturbation spectrum turn more frequent, and the data constrains the amplitude  $\alpha$  to a smaller region.

In Figure 6.3, we have plotted the best fit scalar power spectrum for the quadratic potential with and without the step and the two oscillatory potentials. Further below, in Figure 6.4, we have plotted the matter power spectrum  $P_M(k)$  evaluated *today* corresponding to the different inflationary power spectra in the previous figure. In the inset of the figure, we have highlighted the baryon acoustic oscillations and the halo power spectrum data from SDSS LRG DR7. We should add here that the theoretical best fit curves are unable to fit the data well after  $k \sim 0.1 h \text{ Mpc}^{-1}$  due to the fact that we have not taken the non-linear effects into account in arriving at the matter power spectrum.

#### 6.4.2 Effects of features in the number density and the formation rate of halos

In this section, we shall discuss the effects of the features on the number density and the formation rates of halos in the different inflationary models of our interest. In order

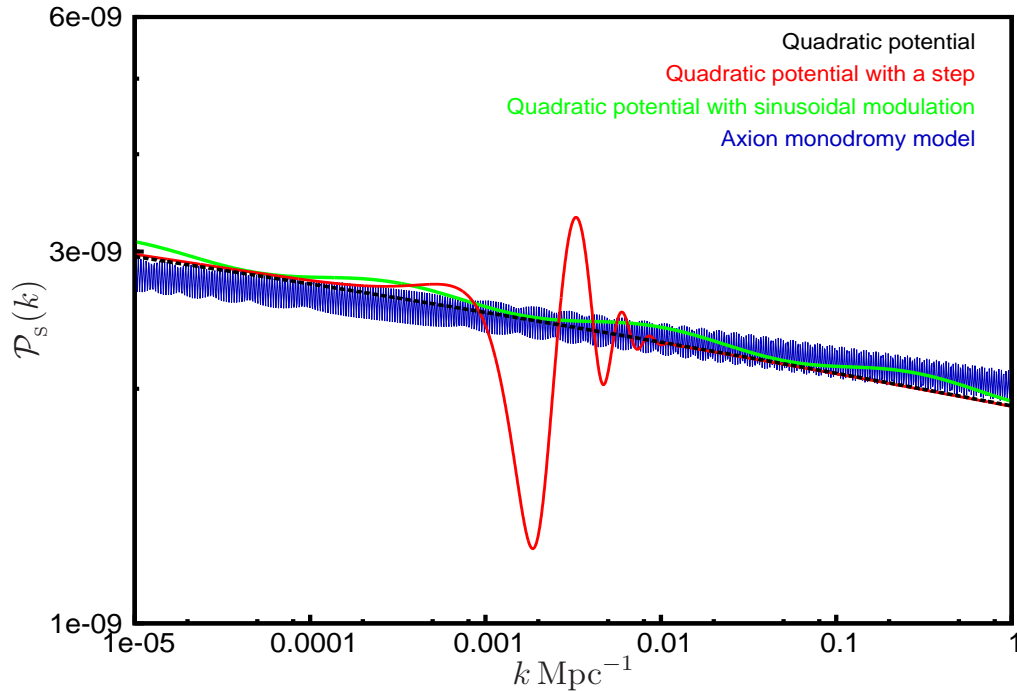


Figure 6.3: The scalar power spectra that arise in the four inflationary models of our interest. These spectra correspond to the best fit values for which we had plotted the evolution of the first two slow roll parameters earlier. Note that, we have worked with the same choice of colors to represent the results from the different models as in the Figure 6.1. We should emphasize that, while the step model leads to features that are localized, the potentials with oscillatory terms lead to modulations in the scalar power spectrum that extend over a wide range of scales.

to highlight the effects purely due to the primordial features, we have frozen the values of the background cosmological parameters, *viz.*  $\Omega_b$ ,  $\Omega_m$ ,  $\Omega_\Lambda$  and  $H_0$ , at the values arrived at upon comparing the smooth quadratic potential with the WMAP and SDSS data (*cf.* Table 6.2). But, we have made use of the best fit values for the potential parameters to compute the inflationary scalar power spectrum and from thereon the matter power spectrum and the number density of halos. In Figure 6.5, we have plotted the percentage of change in the formation rate of halos in the Press-Schechter formalism and the number density of halos in the Sheth-Tormen formalism for different models with respect to the quadratic potential. In the case of the model with the step, the change in the number density due to the step (corresponding to, say, its best fit value) occurs at very high mass halos ( $\sim 10^{17} M_\odot$ ) and hence lies outside our region of interest. Due to this reason, we have only presented the results in the case of the models with oscillatory terms in the

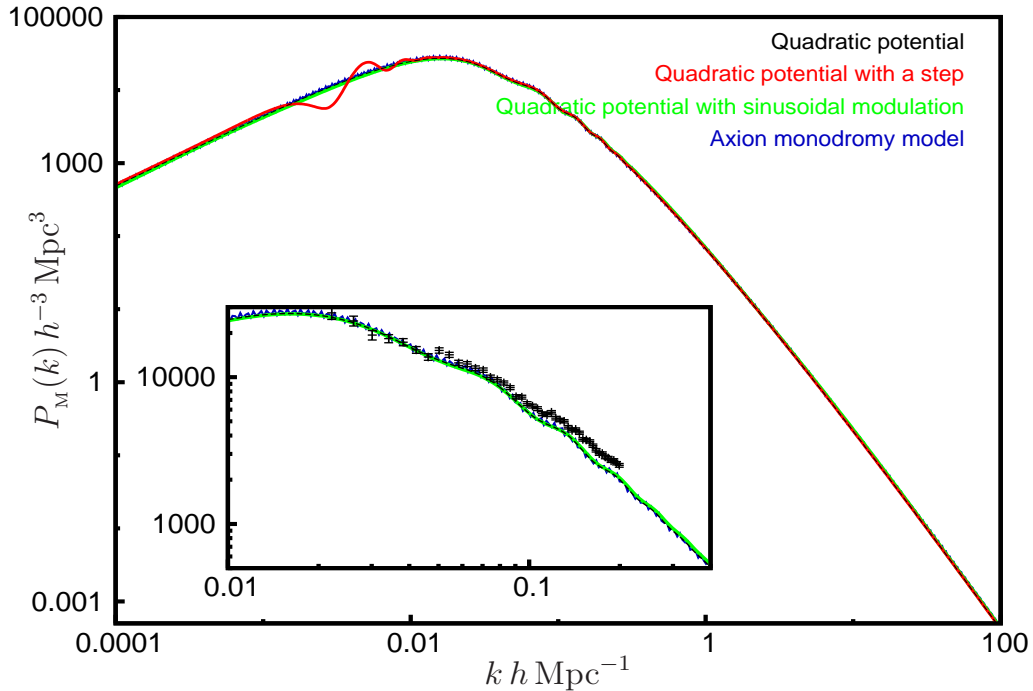


Figure 6.4: The best fit matter power spectrum  $P_M(k)$  corresponding to the different inflationary scalar power spectra we had plotted in the earlier figure. The inset highlights the imprints of the primordial features on the matter power spectrum in the domain where the baryon acoustic oscillations also play a role. The black dots with bars corresponds to the power spectrum data from SDSS obtained upon combining main galaxies and the LRGs with error bars arrived at from the diagonal elements of the corresponding covariance matrix. It should be noted that, since we have plotted the linear power spectrum, without taking into account the non-linear effects, the theoretical best fit curves are unable to fit the data for  $k > 0.1 h \text{ Mpc}^{-1}$ .

potential.

In order to arrive at the maximum possible change in the number density of halos when compared to the conventional nearly scale invariant primordial spectrum, for the models with oscillations in the potential, we have chosen values for the parameters  $\alpha$  and  $\beta$  that lie within  $2\text{-}\sigma$  from the best fit values. We have chosen the parameters in such a way that they create the largest deviation from the nearly scale invariant power spectra that are allowed by the CMB and the LSS data. In Figure 6.5, apart from the results for the best fit values, we have plotted the number density and the formation rates of halos for the cases wherein  $[\alpha, \ln(\beta/M_{\text{Pl}})]$  is set to  $(2 \times 10^{-3}, -1.7)$  and  $(2 \times 10^{-4}, -3.5)$  for the quadratic potential with the sinusoidal modulations and the axion monodromy model, respectively.

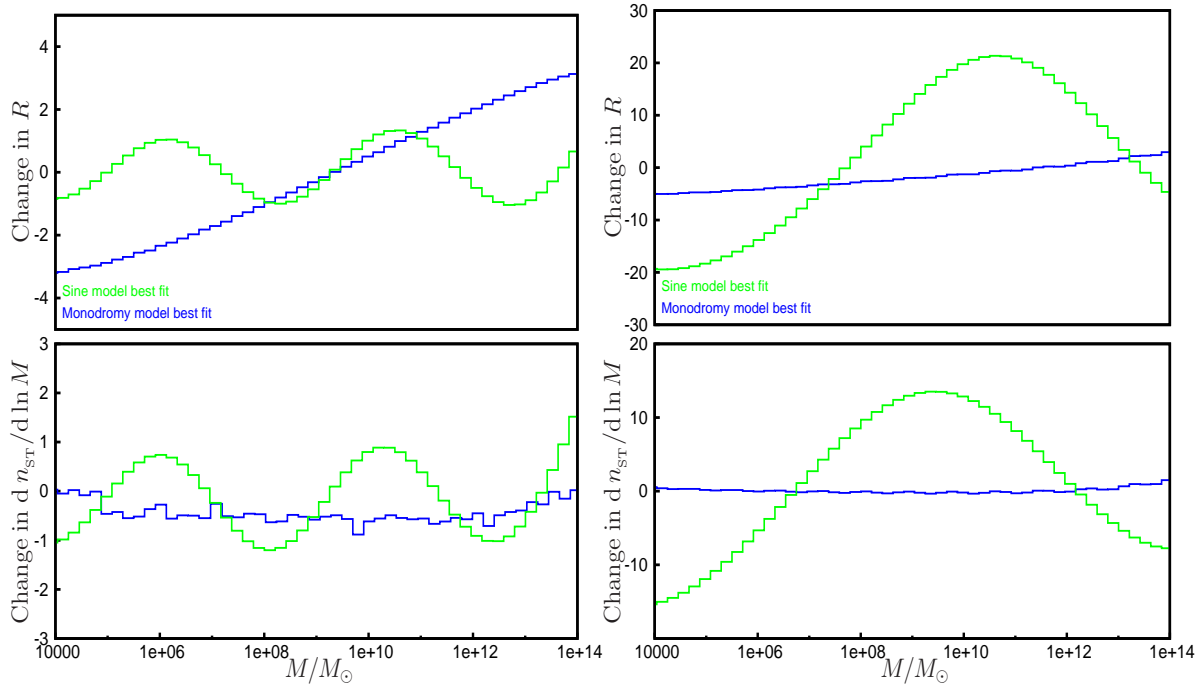


Figure 6.5: The percentage change in the formation rate of halos (in the Press-Schechter formalism, on top) and in their number density (in the Sheth-Tormen formalism, at the bottom) for the two inflationary models containing oscillatory terms with respect to the more conventional quadratic potential. The figures on the left correspond to the best fit values, while those on the right correspond to values chosen within the  $2\text{-}\sigma$  confidence contours of the parameters  $\alpha$  and  $\beta$ , determined from the joint constraints of the WMAP and SDSS data, as shown in Figure 6.2. In order to highlight the effects due to the primordial features, we have frozen the background parameters at the best fit values arrived at when the primordial spectrum is determined by the quadratic potential. We have then worked with the best fit values for the potential parameters to arrive at the figures on the left. We have plotted the percentage change in logarithmic mass bins, *i.e.*  $\Delta \log_{10}(M/M_{\odot})$ , of 0.2. It is clear that the features corresponding to the best fit values do not lead any substantial difference in either the number or the formation rates of the halos. However, note that the quadratic potential with superimposed sinusoidal oscillations leads to a 20% change in the number of halos formed when we choose to work with values of  $\alpha$  and  $\beta$  that lie within the  $2\text{-}\sigma$  contours.

In arriving at the plots, we have fixed the values of the parameter  $m$  and  $\lambda$  at their best fit values as shown in the Table 6.2, since these parameters do not play a role in altering the features in the spectrum. We have also chosen the value of  $\delta$  to be the best fit value for both the models. It is evident from the figure that, for the best fit values of the parameters, the change in the number density is completely negligible ( $\sim 2\%$ ). However, we find

that, for the case of the quadratic potential with sinusoidal modulation, the numbers can change by as much as 20% for values of the potential parameters  $\alpha$  and  $\beta$  that lie within  $2\text{-}\sigma$ . It should also be highlighted that the monodromy model does not seem to lead to the same extent of change in the number density and the rate of formation of halos, despite the fact that it produces fine oscillations in the primordial as well as the linear matter power spectra (*cf.* Figures 6.3 and 6.4). Actually, while the *unbinned* number density does indicate a 5-15% change, we find that, the change proves to be smaller when we bin the numbers in logarithmic mass bins, *i.e.*  $\Delta \log_{10}(M/M_{\odot})$ , of 0.2. Evidently, binning seems to average out the rapid oscillations, resulting in a smaller extent of change in the numbers.

## 6.5 Discussion

In this chapter, we have investigated the effects of primordial features on the matter power spectrum as well as the number of halos formed and their rate of formation. Similar work in this context [126] had suggested that a small change in the parameters describing the inflaton potential would lead to a drastic change in the number of halos formed. The earlier results and conclusions had been arrived at based on the inflationary perturbation spectrum evaluated using the slow roll approximation. In contrast, we have carried a complete and accurate numerical analysis. Further, we have made use of the Sheth-Tormen mass function (instead of the older Press-Schechter one) which is known to fit the data from the  $N$ -body simulations better. We have included the baryon acoustic oscillations in our analysis to have a more realistic comparison. Moreover, we have explicitly compared the potentials we have considered with the WMAP-7 and SDSS LRG DR7 datasets to arrive at the parameter space of interest. We find that, the best fit values for the potential parameters (with the background parameters kept fixed) lead to hardly any change in the number of halos formed when compared to the conventional quadratic potential that generates a nearly scale invariant primordial spectrum. However, partly consistent with the earlier result, we find that values for the potential parameters that lie within  $2\text{-}\sigma$  of the best fit values indeed lead to a reasonable change in the number of halos formed and in the formation rate. For instance, we find that, with superimposed sinusoidal modulations, the quadratic potential leads to as much as a 20% change in the halo number density and the rate of formation [135]. Needless to mention, the step of comparing the models against the data is crucial as this imposes real bounds on the extent of changes in the numbers involved. It is worthwhile to note that the inclusion of SDSS data reduces the maximum change in number density by about 10%, when compared to case

wherein one works with the parameters constrained by the WMAP data alone.

We would like to close this chapter with the following remarks. As we had pointed out before, while comparing with the SDSS data, we have not taken into account the non-linear effects on the matter power spectrum. It is for this reason that the theoretical curve had not fit the observational data well on small scales (*cf.* Figure 6.4). Clearly, a more complete analysis would involve modeling of the non-linear effects and their inclusion in evaluating the matter power spectrum [127]. For instance, it will be interesting to compare the results on the number of haloes formed in numerical simulations, evolved from primordial spectra with features, with the small scale data.



# Chapter 7

## Imprints of primordial non-Gaussianity in the Ly-alpha forest

In this chapter, we shall investigate the possibility of constraining primordial non-Gaussianity using the three dimensional (3D) bi-spectrum of the Ly- $\alpha$  forest. We should mention at the outset that, in this chapter, for convenience, we shall adopt a slightly different notation for a couple of quantities that we have already introduced. We will make clarifying remarks relating them to the earlier quantities, as we encounter them.

As we have discussed, the widely popular paradigm of slow roll inflation driven by a single canonical scalar field generates adiabatic perturbations which are largely Gaussian in nature and leads to a nearly scale invariant power spectrum [6, 7, 49]. Several theoretical predictions, including models leading to deviations from slow roll, however point towards mild to severe departure from Gaussianity [50, 51, 53]. Measuring the degree of non-Gaussianity is hence crucial towards discriminating between various inflationary scenarios thereby enhancing our understanding of the very early universe. It is assumed that on sub-Hubble scales the primordial gravitational potential, say,  $\Phi^P$ , is related to a Gaussian random field, say,  $\Phi_G$ , through a non-linear relation of the following form:

$$\Phi^P = \Phi_G + \frac{f_{\text{NL}}}{c^2} (\Phi_G^2 - \langle \Phi_G^2 \rangle), \quad (7.1)$$

with the departures from Gaussianity being quantified by the parameter  $f_{\text{NL}}$ . Two points need to be emphasized at this stage regarding this expression. Firstly, it should be noted that it is essentially the same as the relation (1.27) through which we had introduced the non-Gaussianity parameter  $f_{\text{NL}}$  earlier. The earlier relation was, in fact, arrived at by extending the above expression to the curvature perturbation, which, as is well known, can be related to the Bardeen potential through a suitable, constant factor [6, 7]. Secondly,

as we had pointed out in Section 1.7, we shall explicitly display the velocity of light  $c$  in this chapter for certain convenience.

In our analysis below, we shall assume that the parameter  $f_{\text{NL}}$  is scale independent, which, as should be evident from our discussion in Chapter 4, is a reasonable prediction for most inflationary models where non-Gaussianity is generated on super-Hubble scales. The value of  $f_{\text{NL}}$  obtained from slow roll inflation turns out to be very small  $\mathcal{O}(10^{-2})$  [49]. This implies that any detection of large  $f_{\text{NL}}$  shall rule out all canonical, single field, slow roll, inflationary models. However, as we have mentioned, the mean value of  $f_{\text{NL}}$  ( $26 \pm 140$  in the equilateral and  $32 \pm 21$  in the local limit, at  $1-\sigma$  confidence level) obtained from the WMAP data [19] seems to indicate large non-Gaussianity. Although the low Signal to Noise Ratio (SNR) in these results indicate that we are yet to detect the primordial non-Gaussianity, it is expected that data from Planck [20] shall lead to much tighter constraints on  $f_{\text{NL}}$  and the error is expected to come down to  $\Delta f_{\text{NL}} \simeq \pm 5$  in the local limit. Other than the CMB observations, a measurement of the bi-spectrum or the three point correlation function of the galaxy distribution is a standard alternative method to constrain primordial non-Gaussianity [136]. These probes however only provide weak bounds on the non-Gaussianity parameter as compared to the CMB observations, with SDSS, for example, being able to measure  $|f_{\text{NL}}|$  of the order of  $10^3$  or  $10^4$ .

In the post reionization epoch, small fluctuations of the neutral hydrogen (HI) density field in a predominantly ionized IGM leads to a series of distinct absorption features, the so-called Ly- $\alpha$  forest in the spectra of background quasars [66]. The Ly- $\alpha$  forest is a well established and powerful probe of cosmology [137, 138]. Traditional Ly- $\alpha$  studies have considered the power spectrum or bi-spectrum of the one dimensional transmitted flux field corresponding to the quasar line of sight [138]. This approach is reasonable when the angular density of quasars on the sky is low. The new generation of quasar surveys (the ongoing BOSS [67] and the future BigBOSS [68]) however promise to achieve a very high quasar density and cover large fractions of the sky. This has led to the possibility of measuring the 3D Ly- $\alpha$  power spectrum along multiple lines of sight [139]. It is worth noting here that the first hydro simulation of the Ly- $\alpha$  forest involving non-Gaussian scenarios has been carried out recently [140].

In this chapter, we shall investigate the possibility of constraining the non-Gaussianity parameter  $f_{\text{NL}}$  using the 3D Ly- $\alpha$  forest bi-spectrum. Similar to the power spectrum studies, the Ly- $\alpha$  flux distribution is assumed to be a biased tracer of the underlying matter field sampled along discrete sight lines. We shall explore the range of observational parameters for the constraints on  $f_{\text{NL}}$  from the 3D analysis to be competitive with the CMB

and the LSS studies.

## 7.1 Formalism

The post reionization matter overdensity field  $\Delta(\mathbf{x})$  in Fourier space ( $\Delta_{\mathbf{k}}$ ) can be related to the primordial gravitational potential ( $\Phi^{\text{P}}$ ) on sub-Hubble scales as follows:

$$\Delta_{\mathbf{k}}(z) = \mathcal{M}(k, z) \Phi_{\mathbf{k}}^{\text{P}}. \quad (7.2)$$

The function  $\mathcal{M}(k, z)$  is given by [cf. Eq. (1.30)]

$$\mathcal{M}(k, z) = -\frac{3}{5} \frac{k^2 T(k)}{\Omega_m H_0^2} D_+(z), \quad (7.3)$$

where, as we had discussed,  $T(k)$  denotes the matter transfer function, while  $D_+(z)$  represents the growth factor associated with the density fluctuations. In our analysis below, we shall make use of the conventional Bardeen-Bond-Kaiser-Szalay (BBKS) transfer function [141] and the cosmological parameters obtained from an MCMC analysis of the WMAP-7 data [85]. Actually, to obtain a more accurate result, a transfer function including the baryonic acoustic oscillations should be made use of. But, since our main motivation here is to arrive at bounds on the bi-spectrum and not to calculate exact numbers, the approximate BBKS transfer function proves to be sufficient. The power spectrum of the density field is defined as

$$\langle \Delta_{\mathbf{k}} \Delta_{\mathbf{k}'} \rangle = P(k) \delta^{(3)}(\mathbf{k} + \mathbf{k}'). \quad (7.4)$$

Clearly, the linear power spectrum of the density field is given by  $P(k) = \mathcal{M}^2(k, z) P_{\Phi}^{\text{P}}(k)$ , where  $P_{\Phi}^{\text{P}}$  denotes the primordial power spectrum of the gravitational potential such that  $P_{\Phi}^{\text{P}} = P_{\Phi_{\text{G}}} + \mathcal{O}(f_{\text{NL}}^2)$ . [Note that the matter power spectrum  $P(k)$  above is the same as the quantity  $P_{\text{M}}(k)$  defined in Eq. (1.30). We shall drop the subscript in this chapter for convenience.] The power spectrum  $P_{\Phi_{\text{G}}}$  of the Gaussian field  $\Phi_{\text{G}}$  shall be assumed to be featureless and scale invariant.

Following the power spectrum which is the two point correlator of the density field, the  $n$  point correlators can be defined as

$$\langle \Delta_{\mathbf{k}_1} \Delta_{\mathbf{k}_1} \dots \Delta_{\mathbf{k}_n} \rangle = \prod_{i=1}^n \mathcal{M}(k_i) \langle \Phi_{\mathbf{k}_1}^{\text{P}} \Phi_{\mathbf{k}_2}^{\text{P}} \dots \Phi_{\mathbf{k}_n}^{\text{P}} \rangle \quad (7.5)$$

and, using the definition above, we define the bi-spectrum as

$$\langle \Delta_{\mathbf{k}_1} \Delta_{\mathbf{k}_2} \Delta_{\mathbf{k}_3} \rangle = B(\mathbf{k}_1, \mathbf{k}_2, \mathbf{k}_3) \delta^{(3)}(\mathbf{k}_1 + \mathbf{k}_2 + \mathbf{k}_3). \quad (7.6)$$

We note that a wide class of inflationary models, including the simplest one comprising of a single inflaton field in a quadratic potential, introduces perturbations that are almost Gaussian and exhibit a power spectrum that is nearly scale invariant. It follows that in the realm of linear perturbation theory the bi-spectrum of the matter field arising from primordial non-Gaussianity is given by

$$B_{123}^L = \mathcal{M}(\mathbf{k}_1) \mathcal{M}(\mathbf{k}_2) \mathcal{M}(\mathbf{k}_3) B_{\Phi_G 123}, \quad (7.7)$$

where we use the notation  $123 \equiv (\mathbf{k}_1, \mathbf{k}_2, \mathbf{k}_3)$  and  $B_{\Phi_G}$  is given by

$$B_{\Phi_G 123} = \frac{2 f_{\text{NL}}}{c^2} [P_{\Phi_G}(\mathbf{k}_1) P_{\Phi_G}(\mathbf{k}_2) + \text{permutations}] + \mathcal{O}(f_{\text{NL}}^3). \quad (7.8)$$

We should point out that the bi-spectrum  $B_{\Phi_G 123}$  differs from the scalar bi-spectrum  $\mathcal{B}_s(\mathbf{k}_1, \mathbf{k}_2, \mathbf{k}_3)$  that we had defined earlier through Eq. (1.26) by the constant factor of  $(2\pi)^{9/2} (5/3) (2/3)^4$ . While the quantity  $(2\pi)^{9/2}$  arises simply due to different conventions, the remaining factors occur as a result of the relation between the curvature perturbation and the Bardeen potential.

Apart from the contribution to the bi-spectrum from primordial fluctuations, non-linear structure formation caused by gravitational instability leads to mode coupling and thereby induces additional non-Gaussianity. This is especially relevant when we use low redshift tracers to implicitly measure  $n$ -point functions of the matter density field. Upon using the second order perturbation theory, one finds that the additional contribution to the matter bi-spectrum is given by

$$B_{123}^{\text{NL}} = 2 F_2(\mathbf{k}_1, \mathbf{k}_2) P(\mathbf{k}_1) P(\mathbf{k}_2) + \text{permutations}, \quad (7.9)$$

and we shall adopt the form of  $F_2(\mathbf{k}_1, \mathbf{k}_2)$  to be [136]

$$F_2(\mathbf{k}_1, \mathbf{k}_2) = \frac{5}{7} + \frac{\hat{k}_1 \cdot \hat{k}_2}{2} \left( \frac{k_1}{k_2} + \frac{k_2}{k_1} \right) + \frac{2}{7} (\hat{k}_1 \cdot \hat{k}_2)^2. \quad (7.10)$$

Finally, the total matter bi-spectrum is a sum of the contributions to non-Gaussianity arising from the intrinsic primordial fluctuations and that generated by the non-linear evolution of an otherwise Gaussian field. Thus, we have  $B_{123} = B_{123}^L + B_{123}^{\text{NL}}$ , where we have ignored the possible contribution from the primordial tri-spectrum. We shall use  $B_{123}$  to obtain the 3D bi-spectrum of the Ly- $\alpha$  forest.

The Ly- $\alpha$  forest spectra are associated with gas distribution in voids or slightly over-dense regions. Noting that the astrophysical structures associated with the spectra are

only mildly non-linear, the transmitted flux  $\mathcal{F}$  through the Ly- $\alpha$  forest may be modeled by assuming that the gas traces the underlying dark matter distribution except on small scales where pressure plays an important role [138]. Further, it is believed that photo-ionization equilibrium that maintains the neutral fraction also leads to a power law temperature-density relation [142]. The fluctuating Gunn-Peterson approximation [143] incorporates these assumptions to relate the transmitted flux  $\mathcal{F}$  to the dark matter overdensity  $\delta$  as

$$\mathcal{F} = \bar{\mathcal{F}} \exp - [A(1 + \delta)^{2-0.7(\gamma-1)}], \quad (7.11)$$

where  $\bar{\mathcal{F}}$  is the mean transmitted flux. In arriving at the above equation, we have made use of the relation between the observed flux ( $\mathcal{F}$ ) and the optical depth ( $\tau$ ) which states,  $\mathcal{F} = \bar{\mathcal{F}} \exp(-\tau)$ . The optical depth is defined as  $\tau = A(1 + \delta)^\alpha$ , where  $\alpha = 2 - 0.7(\gamma - 1)$ . The quantity  $(\gamma - 1)$  is the slope of the temperature-density relation [142] and is defined through the logarithmic derivative of IGM density ( $\rho$ ) with respect to the IGM temperature ( $T$ ) as

$$\gamma - 1 = \frac{d \ln \rho}{d \ln T}. \quad (7.12)$$

We note that  $\gamma$  imprints the reionization history of the universe. The redshift dependent quantity  $A$  [144] depends on a number of parameters, such as the IGM temperature, photo-ionization rate and the cosmological parameters [138].

The fluctuations in the Ly- $\alpha$  transmitted flux is defined as,

$$\delta_{\mathcal{F}} = \frac{\mathcal{F}}{\bar{\mathcal{F}}} - 1. \quad (7.13)$$

On large scales it is reasonable to believe that the fluctuations in the transmitted flux  $\delta_{\mathcal{F}}$  may be expanded as

$$\delta_{\mathcal{F}} = b_1 \delta + \frac{1}{2} b_2 \delta^2, \quad (7.14)$$

where, it is assumed that the Ly- $\alpha$  forest spectrum has been smoothed over some suitably large length scale. This relation allows analytic computation of the statistical properties of  $\delta_{\mathcal{F}}$ . We note that corrections to this on small scales come from peculiar velocities, an effect we have not incorporated in our analysis for simplicity. At our fiducial redshift  $z = 2.5$ , we adopt an approximate  $(\bar{\mathcal{F}}, \gamma, A) \equiv (0.8, 1.5, 0.16)$  from the numerical simulations of Ly- $\alpha$  forest [145] and theoretical predictions [146]. We note however that these numbers are largely uncertain owing to inadequate modeling of the IGM. The bias  $b_1$ , for example, has a sensitive redshift dependence and may depend on the smoothing scale of the Ly- $\alpha$  spectra. Using the local bias model, the power spectrum  $P_{\mathcal{F}}(k)$  and bi-spectrum  $\mathcal{B}_{\mathcal{F}}$  of the

Ly- $\alpha$  forest flux fluctuations  $\delta_{\mathcal{F}}$  are given by

$$\begin{aligned} P_{\mathcal{F}}(k) &= b_1^2 P(k), \\ \mathcal{B}_{\mathcal{F}123} &= b_1^3 B_{123} + b_1^2 b_2 [P(\mathbf{k}_1) P(\mathbf{k}_2) + \text{permutations}]. \end{aligned} \quad (7.15)$$

The bi-spectrum of Ly- $\alpha$  flux is hence completely modeled using the three parameters  $(f_{\text{NL}}, b_1, b_2)$ .

We shall now set up the Fisher matrix for constraining  $f_{\text{NL}}$  using the Ly- $\alpha$  bi-spectrum. Following the formulation described in Ref. [136], we shall define the bi-spectrum estimator as

$$\hat{\mathcal{B}}_{\mathcal{F}123} = \frac{V_{\mathcal{f}}}{V_{123}}, \int_{\mathbf{k}_1} d^3 \mathbf{q}_1 \int_{\mathbf{k}_2} d^3 \mathbf{q}_2 \int_{\mathbf{k}_3} d^3 \mathbf{q}_3 \delta_{\text{D}}(\mathbf{q}_{123}) \Delta_{\mathcal{F}}^{\circ}(\mathbf{k}_1) \Delta_{\mathcal{F}}^{\circ}(\mathbf{k}_2) \Delta_{\mathcal{F}}^{\circ}(\mathbf{k}_3). \quad (7.16)$$

Here  $\mathbf{q}_{123} = \mathbf{q}_1 + \mathbf{q}_2 + \mathbf{q}_3$ , and the integrals are performed over the  $q_i$ -intervals  $(k_i - \delta k/2, k_i + \delta k/2)$ . Also,  $V_{\mathcal{f}} = (2\pi)^3/V$ , where  $V$  is the survey volume. The survey volume is given by

$$V_{123} = \int_{\mathbf{k}_1} d^3 \mathbf{q}_1 \int_{\mathbf{k}_2} d^3 \mathbf{q}_2 \int_{\mathbf{k}_3} d^3 \mathbf{q}_3 \delta_{\text{D}}(\mathbf{q}_{123}) = 8\pi^2 k_1 k_2 k_3 \delta k^3. \quad (7.17)$$

The quantities  $\Delta_{\mathcal{F}}^{\circ}(k_i)$  appearing in the Eq. (7.16) denotes the ‘observed’ Ly- $\alpha$  flux fluctuations in Fourier space. The observed quantity  $\delta_{\mathcal{F}}^{\circ}(\mathbf{r})$  is given by the continuous field  $\delta_{\mathcal{F}}(\mathbf{r})$  sampled along skewers corresponding to line of sight to bright quasars. We therefore have

$$\delta_{\mathcal{F}}^{\circ}(\mathbf{r}) = \delta_{\mathcal{F}}(\mathbf{r}) \rho(\mathbf{r}), \quad (7.18)$$

where the sampling window function  $\rho(\mathbf{r})$  is defined as

$$\rho(\mathbf{r}) = \mathcal{N} \frac{\sum_a w_a \delta_{\text{D}}^2(\mathbf{r}_{\perp} - \mathbf{r}_{\perp a})}{\sum_a w_a}, \quad (7.19)$$

and  $\mathcal{N}$  is a normalization factor such that  $\int dV \rho(\mathbf{r}) = 1$ . The summation extends up to  $N_Q$ , the total number of quasar skewers in the field which are assumed to be distributed with sky locations  $\mathbf{r}_{\perp a}$ . The weights  $w_a$  introduced in  $\rho(\mathbf{r})$  are in general related to the pixel noise and can be chosen with a posteriori criterion of minimizing the variance. The assumption is, the line of sight direction is continuous and the survey measures the Ly- $\alpha$  forest in  $\rho(\mathbf{r})$  spatial window. In Fourier space, we then have

$$\Delta_{\mathcal{F}}^{\circ}(\mathbf{k}) = \tilde{\rho}(\mathbf{k}) \otimes \Delta_{\mathcal{F}}(\mathbf{k}) + \Delta_{\mathcal{F}\text{noise}}(\mathbf{k}), \quad (7.20)$$

where  $\tilde{\rho}$  is the Fourier transform of  $\rho$ , and  $\Delta_{\mathcal{F}\text{noise}}(\mathbf{k})$  denotes a possible noise term.

If the bi-spectrum covariance matrix is diagonal which implies that no correlation exists between different triangle shapes, the simple variance of the estimator  $\hat{\mathcal{B}}_{\mathcal{F}}$  can be calculated as

$$\Delta \hat{\mathcal{B}}_{\mathcal{F}}^2 = \langle \hat{\mathcal{B}}_{\mathcal{F}}^2 \rangle - \langle \hat{\mathcal{B}}_{\mathcal{F}} \rangle^2. \quad (7.21)$$

This is given at the lowest order by

$$\Delta \hat{\mathcal{B}}_{\mathcal{F}}^2 = \frac{V_f}{V_{123}} s P_{\mathcal{F}}^{\text{Tot}}(\mathbf{k}_1) P_{\mathcal{F}}^{\text{Tot}}(\mathbf{k}_2) P_{\mathcal{F}}^{\text{Tot}}(\mathbf{k}_3), \quad (7.22)$$

where  $s = 6, 1$  for equilateral and scalene triangles respectively and  $P_{\mathcal{F}}^{\text{Tot}}(k)$  is the total power spectrum of Ly- $\alpha$  flux given by

$$P_{\mathcal{F}}^{\text{Tot}}(\mathbf{k}) = P_{\mathcal{F}}(\mathbf{k}) + P_{\mathcal{F}}^{\text{1D}}(k_{\parallel}) P_W + N_{\mathcal{F}}. \quad (7.23)$$

The quantity  $P_{\mathcal{F}}^{\text{1D}}(k_{\parallel})$  is the usual one-dimensional (1D) flux power spectrum [138] or the line of sight power spectrum corresponding to individual spectra given by

$$P_{\mathcal{F}}^{\text{1D}}(k_{\parallel}) = (2\pi)^{-2} \int d^2 \mathbf{k}_{\perp} P_{\mathcal{F}}(\mathbf{k}), \quad (7.24)$$

and  $P_W$  denotes the power spectrum of the window function. The quantity  $N_{\mathcal{F}}$  denotes the effective noise power spectra for the Ly- $\alpha$  observations. The term  $P_{\mathcal{F}}^{\text{1D}}(k_{\parallel}) P_W$  referred to as the ‘aliasing’ term, is similar to the shot noise in galaxy surveys and quantifies the discreteness of the 1D Ly- $\alpha$  skewers. It has been shown that a uniform weighing scheme suffices when most of the spectra are measured with a sufficiently high SNR [139]. This gives  $P_W = 1/\bar{n}$ , where  $\bar{n}$  is the two dimensional (2D) density of quasars ( $\bar{n} = N_Q/\mathcal{A}$ , where  $\mathcal{A}$  is the area of the observed field of view or the survey area). We assume that the variance  $\sigma_{\mathcal{F}N}^2$  of the pixel noise contribution to  $\delta_{\mathcal{F}}$  is the same across all the quasar spectra, whereby we have  $N_{\mathcal{F}} = \sigma_{\mathcal{F}N}^2/\bar{n}$  for its noise power spectrum. In arriving at Eq. (7.23), we have ignored the effect of quasar clustering. In reality, the distribution of quasars is expected to exhibit clustering [147]. However, for the quasar surveys under consideration, the Poisson noise dominates over the clustering and the latter may be ignored.

The Fisher matrix for a set of parameters  $p_i$  is constructed as

$$F_{ij} = \sum_{\mathbf{k}_1=k_{\min}}^{k_{\max}} \sum_{\mathbf{k}_2=k_{\min}}^{\mathbf{k}_1} \sum_{\mathbf{k}_3=\tilde{k}_{\min}}^{\mathbf{k}_2} \frac{1}{\Delta \hat{\mathcal{B}}_{\mathcal{F}}^2} \frac{\partial \mathcal{B}_{\mathcal{F}123}}{\partial p_i} \frac{\partial \mathcal{B}_{\mathcal{F}123}}{\partial p_j}, \quad (7.25)$$

where  $\tilde{k}_{\min} = \max(k_{\min}, |\mathbf{k}_1 - \mathbf{k}_2|)$  and the summations are performed using  $\delta k = k_{\min}$ . Assuming the likelihood function for  $p_i$  to be a Gaussian, the errors in  $p_i$  is given by the Cramer-Rao bound  $\sigma_i^2 = F_{ii}^{-1}$ . We have used this to investigate the power of a Ly- $\alpha$  survey to constrain  $f_{\text{NL}}$ .

## 7.2 Results

We consider quasars in the red-shift range  $z = 2$  to  $3$  since the peak in redshift distribution of quasars occur in this range [148]. We note that for a given quasar at redshift  $z = z_Q$ , the proximity effect will not allow the spectrum to be measured in the region  $10,000 \text{ km s}^{-1}$  blue-wards of the Ly- $\alpha$  emission and only the region which is at least  $1,000 \text{ km s}^{-1}$  red-ward of the quasar's Ly- $\beta$  and O-VI lines are considered to avoid the possible confusion with these lines. We have chosen  $z = 2.5$  as our fiducial redshift for the subsequent analysis. We note here that all the parameters involved in the modeling the Ly- $\alpha$  forest, have direct or indirect redshift dependence.

A Ly- $\alpha$  forest survey towards measurement of power spectrum or bi-spectrum is characterized by the survey volume, pixel noise in the spectra and the number density of the quasar skewers. The constraining power of the survey shall depend directly on the choice of these parameters. In the cosmic variance limit, the minimum  $f_{\text{NL}}$  that can be measured depends on the number of Fourier modes in the survey volume  $V$  given by  $N_k = 4\pi/3 k_{\text{max}}^2 V / (2\pi)^3$ . Clearly the minimum detectable  $f_{\text{NL}}$  is a function of  $k_{\text{max}}$  and  $k_{\text{min}}$ . The noise power spectrum  $N_{\mathcal{F}}$  is given by

$$N_{\mathcal{F}} = \bar{\mathcal{F}}^{-2} [S/N]_{\Delta x}^{-2} (\Delta x / 1 \text{ Mpc}), \quad (7.26)$$

where  $[S/N]_{\Delta x}$  is the SNR for a spectrum smoothed to a resolution  $\Delta x$ . We quote  $[S/N]$  here for  $1 \text{ \AA}$  pixels. The main source of noise to the 3D power spectrum comes from the aliasing noise term and one requires a very high density of quasars in the field of view for this term to be sub-dominant.

The bi-spectrum SNR depends on the triangle configurations considered to evaluate it. In this analysis, we have used the simplest equilateral configurations characterized by just a single Fourier mode. This over estimates the noise by at least a factor of  $\sim 2.45$  as compared to the case with arbitrary triangles. In the equilateral limit the 3D Ly- $\alpha$  bi-spectrum can be written as

$$\mathcal{B}_{\mathcal{F}}(k) = P(k)^2 \left[ \frac{a_1}{\mathcal{M}(k)} + a_2 \right], \quad (7.27)$$

where  $a_1 = 6b_1^3 f_{\text{NL}}/c^2$  and  $a_2 = 6b_1^3 F_2 + 3b_1^2 b_2$ . Only two parameters are sufficient to model the bi-spectrum instead of three parameters  $(f_{\text{NL}}, b_1, b_2)$  for the general case. We use the fiducial values  $(f_{\text{NL}}, b_1, b_2) \equiv (0, -0.15, -0.075)$  and choose  $f_{\text{NL}}$  and  $b_1$  to be the free parameters for the Fisher analysis. We recall that in our modeling of the Ly- $\alpha$  forest

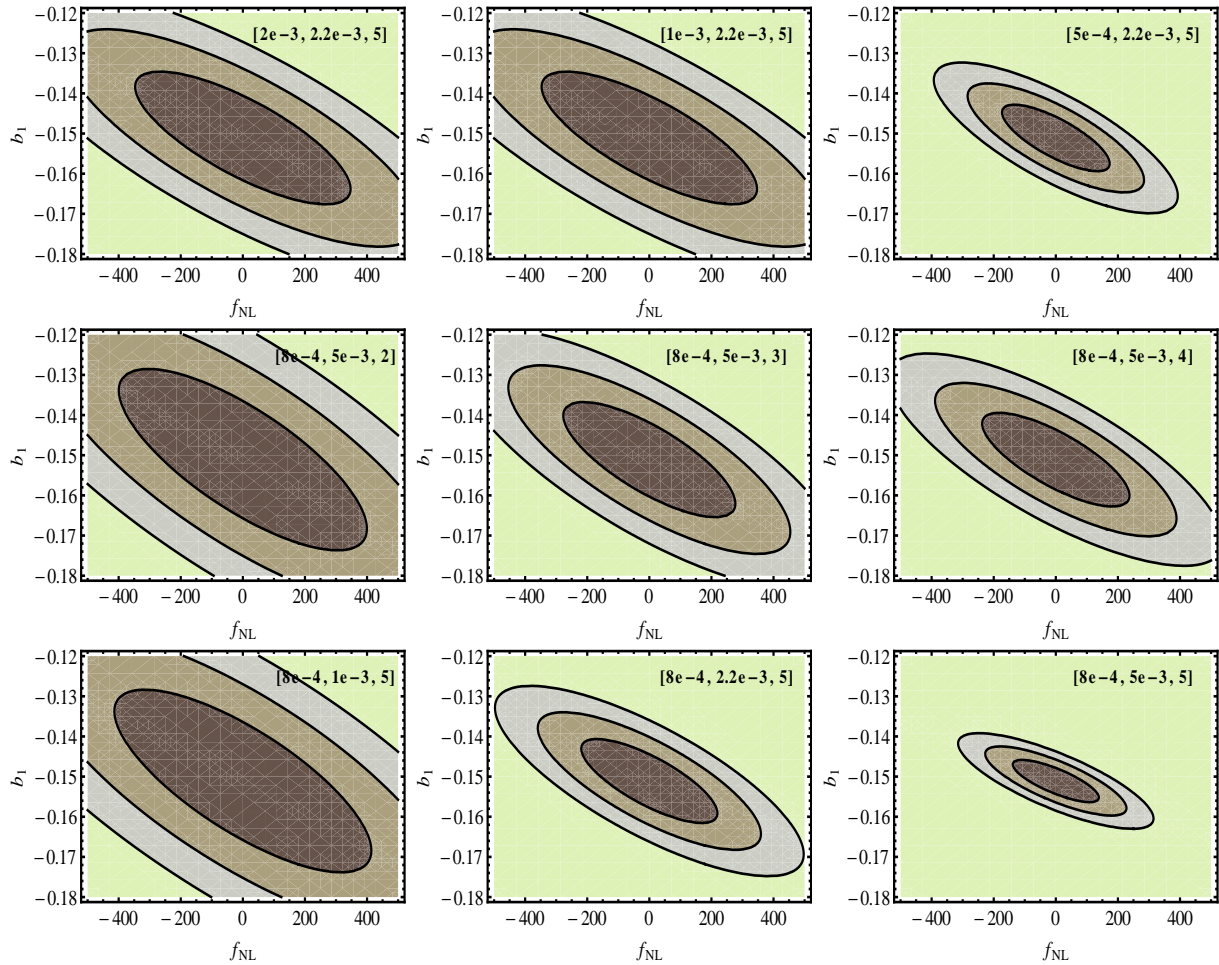


Figure 7.1: The 68.3%, 95.4% and 99.8% likelihood confidence contours for the parameters  $(f_{\text{NL}}, b_1)$ . Shown in the figure are the values  $(k_{\text{min}}, \bar{n}, S/N)$  used to compute the Fisher matrix.

we used the parameters  $(\bar{\mathcal{F}}, A, \gamma)$ . The parameter  $\bar{\mathcal{F}}$  does not appear in  $\delta_{\mathcal{F}}$  and there is degeneracy between the parameters  $A$  and  $\gamma$  which only appears as a product in  $b_1$ . Changing  $b_1$  hence amounts to changing either or both  $A$  and  $\gamma$ .

We assume that the likelihood function is a bivariate Gaussian which yields the confidence ellipses shown in Figure 7.1. The tilt of the error ellipses indicate correlation between the parameters. We quantify this using the correlation coefficient  $r$ , defined as

$$r = F_{12}^{-1} / \sqrt{F_{11}^{-1} F_{22}^{-1}}. \quad (7.28)$$

For the range of parameters chosen we find that this is roughly constant  $r \sim -0.7$ .

In the ideal situation of full sky coverage and negligible Poisson noise we find that

$k_{\min}$ (Mpc <sup>-1</sup> )	$\bar{n}$ (Mpc <sup>-2</sup> )	$S/N$	$\Delta f_{\text{NL}}$	$\Delta b_1$
$2 \times 10^{-3}$	$2.2 \times 10^{-3}$	5	228.84	$1.1 \times 10^{-2}$
$1 \times 10^{-3}$	$2.2 \times 10^{-3}$	5	161.81	$7.7 \times 10^{-3}$
$5 \times 10^{-4}$	$2.2 \times 10^{-3}$	5	114.42	$5.5 \times 10^{-3}$
$8 \times 10^{-4}$	$1.0 \times 10^{-3}$	5	272.95	$1.5 \times 10^{-2}$
$8 \times 10^{-4}$	$2.2 \times 10^{-3}$	5	144.73	$6.9 \times 10^{-3}$
$8 \times 10^{-4}$	$5.0 \times 10^{-3}$	5	91.65	$3.5 \times 10^{-3}$
$8 \times 10^{-4}$	$2.2 \times 10^{-3}$	2	263.52	$1.5 \times 10^{-2}$
$8 \times 10^{-4}$	$2.2 \times 10^{-3}$	3	182.83	$9.5 \times 10^{-3}$
$8 \times 10^{-4}$	$2.2 \times 10^{-3}$	4	156.56	$7.7 \times 10^{-3}$
Ideal case $5 \times 10^{-4}$	1	5	23.72	$2.1 \times 10^{-4}$

Table 7.1: The bounds on  $(f_{\text{NL}}, b_1)$  obtained from a Fisher analysis for various combinations of  $(k_{\min}, \bar{n}, S/N)$ .

$\Delta f_{\text{NL}} \sim 23$  in the equilateral limit. We tabulate our results for varying sky coverage [ $k_{\min}^{-3} = V/(2\pi)^3$ ], Poisson noise ( $\sim 1/\bar{n}$ ) and pixel noise ( $S/N$ ) in Table 7.1. As expected we have tighter constraints on  $(f_{\text{NL}}, b_1)$  with increasing survey volume,  $\bar{n}$  and  $S/N$ . The values of the survey parameters chosen are reasonable and achievable by future Ly- $\alpha$  surveys. Exploiting the entire sky coverage of SDSS we find that one can obtain a bound on  $f_{\text{NL}} \sim 100$  (in the equilateral configuration) for a survey with  $\bar{n} = 5 \times 10^{-3} \text{ Mpc}^{-2}$  when the spectra are measured at 5- $\sigma$  level [149].

Our analysis has largely focused on the equilateral configuration. However we find that the Cramer-Rao bound for  $f_{\text{NL}}$  in the squeezed limit ( $k_3 \ll \min(k_1, k_2)$ ) turns out to be about 40–100 for the cases we have considered. The case of arbitrary triangular configuration is to be addressed in our future work [150]. However, our preliminary estimates show us that we may constrain  $f_{\text{NL}} \sim 1$  in an ideal environment. For example using  $S/N \sim 5$ ,  $\bar{n} \sim 10^{-3} \text{ Mpc}^{-3}$  and  $k_{\min} \sim 10^{-3} \text{ Mpc}^{-1}$ , we have  $\Delta f_{\text{NL}} \sim 5$  in the case of arbitrary triangles, which is competitive with the CMB and the LSS studies. We should mention that we have used the non-linear bias parameter  $b_2$  as a variable of the Fisher matrix analysis in this case.

## 7.3 Conclusions

To conclude, we emphasize that it is possible to put stringent bounds on primordial non-Gaussianity from the measured 3D bi-spectrum of the Ly- $\alpha$  forest along multiple lines of sight and thereby constrain various inflationary scenarios. Our analytic predictions indicate that such studies with future Ly- $\alpha$  surveys may be useful while performing a joint analysis using other data sets involving the CMB or LSS.



# Chapter 8

## Summary and outlook

In this final chapter, after a rapid summary of the main conclusions of this thesis, we shall outline a few of the issues that arise as a logical consequence of the problems investigated here and require to be followed up.

### 8.1 Summary

In this thesis work, we were primarily interested on two aspects, *viz.* features in the primordial spectrum and non-Gaussianities.

In the context of primordial features, we had focussed on investigating the extent to which the recent CMB data permitted the presence of local as well as non-local features in the inflationary perturbation spectrum. We had found that localized features such a burst of oscillations generated due to a step in inflationary potentials leads to a better fit to the data than the more conventional featureless and nearly scale invariant primordial spectrum [85]. Interestingly, we had also found that certain repeated patterns, such as persistent modulations, which are produced due to a resonant phenomenon occurring in potentials with oscillatory terms, also result in an improved fit to the data [101]. Preliminary analysis suggest that ongoing missions such as Planck [20] will be able to help us arrive at stronger constraints on such features [87, 101].

It has been increasingly recognized that the detection of non-Gaussianities, in particular, a non-zero bi-spectrum (*i.e.* the three point correlator of the curvature perturbation) can act as a powerful discriminator amongst the plethora of inflationary models that are consistent with the data at the level of the power spectrum. With the aim of studying non-Gaussianities generated in inflationary models that lead to features in the power spectrum, using the Maldacena formalism, we had developed a numerical code to effi-

ciently evaluate the scalar bi-spectrum. After crosschecking the code for its correctness against certain analytical results that are available, we had utilized the code to evaluate the bi-spectrum in the equilateral limit in inflationary models resulting in features in the primordial spectrum. With the specific aim of examining the discriminatory power of the non-Gaussianity parameter  $f_{\text{NL}}$ , we had evaluated the quantity in classes of models that lead to similar features in the scalar power spectrum. We found that, as one would have expected, the power of the parameter  $f_{\text{NL}}$  to discriminate between the inflationary models is largely determined by the background dynamics. We showed that, while  $f_{\text{NL}}$  can act as a powerful discriminator in certain classes of models, its ability to discriminate between models proves to be rather limited in other classes.

We had also studied the effects of preheating on the scalar bi-spectrum. Assuming that the inflationary potentials behave quadratically around their minima and, utilizing the Maldacena formalism, we had shown that the bi-spectra generated during inflation largely remains unaffected due to preheating in single field models. In fact, we had shown that the contribution to the non-Gaussianity parameter  $f_{\text{NL}}$  during preheating turns out to be extraordinarily small. This conclusion complements similar results that were available in the case of the power spectrum.

The latter part of the thesis had concentrated on studying the imprints of primordial features and non-Gaussianities on the LSS. In this context, we had investigated the effects of primordial features on the formation of halos. Interestingly, we had found that features such as those generated in certain inflationary potentials containing oscillatory terms can lead to a reasonable extent (of about 20%) of change in the number of halos formed. We had also considered the possibility of being able to constrain the non-Gaussianity parameter  $f_{\text{NL}}$  using the 3D bi-spectrum of the Ly- $\alpha$  forest along multiple lines of sight. We had argued that, with a high density of quasars set to observed by surveys such as BOSS [67] and BigBOSS [68], the constraints on  $f_{\text{NL}}$  from the 3D bi-spectrum of the Ly- $\alpha$  forest can become comparable with the constraints arrived at from the CMB and LSS data.

## 8.2 Outlook

We shall now list what we believe are a few issues that are a natural outcome of the methods adopted and the problems analyzed in this thesis.

As far as features in the primordial spectrum are concerned, we had earlier mentioned the point that, despite the fact that specific features lead to an improved fit to the data, the complete statistical significance of such features still remain to be understood satis-

factorily [69, 70]. Rather than the frequentists approach adopted here, it would be worthwhile to carry out a complete Bayesian analysis of the inflationary models leading to features [47]. Moreover, most of the efforts while considering features in the inflationary spectrum have focussed on models involving the canonical scalar field, and it is imperative that such efforts are also extended to non-canonical fields [77, 72, 85]. It will also be worthwhile to explore models that admit departures from slow roll in a more natural fashion, such as those involving more than one scalar field [76, 88, 89].

The numerical analysis of the scalar bi-spectrum in inflationary models leading to features requires to be extended to non-equilateral configurations. Also, the scope of the code itself needs to be enlarged to take into account non-canonical models of the scalar field. Using the code, it will be interesting to investigate if the various consistency relations hold true even in the most general scenarios [53, 110, 111]. Moreover, while we have established that, based on the Maldacena formalism, the scalar bi-spectrum remains unaffected due to preheating, it is important that the formalism and the results be extended to the epoch of reheating as the transfer of energy from the inflaton to radiation takes place because of their mutual coupling. Needless to add, these issues need to be understood satisfactorily if we are to be able to make use of the observations of non-Gaussianities in the CMB to arrive at constraints on the inflationary models.

Lastly, we believe that it will be a worthwhile exercise to extend our effort of utilizing the 3D bi-spectrum of the Ly- $\alpha$  forest along multiple lines of sight to constrain the non-Gaussianity parameter  $f_{\text{NL}}$  for arbitrary triangular configurations of the primordial bi-spectrum. More specifically, it may be also possible to forecast the constraints that one can expect to arrive at from surveys such as BOSS [67] and BigBOSS [68].

We are presently investigating some of these issues.



# Bibliography

- [1] See, <http://magnum.anu.edu.au/~TDFgg/>.
- [2] M. Colless *et al.*, arXiv:astro-ph/0306581v1.
- [3] See, <http://www.sdss.org/>.
- [4] K. Abazajian *et al.*, *Astrophys. J. Suppl.* **182**, 543 (2009).
- [5] P. Sarkar, J. Yadav, B. Pandey and S. Bharadwaj, *Mon. Not. Roy. Astron. Soc.* **399**, L128 (2009).
- [6] E. W. Kolb and M. S. Turner, *The Early Universe* (Addison-Wesley, Redwood City, California, 1990); S. Dodelson, *Modern Cosmology* (Academic Press, San Diego, U.S.A., 2003); V. F. Mukhanov, *Physical Foundations of Cosmology* (Cambridge University Press, Cambridge, England, 2005); S. Weinberg, *Cosmology* (Oxford University Press, Oxford, England, 2008); R. Durrer, *The Cosmic Microwave Background* (Cambridge University Press, Cambridge, England, 2008); D. H. Lyth and A. R. Liddle, *The Primordial Density Perturbation* (Cambridge University Press, Cambridge, England, 2009); P. Peter, J-P. Uzan and J. Brujic, *Primordial Cosmology* (Oxford University Press, Oxford, England, 2009); H. Mo, F. v. d. Bosch and S. White, *Galaxy Formation and Evolution* (Cambridge University Press, Cambridge, England, 2010).
- [7] H. Kodama and M. Sasaki, *Prog. Theor. Phys. Suppl.* **78**, 1 (1984); V. F. Mukhanov, H. A. Feldman and R. H. Brandenberger, *Phys. Rep.* **215**, 203 (1992); J. E. Lidsey, A. Liddle, E. W. Kolb, E. J. Copeland, T. Barreiro and M. Abney, *Rev. Mod. Phys.* **69**, 373 (1997); D. H. Lyth and A. Riotto, *Phys. Rep.* **314**, 1 (1999); A. Riotto, arXiv:hep-ph/0210162; J. Martin, *Braz. J. Phys.* **34**, 1307 (2004); *Lect. Notes Phys.* **669**, 199 (2005); *Lect. Notes Phys.* **738**, 193 (2008); B. Bassett, S. Tsujikawa and D. Wands, *Rev. Mod. Phys.* **78**, 537 (2006); A. D. Linde, *Lect. Notes Phys.* **738**, 1 (2008); W. H.

## BIBLIOGRAPHY

---

- Kinney, arXiv:0902.1529 [astro-ph.CO]; L. Sriramkumar, *Curr. Sci.* **97**, 868 (2009); D. Baumann, arXiv:0907.5424v1 [hep-th].
- [8] See, <http://lambda.gsfc.nasa.gov/product/cobe/>.
- [9] D. J. Fixsen, E. S. Cheng, J. M. Gales, J. C. Mather, R. A. Shafer and E. L. Wright, *Astrophys. J.* **473**, 576( 1996).
- [10] P. Ade *et al.*, *Astrophys. J.* **674**, 22 (2008).
- [11] M. L. Brown *et al.*, *Astrophys. J.* **705**, 978 (2009).
- [12] See, <http://cosmology.berkeley.edu/group/swlh/acbar/>.
- [13] C. L. Reichardt *et al.*, *Astrophys. J.* **694**, 1200 (2009).
- [14] See, <http://www.physics.princeton.edu/act/>.
- [15] J. Dunkley *et al.*, *Astrophys. J.* **739**, 52 (2011).
- [16] See, <http://map.gsfc.nasa.gov/>.
- [17] H. V. Peiris *et al.*, *Astrophys. J. Suppl.* **148**, 213 (2003).
- [18] J. Dunkley *et al.*, *Astrophys. J. Suppl.* **180**, 306 (2009); E. Komatsu *et al.*, *Astrophys. J. Suppl.* **180**, 330 (2009).
- [19] D. Larson *et al.*, *Astrophys. J. Suppl.* **192**, 16 (2011); E. Komatsu *et al.*, *Astrophys. J. Suppl.* **192**, 18 (2011).
- [20] See, <http://www.sciops.esa.int/PLANCK/>.
- [21] See, <http://www.caltech.edu/H0kp/>.
- [22] J. R. Mould *et al.*, *Astrophys. J.* **529**, 786 (2000).
- [23] J. Yang, M. S. Turner, G. Steigman, D. N. Schramm and K. A. Olive, *Astrophys. J.* **281**, 493 (1984).
- [24] K. A. Olive, G. Steigman and T. P. Walker, *Phys. Rep.* **333**, 389 (2000).
- [25] See, <http://supernova.lbl.gov/>.
- [26] S. Perlmutter *et al.*, *Astrophys. J.* **517**, 565 (1999).

- [27] See, <http://cfht.hawaii.edu/SNLS/>.
- [28] J. Guy *et al.*, *Astron. Astrphys.* **523**, A7 (2010).
- [29] M. Sullivan *et al.*, *Astrophys. J.* **737**, 102 (2011).
- [30] A. A. Starobinsky, *JETP Lett.* **30**, 682 (1979); *Phys. Lett. B* **91**, 99 (1980); D. Kazanas, *Astrophys. J.* **241**, L59 (1980); K. Sato, *Mon. Not. Roy. Astron. Soc.* **195**, 467 (1981); A. Guth, *Phys. Rev. D* **23**, 347 (1981); A. D. Linde, *Phys. Lett. B* **108**, 389 (1982); *Phys. Lett. B* **114**, 431 (1982); *Phys. Rev. Lett.* **48**, 335 (1982); A. Albrecht and P. Steinhardt, *Phys. Rev. Lett.* **48**, 1220 (1982).
- [31] V. F. Mukhanov and G. V. Chibisov, *Sov. Phys. JETP Lett.* **33**, 532 (1981); S. W. Hawking, *Phys. Lett. B* **115**, 295 (1982); A. A. Starobinsky, *Phys. Lett. B* **117**, 175 (1982); A. Guth and S.-Y. Pi, *Phys. Rev. Lett.* **49**, 1110 (1982).
- [32] S. Dodelson and L. Hui, *Phys. Rev. Letts.* **91**, 131301 (2003); A. R. Liddle and S. M. Leach, *Phys. Rev. D* **68**, 103503 (2003).
- [33] P. J. Steinhardt and M. S. Turner, *Phys. Rev. D* **29**, 2162 (1984); D. S. Salopek and J. R. Bond, *Phys. Rev. D* **42**, 3936 (1990); A. R. Liddle and D. H. Lyth, *Phys. Letts. B* **291**, 391 (1992); A. R. Liddle, P. Parsons and J. D. Barrow, *Phys. Rev. D* **50**, 7222 (1994); D. J. Schwarz, C. A. Terrero-Escalante and A. A. Garcia, *Phys. Lett. B* **517**, 243 (2001); S. M. Leach, A. R. Liddle, J. Martin and D. J. Schwarz, *Phys. Rev. D* **66**, 023515 (2002).
- [34] J. Bardeen, *Phys. Rev. D* **22**, 1882 (1980); J. M. Stewart, *Class. Quantum Grav.* **7**, 1169 (1990).
- [35] L. P. Grishchuk, *Sov. Phys. JETP* **40**, 409 (1974); A. A. Starobinsky, *Sov. Phys. JETP Lett.* **30**, 682 (1979); V. A. Rubakov, M. V. Sazhin and A. V. Veryaskin, *Phys. Lett. B* **115**, 189 (1982).
- [36] C. Gordon, D. Wands, B. A. Bassett and R. Maartens, *Phys. Rev. D* **63**, 023506 (2001).
- [37] A. J. Christopherson and K. A. Malik, *Phys. Lett. B* **675**, 159 (2009).
- [38] S. Unnikrishnan and L. Sriramkumar, *Phys. Rev. D* **81**, 103511 (2010); F. Arroja and M. Sasaki, *Phys. Rev. D* **81**, 107301 (2010).

- [39] V. N. Lukash, *Sov. Phys. JETP* **52**, 807 (1980); D. H. Lyth, *Phys. Rev. D* **31**, 1792 (1985).
- [40] V. S. Mukhanov, *JETP Lett.* **41**, 493 (1985); M. Sasaki, *Prog. Theor. Phys.* **76**, 1036 (1986).
- [41] T. Bunch and P. C. W. Davies, *Proc. Roy. Soc. Lond. A* **360**, 117 (1978).
- [42] E. D. Stewart and D. H. Lyth, *Phys. Letts. B* **302**, 171 (1993); J. C. Hwang and H. Noh, *Phys. Rev. D* **54**, 1460 (1996).
- [43] See, <http://camb.info/>.
- [44] A. Lewis, A. Challinor and A. Lasenby, *Astrophys. J.* **538**, 473 (2000).
- [45] See, <http://cosmologist.info/cosmomc/>.
- [46] A. Lewis and S. Bridle, *Phys. Rev. D* **66**, 103511 (2002).
- [47] J. Martin, C. Ringeval and R. Trotta, *Phys. Rev. D* **83**, 063524 (2011).
- [48] E. F. Bunn, A. R. Liddle and M. J. White, *Phys. Rev. D* **54**, R5917 (1996).
- [49] J. Maldacena, *JHEP* **0305**, 013 (2003).
- [50] N. Bartolo, E. Komatsu, S. Matarrese, and A. Riotto, *Phys. Rep.* **402**, 103 (2004).
- [51] D. Seery and J. E. Lidsey, *JCAP* **0506**, 003 (2005); X. Chen, *Phys. Rev. D* **72**, 123518 (2005); X. Chen, M.-x. Huang, S. Kachru and G. Shiu, *JCAP* **0701**, 002 (2007); D. Langlois, S. Renaux-Petel, D. A. Steer and T. Tanaka, *Phys. Rev. Lett.* **101**, 061301 (2008); *Phys. Rev. D* **78**, 063523 (2008).
- [52] X. Chen, *Adv. Astron.* **2010**, 638979 (2010).
- [53] X. Chen, R. Easther and E. A. Lim, *JCAP* **0706**, 023 (2007); *JCAP* **0804**, 010 (2008); S. Hotchkiss and S. Sarkar, *JCAP* **1005**, 024 (2010); S. Hannestad, T. Haugbolle, P. R. Jarnhus and M. S. Sloth, *JCAP* **1006**, 001 (2010); R. Flauger and E. Pajer, *JCAP* **1101**, 017 (2011); P. Adshead, W. Hu, C. Dvorkin and H. V. Peiris, *Phys. Rev. D* **84**, 043519 (2011); P. Adshead, C. Dvorkin, W. Hu and E. A. Lim, *Phys. Rev. D* **85**, 023531 (2012).
- [54] J. Martin and L. Sriramkumar, *JCAP* **1201**, 008 (2012).

- 
- [55] F. Arroja, A. E. Romano and M. Sasaki, *Phys. Rev. D* **84**, 123503 (2011); F. Arroja and M. Sasaki, *JCAP* **1208**, 012 (2012).
- [56] A. Gangui, F. Lucchin, S. Matarrese and S. Mollerach, *Astrophys. J.* **430**, 447 (1994); A. Gangui, *Phys. Rev. D* **50**, 3684 (1994); A. Gangui and J. Martin, *Mon. Not. Roy. Astron. Soc.* **313**, 323 (2000); *Phys. Rev. D* **62**, 103004 (2000).
- [57] E. Komatsu and D. N. Spergel, *Phys. Rev. D* **63**, 063002 (2001); E. Komatsu, D. N. Spergel and B. D. Wandelt, *Astrophys. J.* **634**, 14 (2005); D. Babich and M. Zaldarriaga, *Phys. Rev. D* **70**, 083005 (2004); M. Liguori, F. K. Hansen, E. Komatsu, S. Matarrese and A. Riotto, *Phys. Rev. D* **73**, 043505 (2006); C. Hikage, E. Komatsu and T. Matsubara, *Astrophys. J.* **653** (2006) 11 (2006); J. R. Fergusson and E. P. S. Shellard, *Phys. Rev. D* **76**, 083523 (2007); A. P. S. Yadav, E. Komatsu and B. D. Wandelt, *Astrophys. J.* **664**, 680 (2007); P. Creminelli, L. Senatore and M. Zaldarriaga, *JCAP* **0703**, 019 (2007); A. P. S. Yadav and B. D. Wandelt, *Phys. Rev. Lett.* **100**, 181301 (2008); C. Hikage, T. Matsubara, P. Coles, M. Liguori, F. K. Hansen and S. Matarrese, *Mon. Not. Roy. Astron. Soc.* **389**, 1439 (2008); O. Rudjord, F. K. Hansen, X. Lan, M. Liguori, D. Marinucci and S. Matarrese, *Astrophys. J.* **701**, 369 (2009); K. M. Smith, L. Senatore and M. Zaldarriaga, *JCAP* **0909**, 006 (2009); J. Smidt, A. Amblard, C. T. Byrnes, A. Cooray, A. Heavens and D. Munshi, *Phys. Rev. D* **81**, 123007 (2010); J. R. Fergusson, M. Liguori and E. P. S. Shellard, arXiv:1006.1642v1 [astro-ph.CO].
- [58] M. Liguori, E. Sefusatti, J. R. Fergusson and E. P. S. Shellard, *Adv. Astron.* **2010**, 980523 (2010); A. P. S. Yadav and B. D. Wandelt, arXiv:1006.0275v3 [astro-ph.CO]; E. Komatsu, *Class. Quantum Grav.* **27**, 124010 (2010).
- [59] C. Pitrou, J.-P. Uzan and F. Bernardeau, *JCAP* **1007**, 003 (2010).
- [60] J. H. Traschen and R. H. Brandenberger, *Phys. Rev. D* **42**, 2491 (1990); Y. Shtanov, J. H. Traschen and R. H. Brandenberger, *Phys. Rev. D* **51**, 5438 (1995); L. Kofman, A. Linde and A. Starobinsky, *Phys. Rev. D* **56**, 3258 (1997).
- [61] M. S. Turner, *Phys. Rev. D* **28**, 1243 (1983); A. Albrecht, P. J. Steinhardt, M. S. Turner and F. Wilczek, *Phys. Rev. Lett.* **48**, 1437 (1982).
- [62] F. Finelli and R. Brandenberger, *Phys. Rev. Lett.* **82**, 1362 (1999).
- [63] K. Jedamzik, M. Lemoine and J. Martin, *JCAP* **09**, 034 (2010); *JCAP* **04**, 021 (2010).

- [64] R. Easther, R. Flauger and J. G. Gilmore, *JCAP* **04**, 027 (2011).
- [65] M. Takada, E. Komatsu and T. Futamase, *Phys. Rev. D* **73**, 083520 (2006).
- [66] M. Rauch, *Annu. Rev. Astron. Astrophys.* **36**, 267 (1998).
- [67] See, <http://cosmology.lbl.gov/BOSS>.
- [68] See, <http://bigboss.lbl.gov/index.html>.
- [69] S. Hannestad, *Phys. Rev. D* **63**, 043009 (2001); S. L. Bridle, A. M. Lewis, J. Weller and G. Efstathiou, *Mon. Not. Roy. Astron. Soc.* **342**, L72 (2003); P. Mukherjee and Y. Wang, *Astrophys. J.* **599**, 1 (2003); S. Hannestad, *JCAP* **0404**, 002 (2004); A. Shafieloo and T. Souradeep, *Phys. Rev. D* **70**, 043523 (2004); D. Tocchini-Valentini, Y. Hoffman and J. Silk, *Mon. Not. Roy. Astron. Soc.* **367**, 1095 (2006); A. Shafieloo, T. Souradeep, P. Manimaran, P. K. Panigrahi and R. Rangarajan, *Phys. Rev. D* **75**, 123502 (2007); A. Shafieloo and T. Souradeep, *Phys. Rev. D* **78**, 023511 (2008); R. Nagata and J. Yokoyama, *Phys. Rev. D* **79**, 043010 (2009); G. Nicholson and C. R. Contaldi, *JCAP* **0907**, 011 (2009).
- [70] M. Bridges, F. Feroz, M. P. Hobson and A. N. Lasenby, *Mon. Not. Roy. Astron. Soc.* **400**, 1075 (2009); H. V. Peiris and L. Verde, *Phys. Rev. D* **81**, 021302 (2010); Z-K. Guo, D. J. Schwarz and Y.-Z. Zhang, *JCAP* **1108**, 031 (2011).
- [71] A. A. Starobinsky, *Sov. Phys. JETP Lett.* **55**, 489 (1992).
- [72] C. Dvorkin and W. Hu, *Phys. Rev. D* **81**, 023518 (2010); W. Hu, *Phys. Rev. D* **84**, 027303 (2011).
- [73] J. A. Adams, B. Cresswell and R. Easther, *Phys. Rev. D* **64**, 123514 (2001).
- [74] L. Covi, J. Hamann, A. Melchiorri, A. Slosar and I. Sorbera, *Phys. Rev. D* **74**, 083509 (2006); J. Hamann, L. Covi, A. Melchiorri and A. Slosar, *Phys. Rev. D* **76**, 023503 (2007).
- [75] M. J. Mortonson, C. Dvorkin, H. V. Peiris and W. Hu, *Phys. Rev. D* **79**, 103519 (2009).
- [76] M. Joy, V. Sahni, A. A. Starobinsky, *Phys. Rev. D* **77**, 023514 (2008); M. Joy, A. Shafieloo, V. Sahni, A. A. Starobinsky, *JCAP* **0906**, 028 (2009).

- [77] R. K. Jain, P. Chingangbam, J.-O. Gong, L. Sriramkumar and T. Souradeep, JCAP **0901**, 009 (2009); R. K. Jain, P. Chingangbam, L. Sriramkumar and T. Souradeep, Phys. Rev. D **82**, 023509 (2010).
- [78] G. Efstathiou and S. Chongchitnan, Prog. Theor. Phys. Suppl. **163**, 204 (2006).
- [79] D. A. Steer and F. Vernizzi, Phys. Rev. D **70**, 043527 (2004).
- [80] W. H. Kinney and K. T. Mahanthappa, Phys. Rev. D **52**, 5529 (1995); Phys. Lett. B **383**, 24 (1996).
- [81] D. S. Salopek, J. R. Bond and J. M. Bardeen, Phys. Rev. D **40**, 1753 (1989).
- [82] C. Ringeval, Lect. Notes Phys. **738**, 243 (2008).
- [83] R. K. Jain, P. Chingangbam and L. Sriramkumar, JCAP **0710**, 003 (2007).
- [84] See, <http://lambda.gsfc.nasa.gov/>.
- [85] D. K. Hazra, M. Aich, R. K. Jain, L. Sriramkumar and T. Souradeep, JCAP **1010**, 008 (2010).
- [86] M. Aich, *Key Observational Issues in the Cosmic Microwave Background*, Ph.D. Thesis, Inter University Centre for Astronomy and Astrophysics, Pune, India, October 2011.
- [87] M. Benetti, M. Lattanzi, E. Calabrese and A. Melchiorri, Phys. Rev. D **84**, 063509 (2011).
- [88] J. M. Cline, P. Crotty and J. Lesgourgues, JCAP **0309**, 010 (2003).
- [89] P. Hunt and S. Sarkar, Phys. Rev. D **70**, 103518 (2004); Phys. Rev. D **76**, 123504 (2007).
- [90] S. Tsujikawa, D. Parkinson and B. A. Bassett, Phys. Rev. D **67**, 083516 (2003); D. Parkinson, S. Tsujikawa and B. A. Bassett, Phys. Rev. D **71**, 063524 (2005).
- [91] B. Feng and X. Zhang, Phys. Lett. B **570**, 145 (2003); M. Kawasaki and F. Takahashi, Phys. Lett. B **570**, 151 (2003); R. Sinha and T. Souradeep, Phys. Rev. D **74**, 043518 (2006); M. J. Mortonson and W. Hu, Phys. Rev. D **80**, 027301 (2009).

- [92] M. Kawasaki, F. Takahashi and T. Takahashi, *Phys. Letts. B* **605**, 223 (2005); J.-O. Gong, *JCAP* **0507**, 015 (2005); M. Kawasaki and K. Miyamoto, arXiv:1010.3095v2 [astro-ph.CO]; A. Achúcarro, J.-O. Gong, S. Hardeman, G. A. Palma and S. P. Patil, *JCAP* **1101**, 030 (2011); K. Kumazaki, S. Yokoyama and N. Sugiyama, *JCAP* **1112**, 008 (2011).
- [93] J. M. Cline, P. Crotty and J. Lesgourgues, *JCAP* **0309**, 010 (2003); C. R. Contaldi, M. Peloso, L. Kofman and A. Linde, *JCAP* **0307**, 002 (2003); L. Sriramkumar and T. Padmanabhan, *Phys. Rev. D* **71**, 103512 (2005); D. Boyanovsky, H. J. de Vega and N. G. Sanchez, *Phys. Rev. D* **74**, 123006 (2006); *Phys. Rev. D* **74**, 123007 (2006); B. A. Powell and W. H. Kinney, *Phys. Rev. D* **76**, 063512 (2007); C. Destri, H. J. de Vega and N. G. Sanchez, *Phys. Rev. D* **78**, 023013 (2008).
- [94] J. Martin and C. Ringeval, *Phys. Rev. D* **69**, 083515 (2004); *Phys. Rev. D* **69**, 127303 (2004); *JCAP* **0501**, 007 (2005).
- [95] M. Zarei, *Phys. Rev. D* **78**, 123502 (2008).
- [96] P. D. Meerburg, R. Wijers and J. P. van der Schaar, *Mon. Not. Roy. Astron. Soc.* **421**, 369 (2012).
- [97] C. Pahud, M. Kamionkowski and A. R. Liddle, *Phys. Rev. D* **79**, 083503 (2009).
- [98] R. Flauger, L. McAllister, E. Pajer, A. Westphal and G. Xu, *JCAP* **1006**, 009 (2010); R. Flauger and E. Pajer, *JCAP* **1101**, 017 (2011).
- [99] T. Kobayashi and F. Takahashi, *JCAP* **1101**, 026 (2011).
- [100] Z. Huang, *JCAP* **1206**, 012 (2012).
- [101] M. Aich, D. K. Hazra, L. Sriramkumar and T. Souradeep, arXiv:1106.2798v1 [astro-ph.CO].
- [102] A. Gangui, J. Martin and M. Sakellariadou, *Phys. Rev. D* **66**, 083502 (2002); R. Holman and A. J. Tolley, *JCAP* **0805**, 001 (2008); W. Xue and B. Chen, *Phys. Rev. D* **79**, 043518 (2009); P. D. Meerburg, J. P. van der Schaar and P. S. Corasaniti, *JCAP* **0905**, 018 (2009); X. Chen, *JCAP* **1012**, 003 (2010); A. Ashoorioon and G. Shiu, *JCAP* **1103**, 025 (2011); S. Kundu, *JCAP* **1202**, 005 (2012); P. D. Meerburg, R. Wijers and J. P. van der Schaar, *Mon. Not. Roy. Astron. Soc.* **421**, 369 (2012).

- [103] R. Allahverdi, J. Garcia-Bellido, K. Enqvist and A. Mazumdar *Phys. Rev. Lett.* **97**, 191304 (2006); R. Allahverdi, K. Enqvist, J. Garcia-Bellido, A. Jokinen and A. Mazumdar, *JCAP* **0706**, 019 (2007); J. C. B. Sanchez, K. Dimopoulos and D. H. Lyth, *JCAP* **0701**, 015 (2007).
- [104] H. M. Hodges, G. R. Blumenthal, L. A. Kofman and J. R. Primack, *Nucl. Phys. B* **335**, 197 (1990).
- [105] L. F. Abbott and M. B. Wise, *Nucl. Phys. B* **244**, 541 (1984); D. H. Lyth and E. D. Stewart, *Phys. Lett. B* **274**, 168 (1992); J. Martin and D. J. Schwarz, *Phys. Rev. D* **57**, 3302 (1998); L. Sriramkumar and T. Padmanabhan, *Phys. Rev. D* **71**, 103512 (2005).
- [106] W. H. Press, S. A. Teukolsky, W. T. Vetterling and B. P. Flannery, *Numerical Recipes in Fortran 90*, Second edition (Cambridge University Press, Cambridge, England, 1996).
- [107] See, for instance, <http://www.nag.com/> and <http://www.netlib.org/>.
- [108] See, <http://www.wolfram.com/>.
- [109] D. K. Hazra, L. Sriramkumar and J. Martin, arXiv:1201.0926v1 [astro-ph.CO].
- [110] P. Creminelli and M. Zaldarriaga, *JCAP* 0410, 006 (2004).
- [111] S. Renaux-Petel, *JCAP* 1010, 020 (2010).
- [112] J. Martin and C. Ringeval, *JCAP* 0608, 009 (2006); *Phys. Rev. D* **82**, 023511 (2010).
- [113] D. I. Podolsky, G. N. Felder, L. Kofman and M. Peloso, *Phys. Rev. D* **73**, 023501 (2006).
- [114] C. M. Bender and S. A. Orszag, *Advanced Mathematical Methods for Scientists and Engineers* (McGraw Hill, New York, 1978), Chapter 11.
- [115] M. Abramowitz and I. A. Stegun, *Handbook of Mathematical Functions* (Dover, New York, 1965).
- [116] I. S. Gradshteyn and I. M. Ryzhik, *Table of Integrals, Series and Products* (Academic, New York, 1980).
- [117] D. K. Hazra, J. Martin and L. Sriramkumar, *Phys. Rev. D* **86**, 063523 (2012).

- [118] K. Kohri, D. H. Lyth and C. A. Valenzuela-Toledo, JCAP **1002**, 023 (2010).
- [119] A. R. Liddle, D. H. Lyth, K. A. Malik and D. Wands, Phys. Rev. D **61**, 103509 (2000).
- [120] S. Weinberg, Phys. Rev. D **72**, 043514 (2005); Phys. Rev. D **74**, 023508 (2006); Phys. Rev. D **78**, 123521 (2008); Phys. Rev. D **79**, 043504 (2009); Phys. Rev. D **83**, 063508 (2011).
- [121] L. Lorenz, J. Martin and C. Ringeval, Phys. Rev. D **78**, 063543 (2008); Phys. Rev. D **78**, 083513 (2008).
- [122] J. Lachapelle and R. H. Brandenberger, JCAP **0904**, 020 (2009).
- [123] G. I. Rigopoulos, E. P. S. Shellard and B. J. W. van Tent, Phys. Rev. D **73**, 083522 (2006); D. Seery and J. E. Lidsey, JCAP **0509**, 011 (2005); F. Arroja, S. Mizuno and K. Koyama, JCAP **0808**, 015 (2008); X. Gao, JCAP **0806**, 029 (2008); S. Mizuno, F. Arroja and K. Koyama, Phys. Rev. D **80**, 083517 (2009); S. Renaux-Petel, S. Mizuno and K. Koyama, JCAP **1111**, 042 (2011).
- [124] F. Finelli and R. Brandenberger, Phys. Rev. D **62**, 083502 (2000).
- [125] K. Enqvist, A. Jokinen, A. Mazumdar, T. Multamaki and A. Vaihkonen, Phys. Rev. Lett. **94**, 161301 (2005).
- [126] L. F. S. Rodrigues and R. Opher, Phys. Rev. D **82**, 023501 (2010).
- [127] R. E. Smith *et al.*, Mon. Not. Roy. Astron. Soc. **341**, 1311 (2003); M. Tegmark *et al.*, Phys. Rev. D **74**, 123507 (2006); W. J. Percival *et al.*, Astrophys. J. **657**, 645 (2007).
- [128] L. Wang and P. J. Steinhardt, Astrophys. J. **508**, 483 (1998); E. V. Linder and A. Jenkins, Mon. Not. Roy. Astron. Soc. **346**, 573 (2003).
- [129] A. Jenkins, C. S. Frenk, S. D. M. White, J. M. Colberg, S. Cole, A. E. Evrard, H. M. P. Couchman and N. Yoshida, Mon. Not. Roy. Astron. Soc. **321**, 372 (2001).
- [130] R. K. Sheth, H. J. Mo and G. Tormen, Mon. Not. Roy. Astron. Soc. **323**, 1 (2001); R. K. Sheth and G. Tormen, Mon. Not. Roy. Astron. Soc. **329**, 61 (2002).
- [131] W. H. Press and P. Schechter, Astrophys. J. **187**, 425 (1974).

- [132] S. Sasaki, *Publ. Astron. Soc. Jap.* **46**, 427 (1994); E. Ripamonti, *Mon. Not. Roy. Astron. Soc.* **376**, 709 (2007); S. Mitra, G. Kulkarni, J. S. Bagla and J. K. Yadav, *Bull. Astron. Soc. Ind.* **39**, 1,(2011).
- [133] See, <http://www.mpa-garching.mpg.de/~komatsu/CRL/index.html>.
- [134] F. Finelli, J. Hamann, S. M. Leach and J. Lesgourgues, *JCAP* **04** 011 (2010)
- [135] D. K. Hazra, In preparation.
- [136] V. Desjacques and U. Seljak, *Class. Quantum Grav.* **27**, 124011 (2010); R. Scoccamarro, E. Sefusatti, and M. Zaldarriaga, *Phys. Rev. D* **69**, 103513 (2004).
- [137] U. Seljak, A. Slosar and P. McDonald, *JCAP* **10**, 14 (2006); P. McDonald and D. J. Eisenstein, *Phys. Rev. D* **76**, 063009 (2007); R. A. C. Croft, W. Hu and R. Davé, *Phys. Rev. Lett.* **83**, 1092 (1999); S. Gallerani, T. R. Choudhury, and A. Ferrara, *Mon. Not. Roy. Astron. Soc.* **370**, 1401 (2006).
- [138] R. A. C. Croft *et al.*, *Astrophys. J.* **520**, 1 (1999); R. Mandelbaum, P. McDonald, U. Seljak, and R. Cen, *Mon. Not. Roy. Astron. Soc.* **344**, 776 (2003); M. Viel, *et al.*, *Mon. Not. Roy. Astron. Soc.* **347**, L26 (2004); M. Viel *et al.*, *Mon. Not. Roy. Astron. Soc.* **393**, 774 (2009).
- [139] M. McQuinn, and M. White, *Mon. Not. Roy. Astron. Soc.* **415**, 2257 (2011); T. Guha Sarkar, S. Bharadwaj, T. R. Choudhury and K. K. Datta, *Mon. Not. Roy. Astron. Soc.* **410**, 1130 (2011).
- [140] M. Viel *et al.*, *Mon. Not. Roy. Astron. Soc.* **774**, 393 (2009).
- [141] J. M. Bardeen, J. R. Bond, N. Kaiser, A. S. Szalay, *Astrophys. J.* **304**, 15 (1986).
- [142] L. Hui and N. Y. Gnedin, *Mon. Not. Roy. Astron. Soc.* **292**, 27 (1997); N. Y. Gnedin, and L. Hui, *Mon. Not. Roy. Astron. Soc.* **296**, 44 (1998); P. McDonald *et al.*, *Astrophys. J.* **562**, 52 (2001).
- [143] J. E. Gunn and B. A. Peterson, *Astrophys. J.* **142**, 1633 (1965); H. Bi and B. A. David-  
sen, *Astrophys. J.* **479**, 523 (1997)
- [144] T. S. Kim, J. S. Bolton, M. Viel, M. G. Haehnelt and R. F. Carswell, *Mon. Not. Roy. Astron. Soc.* **382**, 1657 (2007).

## BIBLIOGRAPHY

---

- [145] P. McDonald, *Astrophys. J.* **585**, 34 (2003).
- [146] U. Seljak, *JCAP* **1203**, 4 (2012).
- [147] A. D. Myers *et al.*, *Astrophys. J.* **658**, 99 (2007).
- [148] D. P. Schneider *et al.*, *Astrophys. J.* **130**, 367 (2005).
- [149] D. K. Hazra and T. G. Sarkar, *Phys. Rev. Lett.* **109**, 121301, (2012).
- [150] T. G. Sarkar and D. K. Hazra, In preparation.